

Thermal transport in sodium boiling flows for concentrating solar thermal applications

Siddharth Iyer

A thesis submitted for the degree of
Doctor of Philosophy
The Australian National University

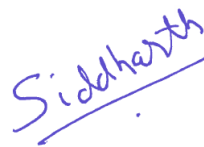
Primary supervisor: Prof. Wojciech Lipiński

December 2022

Supervisory panel

Prof. Wojciech Lipiński	Primary supervisor
A/Prof. Joe Coventry	Associate supervisor
Dr Apurv Kumar	Associate supervisor

Except where otherwise indicated, this thesis is my own original work. No material in this thesis has been previously submitted for the purpose of obtaining a degree in any university or other tertiary education institution.

A handwritten signature in blue ink, reading "Siddharth", with a horizontal line underneath it.

Siddharth Iyer
22 December 2022

To my family

Acknowledgments

I owe my deepest gratitude to my supervisors Prof. Wojciech Lipiński, Associate Professor Joe Coventry and Dr Apurv Kumar for giving me the opportunity to pursue this doctoral project. This work in its current form would not have been possible without their generous support and guidance. They have provided an excellent work environment which has allowed me to grow as a researcher and have mentored me with invaluable career and life advices.

I would like to thank my colleagues in the Solar Thermal Group and the Craig Building for the lively conversations during the numerous coffee breaks and for their help during this study.

Special thanks to all my friends in Canberra for making the last 4.5 years an enjoyable time. Those weekend cricket sessions were a great stress buster and kept me in good physical shape.

I would like to acknowledge the financial support from the Australian Research Council (grant no LP150101189) and thank our project partner Vast Solar Pty Ltd for their support and contributions.

Finally, I would like to thank my family for their unwavering support and for encouraging me to pursue my dreams.

Abstract

Understanding heat and mass transfer phenomena in nucleate boiling of liquid metals such as sodium is an emerging field of study, in particular for the development of next generation concentrating solar thermal power plants with boiling sodium as the heat transfer fluid. The research presented in this doctoral project is focused on advancing the knowledge of sodium boiling by developing comprehensive physics-based bubble growth models. Such models can highlight the governing heat transfer and hydrodynamic phenomena dominating the bubble growth process in sodium, thus aiding the development of efficient sodium boiling systems.

In the first part of this work, two numerical heat transfer models are developed with the aim of quantifying the influence of heat transfer mechanisms on the growth of a bubble in sodium pool boiling. In the first model the governing mass, momentum and energy conservation equations are solved to compute the evaporative heat flux from a region where the liquid–vapour interface of the bubble meets the wall, referred to as the contact line region. The model accounts for the influence of an electron pressure component on the evaporation of the fluid film in the contact line region in sodium. The results show that for the same wall superheat, the heat flux from sodium is six times larger compared to a high Prandtl number fluid, here FC-72, due to the high thermal conductivity of the liquid metal. The second numerical model predicts the growth rate of a sodium bubble based on the heat transferred from a microlayer (which is a thin layer of fluid formed underneath a bubble), the thermal boundary layer, and the bulk liquid surrounding the bubble. The model accounts for the variation in the wall temperature below the bubble as the liquid in the microlayer and the thermal boundary layer evaporates. Predictions from the model for a bubble growing with a constant contact angle indicate that the microlayer evaporation is the dominant heat transfer mechanism during the initial phase of bubble growth after nucleation. In addition, a parametric study conducted to study the effect of wall superheat indicated that the larger the wall superheat, the larger is the growth rate and radius of a sodium bubble.

The development of a comprehensive mechanistic bubble growth model accounting for the variation in the contact angle and the shape of a bubble is pursued next. The heat transfer model that was developed based on the evaporation of the microlayer in the first part of this project is coupled to a force and a contact angle sub-model to study the complete bubble growth process from nucleation to departure in pool boiling. A novel methodology is presented to approximate the balloon-like shape of a bubble prior to departure as a truncated sphere atop a conical bottleneck. The model is extensively

verified and validated against high-fidelity CFD simulations and experimental data on pool boiling of water and methanol from literature, and shows good agreement. The validated mechanistic model is then used to simulate the bubble growth process in sodium and to investigate the effects of wall superheat, contact angle rate, bulk liquid temperature and the accommodation coefficient on the bubble growth and departure characteristics. It is found that a sodium bubble is typically large with departure radius on the order of a few centimetres. In addition, it is observed that smaller the wall superheat, the greater is the tendency of the bubble to have a balloon-like shape at departure.

List of Publications

Journal articles

- **S. Iyer**, A. Kumar, J. Coventry, J. Pye, and W. Lipiński, Micro-scale heat transfer modelling of the contact line region of a boiling-sodium bubble, *International Journal of Heat and Mass Transfer*, vol. 160, p. 120106, 2020.
- **S. Iyer**, A. Kumar, J. Coventry, and W. Lipiński, Heat transfer modelling of an isolated bubble in sodium pool boiling, *International Journal of Thermal Sciences*, vol. 179, p. 107678, 2022.
- **S. Iyer**, A. Kumar, J. Coventry, and W. Lipiński, Modelling of bubble growth and detachment in nucleate pool boiling, *International Journal of Thermal Sciences*, vol. 185, p. 108041, 2023.
- **S. Iyer**, A. Kumar, J. Coventry, and W. Lipiński, Mechanistic modelling of bubble growth in sodium pool boiling, *Applied Mathematical Modelling*, vol. 116, pp. 1–24, 2023.
- W. Lipiński, E. Abbasi-Shavazi, J. Chen, J. Coventry, M. Hangi, **S. Iyer**, A. Kumar, L. Li, S. Li, J. Pye, J. F. Torres, B. Wang, Y. Wang, and V. Wheeler, Progress in heat transfer research for high-temperature solar thermal applications, *Applied Thermal Engineering*, p. 116137, 2021.
- W. Lipiński, J. Chen, J. Coventry, Y. Guo, M. Hangi, **S. Iyer**, A. Kumar, A. Rahbari, J. F. Torres, V. Wheeler, L. Dombrovsky, M. Modest, and A. Steinfeld, Radiative transfer in high-temperature solar thermal energy systems, *Progress in Energy and Combustion Science*, In preparation.

Conference presentations

- **S. Iyer**, A. Kumar, J. Coventry, J. Pye, and W. Lipiński, On microlayer growth in liquid metal boiling flows, *Asia Pacific Solar Research Conference (APSRC)*, UNSW Sydney, December 4–6, 2018. Poster presentation. Best poster award.
- **S. Iyer**, A. Kumar, J. Coventry, J. Pye, and W. Lipiński, Microlayer growth in sodium boiling flows, *10th International Conference on Multiphase Flows*, Rio de

Janeiro, Brazil, May 19–24, 2019. Oral presentation.

- **S. Iyer**, A. Kumar, J. Coventry, and W. Lipiński, Heat transfer modelling of an isolated bubble in sodium pool boiling, *CHT-21, International Symposium on Advances in Computational Heat Transfer*, Virtual, August 15–19, 2021. Oral presentation.
- **S. Iyer**, A. Kumar, J. Coventry, and W. Lipiński, Mechanistic Modelling of isolated bubble growth in sodium pool boiling, *AIChE 4th Solar Energy Systems Conference*, Virtual, May 18–19, 2022. Oral presentation.
- J. Coventry, J. Pye, A. Kumar, **S. Iyer**, Z. Kee, and W. Lipiński, A sodium boiler and phase-change energy storage system, *SolarPACES 2018*, Casablanca, Morocco, October 2–5, 2018. Oral presentation.

Contents

Acknowledgments	vii
Abstract	ix
List of Publications	xi
List of Figures	xv
List of Tables	xx
Nomenclature	xxii
1 Introduction	1
1.1 Background	2
1.2 Motivation	5
1.3 Research objectives	7
1.4 Overview	9
2 Theoretical background and literature review	11
2.1 Single bubble growth in nucleate pool boiling	11
2.2 Bubble growth mechanism	13
2.3 Heat transfer to a bubble in pool boiling	15
2.3.1 Microscale heat transfer	16
2.3.2 Macrolayer and thermal boundary layer heat transfer	24
2.3.3 Bulk liquid heat transfer	24
2.4 Forces acting on a bubble in pool boiling	25
2.5 Contact angle and bubble shape in pool boiling	29
2.6 Characteristics of liquid metal nucleate boiling	31
2.6.1 Wall superheat	33
2.6.2 Heat transfer and bubble growth characteristics in sodium pool boiling	35
2.6.3 Departure diameter and departure time in sodium pool boiling . .	38
2.7 Summary	39

3	Heat transfer modelling of the contact line region	41
3.1	Introduction	41
3.2	Mass, momentum and energy conservation equations	42
3.3	Boundary-value problem	43
3.4	Verification of the model and validation of assumptions	45
3.4.1	Verification of the contact line model	45
3.4.2	Validity of the linear mass transfer model in the boiling sodium contact line region	46
3.5	Results and discussion	48
3.5.1	Contact line region characteristics in sodium and FC-72	49
3.5.2	Effect of wall superheat	52
3.5.3	Effect of vapour temperature	54
3.5.4	Effect of the electron pressure parameter	55
3.5.5	Effect of the accommodation coefficient	58
3.5.6	Utility of contact line models	58
3.6	Summary	60
4	Heat transfer modelling of an isolated bubble in pool boiling	62
4.1	Introduction	62
4.2	Problem description	63
4.3	Heat transfer model	65
4.3.1	Microlayer heat transfer	66
4.3.2	Heat transfer from the macrolayer and thermal boundary layer . .	67
4.3.3	Heat transfer from the bulk liquid to the bubble	68
4.3.4	Heat transfer from the wall to the bulk liquid	68
4.3.5	Total heat transfer to a bubble	69
4.3.6	Heat transfer in the wall	69
4.4	Boundary and initial conditions	70
4.5	Initial conditions	71
4.6	Evaluation of thermal boundary layer heat transfer model assumption . .	71
4.7	Numerical solution and validation	73
4.8	Results and discussion	74
4.8.1	Sodium heat transfer and growth characteristics	76
4.8.2	Effect of wall superheat	79
4.8.3	Effect of contact angle	82
4.8.4	Effect of bulk liquid temperature	85
4.8.5	Effect of accommodation coefficient	87
4.8.6	Comparison with the theoretical relationship of Dwyer	90
4.9	Accuracy consideration	93

4.10	Summary	93
5	Development and validation of a mechanistic bubble growth model	95
5.1	Introduction	95
5.2	Bubble shape transition in pool boiling	97
5.3	Mechanistic model	98
5.3.1	Contact angle and bottleneck sub-model	98
5.3.2	Boundary and initial conditions	100
5.4	Experimental and computational data sets for validation and verification	102
5.5	Results and discussion	103
5.5.1	Model verification and validation	104
5.5.2	Heat transfer and forces acting on a bubble	112
5.6	Summary	113
6	Mechanistic modelling of bubble growth in sodium pool boiling	115
6.1	Introduction	115
6.2	Problem statement	116
6.3	Results and discussion	117
6.3.1	Sodium bubble growth characteristics	117
6.3.2	Effect of wall superheat	120
6.3.3	Effect of the rate of change of the contact angle	125
6.3.4	Effect of the bulk liquid temperature	129
6.3.5	Effect of accommodation coefficient	132
6.4	Summary	133
7	Summary and conclusions	135
7.1	Summary	135
7.2	Outlook	137

List of Figures

1.1	Schematic of a CSP plant with a sodium tubular boiler.	6
1.2	Heat transfer processes involved in the growth of a bubble in pool boiling including the evaporation of the (a) microlayer [14–16, 60] and (b) contact line region [61–63].	8
2.1	Schematic representation of the bubble growth cycle.	12
2.2	Pressure temperature relationship during growth of a bubble in a superheated liquid pool	14
2.3	Schematic of the contact line region in a bubble [59, 61, 89].	17
2.4	Schematic of the microlayer region in a bubble.	21
2.5	Forces acting on a bubble in pool boiling.	27
2.6	Bubble shape during the growth of a bubble in pentane pool boiling recorded at 375 fps in the experiment of Seidel et al. [121]	29
2.7	Bubble shape at four different points in time during the growth of a bubble in water pool boiling experiment of Duan et al. [13].	30
2.8	Variation of wall superheat required for bubble nucleation in sodium and water boiling with cavity radius at atmospheric pressure.	34
2.9	Schematic of the heat transfer to a bubble as proposed by Deane and Rohsenow	37
3.1	Validation of the contact line model with DNS.	46
3.2	Comparison of mass flux obtained using the linear and non-linear mass transfer models for pressure $p_c = 0$ Pa.	47
3.3	Variation of (a) film thickness and (b) contact angle in the contact line region in sodium and FC-72 for a wall superheat of 15 K.	49
3.4	Variation of (a) disjoining pressure and (b) capillary pressure in the contact line region in sodium and FC-72 for a wall superheat of 15 K.	50
3.5	Variation of evaporative heat flux in the contact line region in sodium and FC-72 for a wall superheat of 15 K.	51
3.6	Variation of interface temperature in the contact line region in sodium and FC-72 for a wall superheat of 15 K.	52
3.7	Variation of conductive and total thermal resistance in the contact line region in sodium and FC-72 for a wall superheat of 15 K.	53

3.8	Effect of wall superheat on (a) evaporative heat flux and (b) interface temperature (c) disjoining pressure and (d) capillary pressure in the contact line region in sodium boiling.	54
3.9	Effect of wall superheat on the film thickness in sodium boiling.	55
3.10	Effect of the vapour temperature on (a) evaporative heat flux (b) interface thermal resistance and (c) film thickness in the contact line region for a wall superheat of 25 K.	56
3.11	Effect of the electron pressure parameter on (a) film thickness (b) disjoining pressure (c) evaporative heat flux and (d) integrated heat flux in the contact line region for a wall superheat of 25 K.	57
3.12	Effect of the accommodation coefficient on (a) evaporative heat flux and (b) film thickness in the contact line region for a wall superheat of 25 K. .	59
3.13	Effect of electron pressure parameter on the integrated heat flux at the end of the contact line region for (a) different wall temperature and (b) different vapour temperature.	59
4.1	Heat transfer to a bubble in nucleate pool boiling at times t_1 and t_2 where $t_1 < t_2$	64
4.2	Wall heat transfer and boundary conditions.	70
4.3	Geometry and boundary conditions used for the heat transfer simulation of the thermal boundary layer.	72
4.4	Contour plot of temperature in the thermal boundary layer for $T_v = 1100$ K and $T_\infty = 1098$ K.	73
4.5	Comparison of temperature distribution at a distance of 0.5 mm from the interface with the analytical temperature profile given by Eq. (4.1) for (a) $T_\infty = 1098$ K and (b) $T_\infty = 1073$ K.	73
4.6	Wall temperatures obtained for different cell sizes and time step sizes at time $t = 2.5$ ms.	74
4.7	Comparison of wall temperatures obtained using the present model with temperatures obtained from the experiment of Duan et al. [13] and CFD simulation of Sato et al. [15] at (a) $t = 0.42$ ms (b) $t = 2.5$ ms.	75
4.8	Bubble growth and heat transfer characteristics in sodium pool boiling at a superheat of 50 K and bulk liquid temperature of $T_\infty = 1098$ K: (a) bubble growth rate, (b) vapour temperature, (c) bubble radius and (d) rate of heat transferred from the microlayer \dot{Q}_m , the macrolayer \dot{Q}_{ma} , the thermal boundary layer \dot{Q}_t and bulk liquid \dot{Q}_∞ to the bubble.	77
4.9	Sodium microlayer thickness for a wall superheat of 50 K and bulk liquid temperature of $T_\infty = 1098$ K.	78

4.10	Variation in the parameter E with time in sodium pool boiling at a wall superheat of 50 K and a bulk liquid temperature of $T_{\infty} = 1098$ K.	79
4.11	Effect of wall superheat on the (a) bubble radius, (b) microlayer heat transfer rate \dot{Q}_m , (c) macrolayer heat transfer rate \dot{Q}_{ma} , (d) thermal boundary layer heat transfer rate \dot{Q}_t , (e) bulk liquid heat transfer rate \dot{Q}_{∞} and (f) transient variation of parameter E in sodium pool boiling.	80
4.12	Schematic of bubble profile for different contact angles.	82
4.13	Effect of contact angle on (a) bubble radius, (b) microlayer heat transfer rate \dot{Q}_m (c) macrolayer heat transfer rate \dot{Q}_{ma} , (d) thermal boundary layer heat transfer rate \dot{Q}_t , (e) bulk liquid heat transfer rate \dot{Q}_{∞} and (f) vapour temperature in sodium pool boiling at a wall superheat of 50 K and a bulk liquid temperature of $T_{\infty} = 1098$ K.	84
4.14	Effect of contact angle on the parameter (a) E_m , (b) E_{ma} , (c) E_t and (d) E_{∞} in sodium pool boiling at a wall superheat of 50 K and a bulk liquid temperature of $T_{\infty} = 1098$ K.	85
4.15	Effect of bulk liquid temperature on the (a) bubble radius, (b) vapour temperature, (c) microlayer heat transfer rate \dot{Q}_m and (d) bulk liquid heat transfer rate \dot{Q}_{∞} in sodium pool boiling at a wall superheat of 50 K. . . .	86
4.16	Effect of bulk liquid temperature on the parameter E in sodium pool boiling at a wall superheat of 50 K: (a) E_m , (b) E_{∞} and (c) E_t	88
4.17	Effect of accommodation coefficient on (a) bubble radius, (b) total bubble heat transfer rate, (c) vapour temperature, (d) and bulk liquid heat transfer rate in sodium pool boiling at a wall superheat of 50 K and a bulk liquid temperature of $T_{\infty} = 1098$ K.	89
4.18	Effect of accommodation on the parameter (a) E_m , (b) E_t and (c) E_{∞} in sodium pool boiling at a wall superheat of 50 K and a bulk liquid temperature of $T_{\infty} = 1098$ K.	91
4.19	Comparison of results obtained from the present model with the theoretical relationships of Dwyer [141] for a sodium bubble growing on a nickel heater at a wall superheat of 50 K and bulk liquid temperature of $T_{\infty} = 1123$ K: (a) bubble radius, (b) heat transfer from microlayer and bulk liquid, and (c) contribution of heat transfer from microlayer and bulk liquid to the total heat transferred to the bubble.	92
5.1	Schematic of transition in bubble shape from nucleation to departure. . .	97
5.2	Bottleneck in a bubble: (a) schematic of the bubble shape during the bottleneck phase showing the major dimensions used to model the growth of the bottleneck and (b) control volume used to model the growth of the bottleneck.	99

5.3	Flow chart of the model.	101
5.4	Wall temperatures obtained for different cell sizes and time step sizes at time $t = 2.5$ ms.	105
5.5	Comparison of equivalent bubble radius $r_{b,eq}$ and contact radius r_c obtained from the present model with data recorded from the experiments of Duan et al. [13] and CFD simulation of Sato et al. [15] assuming the formation of a (a) conical bottleneck and (b) cylindrical bottleneck. The variation in the dryout radius r_d with time is also shown.	106
5.6	Comparison of bubble radius obtained from the present model with the radius recorded from the methanol pool boiling experiment of Cole et al. [79].	107
5.7	Comparison of wall temperatures obtained from the present model with experiments of Duan et al. [13] and CFD simulation of Sato et al. [15] at time (a) $t = 0.4$ ms, (b) $t = 2.5$ ms, (c) $t = 6.7$ ms and (d) $t = 8.8$ ms.	109
5.8	Comparison of bubble shape obtained from the present model assuming the formation of a conical and cylindrical bottleneck with experimental observations of Duan et al. [13] and CFD simulation results of Sato et al. [15].	110
5.9	Comparison of microlayer profile obtained from the present model with CFD simulation results of Sato et al. [15] at time (a) $t = 0.5$ ms, (b) $t = 4$ ms and (c) $t = 7$ ms.	111
5.10	Temporal variation in the rate of heat transferred to a bubble from the microlayer \dot{Q}_m , the macrolayer \dot{Q}_{ma} , the thermal boundary layer \dot{Q}_t and the bulk liquid surrounding the bubble \dot{Q}_∞ in pool boiling of water.	113
5.11	Forces acting on a bubble in pool boiling of water (a) at the start of the bottleneck phase and (b) at departure.	113
6.1	Time histories of the bubble radius r_b , contact radius r_c and dryout radius r_d in sodium pool boiling.	117
6.2	Variation of vapour temperature in the bubble in sodium pool boiling.	118
6.3	Rate of heat transferred from the microlayer \dot{Q}_m , macrolayer \dot{Q}_{ma} , thermal boundary layer \dot{Q}_t and the bulk liquid \dot{Q}_∞ to a bubble in sodium pool boiling.	119
6.4	Forces acting on a sodium bubble.	120
6.5	Temporal variation in the shape of a sodium bubble in pool boiling where $t^* = t/t_{dep}$	121
6.6	Effect of wall superheat on the bubble radius r_b and contact radius r_c	122

6.7	Effect of wall superheat on the: (a) microlayer heat transfer rate \dot{Q}_m , (b) bulk liquid heat transfer rate \dot{Q}_∞ , (c) macrolayer heat transfer rate \dot{Q}_{ma} , (d) contribution of microlayer heat transfer E_m (e) contribution of bulk liquid heat transfer E_∞ and (f) contribution of macrolayer heat transfer E_{ma} in sodium pool boiling where $t^* = t/t_{dep}$	123
6.8	Temporal variation in the shape of a bubble in sodium pool boiling at different wall superheats where $t^* = t/t_{dep}$	124
6.9	Effect of rate of change of contact angle on: (a) bubble and contact radius, and (b) the contact angle in sodium pool boiling at a wall superheat of 50 K. 126	
6.10	Effect of rate of change of contact angle on the forces acting on a sodium bubble in sodium pool boiling at a wall superheat of 50 K: (a) Temporal variation in the buoyancy force, (b) temporal variation in the growth force, (c) temporal variation in the drag force and (d) forces acting on the bubble at the start of bottleneck formation.	127
6.11	Effect of rate of change of contact angle on the parameter (a) E_m , (b) E_∞ (c) E_{ma} and (d) the temperature of vapour in the bubble in sodium pool boiling at a wall superheat of 50 K where $t^* = t/t_{dep}$	128
6.12	Effect of rate of change of contact angle on the temporal variation in the shape of a bubble in sodium pool boiling where $t^* = t/t_{dep}$	130
6.13	Effect of bulk liquid temperature on the bubble and contact radius in sodium pool boiling at a wall superheat of 50 K.	131
6.14	Effect of bulk liquid temperature on the parameter E for a bubble growing in a sodium pool of temperature (a) $T_\infty = 1073$ K, (b) $T_\infty = 1098$ K and (c) $T_\infty = 1123$ K where $t^* = t/t_{dep}$	132
6.15	Effect of accommodation coefficient on the bubble and contact radius in sodium pool boiling at a wall superheat of 50 K.	133
6.16	Effect of accommodation coefficient on the total heat transferred to a bubble in sodium pool boiling at a wall superheat of 50 K.	133

List of Tables

1.1	Thermophysical properties of candidate heat transfer fluids at a pressure of 1 bar and 873 K.	3
2.1	Characteristic physical properties of water and sodium at saturation temperature and a pressure of 1 bar.	32
3.1	Thermophysical properties of FC-72 used in the numerical simulations. .	45
3.2	Constant properties of sodium used in the numerical simulations.	48
4.1	Thermophysical properties of nickel used in the numerical simulations. .	75
4.2	Baseline parameters and cases studied.	76
5.1	Thermophysical properties of water and sapphire used to simulate the water pool boiling experiment of Duan et al. [13].	104
5.2	Thermophysical properties of methanol and zirconium used to simulate the pool boiling experiment of Cole et al. [79].	104
6.1	Simulation parameters. The values in bold are for the baseline simulation case.	117
6.2	Bottleneck time, departure time and departure radius in sodium pool boiling at different wall superheats.	120
6.3	Bottleneck time, departure time and departure radius in sodium pool boiling for different rate of change of contact angle relations.	126

Nomenclature

\mathcal{A}	Hamaker constant (J)
A	area (m ²)
c_p	specific heat (J kg ⁻¹ K ⁻¹)
d	diameter (m)
E	parameter defined in Eq. (4.32)
E_o	Etövä number
f	accommodation coefficient
F	force (N)
F_b	buoyancy force (N)
F_{cp}	contact pressure force (N)
F_d	drag force (N)
F_g	growth force (N)
F_s	surface tension force (N)
Gr	Grashoff number
h_{lv}	latent heat (J kg ⁻¹)
h_{nc}	natural convection heat transfer coefficient (W m ⁻² K ⁻¹)
Ja	Jakob number
k	thermal conductivity (W m ⁻¹ K ⁻¹)
m''	mass flux (kg m ⁻² s ⁻¹)
Nu	Nusselt number
p	pressure (Pa)
p_c	difference between vapour and liquid pressure (Pa)

Pr	Prandtl number
\dot{Q}	heat rate (W)
q'	integrated heat flux (W m^{-1})
q''	heat flux (W m^{-2})
r	radial distance along the wall (m)
R_{int}	interface thermal resistance ($\text{m}^2 \text{K W}^{-1}$)
R	thermal resistance ($\text{m}^2 \text{K W}^{-1}$)
Re	Reynolds number
R_{gas}	specific gas constant ($\text{J kg}^{-1} \text{K}^{-1}$)
Ra	Rayleigh number
r_b	bubble radius (m)
T	temperature (K)
t	time (s)
ΔT	wall superheat (K)
Δt	time step size (s)
Δr	cell size in the radial direction (m)
Δz	cell size in the axial direction (m)
V	volume (m^3)
v_b	bubble growth rate (m s^{-1})
z	coordinate perpendicular to the wall (m)

Greek symbols

α	thermal diffusivity ($\text{m}^2 \text{s}^{-1}$)
β	contact angle ($^\circ$)
β	electron pressure parameter
δ	thickness (m)

ϵ_1, ϵ_2	perturbation values used in the contact line model
θ	contact angle in the contact line region ($^\circ$)
κ	curvature (m^{-1})
μ	dynamic viscosity (Pa s)
ν	kinematic viscosity ($\text{m}^2 \text{s}^{-1}$)
Π	total disjoining pressure (Pa)
Π_A	disjoining pressure (Pa)
Π_B	electron pressure (Pa)
ρ	density (kg m^{-3})
σ	surface tension (N m^{-1})

Superscripts

*	dimensionless
---	---------------

Subscripts

ad	adsorbed
b	bubble
bn	bottleneck
c	contact
cap	capillary
cur	curvature
d	dryout
dis	disjoining
e	evaporative
end	end of the contact line region
h	heater
int	interface

l	liquid
ma	macrolayer
max	maximum
min	minimum
m	microlayer
rec	recoil
sat	saturation
t	thermal boundary layer
v	vapour
w	wall
0	initial
∞	bulk liquid

Abbreviations

CFD	computational fluid dynamics
CSP	concentrated solar power
DNS	direct numerical simulation
HSV	high speed video
HTF	heat transfer fluid
PCM	phase change material

Introduction

The development of sustainable energy technologies is vital to meet the increasing global energy demand. In recent years, there has been a growing impetus for research in renewable energy systems to reduce the global dependence on fossil fuels. A majority of these research activities are focused on production of electricity, which accounts for approximately 30% of the global energy consumption [1]. The industrial sector, on the other hand, accounts for nearly 50% of the total energy demand in the form of process heat and only 10% of it is presently supplied by renewables [1, 2]. To ensure sustainable growth and reduce the emission of greenhouse gases, the development of renewable energy technologies addressing the demands of the industrial sector is critical.

Solar energy is widely considered as an attractive source to power industrial processes due its abundance and vast distribution. Among the available solar energy systems, concentrating solar thermal systems are attractive due to their inherent suitability for integrating a heat storage subsystem which improves plant dispatchability [3]. These systems typically use mirrors or lenses to concentrate solar radiation onto a receiver carrying a heat transfer fluid (HTF) which is used to drive a power cycle to produce electricity. Current state-of-the-art concentrated solar power (CSP) plants are limited to applications below 600 °C [4]. Next generation CSP plants proposed as part of the Gen3 Liquid Pathway program are targeting operating temperatures above 700 °C using liquid sodium as the HTF [5]. The use of a boiling liquid metal as a HTF offers a promising solution to extend the operation of CSP plants to high-temperature applications up to 800 °C with the added advantage of providing near-isothermal heat.

The development of a boiler in a CSP system requires a fundamental knowledge of the boiling process. Boiling is a complex phase change process involving a transfer of mass, momentum and energy between a liquid and a vapour phase. During boiling, high heat transfer rates are achieved through the phase change process and localised motion of the liquid–vapour interface. Thus, boiling provides an efficient mechanism for heat removal from a heated surface. This has led to the application of boiling flows in a variety of applications spanning different scales. Boiling flows are used in micro-scale heat exchangers to cool high energy density electronic systems. On the other hand,

boiling is also used on a larger scale for the generation of vapour in boilers in power plants. Due to its wide spread use, boiling flows have been extensively studied in the past and are the focus of ongoing research in groups around the world.

A niche subset of boiling flows, is the boiling of low Prandtl number liquid metals like sodium. Liquid sodium is commonly used as a coolant in nuclear reactors due to its minimal neutron moderation and high thermal conductivity which ensures high heat transfer rates [6, 7]. Although the reactors are not designed to operate with boiling sodium, in the event of an accident, local overheating of the reactor core may cause sodium to boil, a situation that is undesirable. Hence sodium boiling is commonly studied for nuclear reactor safety assessment. Boiling sodium has also been tested as a heat transfer fluid in heat exchangers for space power applications [8]. In the late 1980s, boiling sodium was tested as a latent heat transfer fluid in laboratory-scale solar power plants [9].

The design and safe operation of boiling systems requires a fundamental understanding of the bubble growth process. Bubble growth in boiling of ordinary liquids such as water has been extensively studied [10–21]. However, the specific thermophysical properties of sodium, namely its high thermal conductivity and low surface tension indicate that the characteristics of sodium boiling will be significantly different to ordinary fluids. Studies on bubble growth in sodium boiling are scarce, and hence, the governing mass and heat transfer phenomena dominating bubble growth in sodium are unknown. This research aims to bridge this gap by developing a physics-based bubble growth model. Such models can highlight the governing phenomena dominating the bubble growth process in sodium, and thus aid the development of sodium boiling systems.

1.1 Background

Research on sodium boiling flows has been actively pursued by the CSP and nuclear industry to design efficient and safe energy systems. This section highlights the important outcomes of these activities.

Sodium as a heat transfer fluid in CSP plants. A critical component of a CSP plant is the HTF in the receiver. An ideal HTF should have an extensive temperature range (low melting point to prevent freezing during night and high boiling point to maximise efficiency), possess favourable heat transfer and flow properties (high thermal conductivity and heat capacity, low viscosity), be inexpensive and compatible with common structural materials. Several HTFs of varying thermophysical properties have been tested and used in commercial and laboratory scale CSP systems. Their thermophysical properties are shown in Table 1.1. Among the fluids listed, liquid sodium is attractive in CSP systems due to its high thermal conductivity coupled with moderately low cost.

Table 1.1: Thermophysical properties of candidate heat transfer fluids at a pressure of 1 bar and 873 K [24]. T_{\min} and T_{\max} represents the melting and boiling temperature of the heat transfer fluids, respectively, except for solar salt (chemical stability limit) and gases.

HTF	T_{\min} (K)	T_{\max} (K)	c_p (J kg ⁻¹ K ⁻¹)	k (W m ⁻¹ K ⁻¹)	$\mu \times 10^{-3}$ (Pa s ⁻¹)	Cost (\$/kg)
<i>Alkali metals</i>						
NaK	261	1058	870	26.2	0.18	2
K	337	1039	760	34.9	0.15	2
Na	371	1156	1250	46	0.21	2
Li	453	1615	4160	49.7	0.34	60
<i>Heavy metals</i>						
PbBi	398	1806	150	12.8	1.08	13
Bi	544	1943	150	16.3	1.17	22
Pb	600	2016	150	18.8	1.55	2
<i>Fusible metals</i>						
Ga	303	2510	360	50	0.77	600
In	430	2345	240	47.2	0.75	500
Sn	505	2960	240	33.8	1.01	25
<i>State-of-the-art HTFs</i>						
Air	–	–	1120	0.06	0.03	0
Water/Steam	273	–	2420	0.08	0.03	≈ 0
Solar salt	493	873	1100	0.52	1.33	0.5

The high thermal conductivity of sodium allows receivers to operate at a high heat flux, alleviates thermal stress in tubes carrying the HTF and increases receiver efficiency [22]. In addition, sodium is a promising choice due to the significant operational experience of using it as a coolant in the nuclear industry [23, 24].

Concentrated solar power plants with sensibly heated and latent sodium HTF have been proposed and tested. In a sensibly heated system, the temperature of sodium changes while in a latent system, sodium undergoes a phase change process. In the 1980s, the Small Solar Power Systems project at the Plataforma Solar in Almeria (PSA), Spain, and Rockwell International in association with the US Department of Energy performed on-sun tests on the use of sensibly heated sodium in solar receivers [25–29]. These tests demonstrated good thermal performance and operational benefits with receiver efficiencies above 90% and excellent dynamic response to variations in solar flux [23]. In recent years, Vast Solar in Australia commissioned a 6MW_{th} pilot plant with sodium as the HTF in tubular receivers. Owing to the success of the pilot plant, Vast Solar is presently developing a 50MW_e CSP power plant in Queensland and a 20MW_e plant near Port Augusta in Australia [30]. A comprehensive review of the design specifications and the main outcomes of these test programs is provided in Ref. [23].

Compared to a sensibly heated sodium CSP system, a latent system can reduce fa-

tigue in receiver tubes and be coupled with phase change material systems to maximise storage of useful energy [22]. Sandia National Laboratories pursued the development of sodium receivers with liquid–vapour phase change to provide near-isothermal heat for industrial processes and proposed two concepts: (a) a pool boiler in which the liquid metal floods the entire surface of the absorber [9, 31, 32] and (b) a heat pipe in which a wick-like structure saturated with liquid metal covers the absorber surface [33–35]. In the pool boiler, sodium vapour generated due to boiling of the liquid metal was distributed on to the tubes of the Stirling engine to transfer energy to the engine’s working fluid. One of the major drawbacks of this concept was that a large inventory of sodium was needed to operate the boiler which was deemed to be a significant safety concern by Sandia [23]. Thus, Sandia shifted their focus to the development of the heat pipe concept. In the heat pipe concept, the wick structure was used to distribute sodium on a solar-heated dome where the liquid sodium evaporates. Vapours of sodium from the dome then condense on the tubes of a dish-Stirling engine, thus transferring energy to the engine’s working fluid. On-sun testing of both concepts demonstrated receiver efficiencies of over 90% at operating temperatures of 800 °C [31].

The on-sun test results of using sodium as a latent HTF successfully demonstrated the conceptual viability of the system and highlighted the operational difficulties in controlling sodium boiling. Boiling of liquid metals is inherently less stable compared to ordinary liquids like water and characterised by large temperature fluctuations as a bubble grows and departs from a surface [36]. The tests performed on the pool boiling receiver at Sandia showed that when the heat supplied to the boiler was interrupted for a short period to simulate cloud transients, a very high superheat was needed to re-initiate boiling. To overcome this problem, a small amount of xenon gas was added to sodium vapour which resulted in improved boiler performance at low sun elevations. In addition, X-ray and path-averaged void fraction measurement systems were used to determine bubble departure size and frequencies, and time-averaged void fraction distribution in the pool. Though reliable data on departure diameter and frequency could not be obtained due to light leakage in the measurement system, the void fraction in the pool boiler was found to be around 60–80%, indicating the formation of large bubbles in the liquid [37].

Research on sodium boiling in the nuclear industry. The choice of an effective coolant for the reactor core in a nuclear power plant is critical. Traditional, first generation nuclear power plants used pressurised water to cool nuclear rods. With the advancement in nuclear technology, the development and testing of fast breeder reactors was pursued. Fast breeder reactors are characterised by having relatively high power density in the reactor core compared to traditional first generation nuclear plants and require an efficient coolant to effectively remove heat. Liquid metals, due to their high thermal conductivity and suitable temperature range at low pressures, are a promising

choice. Among liquid metals, sodium has been the most popular choice due to its compatibility with the reactor core material [7]. The temperature of the sodium is typically 200 °C lower than its boiling point during normal operation of the nuclear reactor [38]. Despite the large safety margin, it is common to study the boiling of sodium which may occur in the case of local overheating of a nuclear rod. As a result, experimental and numerical studies were conducted to understand the boiling phenomena in sodium. These studies can be divided into three groups based on their aim: (a) determination of the temperature at which sodium begins to boil [6, 39–42]; (b) development of a boiling heat transfer coefficient correlation [8, 43]; and (c) determination of the maximum heat flux beyond which surface boiling can no longer be sustained, which is called the critical or burnout heat flux [44, 45]. Beyond the critical heat flux, individual bubbles will merge to form a film of vapour. Owing to the low thermal conductivity of the vapour, the coolant can no longer effectively remove heat causing the reactor core to melt. Based on the past work, some important features of the sodium boiling process were identified as: (i) bubbles in sodium tend to be isolated and large in size [7, 36, 46]; (ii) sodium has to be significantly heated above its saturation temperature or superheated to initiate the bubble growth process [6, 36, 39–42]; and (iii) sodium boiling is unstable due to highly wetting nature of sodium [9, 32, 47]. A bubble grows from a cavity in a heated surface when some amount of vapour is trapped in it. However, most of the cavities in a sodium boiling system are flooded with liquid sodium. Thus, sodium flows are characterised by larger periods of heat transfer by convection when the liquid is heated and then a sudden transition to boiling heat transfer once the nucleation temperature is reached. This sudden transition leads to large temperature fluctuations on the heated wall and the unstable boiling nature of sodium.

1.2 Motivation

Solar thermal. This work is primarily motivated by the development of a sodium tubular boiler for a CSP plant to provide high temperature near-isothermal heat for industrial applications. Figure 1.1 shows a schematic diagram of a CSP plant with a sodium tubular boiler. In the proposed system, a set of mirrors, called heliostats, concentrate energy from the sun onto a central receiver containing liquid sodium as the heat transfer fluid. As the liquid sodium is heated, it boils in the tubes of the receiver and its vapours are condensed in direct contact with a phase change material (PCM) in a storage vessel. In the system, sodium chloride is proposed as the PCM, as its melting temperature of 800 °C is well matched to the boiling temperature of sodium under a partial vacuum [48]. However, other PCMs may also be suitable. Thus, with sodium chloride as the PCM, in the storage vessel, the salt melts at 801 °C and stores energy through the solid–liquid phase change process. When energy is demanded by the industrial process, the

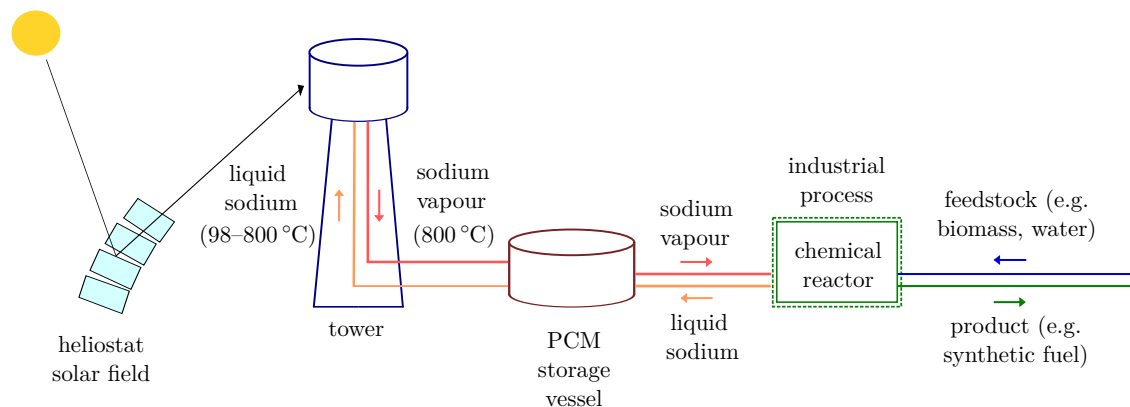


Figure 1.1: Schematic of a CSP plant with a sodium tubular boiler.

salt is re-solidified at a lower pressure, thus releasing heat which results in the evaporation of liquid sodium. The sodium vapours are then passed to a chemical reactor where they condense, thus releasing their latent heat and providing energy to the industrial process at a constant temperature.

An integral component of the proposed system is the sodium tubular boiler. An efficient design of these boilers is primarily hindered by inadequate knowledge of the boiling mechanism of liquid metals in pipes. Over the past few decades, considerable amount of research on boiling of fluids with low thermal conductivity and high Prandtl number ($Pr > 1$) using numerical simulations and experiments have been reported [49–52]. Subsequently, various correlations and mechanistic models describing the heat and mass transfer rates in these fluids have been proposed. Liquid metals, on the other hand, exhibit a low Prandtl number ($Pr < 1$) and thus have a substantially thicker thermal boundary layer compared to ordinary fluids. This results in the heat transfer being dominated by molecular conduction not only in the static layer at the wall, but also in the central bulk flow [43]. Thus, the bubble growth in liquid metals is characterised by a completely different heat and mass transfer mechanism. A thorough knowledge of these mechanisms is important to design sodium boilers and maximise their efficiency.

Boiling simulations. Multiphase computational fluid dynamic (CFD) simulations are used to design and assess the performance of boiling systems. Two numerical methods are commonly adopted for the simulations: (i) the interface tracking method in which the liquid–vapour interface of the bubble is captured as it grows and (ii) the Eulerian–Eulerian two-fluid method in which the conservation equations for each phase are averaged to obtain an inter-penetrating continua without explicitly tracking the liquid–vapour interface [53]. For commercial-scale applications, like the design of a boiler in a CSP plant, the boiling phenomena are generally simulated using the Eulerian–Eulerian method. Within the Eulerian–Eulerian framework for boiling flows, semi-empirical closure relations for the latent heat transfer due to evaporation of the liquid, bubble depar-

ture diameter and frequency are needed. Significant research has been reported on the development and validation of these relations for high Prandtl number fluids [49, 54–57]. However, the applicability of this method to boiling sodium systems is limited due to the unavailability of these closure relations. To address this limitation, the development of physics-based sodium bubble growth models to develop closure relations is desirable.

Nuclear industry. Within the nuclear industry, research on sodium boiling was actively pursued by the groups of Rohsenow at MIT and Sandia National Laboratories in the 1960s [42, 58]. The extreme difficulty in handling liquid metals, the highly unstable nature of their boiling process and the lack of technological know-how at that time limited the scope of these studies [59]. Hence most of the published research was limited to theoretical analysis of the bubble growth process using several simplifications and sometimes relied on correlations developed for high Prandtl number fluids. Experimental studies were also undertaken. However, only limited data on bubble characteristics were reported from them, mainly due to the unavailability of advanced measurement techniques. Traditional optical measurement techniques such as cameras could not be used as sodium is opaque. Experiments using X-rays and acoustic techniques were reported, but they were mainly limited to detection of bubbles and not their characterization [46].

Though certain characteristics of sodium boiling flows have been identified, as alluded to in Section 1.1, the dynamics of the bubble growth process is largely unknown. Bubble characteristics such as departure diameter and frequency are important parameters needed in the design of sodium boiling systems. A bubble size larger than the diameter of a tube in a system may result in the flooding of the tube with vapour, thus leading to a large temperature on the tube wall. Such a scenario is dangerous and may lead to severe accidents. To aid in design and ensure safe operation of nuclear systems employing sodium as a heat transfer fluid, knowledge of bubble growth characteristics is essential.

1.3 Research objectives

The development of heat transfer correlations and semi-empirical relations for the design of commercial-scale applications like sodium boilers and nuclear reactors requires, as a first step, a fundamental understanding of the growth of a single bubble. The growth of a bubble in a liquid pool involves a complex interplay of heat and momentum transfer occurring over varying length scales. Figure 1.2 shows the various heat transfer processes occurring during the growth of a bubble. As the bubble grows, a fluid layer of thickness of a few micrometers is formed below the bubble as shown in Fig. 1.2a. This layer is called the microlayer and its evaporation has been found to

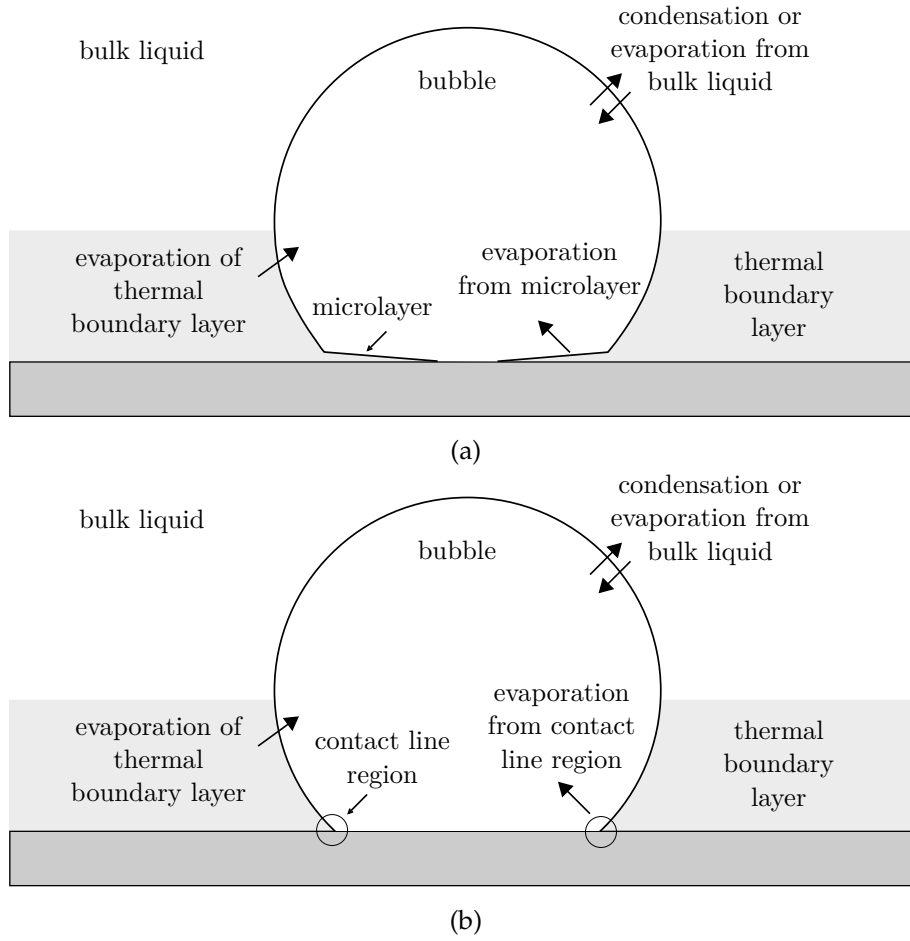


Figure 1.2: Heat transfer processes involved in the growth of a bubble in pool boiling including the evaporation of the (a) microlayer [14–16, 60] and (b) contact line region [61–63].

have a large influence on bubble growth [11, 14–16]. The liquid in the microscopic region where the liquid–vapour interface of the bubble meets the wall is referred to as the contact line region, as shown in Fig. 1.2b. Some studies suggest that the evaporation of the contact line region contributes significantly to bubble growth [61, 62, 64, 65]. In addition to these microscopic heat transfer phenomena, a bubble grows due to the evaporation of the liquid in the thermal boundary and the bulk liquid surrounding the bubble [14, 16, 17, 20, 60, 66]. This occurs over length scales in the order of a few millimetres to centimetres. The combined effect of these heat transfer processes causes a bubble to grow from its initial micron size to its departure size, where forces acting on the bubble lead to its detachment from the wall. Capturing all of these phenomena and determining the most dominant heat transfer mechanism and force acting on a bubble is important for the design of efficient and safe sodium boilers.

The focus of this doctoral thesis is to develop a physics-based model coupling the heat transfer and hydrodynamic phenomena influencing the growth of a single bub-

ble in sodium pool boiling. Past numerical studies on sodium bubble growth either over-simplify the underlying physics or rely on correlations developed for high Prandtl number fluids to model bubble growth. This limitation will be addressed in the present work. In addition, the effect of thermophysical properties of sodium and its high wall superheat on the bubble growth process will be investigated. Results from the model can guide the design of experiments to validate the proposed models and support the design and operation of efficient sodium boilers.

The following tasks are undertaken to achieve the goals of this thesis:

- Development of a numerical model to study the heat and mass transfer phenomena in the contact line region in sodium pool boiling.
- Development of a heat transfer model coupling the evaporation from the microlayer, thermal boundary layer and the bulk liquid to the bubble growth rate in sodium pool boiling.
- Development of a mechanistic model to study the growth of a bubble from nucleation to departure in sodium pool boiling.

1.4 Overview

This thesis is organised into seven chapters to understand the bubble growth process in sodium. Chapter 1 provides a general introduction to the doctoral topic and a background on the application of sodium boiling flows. Chapter 2 is divided into two parts. In the first part, an overview of the bubble growth theory is presented. The governing mechanisms controlling bubble growth along with a mathematical description of the different heat transfer processes and forces acting on a bubble are provided. In the second part of the chapter, specific characteristics of sodium boiling are highlighted. This is followed by a critical review of the theoretical bubble growth models published in literature. In Chapter 3, the heat transfer from the contact line region, i.e. the region where the liquid–vapour interface of the bubble meets the wall, is studied. A mathematical model to compute the evaporation rate from the contact line region is presented along with a solution algorithm. The developed model is used to compare the heat transfer from this region in sodium with a high Prandtl number fluid, fluorocarbon FC-72. A parametric study to estimate the influence of selected parameters is also presented. Chapter 4 introduces a sodium bubble growth model based on heat transferred from the microlayer, i.e. a thin layer of fluid formed below the bubble, the thermal boundary layer and the bulk liquid surrounding the bubble. Results from the model highlight the dominating heat transfer mechanisms that control bubble growth in sodium for different parameters. In Chapter 5, a mechanistic model coupling the heat transfer model devel-

oped in Chapter 4 with a model computing the forces acting on the bubble is presented. A novel method to approximate the transition in shape of a bubble prior to departure is proposed. Verification and validation of the model with experimental and CFD results from literature is presented. The validated model developed in Chapter 5 is extended to study the bubble growth dynamics in sodium pool boiling in Chapter 6. Finally, the key findings of this work are summarised in Chapter 7.

Theoretical background and literature review

This chapter provides an overview of the theory on bubble growth in pool boiling and a literature review on sodium pool boiling. The first part of this chapter describes in detail the bubble growth process in pool boiling. A theoretical description of different mechanisms controlling bubble growth is presented along with a review of the commonly used bubble growth models used in numerical simulations. The different heat transfer processes in bubble growth are introduced, including a mathematical description of micro and macro scale heat transfer mechanisms. This is followed by a brief description of forces acting on a bubble and the transition in shape of a bubble in pool boiling. The second part of this chapter provides an overview of liquid metal boiling characteristics and a review of the past numerical work on modelling bubble growth in sodium. In the last section, the gaps in knowledge in sodium pool boiling are summarised, which will be addressed in this doctoral project.

2.1 Single bubble growth in nucleate pool boiling

Within the scope of this thesis, single bubble growth in nucleate pool boiling is studied to understand the bubble growth mechanism from nucleation to departure. A typical growth cycle of a bubble is shown in Fig. 2.1 and comprises the period in which the bubble grows and the waiting time, that is the period between the departure of one bubble and the nucleation of the next bubble [36]. The presence of an active nucleation site on a surface is essential for the inception of bubble growth in boiling flows. Nucleation sites are imperfections on a heater surface such as cavities which trap gas and serve as nuclei for bubbles [67]. The growth cycle starts with the nucleation of a bubble from a cavity represented by state 1 and rapid expansion of the bubble due to an increase in its curvature as it emerges from the cavity (state 2). This expansion of the bubble is countered by the inertia of the surrounding liquid which causes the bubble to spread on the heater surface, leading to a hemispherical shape [36]. At the same time,

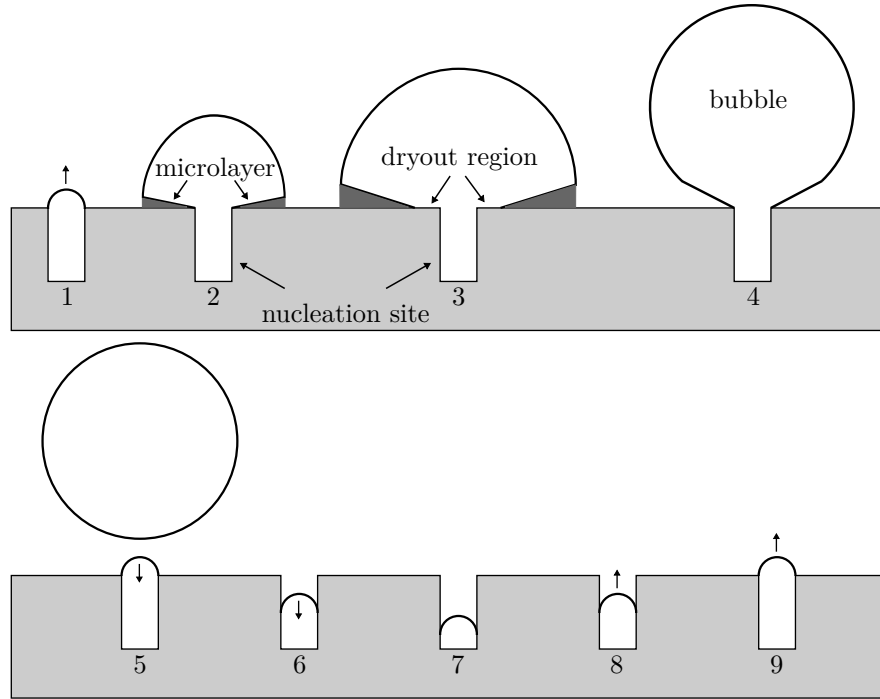


Figure 2.1: Schematic representation of bubble growth cycle. The period 1–4 represents the bubble growth period while 5–9 represents the waiting period [36].

a thin layer of liquid is formed below a bubble called the microlayer [68–70]. The evaporation of this layer, along with the liquid surrounding the bubble, supply the vapour required for bubble growth. As the bubble continues to grow, the microlayer evaporates creating a dryout region below the bubble as shown at state 3 [71–73]. At a certain time, the microlayer evaporates completely resulting in an inflow of surrounding liquid, represented by state 4. At this stage, the bubble is large enough that inertia no longer controls its growth. Buoyancy and surface tension forces acting on the bubble cause it to assume a more spherical shape. When the buoyancy force becomes larger than the surface tension force that is keeping the bubble attached to the wall, the bubble departs from the wall, leaving behind some residual vapour in the cavity [36, 74]. During this period, the area beneath the departing bubble is replenished by the colder liquid from the pool (state 5). The colder liquid causes the vapour in the cavity to condense (state 6). However, as the liquid progresses into the cavity, it is heated by the latent heat from the condensing vapour and sensible heat from the wall. This stops the penetration of liquid into the cavity as represented by state 7. As the liquid continues to heat, the vapour begins to rise from the cavity (state 8) and if the surface temperature reaches a certain critical value needed for bubble nucleation, the vapour emerges from the cavity (state 9). At state 6, if the receding velocity of the vapour is high, then the cavity may become quenched by the cold liquid. This causes the nucleation site to deactivate. To

re-activate the site, high wall superheats are needed and this causes instability in boiling flows [36]. Broadly, for stable boiling flows, the bubble growth can be divided into two phases, namely, the growth phase (state 1 to state 4) and the waiting phase (state 5 to state 9). In the following sections, a description of the mechanism, heat transfer, forces acting on a bubble and shape of a bubble during the growth phase is provided.

2.2 Bubble growth mechanism

The growth of a bubble is controlled by two principal phenomena: inertia and heat transfer. The two mechanisms can be explained using the pressure vs temperature relationship of the vapour in the bubble in a superheated liquid pool shown in Fig. 2.2. A bubble nucleates if the liquid is sufficiently superheated. Point 1 in the plot represents the conditions of the superheated liquid. In the initial period, just after nucleation, the vapour pressure in the bubble is the maximum possible value p_{∞}^* and is represented by point 2. The corresponding temperature of the vapour is T_{∞} . At this state, the bubble growth is primarily driven by the pressure difference between the vapour and the surrounding fluid given by $p_{\infty}^* - p_{\infty}$. During this stage, the heat transfer between the liquid and the vapour has a negligible influence on the bubble growth process as the temperature of the vapour is equal to the bulk liquid temperature, i.e. $T_v = T_{\infty}$. This stage of the growth process also represented by states 1 and 2 in Fig. 2.1, when the pressure of the vapour in the bubble is close to point 2 on the saturation curve, is referred to as the inertia-controlled growth stage. As the bubble grows, the pressure inside the bubble reduces. Assuming the bubble remains in thermodynamic equilibrium with the surrounding liquid, the state of the bubble will move along the saturation curve. When the bubble approaches point 4, the pressure difference between the vapour and the liquid is negligible while the temperature difference $T_{\infty} - T_{\text{sat}}$ completely controls the growth process. This stage of the growth period also represented by state 4 in Fig. 2.1 is referred to as the heat transfer controlled growth stage. State 3 in Fig. 2.1 and point 3 in Fig. 2.2 represent an intermediate stage where the bubble growth is controlled by inertia and heat transfer.

Modelling the growth of a bubble on a heated wall in the inertia and the heat transfer controlled growth stage has been a subject of ongoing research. Early works proposed bubble growth relations either for the inertia controlled growth stage [75–77] or the heat transfer controlled growth stage [78–80] but not a comprehensive relation valid for both stages. Mikic et al. [81] addressed this limitation and proposed one of the most widely used bubble growth model valid for both the inertia and heat transfer controlled growth stage. It is briefly described here and is used in the present work. The authors studied the growth of a bubble on a heated wall in a liquid pool assuming the vapour in the bubble to be in thermodynamic equilibrium with the surrounding liquid and derived

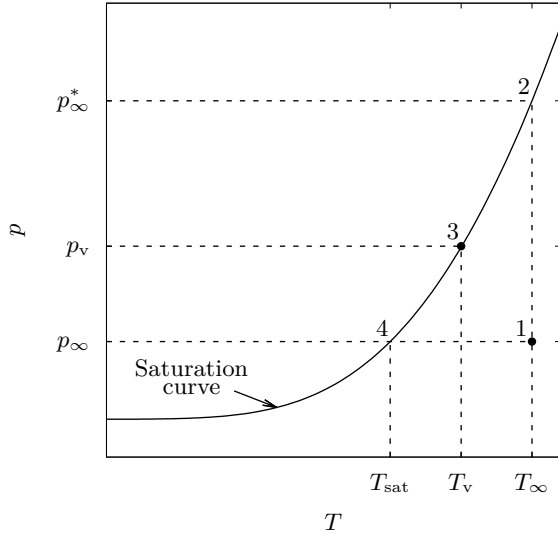


Figure 2.2: Pressure temperature relationship during growth of a spherical bubble in a superheated liquid pool [36]. Description of points: 1. liquid condition; 2. state of bubble at nucleation; 3. bubble conditions at an intermediate state; 4. state of the bubble during heat transfer controlled growth stage [36].

a bubble growth relation for two limiting cases: (a) when the growth of the bubble is completely controlled by the inertia of the surrounding liquid and (b) when the growth of a bubble is controlled by the heat transferred from the wall and the surrounding liquid to the bubble. To derive a bubble growth rate relationship for the inertia controlled growth stage, the authors performed a mechanical energy balance at the liquid–vapour interface by equating the kinetic energy of the liquid displaced by a growing bubble to the work done by the bubble on the surrounding liquid. The resulting equation was simplified using the Clausius–Clapeyron equation which describes the pressure–temperature relationship along the saturation curve to obtain the bubble growth rate in the inertia controlled growth stage as follows:

$$\left(\frac{dr_b}{dt}\right)^2 = C_1^2 \frac{T_v - T_{\text{sat}}}{\Delta T}, \quad (2.1)$$

$$C_1 = \left(\frac{\pi}{7} \frac{\Delta T}{T_{\text{sat}}} \frac{h_{\text{lv}} \rho_v}{\rho_l}\right)^{0.5}, \quad (2.2)$$

where $\Delta T = T_w - T_{\text{sat}}$ is the wall superheat needed to initiate bubble growth, T_v is the vapour temperature, T_w is the wall temperature, h_{lv} is the latent heat of vaporisation, and ρ_l and ρ_v are the density of the liquid and vapour phase, respectively.

The growth rate relation for the heat transfer controlled stage was obtained from an asymptotic solution to an equation describing the radius of a bubble growing in a superheated liquid pool due to heat diffusion from the surrounding liquid. It is given by [81]

$$\frac{dr_b}{dt} = \frac{1}{2} \frac{C_2}{\sqrt{t}} \frac{T_{\infty} - T_v}{\Delta T}, \quad (2.3)$$

$$C_2 = \frac{12}{\pi} \alpha_l \text{Ja}, \quad \text{Ja} = \frac{\rho_l c_{p,l} \Delta T}{\rho_v h_{lv}}, \quad (2.4)$$

where t is bubble growth time, α_l is the thermal diffusivity of the liquid, $c_{p,l}$ is the specific heat of the liquid, and Ja is the Jakob number. Miyatake et al. [82] extended the work of Mikic et al. [81] by considering variable fluid properties and proposed a universal bubble growth relation valid for the inertia and heat transfer controlled growth period. However, the relation was verified with only one numerical solution and was not validated with experimental data.

Equations (2.1) and (2.3) were validated with data obtained from water boiling experiments and were extended to study the growth of sodium bubbles in superheated liquid pools [81]. In addition to the bubble growth rate relations, the authors also proposed a simplified condition to check if the bubble growth is in the inertia controlled or the heat transfer controlled growth stage [81]:

$$\frac{C_1^2 t}{C_2^2} \begin{cases} \ll 1 & \text{inertia controlled,} \\ \gg 1 & \text{heat transfer controlled.} \end{cases} \quad (2.5)$$

2.3 Heat transfer to a bubble in pool boiling

The growth of a bubble in a liquid pool depends on the heat transferred from different mechanisms. Over the years, several experimental and numerical studies have been conducted to identify these heat transfer mechanisms. Han and Griffith [78] performed one of the earliest studies on bubble growth in pool boiling and stated that transient conduction from the bulk liquid to the bubble is the primary heat transfer mechanism controlling the growth of a bubble. With the advent of advanced measurement techniques, the presence of a microlayer was observed [68–70]. The heat transferred from this layer has been found to have a significant influence on the bubble growth process [70, 83]. Other studies have shown that the heat transferred from the contact line region affects the growth of a bubble [61, 63, 84]. In addition to the heat transferred to a bubble from the microlayer and the contact line region, the evaporation of the bulk liquid surrounding the bubble and the macrolayer (which is the layer of fluid in the superheated thermal boundary layer which is trapped below the bubble) supplies part of the vapour needed for bubble growth [66, 85]. The thickness of the macrolayer and superheated thermal boundary layer depend on the Prandtl number of the fluid. Liquid metals are characterised by a low Prandtl number and exhibit thicker thermal boundary layers compared to conventional liquids such as water and organic fluids. Hence, in the case of sodium, the influence of the superheated layer on bubble growth may be significant. Thus, based on results from past studies, the different heat transfer mechanisms

controlling the growth of a bubble are: (i) microscale heat transfer from the microlayer and the contact line region; (ii) heat transferred from the macrolayer; and (iii) heat transferred from the bulk liquid to the bubble. In the following section, a detailed overview of modelling these heat transfer mechanisms is provided.

2.3.1 Microscale heat transfer

Several experimental studies have shown the existence of a thin layer of fluid formed below a bubble which is typically of the order of a few micrometers in boiling flows [86]. Owing to the small thickness of this layer and its vicinity to the superheated wall in boiling systems, the heat flux in this region is significant. This has led researchers to pay special attention to understand the microscale heat transfer from this region in boiling flows. Previous work on modelling the microscale heat transfer is based on two approaches: the contact line model and the microlayer model. In the following section, a brief description of these models is provided.

Contact line model

Past research on boiling of liquids like water and refrigerants has shown that the microscale heat transfer effects in the region where the liquid–vapour interface of the bubble meets the heater wall, referred to as the contact line region, has a significant influence on the bubble growth process. A schematic of the contact line region formed below a bubble of radius r_b is shown in Fig. 2.3. At radial distances $r < 0$, the wall is covered by a thin flat film of adsorbed fluid molecules. The thickness of this layer is significantly less than the adjacent micro region and is of the order of nanometres. The liquid in this region does not evaporate due to the strong intermolecular forces of attraction between the fluid molecules and the wall. On the other end of the contact line region is the macro region where the thickness of the liquid film is significantly larger. Hence the forces of attraction are smaller. The contact line region is a transition region of thickness δ and contact angle θ between the adsorbed layer and the macro region. The fluid flow in this region is influenced by a rapid change in the curvature of the liquid–vapour interface and intermolecular forces which decay rapidly as the film gets thicker. Additionally, owing to the relatively small thickness of the liquid film in this region, the resistance to heat transfer is small, and hence high evaporation rates are expected. As the liquid evaporates at the interface, the resulting pressure drop pulls in fresh liquid from the macro region. Thus, the dynamics of the fluid flow and heat transfer in the contact line region are complex and governed by bulk motion of fluid from the macro region, molecular forces within the contact line region and high evaporation rates which may contribute significantly to the overall heat transfer during the bubble growth process.

Modelling of the thermo-fluid dynamic phenomena in the contact line region has

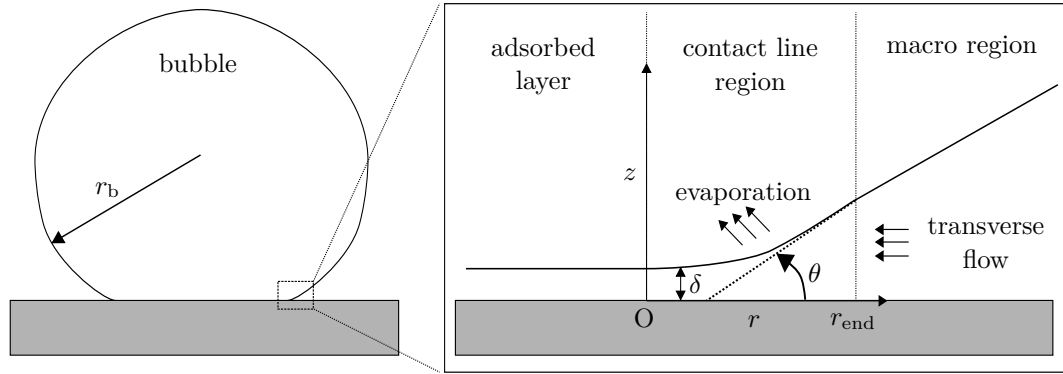


Figure 2.3: Schematic of the contact line region in a bubble [59, 61, 89].

been a subject of significant interest. Potash and Wayner [87] were the first to model the fluid flow and heat transfer in thin films. They developed a model describing the fluid flow in the contact line region resulting from capillarity and disjoining pressure, i.e. pressure resulting from intermolecular forces. Based on their analysis, they calculated the film profile and the variation of the pressure and heat flux in the thin film. Later, Stephan et al. [61] extended the model to study the influence of heat transferred from the contact line region on bubble growth. The authors simplified the governing equations for fluid flow and heat transfer in the thin film using the lubrication theory approximation and described a solution algorithm to solve the resulting system of equations. More recently, Batzdorf [88] validated the model of Stephan using DNS simulation results and extended it to include the effect of moving contact lines.

The model developed by Stephan et al. [61] is used in this work and is described here. To simulate the fluid flow and heat transfer in the contact line region, the authors made a set of assumptions based on which the governing equations were simplified. The assumptions are as follows:

1. Flow in the contact line region is steady and laminar.
2. The wall in the contact line region is isothermal.
3. The liquid in the contact line region is modelled as a continuum.
4. The characteristic length scale along the wall is significantly larger than the length scales normal to the wall. This is valid as long as the contact angles are small, i.e. $\theta \ll 90^\circ$. Additionally, the Reynolds number of the flow in the contact line region is small. Thus, the lubrication theory is valid in the contact line region [90].
5. Heat transfer in the contact line region is governed by 1D conduction normal to the wall.

6. The influence of surface roughness on the fluid flow in the contact line region is neglected.

Based on these assumptions, the mass, momentum and the energy conservation equations for the fluid flow in the contact line region are formulated as follows:

Mass conservation. As the liquid in the contact line region evaporates, it is replenished by fresh liquid from the macro region. Since the flow in the contact line region is steady, the continuity equation for fluid flow can be simplified to

$$m_e'' = -\frac{d}{dr} (m''\delta), \quad (2.6)$$

where m_e'' denotes the evaporative mass flux, m'' is the mass flux from the macro region and δ is the film thickness in the contact line region.

Momentum conservation. The momentum conservation equation for fluid flow in the radial direction is obtained by simplifying the Navier–Stokes equation using the lubrication theory as the thickness of the liquid film in the contact line region is significantly less compared to its radial extent, i.e. $\delta \ll r$. The resulting simplified equation is solved subject to the no-slip boundary condition at the wall ($u = 0$ at $z = 0$) and negligible shear stress at the interface ($\partial u / \partial r = 0$ at $z = \delta$). Thus, the velocity profile for fluid flow in the contact line region is

$$u(r, z) = -\frac{1}{\mu_1} \frac{\partial p_1}{\partial r} \left(\delta z - \frac{z^2}{2} \right), \quad (2.7)$$

where μ_1 and p_1 are the dynamic viscosity of the liquid and liquid pressure, respectively. Thus, the liquid mass flux m'' is given by

$$m'' = \frac{\rho_1}{\delta} \int_0^\delta u(r, z) dz = -\frac{\delta^2}{3\nu_1} \frac{dp_1}{dr}. \quad (2.8)$$

Rearranging the above equation gives the momentum conservation equation in the radial direction as follows:

$$\frac{dp_1}{dr} = -\frac{3\nu_1 m''}{\delta^2}, \quad (2.9)$$

where ν_1 is the kinematic viscosity of the liquid.

The momentum conservation equation normal to the wall for an interface with evaporative mass transfer is formulated based on the augmented Young–Laplace equation. The Young–Laplace equation describes the pressure difference between the vapour in the bubble and the bulk liquid in terms of the curvature of the liquid–vapour interface and the intermolecular force of attraction between the wall and the fluid molecules.

Thus,

$$p_c = p_{\text{dis}} + p_{\text{cap}} + p_{\text{rec}} = \Pi_A(\delta) + \sigma\kappa - \left(\frac{1}{\rho_v} - \frac{1}{\rho_l}\right) m_e''^2, \quad (2.10)$$

where

$$p_c = p_v - p_l. \quad (2.11)$$

In the above equation, κ is the interface curvature and p_v is the vapour pressure. The first term on the right hand side of Eq. (2.10) represents the disjoining pressure p_{dis} which is the pressure resulting from the van der Waals force of attraction between the liquid molecules and wall. It is given by

$$\Pi_A(\delta) = \frac{\mathcal{A}}{\delta^3}, \quad (2.12)$$

where \mathcal{A} is the Hamaker constant. The second term represents the capillary pressure p_{cap} where σ is the surface tension of the liquid and the curvature of the interface κ is given by

$$\kappa = \frac{\delta''}{\sqrt{1 + \delta'^2}}. \quad (2.13)$$

The third term represents the vapour recoil pressure p_{rec} and depends on the evaporative mass flux m_e'' . The recoil pressure inhibits the evaporation of the liquid film in the contact line region [91].

Energy conservation. An energy balance of the contact line region is performed assuming all the heat from the wall is used in evaporating the liquid in the thin film and is expressed in terms of the wall heat flux q_w'' and the evaporative heat flux q_e'' at the interface as follows:

$$q_w'' = q_e'' \sqrt{1 + \delta'^2}. \quad (2.14)$$

The term $\sqrt{1 + \delta'^2}$ is used since the wall heat flux and the evaporative heat flux are related to different surface areas when the interface has a non-zero slope. The wall heat flux in the contact line region is modelled assuming 1D conduction heat transfer between the liquid–vapour interface and the wall as follows:

$$q_w'' = \frac{k_l}{\delta} (T_w - T_{\text{int}}), \quad (2.15)$$

where k_l , T_w and T_{int} are the liquid thermal conductivity, wall temperature and the interface temperature, respectively. The evaporative heat flux at the interface between the liquid and the vapour is determined according to the kinetic theory of gas considerations as proposed by Schrage [92] and the linearised Clausius–Clapeyron equation as

follows:

$$q_e'' = \frac{T_{\text{int}} - T_v \left(1 + \frac{p_c}{h_{lv}\rho_l}\right)}{R_{\text{int}}}, \quad (2.16)$$

where R_{int} is the interface thermal resistance defined as [92]

$$R_{\text{int}} = \frac{2 - f}{2f} \frac{T_v \sqrt{2\pi RT_v}}{h_{lv}^2 \rho_v}. \quad (2.17)$$

In the above equation, f is the accommodation coefficient which denotes the ratio of the number of molecules that condense on an interface to the number of molecules hitting the interface. The optimal value of f is one, but several factors like the presence of impurities in real systems may lower its value [93]. Combining Eqs. (2.14)–(2.16) and eliminating T_{int} gives

$$q_w'' = \frac{T_w - T_v \left(1 + \frac{p_c}{h_{lv}\rho_l}\right)}{\frac{\delta}{k_l} + \frac{R_{\text{int}}}{\sqrt{1+\delta^2}}}. \quad (2.18)$$

The mass, momentum and the energy conservation equations derived above can be represented by a set of four ordinary differential equations and solved using a fourth order Runge–Kutta numerical scheme and is described in detail in Chapter 3.

Microlayer model

In pool boiling, the flow of the fluid at the base of the bubble is impeded owing to viscous stresses at the wall. This results in the formation of a thin layer of fluid sandwiched between the wall and the bubble that is called the microlayer. The presence of a microlayer below the bubble and a mathematical relation to compute its thickness was first reported by Cooper and Lloyd [83]. Subsequently, several experimental and numerical studies have been conducted to quantify the influence of the evaporation of the microlayer on bubble growth in boiling flows [14–16, 72, 94].

A schematic of the microlayer formed below a spherical bubble of radius r_b and contact angle β is shown in Fig. 2.4. The microlayer in a bubble extends from the edge of the dryout region r_d to the bubble contact radius r_c

$$r_c = r_b \sin \beta. \quad (2.19)$$

In nucleate pool boiling, a central dryout region of radius r_d is formed below the bubble as the microlayer evaporates. In this region, the vapour is in direct contact with the wall. Owing to the low thermal conductivity of the vapour, the heat transfer in this region has a negligible influence on the growth of the bubble.

The thermo-fluid dynamics of the microlayer are different compared to the contact line region. The thickness of the liquid film in the microlayer is larger than the contact

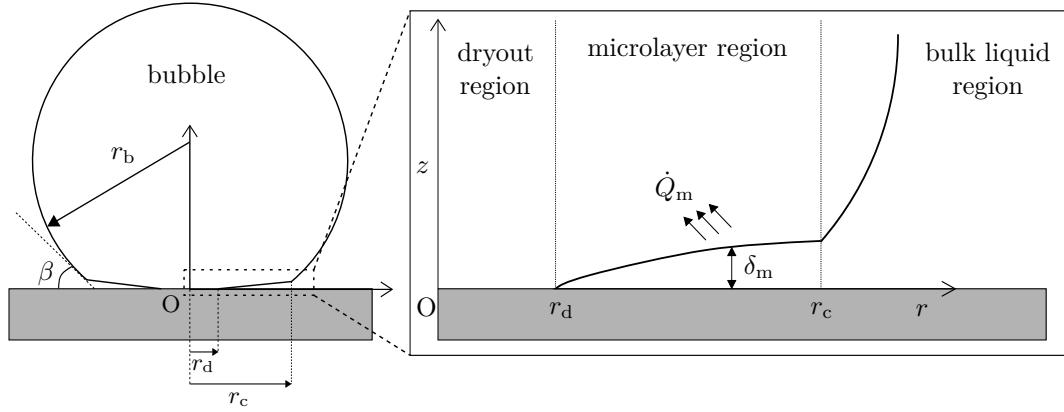


Figure 2.4: Schematic of the microlayer region in a bubble.

line region and may be as high as several tens of micrometers. Additionally, as compared to the contact line region, the microlayer covers a significantly larger area of the heater wall below the bubble [71]. Thus, the heat flux and the mass flux from the microlayer and the contact line region are vastly different.

The governing equations for the heat and the mass transfer from the microlayer to the bubble are derived based on the following assumptions:

1. The bubble is axisymmetric.
2. The microlayer is flat and its curvature is negligible.
3. The disjoining pressure due to the attractive forces between the fluid molecules and wall can be neglected in the microlayer region owing to its larger thickness compared to the contact line region.
4. Heat transfer in the microlayer region is governed by 1D conduction normal to the wall.

The assumptions 2 and 3 listed above imply that a lateral pressure gradient does not exist in the microlayer. Hence, it is not replenished by the fluid from the bulk liquid region [95]. As the bubble grows, the microlayer evaporates and advances on the heater surface. Thus, the length of the microlayer region and the thickness of the microlayer varies with time and radial distance from the nucleation site. A relation for this variation in film thickness and heat transfer from the microlayer to the bubble is formulated based on the governing mass and energy conservation equations as follows:

Mass conservation. The mass flux from the microlayer to the bubble depends on the rate at which the thickness of the microlayer varies and is given by

$$m_e'' = -\rho_l \frac{d\delta_m}{dt}, \quad (2.20)$$

where δ_m represents the thickness of the microlayer.

Energy conservation. The energy conservation equation for the microlayer is formulated assuming 1D conduction heat transfer from the wall to the bubble as follows:

$$q_m'' = m_e'' h_{lv} = \frac{T_w - T_v}{\delta_m / k_l + R_{int}}, \quad (2.21)$$

$$\dot{Q}_m = \int_{r_d}^{r_c} q_m'' dA, \quad (2.22)$$

where q_m'' and \dot{Q}_m represent the heat flux and the heat transfer rate from the microlayer to the bubble, respectively. Eliminating the evaporative mass flux m_e'' from Eqs. (2.20) and (2.21) gives the equation for the variation of the microlayer thickness

$$\frac{d\delta_m}{dt} = -\frac{T_w - T_v}{(\delta_m / k_l + R_{int}) \rho_l h_{lv}}. \quad (2.23)$$

Integrating Eq. (2.23) subject to an initial microlayer thickness profile, i.e. the variation in the thickness of the microlayer immediately after nucleation gives the microlayer thickness as a function of radial distance and time. The radius of the dryout region r_d is the location at which the microlayer evaporates completely and the thickness of the liquid film is zero, i.e.

$$\delta_m(r = r_d, t) = 0. \quad (2.24)$$

The prediction of microlayer dynamics depends on an initial microlayer profile. Cooper et al. [83] were the first to derive an expression for the initial microlayer profile based on a laminar boundary layer analysis for heat transfer controlled bubble growth. Later, Dwyer and Hsu [96] extended the model to provide a general relation for the initial microlayer profile for both the inertia and the heat transfer controlled growth stages. The authors modelled the hydrodynamics of the flow around the outer edge of a hemispherical bubble and assumed the microlayer thickness to be equal to the displacement thickness of the hydrodynamic boundary layer. Accordingly, the following relation was proposed:

$$\delta_0(r) = C\sqrt{v_1 t}. \quad (2.25)$$

Equation (2.25) can be written in terms of the radial distance r using the bubble growth relation for an inertia controlled growth process $r_b = C_1 t$ where C_1 is a constant defined in Eq. (2.2) [81]. At $r_b = r$, the initial microlayer profile becomes

$$\delta_0(r) = C\sqrt{v_1 (r/C_1)} = C_0\sqrt{r}. \quad (2.26)$$

This dependence of the initial microlayer profile on the square root of the radial distance was experimentally validated for inertia controlled bubble growth in water [97].

Recently, Utaka et al. [94] performed experiments on boiling of water and ethanol to find the initial microlayer thickness for fluids whose growth is primarily heat transfer controlled. They reported that the initial microlayer thickness increases linearly with radial distance from the nucleation site. Accordingly, they proposed the following equation for $\delta_0(r)$:

$$\delta_0(r) = Cr, \quad (2.27)$$

where $C = 4.46 \times 10^{-3}$ for water and 10.2×10^{-3} for ethanol. These values are commonly used in numerical simulations but are limited to only the fluids that were tested. In general, more experiments are needed to find a correlation for C valid for a range of fluids.

In summary, two models to describe the microscale heat transfer have been proposed in literature. In bubble growth models, either the contact line or the microlayer model is employed to quantify microscale heat transfer in boiling flows. In the past, studies have been conducted to formulate a criterion to identify if the microlayer or the contact line is formed in pool boiling. Fischer et al. [65] performed experiments on thin film evaporation of a fluorocarbon FC-72 and proposed the following criterion based on the ratio of the evaporative mass flux to the deposited mass flux to decide the dominating microscale heat transfer mechanism:

$$A = \frac{\text{evaporative mass flux}}{\text{deposited mass flux}} = \frac{k_1(T_w - T_{\text{sat}})}{h_{lv}\rho_l v_{\text{int}}\delta_0}, \quad (2.28)$$

$$A \begin{cases} < 1 & \text{microlayer heat transfer,} \\ > 1 & \text{contact line heat transfer,} \end{cases} \quad (2.29)$$

where v_{int} and δ_0 are the velocity of the liquid–vapour interface and film thickness, respectively. In boiling flows, however, the interface velocity is not known *a priori* and hence the ratio cannot be used to decide what model to use. Other authors used numerical simulations to predict the dominating microscale heat transfer phenomenon. Urbano et al. [98] and Hänsch et al. [72] performed CFD studies on the fluid flow at the base of the bubble in water and concluded that a contact line region is formed at low Ja numbers (or low wall superheats) while at a larger Ja number, a microlayer region is formed. However, these studies were limited to only the fluid being studied and their validity for low Prandtl number fluids has not been tested. Recently, Bureš et al. [99] proposed that if the velocity of the liquid–vapour interface of the bubble is larger than a certain critical velocity, i.e. $v_{\text{int}} > v_{\text{crit}}$, a microlayer is formed. However, the value of the critical velocity depends on empirical constants whose value is largely unknown. Thus, the development of a universal criterion to determine the dominating microscale heat transfer valid for all fluids is still a subject of ongoing research.

2.3.2 Macrolayer and thermal boundary layer heat transfer

In addition to the microscale heat transfer, a bubble in a liquid pool grows due to the evaporation of the superheated thermal boundary layer formed adjacent to the heater wall. In literature, two approaches are used to model the heat transfer from the thermal boundary layer to the bubble: (a) assuming 1D conduction heat transfer from the wall to the bubble in the layer of liquid in the thermal boundary layer trapped below the bubble called the macrolayer [18, 66, 85, 100] and (b) based on an approximate solution to an equation describing diffusion heat transfer to bubble in an infinite superheated liquid pool [60, 101]. The use of first approach is more desirable as it accounts for the influence of the variation in wall temperature on the evaporation rate from the thermal boundary layer. The second approach is based on a approximate solution the validity of which has not been tested for low Prandtl number fluids. The first approach is used in this work and the equations to model the heat transfer from the macrolayer and the thermal boundary layer are discussed in Chapter 4.

2.3.3 Bulk liquid heat transfer

In pool boiling, as the bubble grows, a portion of its surface will be in contact with the bulk liquid. In this region, the bubble may undergo evaporation or condensation depending on the magnitude of the bulk liquid temperature T_∞ and the vapour temperature T_v [16, 18, 100, 102–104]. If $T_\infty > T_v$, the bubble growth rate will increase due to evaporation of bulk liquid at the liquid–vapour interface and the rate of heat transferred from the bulk liquid to the bubble \dot{Q}_∞ will be positive. On the other hand, if $T_\infty < T_v$, the vapour in the bubble will condense leading to a negative value of \dot{Q}_∞ and the bubble growth rate to reduce.

Different models have been proposed to quantify the bulk liquid heat transfer. Han and Griffith [78] proposed a theory for bubble growth on a heated wall in a liquid pool based on the heat diffusion from the bulk liquid. The authors did not consider the heat transfer from the thermal boundary layer. The authors proposed the formation of a superheated layer around the bubble and modelled the bulk liquid heat transfer based on the heat diffusion from this superheated layer. The authors suggested that the superheated layer would continue to encompass the bubble even after the bubble had grown outside the wall thermal boundary layer. The model was validated against pool boiling experiments of distilled water on a copper plate and showed good agreement. The validated model was also used by Mikic et al. [81] to determine the bubble growth rate in the heat transfer controlled growth stage of a bubble. The formation of a thermal boundary layer around a bubble has also been observed in experiments investigating the growth of a bubble in pool boiling [17, 19, 20]. More recently, numerical studies on modelling the bubble growth in pool boiling of high Prandtl number fluids use

the Ranz–Marshall correlation to compute the heat flux from the bulk liquid via the boundary layer to the bubble as follows [18, 105, 106]:

$$q''_{\infty} = h_{\infty}(T_v - T_{\infty}), \quad (2.30)$$

$$h_{\infty} = \frac{k_l}{d_b} (2 + 0.6\text{Re}^{0.5}\text{Pr}^{0.3}), \quad (2.31)$$

where h_{∞} is the heat transfer coefficient, d_b is the bubble diameter, Re is the Reynolds number and Pr is the Prandtl number of the fluid. The rate of heat transferred to the bubble from the bulk liquid is

$$\dot{Q}_{\infty} = q''_{\infty} A_{\infty}, \quad (2.32)$$

where A_{∞} is the area of the bubble in contact with the bulk liquid which depends on the bubble radius and the thickness of the thermal boundary layer.

The validity of the Ranz–Marshall correlation is limited to fluids having a $\text{Pr} > 0.71$. The Prandtl number of liquid metals like sodium is of the order of 0.001, and a validated correlation for low Prandtl number fluids does not exist. To overcome this problem, Bankoff et al. [107] suggested a method to compute the bulk liquid heat transfer to a bubble based on the theory of Han and Griffith [78]. The authors assumed the formation of a boundary layer around a bubble and calculated the heat flux from the bulk liquid based on the thermal resistance of the boundary layer in series with an interface resistance. Thus, the heat flux from the bulk liquid to the bubble is given by

$$q''_{\infty} = \frac{T_{\infty} - T_v}{\sqrt{\pi\alpha_1 t}/k_l + R_{\text{int}}}, \quad (2.33)$$

where $\sqrt{\pi\alpha_1 t}$ is the thickness of a thermal boundary layer formed around the bubble, α_1 is the thermal diffusivity of the liquid and t is the bubble growth time.

2.4 Forces acting on a bubble in pool boiling

The departure of a bubble from a heated wall depends on the forces acting on it. The forces acting on a bubble are influenced by the orientation of the heater surface, boiling type (pool or flow) and direction of flow in case of flow boiling. One of the earliest force balance models to compute the departure diameter in boiling flows was proposed by Klausner et al. [108]. The authors identified the individual forces acting on a growing bubble as the buoyancy force, surface tension force, growth force which accounts for the distribution of pressure on a growing bubble, drag force, and a contact pressure force accounting for the presence of a wall below the bubble. The authors also proposed a set of equations to model the individual forces. Subsequently, Thorncroft et al. [74] extended the model of Klausner and proposed a generalised criterion to compute bubble

departure diameter valid for pool and flow boiling. Over the years, force balance models with different set of equations to model the individual forces identified by Klausner et al. [108] have been proposed. Jiang et al. [60] modelled bubble departure based on surface tension, drag, buoyancy and inertial forces exerted on a bubble by the vapour and the expelled liquid. The authors also considered the drag force exerted by the wake flow of a detaching bubble in their force balance model. The authors validated their model with several experimental data sets. Wang et al. [109] computed bubble departure diameter in pool boiling based on a balance of inertia, buoyancy, drag, Marangoni and excess pressure force. The authors modelled the excess pressure force as a sum of the force due to capillary pressure and excess vapour pressure which depends on a drag coefficient and bubble growth rate. Bhati et al. [110] and Paruya et al. [111] used the model proposed by Thorncroft et al. [74] but neglected the drag force and the contact pressure force. More recently, Bucci et al. [112] critically assessed the force balance model of Klausner et al. [108] and Thorncroft et al. [74] and concluded that the analytical expressions used to model the individual forces may not be accurate. The authors suggested a different set of equations to model the forces acting on a bubble which relies on accurately modelling the bubble base curvature and the curvature of the liquid–vapour interface. Several other models with varied levels of accuracy have been proposed in literature [105, 113, 114]. In the absence of a well established theory on the forces acting on a bubble valid for all fluids and under all conditions, the most widely used force balance model of Klausner et al. [108] and Thorncroft et al. [74] is used to model bubble departure in this work. The model of Klausner and Thorncroft has been used to compute bubble departure diameters in pool and flow boiling of different liquids and has shown good agreement with experimental results [18, 100, 115, 116]. The main forces acting on a bubble are shown in Fig. 2.5 where F_b , F_s , F_g , F_d and F_{cp} represent the buoyancy force, surface tension force, growth force, drag force and the contact pressure force, respectively. In horizontal pool boiling, assuming symmetric bubble growth, the net resultant force in the wall tangential direction will be zero and hence is not considered. The resultant force normal to the wall is

$$\Sigma F = F_g + F_d + F_{cp} + F_b + F_{s,z}, \quad (2.34)$$

where $F_{s,z}$ is the component of the surface tension force acting normal to the wall.

Growth force. Klausner et al. [108] studied the unsteady force due to the pressure distribution on a hemispherical bubble attached to a surface. According to the Rayleigh equation, the liquid pressure on the bubble can be described in terms of the motion of

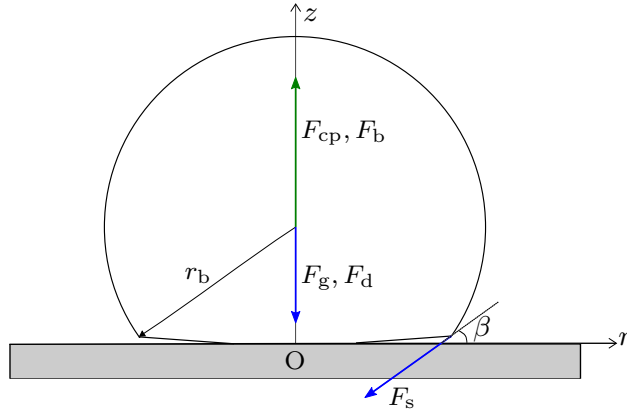


Figure 2.5: Forces acting on a bubble in pool boiling.

the liquid–vapour interface as

$$p_l(r_b) = \rho_l \left[r_b \frac{d^2 r_b}{dt^2} + \frac{3}{2} \left(\frac{dr_b}{dt} \right)^2 \right], \quad (2.35)$$

where r_b is the bubble radius at an instant of time t . Integrating the above equation gives the growth force

$$F_g = -\rho_l \pi r_b^2 \left[r_b \frac{d^2 r_b}{dt^2} + \frac{3}{2} \left(\frac{dr_b}{dt} \right)^2 \right]. \quad (2.36)$$

Drag force. Drag force F_d arises during bubble growth due to the relative motion of vapour with respect to the surrounding liquid. In horizontal pool boiling, assuming symmetric bubble growth, the drag force acting in the wall normal direction is given by [18]

$$F_d = -\frac{1}{2} \rho_l v_b^2 \pi r_b^2 C_D, \quad (2.37)$$

where v_b is the bubble growth rate and C_D is the drag coefficient which depends on the fluid and given by [18, 115, 117]

$$C_D = \frac{16}{\text{Re}} (1 + 0.15 \text{Re}^{0.5}) \quad \text{water and organic liquids,} \quad (2.38)$$

$$C_D = 0.5 \quad \text{sodium.} \quad (2.39)$$

In the above equation, Re represents the bubble Reynolds number and is given by

$$\text{Re} = \frac{d_b v_b}{\nu_l}, \quad (2.40)$$

where d_b and ν_l are the diameter of the bubble and the kinematic viscosity of the liquid, respectively.

Contact pressure force. The contact pressure force accounts for the presence of the wall below the bubble. An equation for the contact pressure force is formulated by integrating the pressure difference across the base of the bubble:

$$\vec{F}_{cp} = \int_{S_{base}} (p_c - p_v) \hat{n} dA, \quad (2.41)$$

where S_{base} is the bubble base area, p_c is the pressure at the base of the bubble, p_v is the vapour pressure in the bubble and \hat{n} is a unit vector normal to the wall. Klausner et al. [108] proposed that the pressure difference $p_c - p_v$ over the area S_{base} will be balanced by the surface tension at the base of the bubble. Thus,

$$F_{cp} = A_c \frac{2\sigma}{r_{cur}} = \frac{1}{2} \pi d_c^2 \frac{\sigma}{r_{cur}}. \quad (2.42)$$

In the above equation, $d_c = 2r_c$ is the contact diameter where r_c is given by Eq. (2.19). The term r_{cur} represents the radius of curvature at the bubble base and σ is the surface tension of the liquid. The following relationship for the radius of curvature in terms of the bubble radius was proposed by Klausner et al. [108]:

$$r_{cur} = 5r_b, \quad (2.43)$$

and is used in the present work.

Buoyancy force. The difference in density of the liquid and vapour in boiling flows results in a buoyancy force. In horizontal pool boiling, the buoyancy force is defined as

$$F_b = (\rho_l - \rho_v) V_b g, \quad (2.44)$$

where V_b is the volume of the bubble and g is the acceleration due to gravity.

Surface tension force. The surface tension force F_s keeps the bubble attached to the wall. It acts along the liquid–vapour interface of the bubble. The component of the surface tension force normal to the wall $F_{s,z}$ is given by

$$F_{s,z} = -\pi d_c \sigma \sin \beta. \quad (2.45)$$

In pool boiling, a bubble will begin to depart from a heated wall if the forces acting in the wall normal direction exceed the forces which keep the bubble attached to the wall. Thus,

$$\Sigma F = F_g + F_d + F_{cp} + F_b + F_{s,z} > 0, \quad (2.46)$$

signals the start of bubble departure.

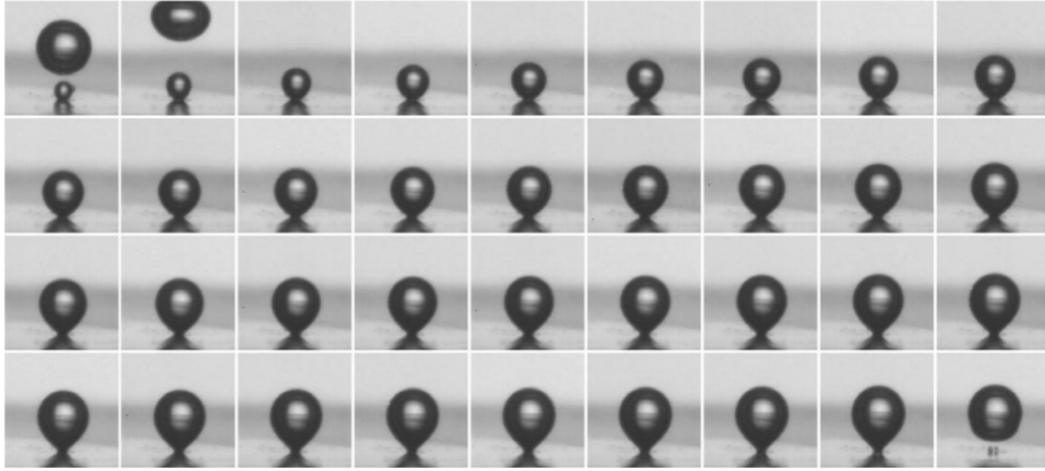


Figure 2.6: Bubble shape during the growth of a bubble in pentane pool boiling recorded at 375 fps in the experiment of Seidel et al. [121]

2.5 Contact angle and bubble shape in pool boiling

The contact angle and shape of a bubble changes as it grows in a liquid pool. A bubble growing on a moderately wetting surface is typically hemispherical immediately after nucleation with a contact angle of 90° . As it grows, owing to the surface tension forces acting on the bubble, its shape transitions to a truncated sphere with a contact angle $\beta < 90^\circ$ and then to a balloon-like shape before departure. Significant effort has been dedicated to experimentally study and accurately model this change in contact angle and shape of a bubble in pool boiling to study its effect on the growth of a bubble. Johnson et al. [118] performed one of the earliest set of experiments to study the effect of bubble shape on growth rate. The authors concluded that spherical bubbles were characterised by a lower growth rate compared to hemispherical-shaped bubbles. This was later confirmed by Hospetil et al. [119] who showed that the contribution of microlayer evaporation on the bubble growth process decreases as the bubble shape changes from a hemisphere to an oblate sphere. Building upon this, several studies proposed the use of a dynamic contact angle relation based on the evaporation of the microlayer to model the variation in the shape of the bubble [18, 60, 66, 120]. Ardron et al. [101] used equilibrium thermodynamics to predict the variation in the contact angle and shape of a bubble. The authors showed that the contact angle of a bubble depends on the Jakob number of the fluid and decreases asymptotically with time. More recently, Bhati et al. [110] and Paruya et al. [111] proposed an analytical bubble growth model where the shape of the bubble was simplified to be an ellipsoidal sphere.

Experiments on bubble growth in pool boiling show that the shape of a bubble transitions from a hemisphere at nucleation to a balloon-like shape at departure as seen in Figs. 2.6 and 2.7 [13, 121]. Capturing this change in shape of the bubble is critical to

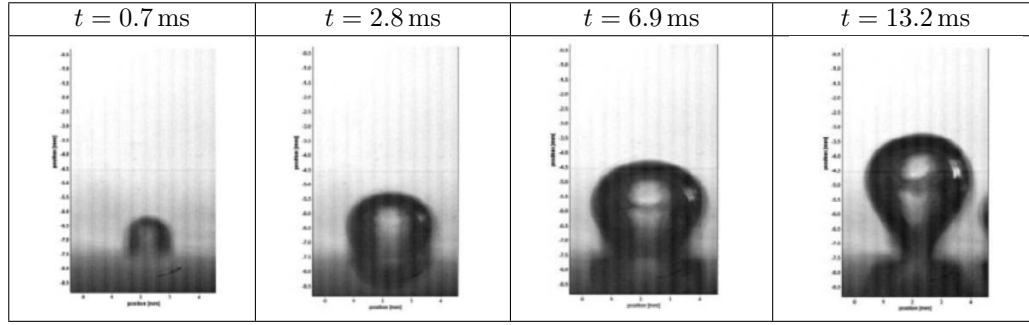


Figure 2.7: Bubble shape at four different points in time during the growth of a bubble in water pool boiling experiment of Duan et al. [13].

understand the dynamics of the bubble growth process. Most of the earlier numerical works on studying the bubble growth dynamics in pool boiling assumed the bubble to be spherical throughout the growth period [78, 122] or to grow with a constant contact angle [74, 108]. In the past, different approaches have been used to approximate the balloon-like shape of the bubble formed before departure. Owing to the complexity in accurately modelling the transition in shape, Kiper et al. [123] considered the bubble to be a sphere with a small neck connecting it to a wall. The authors stated that modelling the formation of the neck is important in predicting the departure diameter of a bubble. Later, Lesarge et al. [124] simplified the bubble shape to be a sphere atop a cylindrical neck and proposed an analytical bubble growth model to determine the bubble detachment characteristics like the shape, aspect ratio and the departure time. Recently, Ding et al. [18] developed a mechanistic model assuming the formation of a cylindrical bottleneck which was similar to the bubble profile suggested by Lesarge et al. [124]. The authors solved a governing equation for the conservation of fluid volume in the bottleneck to compute the variation in the height and the radius of the cylindrical neck as the bubble grows. A bubble was assumed to depart when the bottleneck breaks or the diameter of the base of the bubble reduces to zero. Though the formation of a neck has been included in mechanistic models, the balloon-like shape has not been modelled accurately before.

The studies highlighted above assumed a bubble to grow on a moderately wetting surface with a static contact angle between $30\text{--}100^\circ$. In pool boiling on highly wetting or superhydrophilic surfaces with static contact angle less than 10° , the bubble growth time increases, and it takes a substantially longer amount of time for a bubble to nucleate [125]. Thus, the waiting time between the detachment of a bubble and the nucleation of the next bubble is large which results in a decrease in the bubble detachment frequency [125, 126]. In addition, a bubble growing on superhydrophilic surface has an almost spherical shape at departure [125–127]. Experimental studies on pool boiling on superhydrophobic surfaces with static contact angle greater than 150° have shown

the formation of a vapour film on the surface and a bubble grows from this vapour film [128–130]. In addition, it was reported that the temperature of the surface below a bubble does not change during the bubble growth process [130]. This is in contrast to experimental observations on the growth of a bubble on a moderately wetting surface where the wall temperature changes as the liquid in the contact line or the microlayer region evaporates [13, 71, 131]. Thus, the dynamics of bubble growth on surfaces with extreme static contact angles are different. In the present work, the growth of a bubble in pool boiling on a moderately wetting surface is studied. Modelling bubble growth on superhydrophilic and superhydrophobic surfaces is beyond the scope of this study.

Sections 2.2–2.5 provided an overview of the general theory of single bubble growth in pool boiling flows including a mathematical representation of the heat transfer mechanisms and forces acting on a bubble. In the next section, characteristics of liquid metal boiling flows along with a review of relevant literature are presented.

2.6 Characteristics of liquid metal nucleate boiling

Liquid metal boiling is fundamentally different from the boiling of high Prandtl liquids. This is primarily due to the different thermophysical properties of the fluids. A comparison of the thermophysical properties of water and sodium at the saturation temperature and a pressure of 1 bar is shown in Table 2.1. The surface tension, latent heat and specific heat of the fluid determine the superheat needed for bubble nucleation while the thermal conductivity, liquid density and liquid to vapour density ratio influence the boiling characteristics. The surface tension and latent heat of sodium is double that of water while the specific heat is significantly lower. This indicates that sodium will superheat substantially before it nucleates. Due to the large thermal conductivity of sodium, boiling would essentially take place in a uniform temperature field. Performing a mass balance at the interface of a bubble gives

$$\dot{V}_v = \frac{\rho_l}{\rho_v} \dot{V}_l, \quad (2.47)$$

where \dot{V} is the volumetric flow rate. For sodium, the ratio of the liquid to vapour density is about three times that of water, thus implying large growth rates. Furthermore, due to the high thermal conductivity, a large thermal boundary layer is expected to form in sodium. Hence predominantly a sodium bubble will be surrounded by high temperature liquid as compared to water where the relatively thin thermal boundary layer would mean that a bubble would come in contact with the surrounding subcooled liquid, thus limiting its growth. Therefore, based on thermophysical properties, sodium boiling is expected to be characterised by large boiling superheats, large growth rates and owing to the high surface tension, large departure diameters as compared to ordi-

Table 2.1: Characteristic physical properties of water and sodium at saturation temperature and a pressure of 1 bar.

Property	Water	Sodium	Unit
Boiling point	100	882	°C
Surface tension	0.059	0.119	N m ⁻¹
Latent heat	2.2×10^6	3.8×10^6	J kg ⁻¹
Specific heat, C_p	4215	1270	J kg ⁻¹ K ⁻¹
Thermal conductivity	0.68	48.6	W m ⁻¹ K ⁻¹
Liquid density	958	742	kg m ⁻³
Liquid to vapour density ratio	850	2520	-

nary high Prandtl number liquids. These characteristics also indicate that the bubble growth in sodium will be predominantly inertia controlled [36].

Studies on inertia controlled bubble growth in liquid metals are scarce. Experiments on boiling liquid metals were pursued in the 1960s to predict the behaviour of nuclear reactor systems during accidents. Kottowski et al. [6] studied boiling in thin reactor tube bundles and reported large fluctuations in wall temperature and pressure during boiling. Akiyama et al. [132] and Johnson et al. [118] observed that when inertia dominates the bubble growth process, bubbles tend to be hemispherical. In the late 1980s, Sandia National Laboratories performed experiments on sodium and sodium-potassium boiling in pool and tubular boilers in laboratory-scale CSP systems [31, 32]. The unstable boiling nature of liquid metals and the lack of advanced measurement systems at that time limited the scope of these studies to only detection of bubbles. A major conclusion from these experimental studies was that bubbles in sodium boiling systems tended to be large and isolated compared to conventional fluids like water [46].

Prior studies on sodium boiling concluded that the sodium boiling process is highly unstable. In single bubble pool boiling flows, boiling instability is the sporadic switching between liquid phase natural convection heat transfer during the waiting phase and heat transfer associated with low frequency nucleate boiling during the bubble growth phase [36]. As compared to ordinary liquids, boiling of liquid metals is less stable due to long waiting times between the departure of a bubble and inception of the next bubble.

Unstable boiling generally takes place at low average wall heat flux if a nucleation site is quenched, i.e. the cavity is completely filled with liquid. In the absence of vapour in a cavity, heat transfer takes place by natural convection. During this waiting period, the wall temperature rises gradually till it reaches a threshold value at which a bubble nucleates and grows. In the growth period, heat transfer is governed by nucleate boiling. If the wall heat flux is not high enough to maintain the boiling process, the cavity will quench again and heat transfer switches back to natural convection. Thus, typical unstable boiling temperature profiles show large periods of natural convection heating where the temperature rises gradually followed by a rapid cooling of the surface when a bubble is formed.

The following sections provide further insights on the heat transfer and hydrodynamics of bubble growth in sodium boiling. A review of relevant literature on the wall superheat required to initiate bubble growth in sodium is presented. Also included are a brief description of past studies on heat transfer, bubble growth and departure characteristics in sodium pool boiling along with a review of published numerical heat transfer models to describe the bubble growth process in sodium boiling flows.

2.6.1 Wall superheat

The onset of bubble growth in nucleate boiling depends on the wall superheat. Superheat is defined as the difference between the wall and saturation temperature at the nucleation site. A vapour bubble grows from a cavity if it is in thermodynamic and mechanical equilibrium with the surrounding liquid. Several authors have discussed the mechanism of boiling incipience and the effect of system parameters like dissolved gases, system pressure, surface conditions on the boiling superheat in low and high Prandtl number fluids. Hsu et al. [39] proposed that an entrapped vapour embryo in a cavity will form a bubble if the temperature at the tip of the embryo, i.e. the point on the embryo that is farthest from the wall, is at least equal to the saturation temperature corresponding to the vapour pressure of the bubble. Thus, this criterion requires the bubble to be completely surrounded by a layer of superheated liquid. Assuming this mechanism, Shai et al. [40] proposed the following expression for the wall superheat:

$$\Delta T = \frac{T_{\text{sat}}^2}{B} \log \left(1 + \frac{2\sigma}{r_{\text{cavity}} p_{\text{sat}}} \right), \quad (2.48)$$

where B is an empirical fluid constant and is equal to 4565.5 K for sodium and 2070 K for water, r_{cavity} is the cavity radius, and T_{sat} and p_{sat} are the saturation temperature and pressure, respectively. Figure 2.8 shows the comparison of superheat needed for boiling of sodium and water calculated using Eq. (2.48). Liquid metals are characterised by high surface tension and good wettability compared to high Prandtl number fluids like water and refrigerants. This causes all large cavities on a heater surface to be flooded with the liquid resulting in high wall superheat for nucleation.

Various parameters like gas entrainment levels, oxide levels, surface conditions, heating surface material, heat flux and in the case of flow boiling, velocity of the bulk liquid influence the boiling superheat of liquid metals. Kottowski et al. [6] observed that the boiling superheat decreases with increasing oxide impurity and gas entrainment. Based on a review of sodium loop experiments, they concluded that wall superheat for clean sodium (O_2 impurity of about 5–10 ppm) was 80 ± 30 K and that for sodium with oxide impurity of about 40 ppm was 25 ± 20 K. Singer and Holtz [41] theoretically studied the influence of inert gas entrainment on the boiling superheat. They provided an ana-

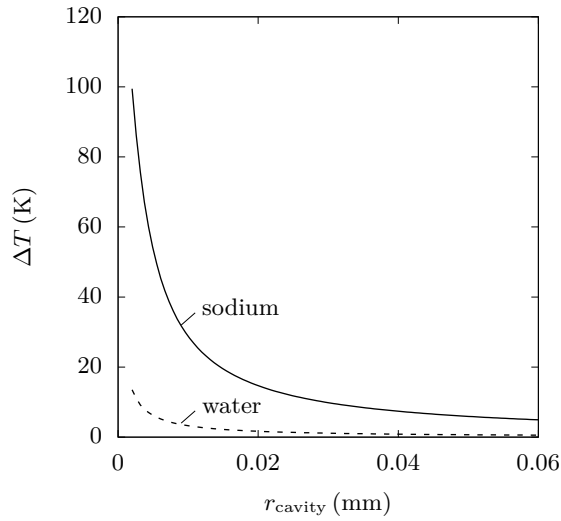


Figure 2.8: Variation of wall superheat required for bubble nucleation in sodium (solid line) and water (dashed line) boiling with cavity radius at atmospheric pressure.

lytical relation for the wall superheat based on the cavity size, saturation conditions of the liquid and the partial pressure of the dissolved inert gas. Results from their analysis showed that the wall superheat decreases with increasing gas entrainment.

Marto et al. [42] from their experiments concluded that the wall superheat decreased on roughening the heater surface. With regards to the system pressure and the velocity of the bulk fluid, it was observed that the boiling superheat decreased with increasing system pressure and flow velocity. Several possible reasons were proposed to explain the decrease in superheat with increasing flow velocity. In experiments performed to measure the superheat in a recirculating sodium boiling loop with argon cover gas, significant gas entrainment was reported at large flow velocities (above 1.4 m/s) which reduced the wall superheat. Chen et al. [133] postulated that the large flow velocity in boiler tubes would lead to large pressure fluctuations at potential nucleation sites due to the increased flow turbulence. A sudden drop in the local pressure could cause a bubble to nucleate at relatively low superheats. Dwyer [36] added to the turbulence theory by suggesting that due to the combined effect of pressure and temperature fluctuations at the walls of a heater, there is a sudden spike in temperature along with a decrease in the local pressure at the nucleation site that leads to the inception of bubbles. Dwyer et al. [134] proposed that the energy required for bubbles to nucleate is provided not only by the heated wall and superheated liquid in the thermal boundary layer but also by the decelerating turbulent eddies as they approach the walls of the heater. Though significant research has been reported on the wall superheat of sodium, a consensus has not been reached on the dominating mechanism that controls the nucleation of bubbles. This is primarily due to the difficulty in performing experiments with sodium and the lack of knowledge of turbulence in liquid metal flows.

2.6.2 Heat transfer and bubble growth characteristics in sodium pool boiling

The growth of a bubble in sodium, like any other liquid, is controlled by microscale and macroscale heat transfer effects. In this section, research on heat transfer in sodium boiling and the proposed numerical models are reviewed.

Microscale heat transfer in sodium pool boiling. In liquid metals, like high Prandtl number liquids, a microlayer is formed below the bubble. However, according to the author's knowledge, no experimental data on microlayer thickness and heat flux in liquid metals has been reported in open literature. Hence, the analysis of microscale heat transfer in liquid metals is purely theoretical. Dwyer and Hsu [96] theoretically analysed the fluid flow in the microlayer at the time of bubble inception for inertia controlled bubble growth in liquid metals as reported earlier in Section 2.3.1 and proposed a relation for the initial microlayer thickness (Eq. (2.26)). Later, Deane and Rohsenow [58] proposed a bubble growth model by accounting for heat transferred from the microlayer. However, the authors postulated the microlayer to be fluid layer of uniform thickness which is contrary to experimental observations in boiling of high Prandtl number fluids [71]. Recently, Giustini et al. [135] simulated the growth of a sodium bubble in a liquid pool using a validated interface-tracking algorithm and demonstrated the formation of a liquid microlayer below a bubble. The authors showed that the thickness of the microlayer in sodium varies with radial distance from the nucleation site as opposed to the assumption of Deane and Rohsenow [58].

Reported studies of microscale heat transfer in boiling of liquid metals are restricted to the microlayer region. Studies of contact line modelling of alkali liquid metals in general, and sodium in particular, are scarce. One of the key characteristics of liquid metals is the presence of free electrons, while conventional fluids are dielectric [136]. In thin metallic films the motion of these electrons is confined, which causes an increase in their energy density according to Heisenberg's uncertainty principle [137]. This produces an effective electron pressure which adds to the disjoining pressure in the contact line region. The magnitude of this pressure depends on the work function, i.e. the amount of energy needed to move an electron from the surface of a wall to the liquid and can be estimated by solving complex quantum mechanical equations.

One of the first studies on modelling the contact line region in liquid metals by considering the electronic pressure component was reported by Ajaev et al. [138, 139]. The authors studied the fluid flow and rupture of thin molten metal films resulting from irradiation by a Gaussian laser beam. Since no experimental data was available to model the disjoining pressure, and their accurate theoretical prediction would require solving complex quantum mechanical equations, the authors proposed the total disjoining pressure to be a linear combination of the individual components which they called dispersion pressure (pressure resulting from van der Waals forces in the absence

of electrons) and electronic pressure. They presented a parametric study and discussed the trends in film shape and rupture time of metal films for different combinations of the pressure components. Later Tipton et al. [136] and Yi et al. [140] provided a more comprehensive model to study thin film evaporation of sodium flows on a stainless steel substrate. The authors solved a complete van der Waals equation, including electronic forces, to study the film dynamics for a range of electronic-to-dispersion pressure ratios. However, they noted that an accurate prediction of the pressure components would require knowledge of the work functions, which is difficult to obtain as it relies heavily on accurate quantum description of the system which is not available. Furthermore, they limited their discussion to a wall superheat of 0.0005 K and did not study the influence of higher superheats.

Numerical heat transfer models. Numerical simulations of bubble growth in sodium boiling are scarce. Deane and Rohsenow [58] proposed one of the earliest numerical heat transfer models to study the temperature fluctuations on the heater wall during bubble growth in sodium including microscale heat transfer. A schematic of the assumed heat transfer process in their model is shown in Fig. 2.9. The authors divided the entire bubble cycle into two phases: (a) the bubble growth phase up to the departure time $t = t_c$, during which the microlayer is in contact with the wall and (b) the waiting period from $t = t_c$ to the time at which the next bubble nucleates $t = \tau$ during which liquid sodium is in contact with the wall. The times t_c and τ were an input to the model obtained from water boiling experiments. The authors assumed heat transfer via 1D conduction in the wall and sodium. The following quantities were used in formulating the model:

$$\theta_w(x, t) = T_w(x, t) - T_{\text{sat}}, \quad (2.49)$$

$$\theta_l(y, t) = T_l(y, t) - T_{\text{sat}}. \quad (2.50)$$

During the bubble growth phase, heat transfer at the solid–fluid interface was computed assuming an equivalent heat transfer coefficient, h_{eq} which accounts for evaporation of the microlayer and the interface thermal resistance. The authors noted that since no method was available to accurately predict h_{eq} , its value was assumed in order to bring the predicted results from the model in agreement with their in-house experimental results. In addition, the authors assumed the microlayer to be a fluid layer of uniform thickness, which is contrary to experimental observations in boiling of high Prandtl number fluids and CFD simulation of microlayer formation in sodium boiling flows [71, 135]. During the waiting phase, temperature at the solid–liquid interface was computed from a flux continuity equation, i.e. heat flux in the solid wall is equal to the heat flux in liquid sodium. A major conclusion from this study was that the magnitude of temperature fluctuations during bubble growth due to evaporation of the microlayer is significantly greater than the fluctuations caused by surface quenching at bubble departure.

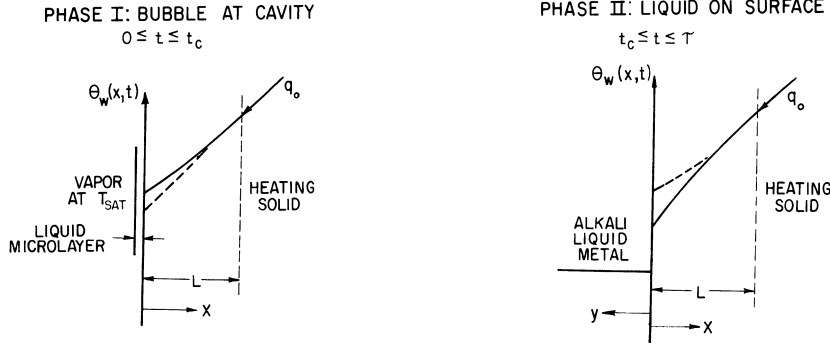


Figure 2.9: Schematic of the heat transfer to a bubble as proposed by Deane and Rohsenow [58].

Dwyer et al. [141] proposed a relation to model bubble growth in terms of the wall superheat, the pressure of the liquid pool, and thermophysical properties of the heater wall and liquid metal. The relation was derived for hemispherical bubbles assuming that the microlayer exists throughout the bubble growth process and at no point evaporates completely. This implied that a dryout region was not formed throughout the growth process. The authors assumed the heat transfer from the microlayer to the bubble to be similar to a semi-infinite heater of uniform temperature coming in contact with a heat sink at a lower temperature. Thus, the microlayer heat flux q''_m and the microlayer heat transfer rate \dot{Q}_m are

$$q''_m = \frac{k_w (T_{w,0} - T_v)}{\sqrt{\pi \alpha_w t}}, \quad (2.51)$$

and

$$\dot{Q}_m = 2\pi \int_0^{r_b} q''_m r dr = \frac{2r_b^2}{\sqrt{t}} (\pi k_w c_{p,w} \rho_w)^{1/2} (T_{w,0} - T_v), \quad (2.52)$$

where $T_{w,0}$ is the wall temperature at which the bubble nucleates. k_w , $c_{p,w}$, and ρ_w are the thermal conductivity, specific heat and density of the heater wall, respectively. A relationship for the heat transfer from the bulk liquid to the bubble was also derived using a similar analogy. The heat transfer to the bubble from the bulk liquid was assumed to be the same as that of conduction heat transfer to a spherical bubble growing in a uniformly heated liquid. Based on this analogy, heat transfer from the bulk liquid was given by

$$\dot{Q}_\infty = q''_\infty A_\infty = \frac{\sqrt{3} k_l (T_{w,0} - T_v)}{\sqrt{\pi \alpha_l t}} (2\pi r_b^2) = \frac{2\sqrt{3} r_b^2}{\sqrt{t}} (\pi k_l c_{p,l} \rho_l)^{1/2} (T_{w,0} - T_v), \quad (2.53)$$

where q''_∞ and A_∞ are the bulk liquid heat flux and the curved surface area of the hemispherical bubble, respectively. An equation for the bubble radius as a function of time was obtained as follows from an overall energy balance equation of the bubble, i.e.

$\dot{Q}_b = \dot{Q}_m + \dot{Q}_\infty$, and substituting for T_v from Eq. (2.1):

$$r_b = \frac{8}{3} \frac{(\Delta T) C^2}{C_1^4} \left[\left(C_1^2 + \frac{C_1^4 t}{4(\Delta T)^2 C^2} \right)^{3/2} - C_1^3 \right] - \frac{C_1^2 t^{3/2}}{3\Delta T C}, \quad (2.54)$$

$$\Delta T = T_{w,0} - T_{\text{sat}}, \quad (2.55)$$

$$C = \frac{1}{\rho_v h_{lv} \pi^{1/2}} \left[(k_w c_{p,w} \rho_w)^{1/2} + (3k_l c_{p,l} \rho_l)^{1/2} \right], \quad (2.56)$$

where C_1 is the constant defined in Eq. (2.2). The Dwyer model was the first to consider the effect of heat transfer from the microlayer and the bulk liquid on bubble growth in sodium. However, the model was derived for a specific case, i.e. a hemispherical bubble growing in a liquid pool of temperature equal to the wall temperature. In addition, the microlayer heat transfer was computed based on the properties of the wall. During the bubble growth process, the microlayer profile changes as the amount of liquid underneath the bubble increases with an increase in the bubble radius. This was not accounted for in the model.

2.6.3 Departure diameter and departure time in sodium pool boiling

The size of a departing bubble and departure time are important parameters in predicting the performance of a sodium boiling system. According to the author's knowledge, no reliable experimental data is available on the departure diameter and departure time of a bubble in sodium pool boiling. This is a consequence of the difficulty in performing experiments with sodium. Optical experimental techniques, like the use of a high-speed camera, are inapplicable as sodium is opaque. Experiments measuring the surface temperature fluctuations with transparent heaters and thermocouples embedded in the heater wall are commonly used to determine bubble departure time in water [13, 71]. However, such techniques are difficult to implement in sodium as measuring the rapid surface temperature fluctuations below a growing sodium bubble would require highly sensitive thermocouples. Thus, most of the published studies on departure diameter and departure time in sodium and other liquid metals in general are either based on theoretical modelling or correlations derived from experimental data on bubble growth in conventional liquids.

Bubble departure characteristics in high Prandtl liquids have been studied extensively. Some of these studies have been extended to sodium. Cole and Rohsenow [142] proposed the following correlation for the bubble departure diameter in high Prandtl

liquids based on the thermophysical properties of the liquid and the vapour:

$$Eo = 1.5 \times 10^{-4} Ja^{5/4}, \quad (2.57)$$

$$Eo = \frac{g(\rho_l - \rho_v) d_{dep}^2}{\sigma}, \quad (2.58)$$

where Eo , Ja and d_{dep} are the Etövis number, Jakob number and bubble departure diameter, respectively. Deane et al. [58] extended the model to sodium. The authors stated that the Jakob number of water is similar to that of sodium at the same pressure and hence Eq. (2.58) can be used to predict the departure diameter in sodium. The validity of the equation is questionable since the relation was derived for spherical bubbles, however, bubbles in sodium tend to be hemispherical. Nevertheless, Dwyer et al. [36] argued that the bubble departure time calculated using Eqs. (2.54) and (2.58) are reasonable (of the order of a few milliseconds) and thus the predicted departure diameters are at least qualitatively correct.

Bankoff et al. [107] improved the model of Deane et al. [58] by extending it to non-hemispherical bubbles. In their model, the bubbles were assumed to grow with a constant contact angle and the bubble radius at an instant was assumed to be a quadratic function of time. The departure diameter was calculated based on a balance of the buoyancy force and the drag force acting on the bubble as follows:

$$\frac{\pi r_{dep}^2}{3} (2 + 3 \cos \beta - \cos^3 \beta) g (\rho_l - \rho_v) = \frac{1}{2} \rho_l C_D v_b^2 \pi r_{dep}^2 (1 + \cos \beta). \quad (2.59)$$

A drawback of the model was that the authors did not provide a sound justification for choosing the quadratic bubble growth rate relation. In addition, the coefficients in the quadratic relation were obtained based on assuming a bubble departure time from the work of Deane et al. [58] rather than calculating it from a force balance. The authors also did not validate their results with sodium or any other liquid.

2.7 Summary

Though significant efforts have been dedicated to understand the boiling process in sodium, a comprehensive model incorporating all physical phenomena has not been developed yet. Based on a review of past work, the following gaps in knowledge are identified and will be addressed in this doctoral project.

As discussed in Section 2.3.1, two models for computing the microscale heat transfer rate in boiling have been proposed. Pool boiling bubble growth models either use the contact line model or the microlayer model. However, due to the lack of experimental data on sodium boiling, the dominating microscale heat transfer mechanism in sodium

is unknown. Thus, in this work, the contact line region and the microlayer region will be modelled to provide an insight into the heat transferred from each region.

To the best of the author's knowledge, the contact line region in sodium pool boiling has not been modelled yet. In addition to the presence of free electrons, sodium is characterised by high thermal conductivity and a large wall superheat as alluded to in Section 2.6.1. The influence of these parameters on the contact line region has not been studied. This work will address this gap in knowledge by highlighting the major differences in the contact line dynamics in boiling of high and low Prandtl number liquids. In addition, the effect of wall superheat and electronic pressure component on the heat transferred from the contact line region in sodium boiling will be investigated.

Numerical heat transfer and force models to compute the growth rate and departure characteristics of a bubble in sodium pool boiling have been proposed in literature [58, 107]. However, these models over-simplify the bubble growth process and are not comprehensive enough in considering all the underlying physics as reported in Sections 2.6.2 and 2.6.3. Previously published heat transfer models for bubble growth in sodium boiling were derived assuming the bubble to be hemispherical throughout the growth process and do not consider the heat transferred from the thermal boundary layer to the bubble. However, in reality, the shape of a bubble changes as it grows which has a significant influence on the bubble growth and departure characteristics. Also, the temperature of the heater surface below the bubble varies during the growth process, which was not considered in some models like the one proposed by Dwyer [141].

Thus, to overcome these limitations, in the present work, it is proposed to develop a physics-based mechanistic bubble growth model. The model will couple the heat transferred from all mechanisms to the bubble with the forces acting on it and account for the change in shape by incorporating a dynamic contact angle model. In addition, the variation of wall temperature will be predicted based on the evaporation rate from the microlayer and the macrolayer. Such a model will be useful in assessing the importance of different mechanisms of heat transfer and forces acting on a bubble. This knowledge is important in understanding the dynamics of sodium boiling flows.

Heat transfer modelling of the contact line region¹

This chapter describes the modelling of the heat transfer from the contact line region to a bubble in sodium pool boiling. A brief description of the contact line region formed underneath a bubble along with the governing conservation equations was provided in Section 2.3.1. The governing equations are used to formulate a mathematical model including the effect of electron pressure component, which is unique to liquid metals. The assumptions made in deriving the model are critically assessed to determine its validity for modelling microscale evaporation in sodium. The model is used to compare the evaporative heat flux from the contact line region in sodium and a high Prandtl number fluorocarbon FC-72. The effect of specific characteristics of sodium—high boiling superheat and presence of an electron pressure—on the evaporative heat flux from the contact line region is investigated. In addition, a methodology to incorporate the model into high fidelity CFD simulations is introduced.

3.1 Introduction

A schematic of the contact line region formed below a bubble of radius r_b , and the underlying fluid flow and heat transfer phenomena, were introduced in Section 2.3.1. The contact line region is a transition region between a non-evaporating adsorbed layer and the macro region. The fluid film in the contact line region is characterised by a strong change in its curvature and the presence of a disjoining pressure, i.e. the pressure resulting from intermolecular forces of attraction between the wall and the fluid molecules. In addition, due to the relatively small thickness of the fluid film, high evaporation rates are expected. As the liquid in the contact line region evaporates, a lateral pressure gradient is developed which pulls in fresh liquid from the macro

¹Material in this chapter has been published as: S. Iyer, A. Kumar, J. Coventry, J. Pye, and W. Lipiński, Micro-scale heat transfer modelling of the contact line region of a boiling-sodium bubble, *International Journal of Heat and Mass Transfer*, vol. 160, p. 120106, 2020.

region. A mathematical model to describe these complex fluid flow and heat transfer mechanisms was proposed by Stephan et al. [61] which is extended in this work to study the contact line dynamics in sodium boiling.

A key characteristic of thin liquid sodium films, which differentiates it from conventional fluids is the presence of free electrons which adds to the disjoining pressure [136]. In this work, the proposed method of Ajaev et al. [138, 139] is used to include the effect of electron pressure in the governing conservation equations of fluid flow and heat transfer in the contact line region. In addition to the presence of free electrons, sodium is characterised by high thermal conductivity and large boiling superheats, the influence of which on the contact line region has not been studied. This work seeks to address these gaps in knowledge by first highlighting the major differences in the contact line dynamics between high and low Prandtl number fluids. Secondly, a parametric analysis is presented to study the influence of wall superheat, the electron pressure component, vapour temperature and the accommodation coefficient on the contact line region in sodium boiling.

3.2 Mass, momentum and energy conservation equations

The governing mass, energy and the momentum conservation equation in the radial direction representing the complex interplay of heat transfer and fluid flow in the contact line region are represented by Eqs. (2.6), (2.9) and (2.18) provided in Section 2.3.1, respectively. The momentum conservation equation normal to the wall represented by Eq. (2.10) is extended to include effect of the electron pressure as follows:

$$p_c = p_v - p_l = p_{\text{dis}} + p_{\text{cap}} + p_{\text{rec}} = f(\Pi) + \sigma\kappa - \left(\frac{1}{\rho_v} - \frac{1}{\rho_l} \right) m_e''^2. \quad (3.1)$$

The term $f(\Pi)$ in Eq. (3.1) represents the total disjoining pressure which includes the effect of the disjoining and the electron pressure. An accurate estimation of the disjoining and electron pressure components will require the modelling of the complete van der Waals and complex quantum mechanical equations [143], which are beyond the scope of this work. Hence, to simplify the model, the influence of the electron pressure is taken into account using the additive method suggested by Ajaev et al. [138] as follows:

$$f(\Pi) = \Pi_A(\delta) + \Pi_B(\delta), \quad (3.2)$$

$$\Pi_A(\delta) = \frac{\mathcal{A}}{\delta^3} \quad \text{and} \quad \frac{\Pi_B(\delta)}{\Pi_A(\delta)} = \beta, \quad (3.3)$$

where \mathcal{A} is the Hamaker constant and the electron pressure component $\Pi_B(\delta)$ is taken into account using the parameter β such that $0 < \beta < 100$ [138].

3.3 Boundary-value problem

The governing equations described in the previous section are rearranged into a set of ordinary differential equations to formulate a mathematical model to predict the contact line characteristics in liquid metal boiling flows [88, 144].

$$\frac{d\delta}{dr} = \delta', \quad (3.4a)$$

$$\frac{d\delta'}{dr} = \frac{(1 + \delta'^2)^{1.5}}{\sigma} \left[p_c - f(\Pi) + \left(\frac{1}{\rho_v} - \frac{1}{\rho_l} \right) f(\delta, \delta', p_c) \right], \quad (3.4b)$$

$$\frac{dp_c}{dr} = -\frac{3\mu_l}{\delta^3 \rho_l h_{lv}} q'_w, \quad (3.4c)$$

$$\frac{dq'_w}{dr} = \frac{T_w - T_v \left(1 + \frac{p_c}{h_{lv} \rho_l} \right)}{\frac{\delta}{k_l} + \frac{R_{int}}{\sqrt{1 + \delta'^2}}}, \quad (3.4d)$$

where

$$f(\delta, \delta', p_c) = \frac{1}{h_{lv}^2} \left[\frac{T_w - T_v \left(1 + \frac{p_c}{h_{lv} \rho_l} \right)}{\frac{\delta \sqrt{1 + \delta'^2}}{k_l} + R_{int}} \right]^2.$$

The boundary conditions to solve Eqs. (3.4a)–(3.4d) are derived based on the conditions in the adsorbed film. As the adsorbed layer is flat, its slope and hence its curvature is zero. Additionally, the high disjoining pressure in this layer prevents the evaporation of the liquid film. Hence, the evaporative mass flux, heat flux and the integrated heat flux $q'_{w,ad}$ are zero. Substituting $\kappa = 0$ and $m''_e = 0$ in Eq. (3.1) gives the pressure $p_{c,ad}$ in the adsorbed layer. Similarly, the thickness of the layer δ_{ad} is obtained by substituting $q''_w = 0$ and $p_c = p_{c,ad}$ in Eq. (2.18). Therefore, the boundary conditions to solve the mathematical model are:

$$\delta(r = 0) = \delta_{ad} = \left[\frac{\mathcal{A}(1 + \beta)}{\rho_l h_{lv} \left(\frac{T_w}{T_v} - 1 \right)} \right]^{1/3}, \quad (3.5a)$$

$$\delta'(r = 0) = 0, \quad (3.5b)$$

$$p_c(r = 0) = p_{c,ad} = \frac{\mathcal{A}(1 + \beta)}{\delta_{ad}^3}, \quad (3.5c)$$

$$q'_w(r = 0) = q'_{w,ad} = 0. \quad (3.5d)$$

The scales of the terms r , δ , δ' , p_c and q'_w in Eqs. (3.4) and (3.5) vary significantly. In the contact line region, the film thickness is of the order of a few micrometers while the variations in the disjoining pressure, owing to the inverse power law dependence on the film thickness, are on the order of $1 \times 10^6 \text{ N m}^{-2}$. To cater for such large variations in the scales of the variables, Eqs. (3.4a)–(3.4d) and the boundary conditions are non-

dimensionalised using the adsorbed layer thickness δ_{ad} , pressure $p_{\text{c,ad}}$ and heat flux in the contact line region $k_1(T_w - T_v)$.

$$r^* = \frac{r}{\delta_{\text{ad}}}; \delta^* = \frac{\delta}{\delta_{\text{ad}}}; \delta^{*'} = \delta'; p_c^* = \frac{p_c}{p_{\text{c,ad}}}; q_w^{*'} = \frac{q_w'}{k_1(T_w - T_v)} \quad (3.6)$$

The resulting dimensionless equations, Eqs. (3.7a)–(3.7d) and the boundary conditions, Eqs. (3.9a)–(3.9d) are given below and are solved using a shooting method implemented in MATLAB [145].

$$\frac{d\delta^*}{dr^*} = \delta^{*'}, \quad (3.7a)$$

$$\frac{d\delta^{*'}}{dr^*} = C_1 (1 + \delta^{*2})^{1.5} \left(p_c^* - \frac{1}{\delta^{*3}} + C_2 \left(\frac{1 - p_c^*}{\delta^* \sqrt{1 + \delta^{*2}} + C_3} \right)^2 \right), \quad (3.7b)$$

$$\frac{dp_c^*}{dr^*} = -\frac{C_4 q_w^{*'}}{\delta^{*3}}, \quad (3.7c)$$

$$\frac{dq_w^{*'}}{dr^*} = \frac{1 - p_c^*}{\delta^* + \frac{C_3}{\sqrt{1 + \delta^{*2}}}}, \quad (3.7d)$$

where

$$C_1 = \frac{\delta_{\text{ad}} p_{\text{c,ad}}}{\sigma}, \quad (3.8a)$$

$$C_2 = \frac{k_1^2 (T_w - T_v)}{p_{\text{c,ad}} \delta_{\text{ad}}^2 h_{\text{lv}}^2} \left(\frac{1}{\rho_v} - \frac{1}{\rho_l} \right), \quad (3.8b)$$

$$C_3 = \frac{R_{\text{int}} k_1}{\delta_{\text{ad}}}, \quad (3.8c)$$

$$C_4 = \frac{3\mu_l k_1 (T_w - T_v)}{\rho_l h_{\text{lv}} \delta_{\text{ad}}^2 p_{\text{c,ad}}}. \quad (3.8d)$$

$$\delta^*(r^* = 0) = 1 + \epsilon_1, \quad (3.9a)$$

$$\delta^{*'}(r^* = 0) = 0, \quad (3.9b)$$

$$p_c^*(r^* = 0) = 1, \quad (3.9c)$$

$$q_w^{*'}(r^* = 0) = \epsilon_2. \quad (3.9d)$$

In the above equation, ϵ_1 and ϵ_2 are perturbations necessary to obtain a non-trivial solution. A fourth-order Runge–Kutta numerical scheme based on Dormand–Prince (4,5) pair is used to integrate Eq. (3.7) [146]. The value of $\epsilon_1 = 0.001$ is prescribed in the model while the value of ϵ_2 is computed iteratively using a bisection method such that the slope of the film is neither non-negative (which occurs at large values of ϵ_2) nor infinite (occurs if the predicted ϵ_2 is small). A detailed solution procedure is provided

in the work of Batzdorf [88]. In addition, to minimise the influence of perturbations on the solution, Schäfer [147] suggested that the ratio of ϵ_2 to the overall heat transfer at the end of the integration domain should be less than 5%. For all the results presented in this work, it was ensured that this criterion was met. The value of the ratio was found to increase with wall superheat, with a maximum value of 4% obtained at a superheat of 40 K.

3.4 Verification of the model and validation of assumptions

3.4.1 Verification of the contact line model

The model developed in this work is verified and not validated due to the lack of available experimental data on contact line film characteristics of sodium. Previous experimental studies on bubble growth in high Prandtl number fluids have reported the contribution of contact line evaporation to the overall bubble growth process [64, 148]. However, the use of data from these studies to validate the current model will require coupling the contact line model to high-fidelity bubble growth simulations which is beyond the scope of this work. Hence, only a verification study is performed.

The mathematical model and solution algorithm were verified by comparing the results with those obtained from direct numerical simulations (DNS) of Batzdorf [88]. The DNS simulations were performed to study the contact line dynamics for a fluorocarbon FC-72 for wall superheats ranging from 0 K to 20 K and assuming the length of the contact line region $r_{\text{end}} = 0.5 \mu\text{m}$. The vapour temperature was assumed to be equal to the saturation temperature. Table 3.1 summarises the thermophysical properties of FC-72 used in the numerical simulations. Figure 3.1 shows the comparison of the contact angle $\theta_{\text{end}} = \tan^{-1}(\delta'(r_{\text{end}}))$ and integrated wall heat flux $q'_{\text{w, end}} = q'_{\text{w}}(r_{\text{end}})$ at the end of the contact line region calculated from the present model with the simulation results of Batzdorf [88]. The agreement between the model and the simulations results is good,

Table 3.1: Thermophysical properties of FC-72 used in the numerical simulations [88].

Property	Symbol	Value	Unit
Saturation temperature	T_{sat}	329.75	K
Density of liquid	ρ_l	1619.82	kg m^{-3}
Density of vapour	ρ_v	13.36	kg m^{-3}
Dynamic viscosity	μ_l	4.5306×10^{-4}	Pa s
Thermal conductivity	k_l	0.05216	$\text{W m}^{-1} \text{K}^{-1}$
Surface tension	σ	0.008273	N m^{-1}
Latent heat	h_{lv}	84515	J kg^{-1}
Hamaker constant	\mathcal{A}	4.37×10^{-21}	J
Accommodation coefficient	f	0.5	–

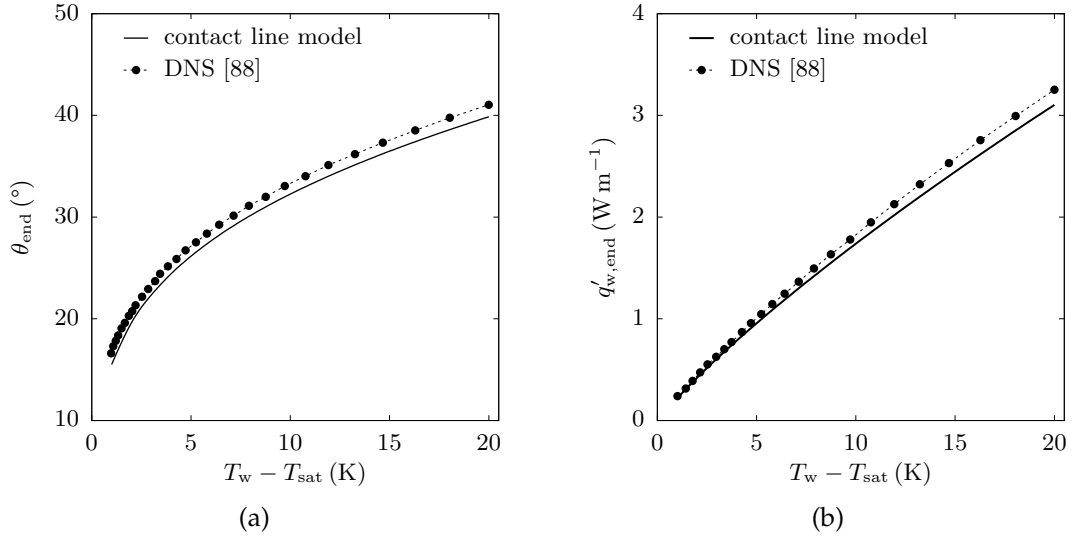


Figure 3.1: Validation of the contact line model with DNS of Batzdorf [88]: (a) contact angle and (b) integrated heat flux.

with a maximum relative error of 2.9% and 3.8% in the contact angle and integrated heat flux, respectively, at a superheat of 20 K.

3.4.2 Validity of the linear mass transfer model in the boiling sodium contact line region

In the contact line region, the net mass flux through the liquid–vapour interface in sodium is calculated using the relation proposed by Schrage [92]. As reviewed by Wang et al. [90], the Schrage model defined the net mass flux through an interface as the difference between the flux due to pure condensation and evaporation, i.e. $m''_e = m''_{\text{evp}} - m''_{\text{con}}$. The magnitude of these fluxes depends on condensation and evaporation coefficients (also known as accommodation coefficients). Assuming these coefficients to be equal based on the previous works on contact line modelling, a simplified form of the Schrage model is obtained as

$$m''_e = \frac{2f}{2-f} \frac{1}{\sqrt{2\pi R_{\text{gas}}}} \left(\frac{p_{v,\text{int}}}{\sqrt{T_{\text{int}}}} - \frac{p_v}{\sqrt{T_v}} \right), \quad (3.10)$$

where $p_{v,\text{int}}$ is the interface pressure at which the vapour is in equilibrium with the liquid. In the absence of disjoining and capillary pressures, the interface pressure will be equal to the saturation pressure at T_{int} , i.e. $p_{v,\text{int}}(T_{\text{int}}) = p_{\text{sat}}(T_{\text{int}})$. However, in the contact line region, due to the presence of the disjoining and capillary pressure, $p_{v,\text{int}}(T_{\text{int}})$ is not equal to $p_{\text{sat}}(T_{\text{int}})$ and is given by [88]

$$p_{v,\text{int}} = p_{\text{sat}} \exp \left[\frac{p_{v,\text{int}} - p_{\text{sat}} - p_c}{\rho_l T_{\text{int}} R_{\text{gas}}} \right], \quad (3.11)$$

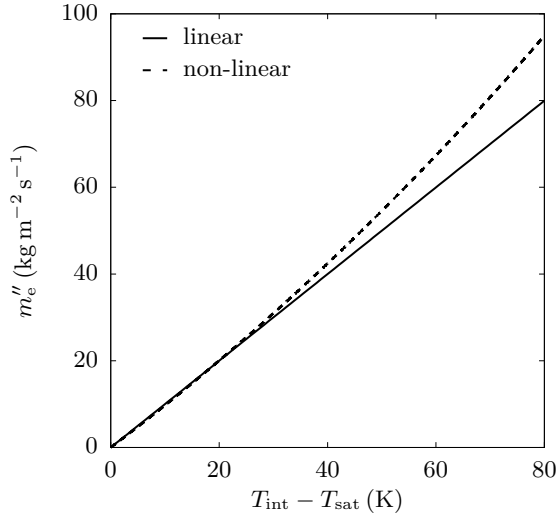


Figure 3.2: Comparison of mass flux obtained using the linear and non-linear mass transfer models for pressure $p_c = 0$ Pa.

where the saturation pressure p_{sat} is obtained by integrating the Clausius–Clapeyron equation

$$p_{\text{sat}} = p_v \exp \left[\frac{h_{lv}}{R_{\text{gas}}} \left(\frac{1}{T_v} - \frac{1}{T_{\text{int}}} \right) \right]. \quad (3.12)$$

Equations (3.10)–(3.12) constitute a non-linear evaporative mass transfer model. For a given value of the pressure p_c and the interface temperature T_{int} , the equations can be solved together to obtain $p_{v,\text{int}}$, p_{sat} and m_e'' .

The contact line model developed in this work is based on the mass transfer model proposed by Wayner et al. [149] which is a linearised form of the Schrage [92] model. The linear mass flux model is based on the assumption that the difference between the interface and saturation temperature is significantly smaller than the absolute value of the interface temperature, i.e. $T_{\text{int}} - T_{\text{sat}} \ll T_{\text{int}}$, and the vapour pressure at the interface can be described by the Thomson equation as follows:

$$p_{v,\text{int}} = p_{\text{sat}} - \frac{\rho_v}{\rho_l - \rho_v} p_c. \quad (3.13)$$

The saturation pressure p_{sat} can be determined using the linearised Clausius–Clapeyron relation as follows:

$$\frac{p_{\text{sat}} - p_v}{T_{\text{int}} - T_v} = \frac{\rho_l \rho_v h_{lv}}{(\rho_l - \rho_v) T_v}. \quad (3.14)$$

Substituting Eqs. (3.13) and (3.14) into Eq. (3.10) gives a relation for the evaporative mass flux from the contact line region

$$m_e'' = \frac{2f}{2-f} \frac{1}{T_v \sqrt{2\pi R_{\text{gas}} T_v}} \left[T_{\text{int}} - T_v \left(1 + \frac{p_c}{h_{lv} \rho_l} \right) \right]. \quad (3.15)$$

Liquid sodium systems can boil at a wide range of superheats ranging from as low as 10 K to as high as 80 K depending on the system pressure and the size of the nucle-

ation sites as discussed in Section 2.6.1. To check the validity of the linear mass transfer model for this range of superheat values, the evaporative mass fluxes calculated using Eqs. (3.10) and (3.15) are compared. In the contact line region, for a given superheat, the largest evaporation rate is expected when the vapour temperature is equal to saturation temperature and the pressure difference between the liquid and vapour becomes negligible, i.e. when the sum of the disjoining, capillary and recoil pressures is close to zero. Hence the comparison is performed assuming $p_c = 0$. Figure 3.2 shows the results of the comparison. For superheat up to 40 K, the linear model predicts mass flux within an error of 5% compared to the non-linear model, while for larger superheats the error increases exponentially. Hence in this study the analysis will be limited to cases with wall superheat up to 40 K.

3.5 Results and discussion

The dynamics of the contact line region predicted from the mathematical model are discussed in this section. The differences in the characteristics of the contact line region in sodium and a high Prandtl number fluid FC-72 are highlighted. Additionally, the influence of specific parameters such as the wall superheat, the vapour temperature, the electron pressure component and the accommodation coefficient are presented. The thermophysical properties of sodium as a function of temperature and the constants used in the numerical simulations are given by Eq. (3.16) and in Table 3.2, respectively [150]. Since sodium is highly conductive, the thermophysical properties of liquid sodium in the contact line region are evaluated at the wall temperature while the properties of sodium vapour are evaluated at the vapour temperature. For all results discussed in this section, the numerical simulations were performed for a bubble radius of 2.5 mm, based on which the macroscopic curvature is computed ($\kappa_{\text{mac}} = 1/r_b$). Another input parameter to the model is the geometric length of the contact line region r_{end} (shown in Fig. 2.3). As long as the extent of the contact line region is large enough such that the disjoining pressure is negligible at the end of the domain, the predicted results from the model are found to be insensitive to the choice of the bubble radius and the length of the contact line region. Thus, the overall predicted dynamics, i.e. the film thickness and heat flux in the contact line region are practically independent of the choice of input parameters.

Property	Symbol	Value	Unit
Saturation temperature	T_{sat}	1156	K
Hamaker constant	\mathcal{A}	1×10^{-20}	J
Accommodation coefficient	f	1	–

Table 3.2: Constant properties of sodium used in the numerical simulations [47, 138, 150, 151].

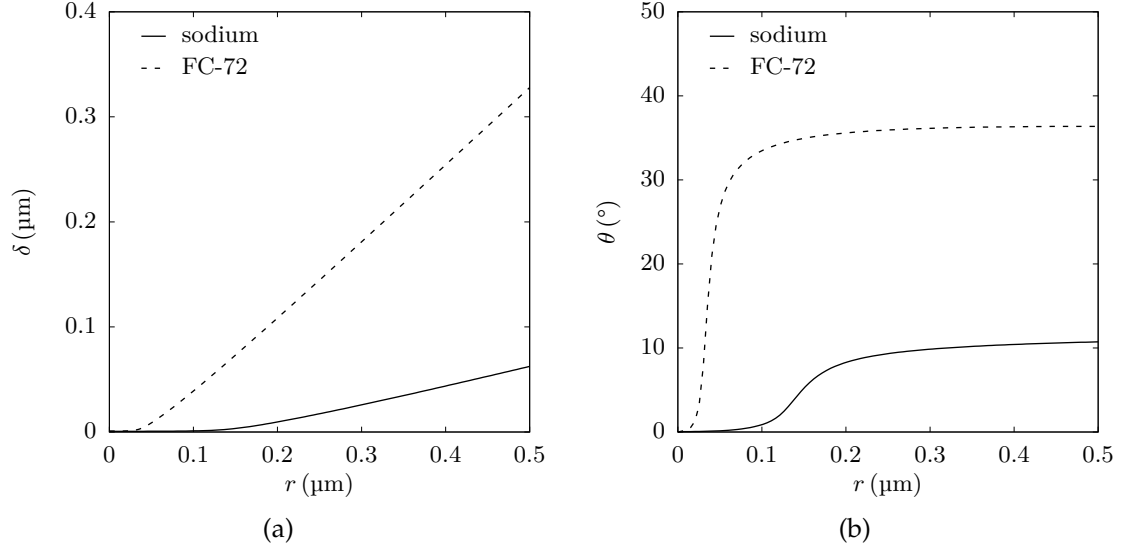


Figure 3.3: Variation of (a) film thickness and (b) contact angle in the contact line region in sodium and FC-72 for a wall superheat of 15 K.

$$k_l = 124.67 - 0.1138T_w + 5.5226 \times 10^{-5}T_w^2 - 1.1842 \times 10^{-8}T_w^3 \quad (3.16a)$$

$$\rho_l = 219 + 275.32 \left(1 - \frac{T_w}{2503.7}\right) + 511.58 \left(1 - \frac{T_w}{2503.7}\right)^{0.5} \quad (3.16b)$$

$$\rho_v = 6.59 - 0.03T_w + 4.76 \times 10^{-5}T_w^2 - 3.29 \times 10^{-8}T_w^3 + 8.86 \times 10^{-12}T_w^4 \quad (3.16c)$$

$$\mu_l = \exp \left(-6.4406 - 0.3958 \ln T_w + \frac{556.835}{T_w} \right) \quad (3.16d)$$

$$\sigma = 0.2405 \left(1 - \frac{T_w}{2503.7}\right)^{1.126} \quad (3.16e)$$

$$h_{lv} = 393370 \left(1 - \frac{T_w}{2503.7}\right) + 4398600 \left(1 - \frac{T_w}{2503.7}\right)^{0.29302} \quad (3.16f)$$

3.5.1 Contact line region characteristics in sodium and FC-72

The contact line region film thickness, contact angle, pressure and heat transfer characteristics in sodium and FC-72 boiling flows evaluated for a wall superheat of 15 K, are compared in this section. For the results reported here, the electron component of the disjoining pressure β in sodium is neglected and vapour temperature is assumed to be equal to the saturation temperature.

Film thickness and contact angle. Film thickness and contact angle in sodium and FC-72 pool boiling are shown in Fig. 3.3. In the vicinity of the adsorbed layer ($r =$

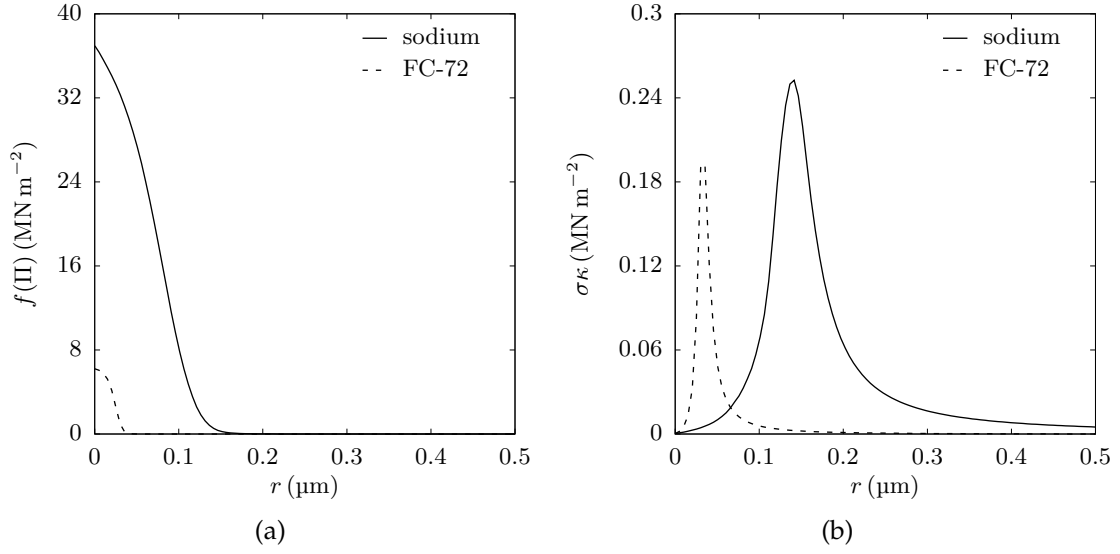


Figure 3.4: Variation of (a) disjoining pressure and (b) capillary pressure in the contact line region in sodium and FC-72 for a wall superheat of 15 K.

0), the film remains attached to the wall as observed in Fig. 3.3a due to the forces of attraction between the wall and the liquid. These forces are accounted for by the disjoining pressure acting on the liquid and depend on the Hamaker constant of the fluid. The higher Hamaker constant of sodium, compared to FC-72, leads to a larger adhesion force in sodium due to the disjoining pressure. This keeps the film attached to the wall for a larger radial distance in sodium compared to FC-72. Once the disjoining pressure decays, the film thickens and its slope remains almost constant. Figure 3.3b shows the variation of this slope in terms of the contact angle which is defined as $\theta = \tan^{-1}(\delta')$. The magnitude of the peak contact angle depends on the evaporative mass flux of the fluid. The higher the mass flux, the more liquid is pulled into the contact line region, which leads to an increase in the film slope and the contact angle. The evaporative heat flux in sodium is expected to be higher than FC-72 due to its high thermal conductivity. However, due to the higher latent heat of sodium, the evaporative mass flux in sodium is found to be lower than FC-72. This is explained in more detail later in this section. Thus, the lower mass flux leads to a lower contact angle and a thinner liquid film in sodium compared to FC-72.

Pressure. Figure 3.4 shows the variation of the disjoining $f(\Pi)$ and capillary $\sigma\kappa$ pressure in the contact line region in sodium and FC-72 pool boiling. The recoil pressure is negligible compared to the other pressure components and is not included in the plot. The disjoining pressure is dominant close to the adsorbed layer as seen in Fig. 3.4a and as the film thickness increases, it rapidly decreases. In sodium, this pressure acts over a larger distance compared to FC-72 due to the higher Hamaker constant and lower film thickness.

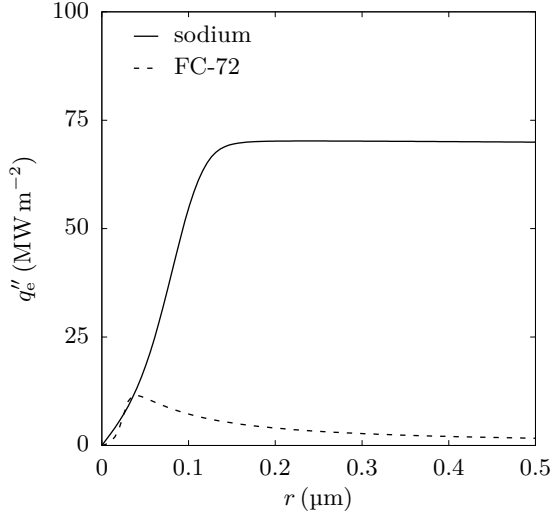


Figure 3.5: Variation of evaporative heat flux in the contact line region in sodium and FC-72 for a wall superheat of 15 K.

In contrast to the disjoining pressure which is maximum at the beginning of the contact line region, the capillary pressure is zero at $r = 0$ as observed in Fig. 3.4b. As the disjoining pressure decreases, the capillary pressure increases till it reaches a peak value. The radial location of this peak corresponds to the point where the disjoining pressure becomes negligible and the film thickness starts to increase. After the peak value, the capillary pressure reduces and becomes equal to the macroscopic bubble curvature ($1/r_b$) for both fluids.

The magnitude of the peak capillary pressures in both fluids are approximately equal as seen in Fig. 3.4b. The capillary pressure depends on the film curvature which in turn is determined by the slope of the film according to Eq. (2.13). As mentioned above, the slope of the film is smaller in sodium compared to FC-72. This leads to a lower film curvature in sodium. However, the peak capillary pressures are almost equal in magnitude since the surface tension of sodium is larger than FC-72.

Heat transfer characteristics. Figures 3.5–3.7 show the variation in the evaporative heat flux, interface temperature, and total R_{total} and conductive $R_{\text{cond}} = \delta/k_l$ thermal resistance in sodium and FC-72 pool boiling, respectively. The evaporative heat flux in the contact line region shown in Fig. 3.5 is governed by the interface temperature and the total thermal resistance. The total thermal resistance is the sum of the interface R_{int} and conductive thermal resistance. At the edge of the adsorbed layer, no evaporation takes place according to the boundary condition Eq. (3.5d). Hence the interface film temperature is equal to the wall temperature. As the film grows and the disjoining pressure reduces, the interface temperature drops to the saturation temperature as shown in Fig. 3.6. This drop in interface temperature corresponds to an increase in the temperature difference $T_w - T_{\text{int}}$ and consequently, an increase in the heat flux which reaches a peak value and remains almost uniform for sodium. Though the decrease in the interface temperature is the same for both fluids (equal to the input wall superheat of 15 K), a

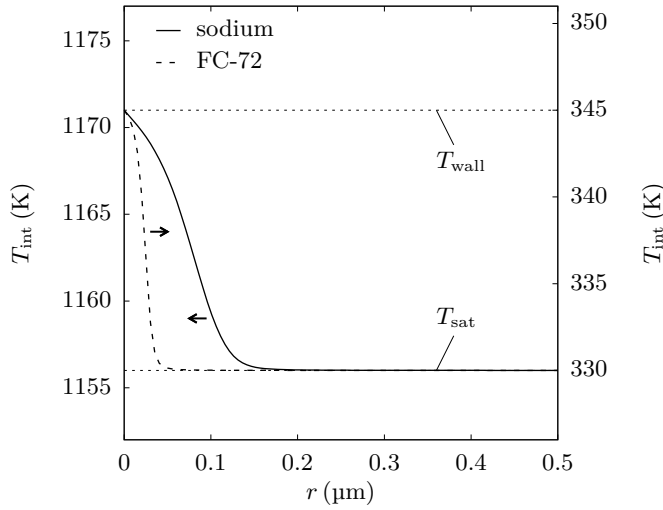


Figure 3.6: Variation of interface temperature in the contact line region in sodium and FC-72 for a wall superheat of 15 K.

significantly larger heat flux is observed in sodium because of the substantially smaller total thermal resistance as seen in Fig. 3.7. The total thermal resistance of sodium appears to be constant because it is dominated by interface thermal resistance, which is constant and an order of magnitude larger than the conductive thermal resistance in the liquid film. Even though the peak heat flux is larger in sodium compared to FC-72, the peak mass flux is lower as mentioned before, due to the higher latent heat of sodium. For a wall superheat of 15 K, the peak mass flux from the contact line region in sodium is $18.2 \text{ kg m}^{-2} \text{ s}^{-1}$ while a substantially larger flux of $137 \text{ kg m}^{-2} \text{ s}^{-1}$ is seen in FC-72.

Figure 3.7 also shows a comparison of the conductive thermal resistance R_{cond} in sodium and FC-72. The conductive thermal resistance increases with radial distance for both fluids as the film thickness increases but is significantly smaller in sodium compared to FC-72 due to the larger thermal conductivity of sodium. Thus, its influence on the heat transfer characteristics in sodium is negligible. This is in contrast with observations for FC-72, where due to the high conductive resistance, the heat flux decreases substantially after it reaches a peak value as seen in Fig. 3.5.

3.5.2 Effect of wall superheat

Sodium boiling systems typically require a large superheat, which can be up to 80 K to initiate the bubble growth process as compared to conventional fluids such as water. However, as mentioned in Section 3.4.2, the analysis in this study is limited to superheats of 40 K due to the large errors induced by the linear mass transfer model for higher superheat values.

Figure 3.8 shows the effect of wall superheat on the evaporative heat flux, interface temperature, disjoining and capillary pressure in the contact line region in sodium pool boiling assuming the electron pressure component $\beta = 0$. On increasing the superheat

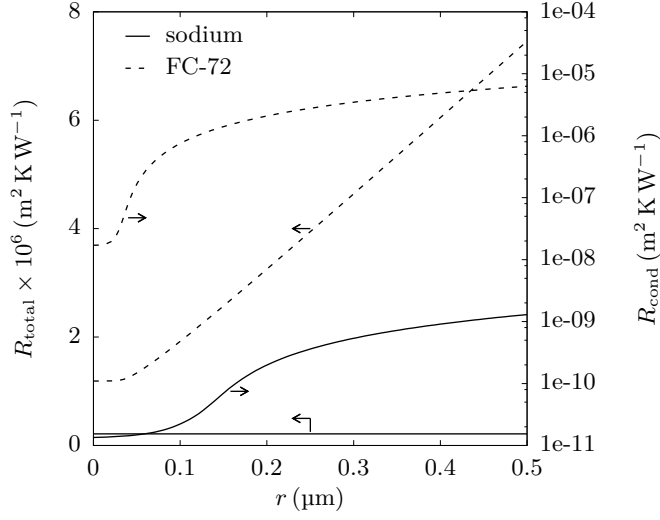


Figure 3.7: Variation of conductive and total thermal resistance in the contact line region in sodium and FC-72 for a wall superheat of 15 K.

by four times from 10 K to 40 K, the peak heat flux also increases by approximately four times from 47 MW m^{-2} to 185 MW m^{-2} as shown in Fig. 3.8a. As mentioned in the previous section, the peak heat flux depends strongly on the interface temperature. At higher superheats, a larger drop in the interface temperature is observed close to the adsorbed layer as seen in Fig. 3.8b. This leads to a larger temperature difference $T_w - T_{int}$ which drives the heat transfer in the contact line region and causes the heat flux to peak. For all cases, the peak heat flux is obtained in the region between $0.1 \mu\text{m} < r < 0.2 \mu\text{m}$. This also corresponds to the location at which the disjoining pressure inhibiting heat transfer decays completely and the capillary pressure, enhancing heat transfer, peaks as shown in Figs. 3.8c and 3.8d, respectively.

The variation in the thickness of the liquid film for different values of superheat is shown in Fig. 3.9. As the superheat, and thus the heat flux increases, a larger amount of liquid from the contact line region evaporates. In order to conserve mass, and as the flow in the contact line region is assumed to be steady, with an increase in the evaporation rate, more liquid is pulled into the contact line region, thus leading to a thicker film.

It can also be seen in Fig. 3.9 that the slope of the film increases with superheat and remains constant beyond a certain radial distance. The film thickness starts increasing at the radial location where the disjoining pressure becomes insignificant and the capillary pressure reaches a peak value. However, beyond this radial distance (here $r = 0.3 \mu\text{m}$), the slope of the film is nearly constant. This confirms the assumption that the extent of the contact line domain does not affect the predicted film dynamics as long as it is large enough, i.e. it captures the location where the film profile changes its slope, or the disjoining pressure decreases. Thus, at any distance $r > 0.3 \mu\text{m}$, the dynamics of the contact line region stays the same.

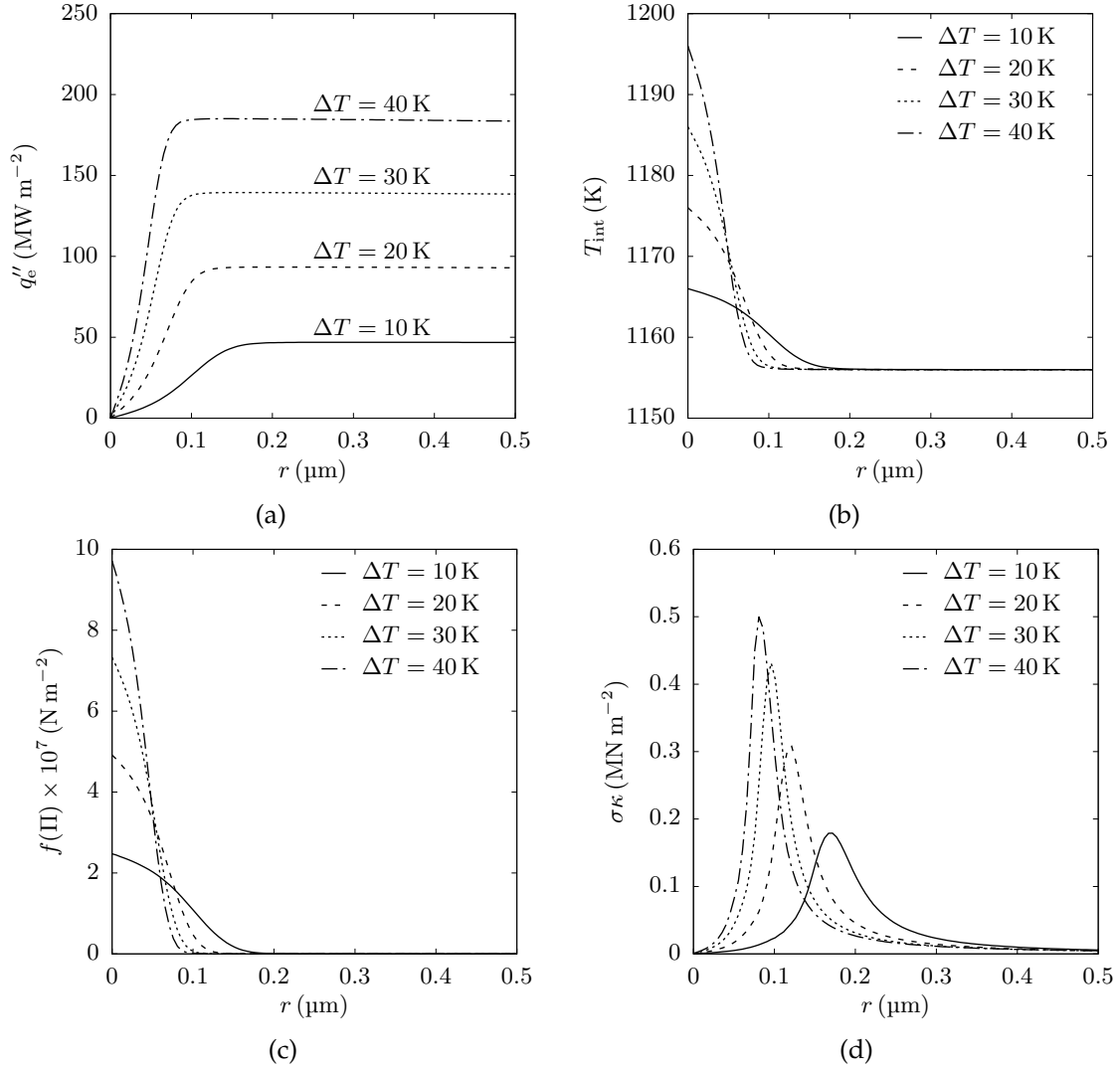


Figure 3.8: Effect of wall superheat on (a) evaporative heat flux and (b) interface temperature (c) disjoining pressure and (d) capillary pressure in the contact line region in sodium boiling.

3.5.3 Effect of vapour temperature

The growth of a bubble in sodium is primarily dominated by the inertia of the liquid being displaced. In the inertia controlled growth phase, the bubble growth rate depends on the pressure difference between the vapour and the liquid surrounding the bubble, i.e. $p_v(T_v) - p_l(T_\infty)$, where T_∞ is the temperature of the bulk liquid. Immediately after bubble nucleation, the vapour inside the bubble is at the wall temperature and its pressure is equal to the saturation pressure evaluated at the wall temperature. As the bubble grows, the temperature of the vapour in the bubble reduces and at a certain stage during the growth process, the vapour temperature inside the bubble becomes equal to the bulk liquid temperature T_∞ . The corresponding vapour pressure at this stage is

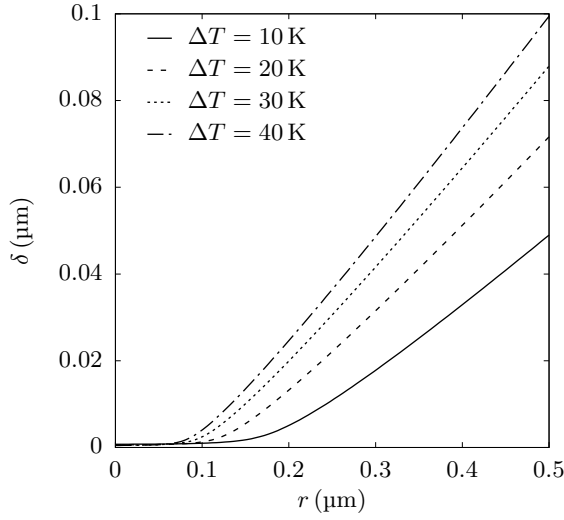


Figure 3.9: Effect of wall superheat on the film thickness in sodium boiling.

$p_v(T_\infty)$. Thus as a bubble grows, the vapour temperature varies from T_w to T_∞ . This is in contrast to heat transfer controlled bubble growth in conventional fluids where the vapour temperature is assumed to be constant.

Figure 3.10 shows the effect of reduction in vapour temperature T_v on the evaporative heat flux, interface thermal resistance and film thickness in the contact line region in sodium pool boiling for a wall superheat of 25 K assuming $T_\infty = T_{\text{sat}}$. The influence of decreasing the vapour temperature is similar to increasing the wall superheat. As T_v decreases, the difference in temperature between the wall and vapour in the bubble increases. This leads to higher heat fluxes as seen in Fig. 3.10a. Decreasing the temperature of the vapour also affects the interface thermal resistance. However this variation was found to be negligible as seen in Fig. 3.10b and does not have a significant influence on the heat flux. An increase in the evaporative heat flux leads to thicker liquid films in the contact line region as shown in Fig. 3.10c due to the larger amount of liquid flow from the macro region as explained in Section 3.5.2.

3.5.4 Effect of the electron pressure parameter

A key characteristic of thin sodium films is the presence of free electrons. As explained previously, these electrons are confined in thin films which produces an effective electron pressure that enhances the disjoining pressure. The effect of this phenomenon on the contact line characteristics is discussed.

Figure 3.11 shows the effect of the electron pressure parameter β on the film thickness, disjoining pressure, evaporative heat flux, and the integrated heat flux in the contact line region in sodium boiling for a wall superheat of 25 K. As β increases, the film thickness decreases as observed in Fig. 3.11a. In the results presented $\beta = 0$ denotes the absence of electron pressure in the contact line region. As β increases, the van der Waals

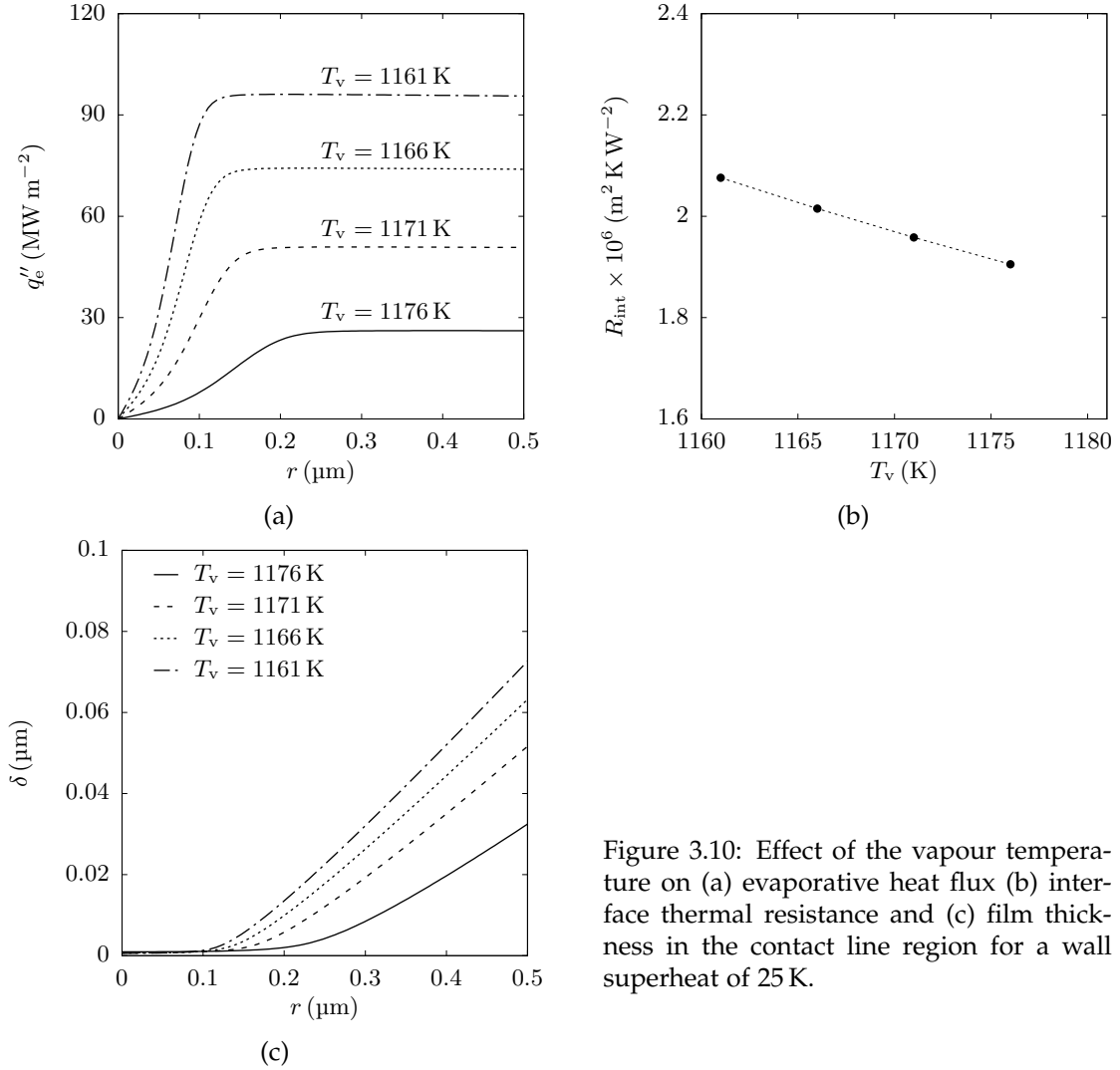


Figure 3.10: Effect of the vapour temperature on (a) evaporative heat flux (b) interface thermal resistance and (c) film thickness in the contact line region for a wall superheat of 25 K.

force, which keeps the film attached to the wall increases, thus reducing film thickness. It is also important to note that as the electron pressure component increases, the length of the contact line region increases. As mentioned in Section 3.3, the length of the contact line region is chosen such that it captures the region from the adsorbed layer to the location where the disjoining pressure becomes negligible. On increasing the electron pressure parameter from 0 to 100, the disjoining pressure acts over a larger distance as shown in Fig. 3.11b, thus increasing the length of the contact line region.

Figure 3.11c shows the influence of the electron parameter on the heat flux in the contact line region. In the vicinity of the adsorbed layer, the disjoining pressure inhibits heat transfer due to increased forces of attraction between the fluid molecules and the wall. This can be seen in the plot where the gradient in the heat flux close to the adsorbed layer rises gradually for the $\beta = 100$ case while it increases sharply as β decreases. Once the disjoining pressure decays, the heat flux attains a peak value, which remains the same for all three cases since the wall superheat is the same.

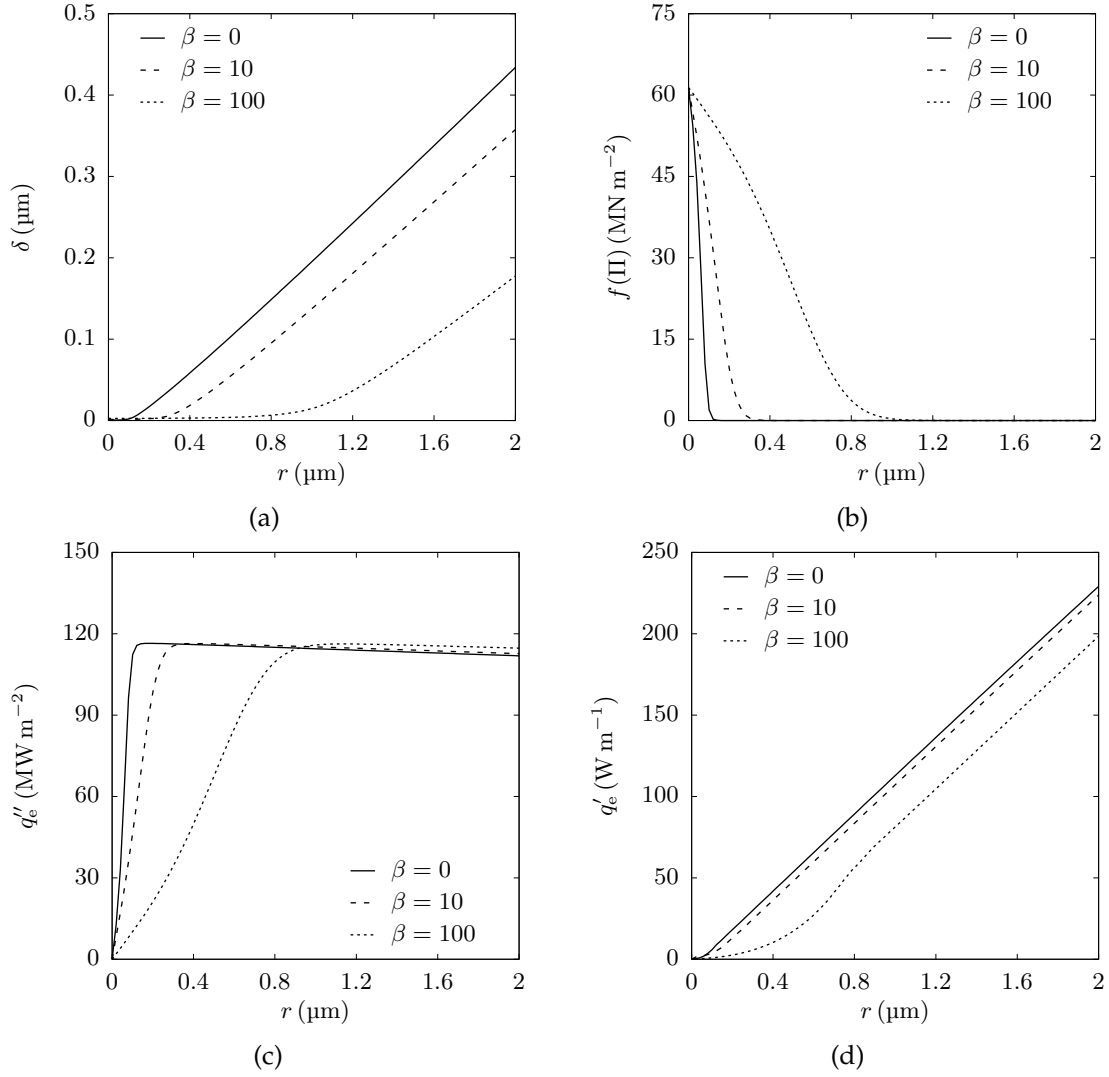


Figure 3.11: Effect of the electron pressure parameter on (a) film thickness (b) disjoining pressure (c) evaporative heat flux and (d) integrated heat flux in the contact line region for a wall superheat of 25 K.

To quantify the influence of the electron pressure parameter on the overall heat transferred from the contact line region, the variation of the integrated heat flux is plotted in Fig. 3.11d. The integrated heat flux represents the area under the heat flux curve shown in Fig. 3.11c. As explained above, with an increase in the electron pressure component, the gradient of the heat flux reduces and thus the overall heat transferred from the contact line region reduces. It is seen that as the electron pressure component increases by two orders of magnitude, the overall heat transferred from the contact line region reduces by approximately 15%.

3.5.5 Effect of the accommodation coefficient

According to the kinetic theory of gases, the net mass flux through a liquid–vapour interface depends on the velocity distribution of the vapour and liquid molecules, and on an accommodation coefficient which is defined as the number of molecules that evaporate on the liquid–vapour interface to the total number of molecules hitting the interface. The value of the accommodation coefficient is typically chosen as one which is an optimal value indicating all the molecules hitting the interface undergo a phase change [47, 152]. However several factors, such as the presence of impurities, molecular structure and interface shape affect the molecule velocity distribution [153]. This in turn affects the number of molecules that actually penetrate the liquid vapour interface thus leading to different values of the accommodation coefficient. An accurate estimation of this coefficient would require detailed molecular dynamic simulations and experiments which haven't been performed for liquid sodium. Hence the effect of different accommodation coefficient values on the dynamics of the contact line region are studied.

In the results discussed in the preceding sections, the accommodation coefficient f was taken to be one, which as mentioned above is an optimal value. However, several factors, such as the presence of impurities or condensable gases in real sodium boiling systems, may lower its value. Figure 3.12 shows the effect of the accommodation coefficient on the evaporative heat flux and film thickness in the contact line region in sodium for a wall superheat of 25 K. With increasing f , the interface thermal resistance decreases according to Eq. (2.17). This promotes evaporation. The effect of increasing the accommodation coefficient or decreasing the interfacial thermal resistance is similar to increasing the wall superheat. An overall decrease in the thermal resistance increases the heat flux from the contact line region. This can be seen in Fig. 3.12a. As the accommodation coefficient increases from 0.25 to 1, the peak heat flux value increases by approximately six times. This increased heat flux leads to an increase in the mass of liquid evaporated. This causes more liquid to be fed in to the contact line region from the macro region, which makes the film thicker as shown in Fig. 3.12b.

3.5.6 Utility of contact line models

As the contact line region in sodium boiling flows has not been studied previously, its contribution to the overall bubble growth process is unknown. Experiments on bubble growth in sodium or other liquid metals in general examined wall temperature fluctuations to understand the boiling process. However, these studies were not extended to understand the heat transfer mechanism involved during the growth of a bubble. A possible way to overcome this gap in knowledge is to perform high-fidelity numerical simulations to quantify the contribution of different heat transfer paths, namely microscale heat transfer from the contact line region and macroscale heat transfer from

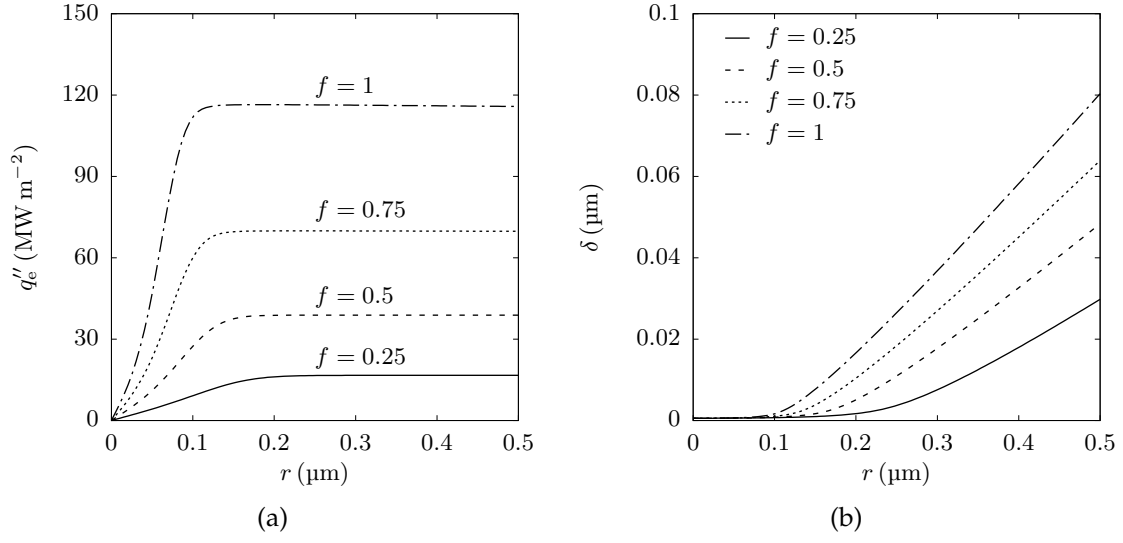


Figure 3.12: Effect of the accommodation coefficient on (a) evaporative heat flux and (b) film thickness in the contact line region for a wall superheat of 25 K.

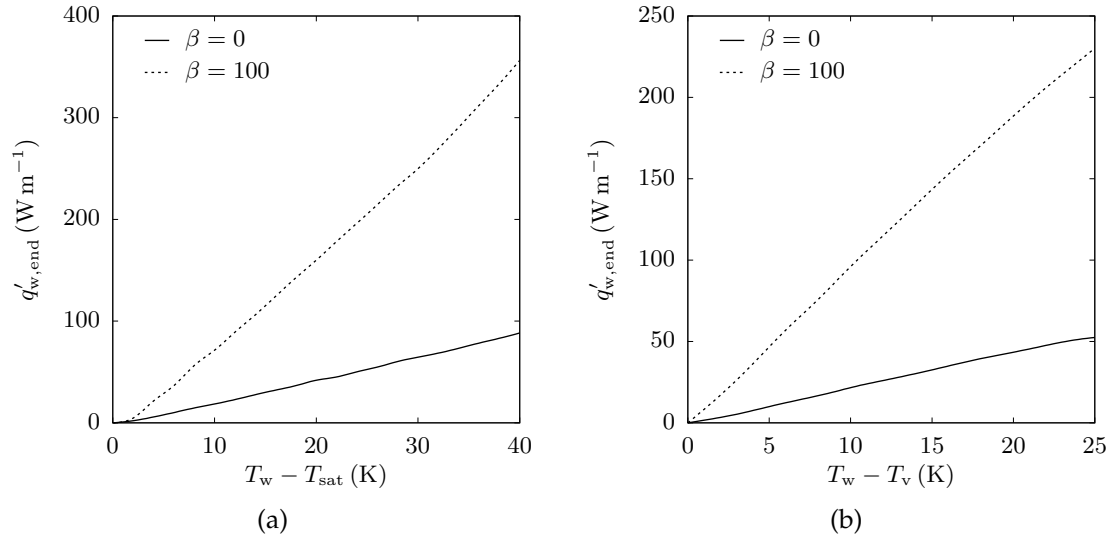


Figure 3.13: Effect of electron pressure parameter on the integrated heat flux at the end of the contact line region for (a) different wall temperature values assuming a constant vapour temperature $T_v = T_{sat}$ and (b) different vapour temperature values assuming a constant wall temperature $T_w = T_{sat} + \Delta T$ where the wall superheat $\Delta T = 25$ K. The length of the contact line region for $\beta = 0$ and $\beta = 100$ cases is $0.5 \mu\text{m}$ and $2 \mu\text{m}$ respectively.

the bulk liquid to the growth of a bubble. CFD simulations considering contact line evaporation have been performed for high Prandtl number fluids [62, 88]. These studies modelled the contact line region separately and correlations for the microscale wall heat flux as a function of wall superheat were developed. These correlations were then coupled to CFD simulations to study bubble growth. A similar approach can be used to study bubble growth in sodium.

Figure 3.13 shows the variation of the integrated wall heat flux $q'_{w,end}$ at the end of the contact line region with superheat and vapour temperature for two values of the electron pressure parameter. The effect of wall superheat on the integrated wall heat flux at the end of the contact line region, assuming a constant vapour temperature $T_v = T_{sat}$, is shown in Fig. 3.13a. With increasing electron pressure parameter β , the integrated wall heat flux increases substantially. This is mainly because, as β increases from 0 to 100, the extent of the contact line region increases from $0.5\ \mu\text{m}$ to $2\ \mu\text{m}$, as explained in Section 3.5.4. Thus, the area under the heat flux curve increases, leading to a larger integrated heat flux from the contact line region. A similar trend is observed on varying the vapour temperature at a constant wall temperature of $T_w = T_{sat} + \Delta T$ as seen in Fig. 3.13b where ΔT was assumed to be 25 K. As mentioned previously, having a larger electron pressure leads to a larger contact line region and thus larger integrated heat flux.

In sodium, since the integrated heat flux depends on the wall and vapour temperature, the contact line model can be run *a priori* for different values of wall and vapour temperatures to generate a look-up table. Such tables can be coupled to CFD simulations to quantify the influence of the contact line evaporation on the overall bubble growth process. These simulations will aid in understanding the partitioning of heat flux in sodium boiling flows. This effect merits further exploration as part of future work.

3.6 Summary

The contact line region in sodium boiling flows has been modelled in this chapter using a boundary-value problem model based on the governing conservation equations. The specific characteristics of sodium—high wall superheat and the presence of an electron pressure—make the contact line dynamics fundamentally different from that in conventional fluids such as water and refrigerants. The present work proposes a simple method, as a first step, to assess the effect of the electron pressure component, high boiling superheats, vapour temperature and accommodation coefficient in estimating the evaporation rate from the contact line region in sodium pool boiling.

The input parameters to the developed boundary-value problem model were the bubble radius, length of the contact line region, accommodation coefficient, electron pressure, wall superheat, vapour temperature and a perturbation parameter which was chosen as $\epsilon_1 = 0.001$. The bubble radius and length of the contact line region were found to have an insignificant effect on the predicted results, while the wall superheat, electron pressure parameter, vapour temperature and the accommodation coefficient had a significant influence and were studied extensively. A verification study performed showed the model agreed well with DNS simulation results of Batzdorf [88] with a maximum relative error of 2.9% and 3.8% in the contact angle and integrated heat flux, respectively, at a superheat of 20 K.

The dynamics of the contact line region varies significantly with the thermophysical properties of the fluid. A comparison of the film characteristics of sodium and a fluorocarbon FC-72, representing a low and high Prandtl number fluid, respectively, showed that the film thickness in the contact line region in sodium is significantly smaller, while the heat flux is six times larger at a wall superheat of 15 K. The high disjoining pressure in sodium, associated with the larger Hamaker constant, keeps the film attached to the wall thus limiting the film thickness. From a heat transfer perspective, the high disjoining pressure, due to the high van der Waals forces, acts to inhibit evaporation from the contact line region. However, the high thermal conductivity of sodium negates the latter effect leading to higher evaporative heat fluxes in sodium compared to FC-72.

A parametric analysis was employed to deduce the effect of wall superheat, vapour temperature, electron pressure parameter and the accommodation coefficient on the contact line characteristics. The main results from the parametric study are as follows:

- The influence of the wall superheat was found to be consistent with observed contact line region dynamics of high Prandtl number fluids, i.e. as the wall superheat was increased, the evaporative heat flux and the film thickness also increased. The variation in the peak heat flux with wall superheat was found to be linear, i.e. as the wall superheat was increased by four times from 10 K to 40 K, the peak heat flux also increased by four times.
- The effect of decreasing vapour temperature was found to be similar to increasing the wall superheat. As the vapour temperature was decreased from 1176 K to 1161 K at a wall superheat of 25 K, the heat flux increased by approximately 3.5 times.
- The electron pressure was found to have a significant effect on the contact line region characteristics. On increasing the electron pressure parameter from 0 to 100 at a constant superheat of 25 K, the length of the contact line region increased while the integrated heat flux reduced by 15%.
- A decrease in the accommodation coefficient from 1 to 0.25, which may occur in the presence of impurities, was observed to decrease the evaporative heat flux in sodium by approximately six times at a wall superheat of 25 K.

Lastly, the application of the contact line model to study bubble growth in sodium boiling was discussed. A look-up table generated using the model can be integrated with CFD simulations to study the influence of parameters like the electron pressure and accommodation coefficient on the bubble growth process in liquid sodium. This will be explored as part of future work.

Heat transfer modelling of an isolated bubble in pool boiling²

In the previous chapter, the heat transfer from the contact line region was modelled. In the present chapter, a reduced-order heat transfer model accounting for the evaporation of the microlayer, the macrolayer, the thermal boundary layer and the bulk liquid is presented to study the growth of a sodium bubble in a liquid pool. A transient 2D conduction equation is solved to model the cooling of the wall below the bubble due to evaporation of the microlayer and the macrolayer. The model is used to study the growth of a sodium bubble in a liquid pool and analyse the relative contribution of different heat transfer mechanisms to the growth process. Furthermore, a parametric study is conducted to investigate the effect of wall superheat, contact angle, temperature of the bulk liquid and the accommodation coefficient on the bubble growth process.

4.1 Introduction

Nucleate boiling is an effective mode of heat transfer and has been extensively studied for high Prandtl number fluids [10, 12]. These studies cannot be directly extended to low Prandtl number fluids like sodium since the fundamental mechanism controlling bubble growth is different. Bubble growth in high Prandtl number fluids is primarily heat transfer controlled and characterised by low growth rates and a constant vapour temperature. In contrast, bubble growth in sodium is inertia controlled and owing to the high thermal conductivity of the liquid metal, high growth rates are expected.

In this chapter, a reduced-order bubble growth model based on the heat transferred to a bubble from different mechanisms, i.e. evaporation of the microlayer, macrolayer, thermal boundary layer and bulk liquid is proposed to study the growth of an isolated sodium bubble in a superheated liquid pool. Such models can be incorporated into

²Material in this chapter has been published as: S. Iyer, A. Kumar, J. Coventry and W. Lipiński, Heat transfer modelling of an isolated bubble in sodium pool boiling, *International Journal of Thermal Sciences*, vol. 179, p. 107678, 2022.

simulations of bubbles departing from a heated wall and in large scale system-level CSP plant models to assess their techno-economic viability. Techno-economic analysis often requires reduced-order models, as these analyses are done over a large period of plant operation such as days, weeks or years, and are computationally intensive.

The relative contribution of different heat transfer mechanisms influencing the growth of a bubble is analysed in this chapter. In addition, the effect of parameters such as the wall superheat, contact angle, bulk liquid temperature and the accommodation coefficient on the bubble radius, growth rate, and heat transferred to the bubble are investigated.

4.2 Problem description

The heat transfer to a bubble from the different mechanisms introduced in Chapter 2 is used to develop a bubble growth model. Figure 4.1 shows a schematic diagram of the heat transfer processes involved during the growth of a bubble of radius r_b and contact angle β in a liquid pool of temperature T_∞ and pressure p_∞ . The radius and the thickness of the heater wall are r_h and δ_h , respectively. h_b denotes the distance of the bubble centre from the wall. The temperature and pressure of the vapour in the bubble are T_v and p_v , respectively. A thermal boundary layer of thickness δ_t is formed adjacent to the wall. In pool boiling, a bubble nucleates when a sufficient superheat is reached at a nucleation site [36]. As the bubble grows, a microlayer is formed below the bubble. The thickness of this layer is of the order of a few micrometers and the rate of heat transfer from this region \dot{Q}_m contributes to the growth of the bubble. In nucleate pool boiling, a central dryout region of radius r_d is formed below the bubble as the liquid in the microlayer evaporates. In this region, the vapour is in direct contact with the wall. Owing to the low thermal conductivity of the vapour, the heat transfer in this region has a negligible influence on the growth of the bubble.

Liquid metals like sodium are characterised by the formation of a thick thermal boundary layer compared to ordinary liquids like water. During bubble growth, some portion of the liquid in the thermal boundary layer will be trapped below the bubble in the macrolayer as shown in Fig. 4.1. The rate of heat transferred from this region to the bubble is represented by \dot{Q}_{ma} . The macrolayer extends from the bubble contact radius r_c to the radial distance r_t . The distance r_t depends on the height of the bubble centre from the wall and the thickness of the thermal boundary layer.

During the initial stage of bubble growth, a part of the liquid in the thermal boundary layer will be in contact with the liquid–vapour interface of the bubble as represented by the red interface in Fig. 4.1. The rate of heat transferred from this region to the bubble is referred to as the thermal boundary layer heat transfer rate and denoted by \dot{Q}_t . As the bubble grows, the macrolayer will expand. Thus, the part of the bubble in contact

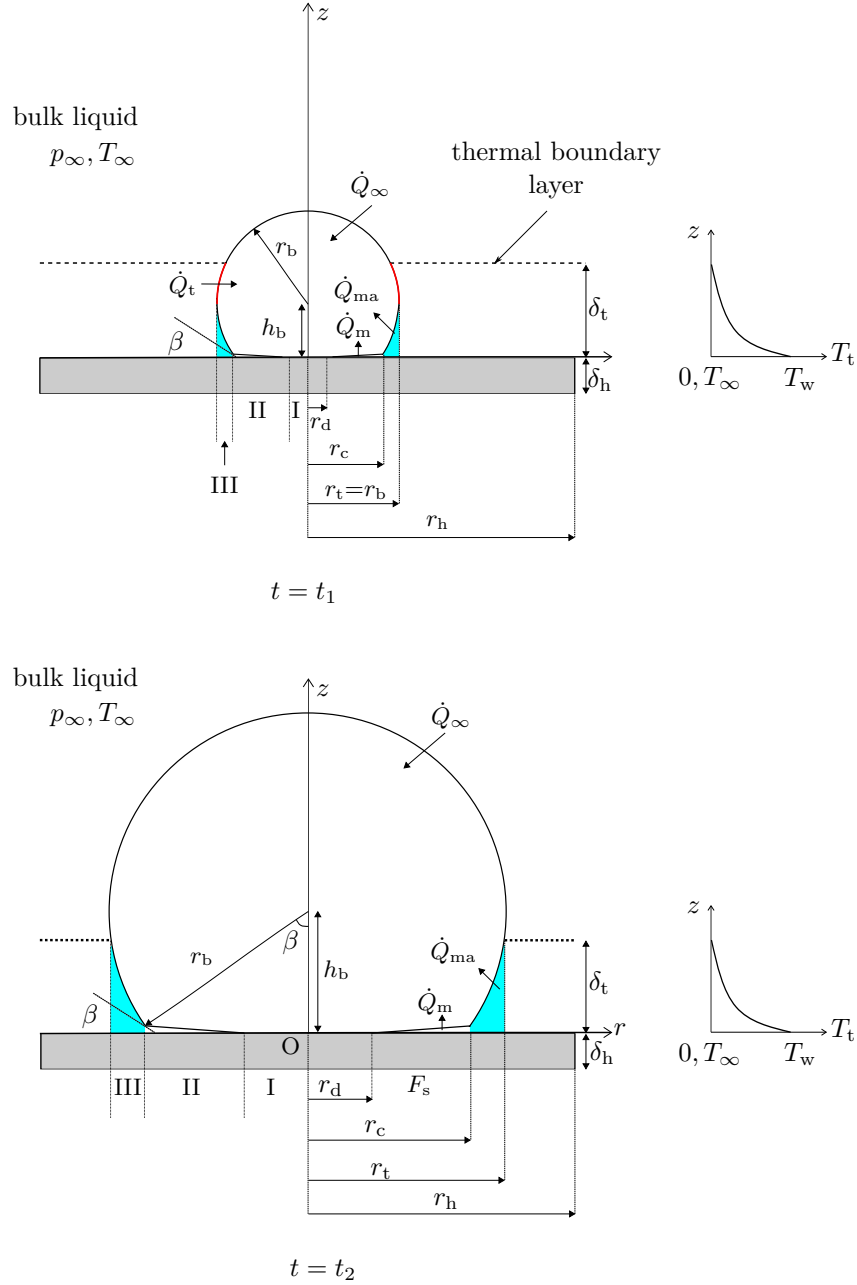


Figure 4.1: Heat transfer to a bubble in nucleate pool boiling at times t_1 and t_2 where $t_1 < t_2$. I, II and III represent the dryout, microlayer and macrolayer regions, respectively. The blue region represents the liquid in the macrolayer while the red interface represents the portion of the bubble in contact with the liquid in the thermal boundary layer.

with the thermal boundary layer will decrease and at some time t_2 all of the liquid in the thermal boundary layer will be confined to the macrolayer as shown in Fig. 4.1. As the bubble grows, a portion of its surface will be in contact with the bulk liquid. The heat transferred from the bulk liquid is denoted by \dot{Q}_∞ .

4.3 Heat transfer model

A model coupling the microlayer, the macrolayer, the thermal boundary layer and the bulk liquid heat transfer rate to the transient heat conduction in the wall is developed to study the growth of a sodium bubble in nucleate pool boiling. The governing conservation equations for the model are derived based on the following assumptions:

1. The bubble is axisymmetric.
2. Heat transfer in the microlayer and macrolayer is governed by 1D conduction normal to the wall owing to the small thickness of the fluid layer and the high thermal conductivity of sodium.
3. The temperature profile in the thermal boundary layer is given by [154]

$$\frac{T_t(z) - T_w}{T_\infty - T_w} = \frac{3}{2} \frac{z}{\delta_t} - \frac{1}{2} \left(\frac{z}{\delta_t} \right)^3, \quad (4.1)$$

where T_t is the temperature of the liquid in the thermal boundary layer. The thermal boundary layer thickness δ_t for a uniformly heated wall is calculated from the input heat flux q''_{in} as follows [85]:

$$\delta_t = \frac{k_l (T_w - T_\infty)}{q''_{\text{in}}}. \quad (4.2)$$

4. Thickness of the thermal boundary layer is constant throughout the growth period.
5. The contact angle is constant throughout the growth period.
6. The effect of forced convection induced by bubble growth on the wall is negligible.

The conservation equations to model the heat transfer from the microlayer and the bulk liquid surrounding the bubble were introduced in Chapter 2 and are summarised below. The equations to model the heat transfer from the macrolayer and the thermal boundary layer are formulated in this section.

4.3.1 Microlayer heat transfer

The heat transfer in the microlayer is driven by one-dimension heat conduction from the wall to the vapour in the bubble

$$\dot{Q}_m = \int_{r_d}^{r_c} q_m'' dA = \int_{r_d}^{r_c} \frac{T_w - T_v}{\delta_m/k_l + R_{int}} dA, \quad (4.3)$$

where q_m'' is the heat flux from the microlayer and δ_m is the thickness of the microlayer. k_l and R_{int} are the thermal conductivity of the liquid and the interface resistance, respectively. T_w and T_v are the temperature of the wall and vapour, respectively. The microlayer in a bubble extends from the edge of a dryout region r_d to the bubble contact radius r_c .

$$r_c = r_b \sin \beta \quad (4.4)$$

The radius of the dryout region r_d is the location at which the microlayer evaporates completely and the thickness of the liquid film is zero, i.e.

$$\delta_m(r = r_d, t) = 0. \quad (4.5)$$

As the liquid in the microlayer evaporates, the thickness of the microlayer changes. This transient and spatial variation in the microlayer thickness is evaluated as follows:

$$\frac{d\delta_m}{dt} = -\frac{T_w(r, t) - T_v}{(\delta_m(r, t)/k_l + R_{int})\rho_l h_{lv}}. \quad (4.6)$$

The microlayer thickness $\delta(r, t)$ is obtained by integrating Eq. (4.6) using an explicit Euler time integration scheme.

A relationship for the initial microlayer profile δ_0 , i.e. the variation in the thickness of the microlayer immediately after bubble nucleation at time $t = 0$ is needed to initiate the calculation of the microlayer heat transfer. The relationship for the initial microlayer profile depends on the mechanism dominating the growth process. The microlayer profile equation used in this work is based on the early works of Cooper et al. [83] who modelled the flow around the outer edge of a bubble and proposed the following relation:

$$\delta_0 = C\sqrt{\nu_l(r/C_1)} = C_0\sqrt{r}, \quad (4.7)$$

where C and C_0 are constants and ν_l is the kinematic viscosity of the liquid.

The value of the constant C in the Eq. (4.7) in high Prandtl number fluids was experimentally determined [94]. In liquid metals, the presence of the microlayer below a bubble has been detected [58]. However, owing to the difficulty in performing detailed experiments with liquid metals, these studies do not report the variation in the thickness of this layer. To overcome this problem, Dwyer and Hsu [96] theoretically

analysed the hydrodynamics of microlayer formation during inertia-controlled growth of a hemispherical bubble. The authors simplified the continuity equation of fluid flow in the microlayer region assuming the thickness of the microlayer to be significantly less than the bubble radius. Hence the lubrication theory was used. The resulting simplified continuity equation was solved subject to the no-slip boundary condition at the bubble interface to obtain the constant $C = 0.6$. Since this value of C has not been validated for sodium boiling, a sensitivity study is performed to assess its influence on the growth of a sodium bubble and reported in Section 4.8.1.

4.3.2 Heat transfer from the macrolayer and thermal boundary layer

The thickness of the macrolayer is typically small during the initial bubble growth period when the bubble is submersed in the thermal boundary layer and increases to a maximum thickness equal to the height of the thermal boundary layer. An accurate estimation of the heat transferred from the macrolayer and the thermal boundary layer region to the bubble would require detailed 2D modelling of the temperature profile around the bubble using high fidelity CFD simulations. Such simulations are computationally expensive and beyond the scope of this work. Thus, to simplify the model, the heat transferred from the macrolayer and the thermal boundary layer are separated in this work. The rate of heat transferred from the macrolayer to the bubble is computed assuming 1D conduction normal to the wall

$$\dot{Q}_{\text{ma}} = \int_{r_c}^{r_t} q''_{\text{ma}} dA = \int_{r_c}^{r_t} \frac{T_w - T_v}{\delta_{\text{ma}}/k_l + R_{\text{int}}} dA, \quad (4.8)$$

where the thickness of the liquid film, δ_{ma} is

$$\delta_{\text{ma}} = h_b - \sqrt{r_b^2 - r^2}, \quad r_c < r < r_t, \quad (4.9)$$

and the height of the centre of the bubble from the wall is

$$h_b = \sqrt{r_b^2 - r_c^2}. \quad (4.10)$$

The radial distance r_t depends on the height of the centre of the bubble from the wall and the thermal boundary layer thickness as follows:

$$r_t = r_b, \quad h_b < \delta_t, \quad (4.11)$$

$$r_t = \sqrt{r_b^2 - (h_b - \delta_t)^2}, \quad h_b > \delta_t. \quad (4.12)$$

As the bubble grows, a portion of its interface will be in contact with the liquid in the thermal boundary layer. In this region, the heat transferred to the bubble is given by

$$\dot{Q}_t = \int_{\delta(r_t)}^{\delta_t} q_t'' dA = \int_{\delta(r_t)}^{\delta_t} \frac{T_{\text{int}} - T_v}{R_{\text{int}}} dA, \quad (4.13)$$

where T_{int} is the temperature of the bubble interface in contact with the liquid in the thermal boundary layer. As mentioned above, CFD simulations would be required to accurately predict T_{int} . To simplify the model, the interface temperature is assumed to be equal to the temperature of the liquid in the thermal boundary layer, i.e. $T_{\text{int}} = T_t(z)$. The temperature of the liquid in the thermal boundary layer is given by Eq. (4.1). A discussion on the error introduced by this assumption is provided in Sections 4.6 and 4.9.

4.3.3 Heat transfer from the bulk liquid to the bubble

The heat transferred from the bulk liquid to the bubble is computed assuming the presence of a thin boundary layer around the bubble and given by

$$\dot{Q}_\infty = q_\infty'' A_\infty = \left(\frac{T_\infty - T_v}{\sqrt{\pi \alpha_l t} / k_l + R_{\text{int}}} \right) A_\infty, \quad (4.14)$$

where $\sqrt{\pi \alpha_l t}$ is the thickness of the boundary layer around the bubble, α_l is the thermal diffusivity of the liquid and t is the bubble growth time. A_∞ is the surface area of the bubble in contact with the bulk liquid given by

$$A_\infty = 2\pi r_b (r_b + h_b - \delta_t). \quad (4.15)$$

4.3.4 Heat transfer from the wall to the bulk liquid

In a pool boiling system, a part of the wall will be in contact with the bulk liquid. The heat flux from in this region is computed assuming natural convection heat transfer from the wall to the bulk liquid

$$q_{\text{nc}}'' = h_{\text{nc}} (T_w - T_\infty), \quad (4.16)$$

where T_∞ is the temperature of the bulk liquid and h_{nc} is a natural convection heat transfer coefficient obtained from Sheriff et al. [155]

$$\text{Nu} = \frac{h_{\text{nc}} r_h}{k_l} = 0.262 (\text{Gr Pr}^2)^{0.35}, \quad (4.17)$$

where Gr and Pr are the Grashoff and Prandtl number of the liquid, respectively.

4.3.5 Total heat transfer to a bubble

A bubble grows due to heat transfer from the microlayer, the macrolayer, the thermal boundary layer and the bulk liquid surrounding the bubble. Thus, the overall rate of heat transferred to the bubble is

$$\dot{Q}_b = \rho_v h_{lv} A_b \frac{dr_b}{dt} = \dot{Q}_m + \dot{Q}_{ma} + \dot{Q}_t + \dot{Q}_\infty, \quad (4.18)$$

where ρ_v is the vapour density and A_b is the total surface area of the bubble given by

$$A_b = 2\pi r_b^2 (1 + \cos \beta). \quad (4.19)$$

Rearranging Eq. (4.18) gives a relation for the bubble growth rate as follows:

$$\frac{dr_b}{dt} = \frac{1}{\rho_v h_{lv} A_b} (\dot{Q}_m + \dot{Q}_{ma} + \dot{Q}_t + \dot{Q}_c). \quad (4.20)$$

The above bubble growth rate equation was obtained assuming the formation of a microlayer below the bubble. If the contact line region is formed, the bubble growth rate can be obtained by replacing the heat transferred from the microlayer in Eq. (4.20) with the heat transferred from the contact line region. However, coupling the heat transferred from the contact line region with the evaporation rate of the thermal boundary layer and the bulk liquid to accurately compute the bubble growth rate requires detailed CFD simulations as alluded to in Section 3.5.6 which are beyond the scope of this work.

The vapour temperature T_v in Eqs. (4.3), (4.6), (4.8), (4.13) and (4.14) is calculated by equating the bubble growth rate obtained from Eq. (4.20) with a validated bubble growth rate relation for the inertia controlled growth stage derived based on a mechanical energy balance of the liquid–vapour interface in the bubble [81]:

$$\left(\frac{dr_b}{dt} \right)^2 = C_1^2 \frac{T_v - T_{sat}}{\Delta T}, \quad (4.21)$$

where ΔT is the wall superheat and C_1 is a constant defined in Eq. (2.2).

4.3.6 Heat transfer in the wall

In pool boiling of sodium, as the bubble grows, the wall below the bubble is cooled owing to the evaporation of the liquid in the microlayer and the macrolayer region. The following transient heat conduction equation is solved to compute this variation in the wall temperature:

$$\rho_w c_{p,w} \frac{\partial T}{\partial t} = k_w \nabla^2 T, \quad (4.22)$$

where ρ_w , $c_{p,w}$ and k_w are the density, specific heat and thermal conductivity of the wall, respectively.

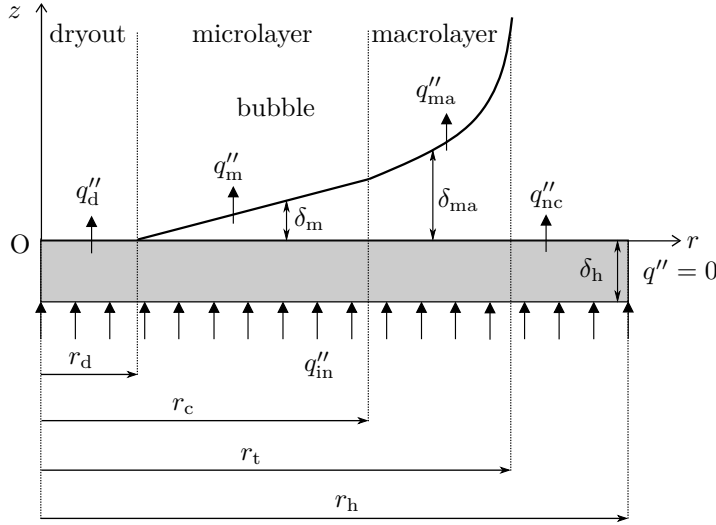


Figure 4.2: Wall heat transfer and boundary conditions.

4.4 Boundary and initial conditions

The boundary conditions to solve the transient conduction equation in the wall (Eq. (4.22)) are shown in Fig. 4.2 and summarised below.

- At the left boundary, an axisymmetric boundary condition is prescribed. Thus,

$$\left. \frac{dT}{dr} \right|_{r=0,z} = 0. \quad (4.23)$$

- At the right boundary, an adiabatic boundary condition is prescribed. Thus,

$$q''(r = r_h, z) = 0. \quad (4.24)$$

- An input heat flux of q''_{in} is provided at the bottom of the wall. Thus, the boundary condition at the bottom surface of the wall is

$$q''(r, z = -\delta_h) = q''_{in}. \quad (4.25)$$

- In the dryout region, the wall is in contact with the vapour. Owing to the low thermal conductivity of the vapour, the heat transferred from this region is assumed to be zero. Thus,

$$q''(r < r_d, z = 0) = q''_d = 0. \quad (4.26)$$

- The boundary condition in the microlayer region is

$$q''(r_d < r < r_c, z = 0) = q''_m. \quad (4.27)$$

- The boundary condition in the macrolayer region is

$$q''(r_c < r < r_t, z = 0) = q''_{\text{ma}}. \quad (4.28)$$

- A portion of the wall will be in contact with the bulk liquid as shown in Fig. 4.2. The boundary condition in this region is,

$$q''(r_t < r < r_h, z = 0) = q''_{\text{nc}}. \quad (4.29)$$

4.5 Initial conditions

The numerical simulations are initialised from a bubble of radius $r_b = 50 \mu\text{m}$ and assuming the wall to be at a uniform temperature equal to the wall temperature needed to initiate bubble growth. Thus,

$$T_{w,0} = T_w(t = 0) = T_{\text{sat}} + \Delta T. \quad (4.30)$$

The vapour temperature in the bubble is assumed to be 0.1 K less than the wall temperature. This perturbation is needed to initiate bubble growth.

$$T_{v,0} = T_v(t = 0) = T_{w,0} - 0.1. \quad (4.31)$$

4.6 Evaluation of thermal boundary layer heat transfer model assumption

In the developed model, the rate of heat transfer from the thermal boundary layer \dot{Q}_t is estimated assuming the temperature of the interface is equal to the temperature of the liquid in the thermal boundary layer. However, in reality, the temperature of the wall and the vapour in the bubble will influence the temperature of the liquid at the interface. Thus, the assumption made in this work may introduce an error in the computed heat transfer from the thermal boundary layer. To assess the error introduced by this assumption, the assumed temperature profile in the thermal boundary layer is compared with temperature obtained from a 2D heat transfer simulation of the thermal boundary layer. Figure 4.3 shows the geometry along with the boundary conditions prescribed for the simulation. A hemispherical sodium bubble of radius 15 mm growing on a heater of diameter 50 mm in a liquid pool of pressure 0.5 atm is chosen for the study. This pressure corresponds to a saturation temperature of 1073 K. The bubble is assumed to be hemispherical to maximise the surface area of the bubble in contact with the thermal boundary layer. The natural convection heat transfer coefficient is calculated assuming the wall to be at a temperature of 1123 K which represents a su-

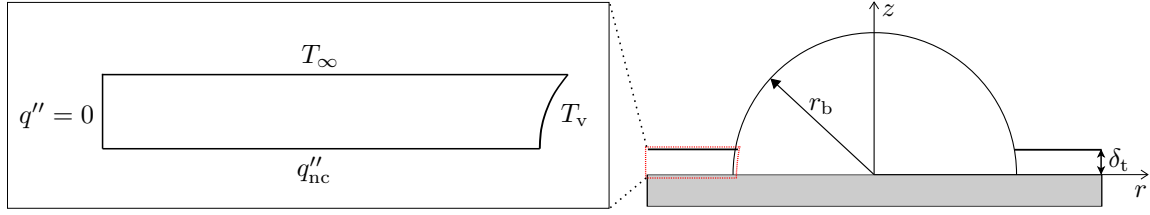


Figure 4.3: Geometry and boundary conditions used for the heat transfer simulation of the thermal boundary layer.

perheat of $\Delta T = 50$ K. The thermal boundary layer thickness is calculated assuming an input heat flux of $q''_{\text{in}} = 500 \text{ W m}^{-2}$. The simulations are performed for three different vapour temperature values $T_v = 1105 \text{ K}, 1100 \text{ K}, 1095 \text{ K}$ since the vapour temperature is expected to reduce as a bubble grows. These conditions are selected as they are similar to those used in the present study. Simulations are performed for two values of bulk liquid temperature: $T_\infty = (T_w + T_{\text{sat}})/2 = 1098 \text{ K}$ and $T_\infty = T_{\text{sat}} = 1073 \text{ K}$. The corresponding values of the thermal boundary layer thickness calculated using Eq. (4.2) are $\delta_t = 2.5 \text{ mm}$ and $\delta_t = 5 \text{ mm}$, respectively.

Figure 4.4 shows the contour plot of the temperature distribution in the thermal boundary layer obtained from the heat transfer simulation for a bulk liquid temperature of $T_\infty = 1098 \text{ K}$ and vapour temperature of $T_v = 1100 \text{ K}$. The temperature of the vapour and the wall affects the temperature distribution in the thermal boundary layer, as seen from the contour plot. To analyse the error introduced by the assumption made in calculating the heat transfer rate from the thermal boundary layer in the present model, the temperature profile at a distance of 0.5 mm from the interface is compared with the analytical temperature profile given by Eq. (4.1) as shown in Fig. 4.5. The assumed analytical temperature profile differs from the simulated temperature in the thermal boundary as shown in Figs. 4.5a and 4.5b. This difference introduces an error in the calculated thermal boundary layer heat transfer rate. For the $T_\infty = 1098 \text{ K}$ case, the use of the analytical temperature profile is found to be reasonable and the error in the temperature is found to be lower than that for the $T_\infty = 1073 \text{ K}$ case. In general, the error increases as the temperature difference between the wall and the bulk liquid increases. Hence, in this work, the bubble growth analysis is limited to cases with the bulk liquid temperature $T_\infty \geq (T_w + T_{\text{sat}})/2$.

The results discussed in this section were obtained assuming a hemispherical bubble. In reality, a bubble may not be hemispherical throughout its growth period. In non-hemispherical bubbles, the portion of the bubble interface in contact with the liquid in the thermal boundary layer will reduce with time. Thus, the error introduced by the assumed analytical temperature profile on the thermal boundary layer heat transfer, \dot{Q}_t , will also reduce with time. This is further discussed in Section 4.9.

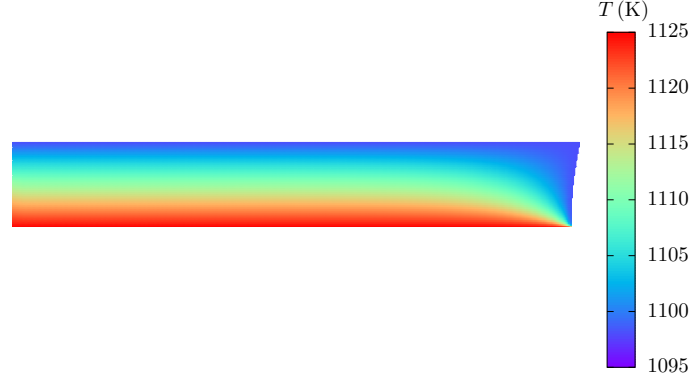


Figure 4.4: Contour plot of temperature in the thermal boundary layer for $T_v = 1100$ K and $T_\infty = 1098$ K.

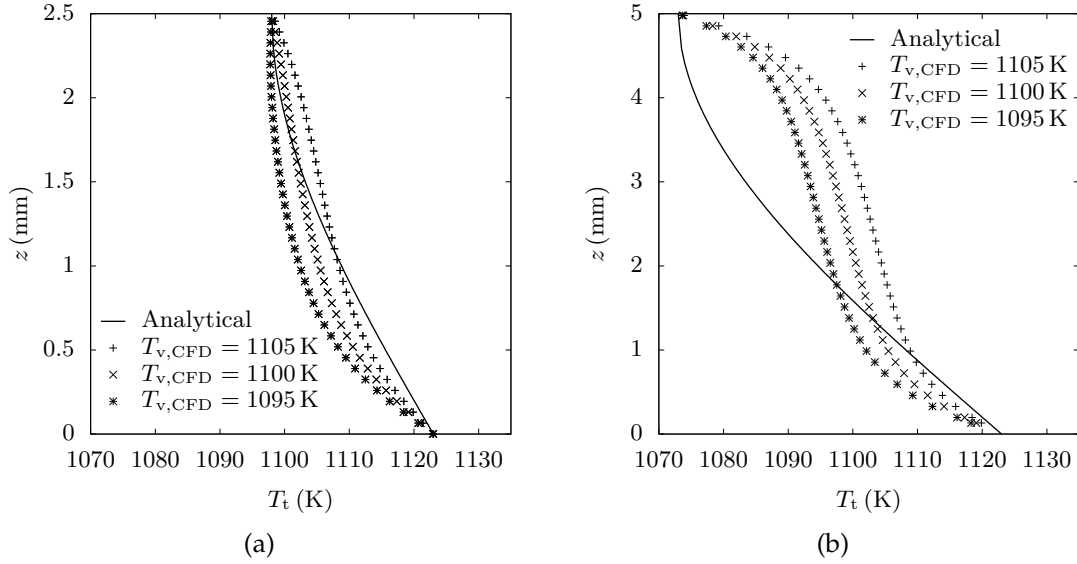


Figure 4.5: Comparison of temperature distribution at a distance of 0.5 mm from the interface with the analytical temperature profile given by Eq. (4.1) for (a) $T_\infty = 1098$ K and (b) $T_\infty = 1073$ K.

4.7 Numerical solution and validation

The two-dimensional transient conduction equation in the wall Eq. (4.22) is numerically solved using a finite volume method and a first order implicit time integration scheme of the commercial CFD code ANSYS Fluent 17.1 [156]. The water boiling experiment of Duan et al. [13] is first simulated using the reduced-order bubble growth model developed in this work for an input heat flux of $q''_{\text{in}} = 28.7 \text{ kW m}^{-2}$, to validate the model. A constant contact angle of $\beta = 45^\circ$ is prescribed for the simulation [18, 157]. The thermophysical properties of the wall are obtained from Ref. [15]. An accommodation coefficient $f = 0.03$ is used to calculate the interface resistance and the initial microlayer profile is given by $\delta_0 = 4.46 \times 10^{-3} r$ [93, 94, 158]. Prior to validating the model, a grid

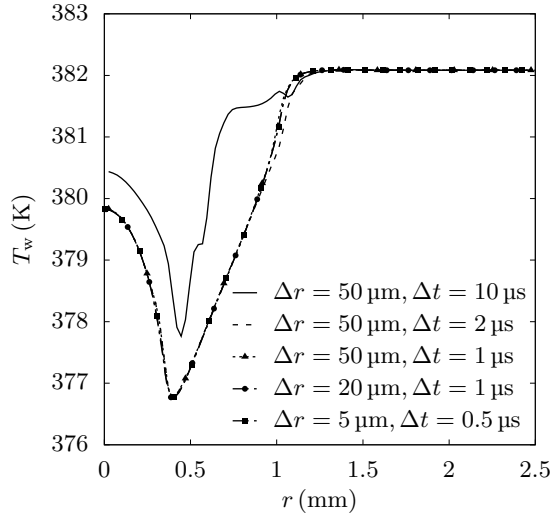


Figure 4.6: Wall temperatures obtained for different cell sizes and time step sizes at time $t = 2.5$ ms.

independence study is performed to ensure the solution obtained from the model is independent of the choice of the mesh size. The wall temperatures obtained from five cases with different time step and cell sizes in the radial direction at $t = 2.5$ ms are shown in Fig. 4.6. The cell size in the axial direction for all cases is $\Delta z = 50 \mu\text{m}$. The model prediction is found to be insensitive for cell sizes less than $\Delta r = 50 \mu\text{m}$ and time step size less than $\Delta t = 1 \mu\text{s}$. Thus, the cell size and time step size chosen for this work are $\Delta r = 50 \mu\text{m}$, $\Delta z = 50 \mu\text{m}$ and $\Delta t = 1 \mu\text{s}$.

Figure 4.7 shows the comparison of the wall temperature obtained using the present model with the temperatures obtained from the experimental study of Duan et al. [13] and CFD simulation of Sato et al. [15] at $t = 0.42$ ms and $t = 2.5$ ms for an input heat flux of $q''_{\text{in}} = 28.7 \text{ kW m}^{-2}$. All input parameters are the same as that used in the mesh independence study. For the verification and validation study, the initial period of the growth process until $t = 5$ ms is simulated where the shape of the bubble is a truncated sphere. The agreement between the wall temperatures obtained from the model with experimental and CFD results is found to be reasonable.

4.8 Results and discussion

The heat transfer and growth characteristics of a sodium bubble on a nickel heater of thickness 1 mm and radius 6 cm are discussed in this section. The thermophysical properties of sodium used in the simulation are given by Eq. (3.16). The thermophysical properties of the nickel heater are given in Table 4.1.

The growth of a bubble in a sodium pool tends to be inertia controlled and characterised by a high contact angle [141]. Hence a baseline contact angle of $\beta = 80^\circ$ is assumed for the simulations performed. The bulk liquid temperature is assumed to be $T_\infty = (T_{\text{sat}} + T_{w,0})/2$ where $T_{\text{sat}} = 1073 \text{ K}$ is the saturation temperature corresponding

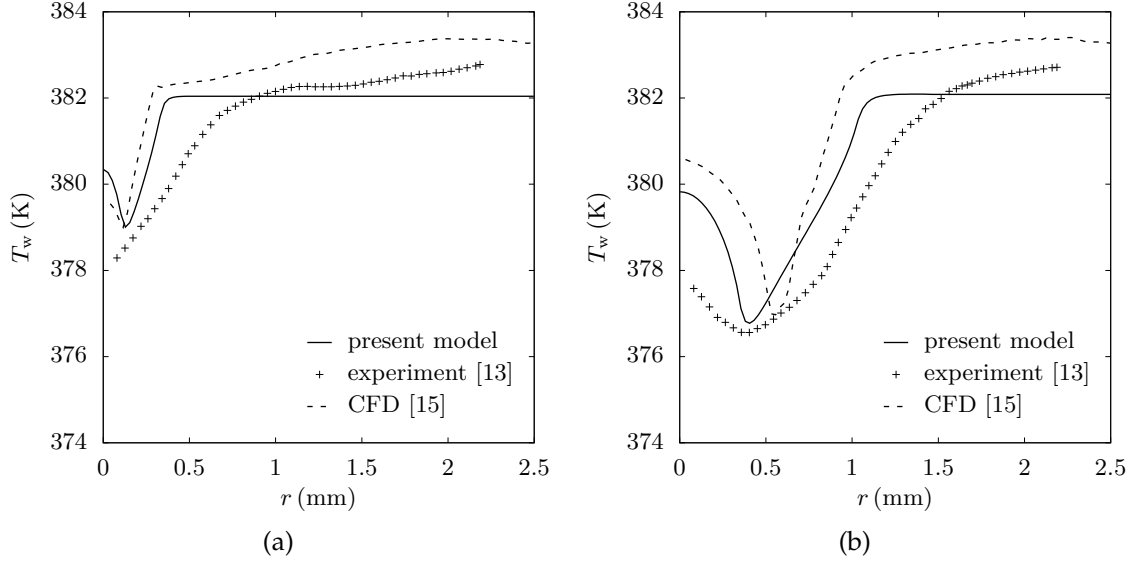


Figure 4.7: Comparison of wall temperatures obtained using the present model with temperatures obtained from the experiment of Duan et al. [13] and CFD simulation of Sato et al. [15] at (a) $t = 0.42$ ms (b) $t = 2.5$ ms.

to a pressure of 0.5 atm. An accommodation coefficient of $f = 1$ is used in calculating the interface resistance [47]. Since an accurate value of the accommodation coefficient of sodium is not known, a sensitivity study is performed to assess its influence on the bubble growth rate and reported in Section 4.8.5. Additionally, the influence of parameters like the wall superheat, contact angle and bulk liquid temperature on the growth of a sodium bubble are presented. A summary of the baseline parameters and cases studied is provided in Table 4.2.

Four dimensionless numbers E_m , E_{ma} , E_t and E_∞ are defined as follows to quantify the contribution of the microlayer, macrolayer, thermal boundary layer and bulk liquid heat transfer to the overall heat transferred to the bubble, respectively. The larger the value of E , the greater is the influence of the particular heat transfer mechanism on the bubble growth process.

$$E_m = \frac{\dot{Q}_m}{\dot{Q}_b}; E_{ma} = \frac{\dot{Q}_{ma}}{\dot{Q}_b}; E_t = \frac{\dot{Q}_t}{\dot{Q}_b}; E_\infty = \frac{\dot{Q}_\infty}{\dot{Q}_b} \quad (4.32)$$

Table 4.1: Thermophysical properties of nickel used in the numerical simulations [159].

Property	Value	Unit
ρ_w	8900	kg m^{-3}
$c_{p,w}$	$476.1 + 0.01287T_w + 5.824 \times 10^{-5}T_w^2$	$\text{J kg}^{-1} \text{K}^{-1}$
k_w	$42.27 + 0.01519T_w + 4.511 \times 10^{-6}T_w^2$	$\text{W m}^{-1} \text{K}^{-1}$

Table 4.2: Baseline parameters and cases studied.

Case	$\beta(^{\circ})$	$\Delta T(K)$	$T_{\infty}(K)$	f
Baseline	80	50	1098	1
Effect of β	30, 60, 80, 90	50	1098	1
Effect of ΔT	80	20, 50, 80	$(T_{\text{sat}} + T_{w,0})/2$	1
Effect of T_{∞}	80	50	1098, 1110.5, 1123	1
Effect of f	80	50	1098	0.25, 0.5, 0.75, 1

4.8.1 Sodium heat transfer and growth characteristics

The heat transfer and growth characteristics of a bubble growing in a liquid pool with a contact angle of 80° at a superheat of 50 K and bulk liquid temperature of $(T_{\text{sat}} + T_{w,0})/2 = 1098$ K is presented in this section. This bulk liquid temperature results in a thermal boundary layer of thickness 2.5 mm.

Figure 4.8 shows the growth rate, variation in the vapour temperature, bubble radius and the rate of heat transferred from the microlayer, the macrolayer, the thermal boundary layer and the bulk liquid to a bubble in sodium pool boiling at a superheat of 50 K. The growth rate of a bubble is directly proportional to the total heat transferred to the bubble and inversely proportional to its surface area, according to Eq. (4.20). Immediately after nucleation, an increase in the bubble radius and surface area leads to a sharp decrease in the growth rate as seen in Fig. 4.8a. Subsequently, the growth rate reduces gradually due to an exponential increase in the total heat transferred to the bubble, as shown in Fig. 4.8d. As the bubble grows, the vapour pressure in the bubble decreases. This leads to a decrease in the vapour temperature as seen in Fig. 4.8b. The magnitude of the vapour temperature is proportional to the square of the bubble growth rate, according to Eq. (2.1). Hence the vapour temperature drops rapidly after nucleation and then gradually decreases as the bubble grows.

Figures 4.8c and 4.8d show the bubble radius and the rate of heat transferred from the microlayer, the macrolayer, the thermal boundary layer and the bulk liquid to a sodium bubble at a superheat of 50 K, respectively. The bubble radius increases with time, as shown in Fig. 4.8c due to an increase in the rate of heat transferred \dot{Q}_b to the bubble. As the bubble grows, the amount of liquid trapped below it in the microlayer and the macrolayer increases. This leads to an increase in the rate of heat transferred from the microlayer and macrolayer with time, as shown in Fig. 4.8d. The magnitude of the macrolayer heat transfer rate is small compared to the microlayer as the bubble contact angle is high which implies $r_c \approx r_t$. Thus, the macrolayer area $A = \pi(r_t^2 - r_c^2)$ is small which leads to less heat transferred through the macrolayer. The rate of heat transferred from the thermal boundary layer, \dot{Q}_t , initially increases when the bubble is small and is exposed to the high temperature liquid in the thermal boundary layer close to the wall. After $t = 1.2$ ms, \dot{Q}_t reduces and subsequently becomes negative as the

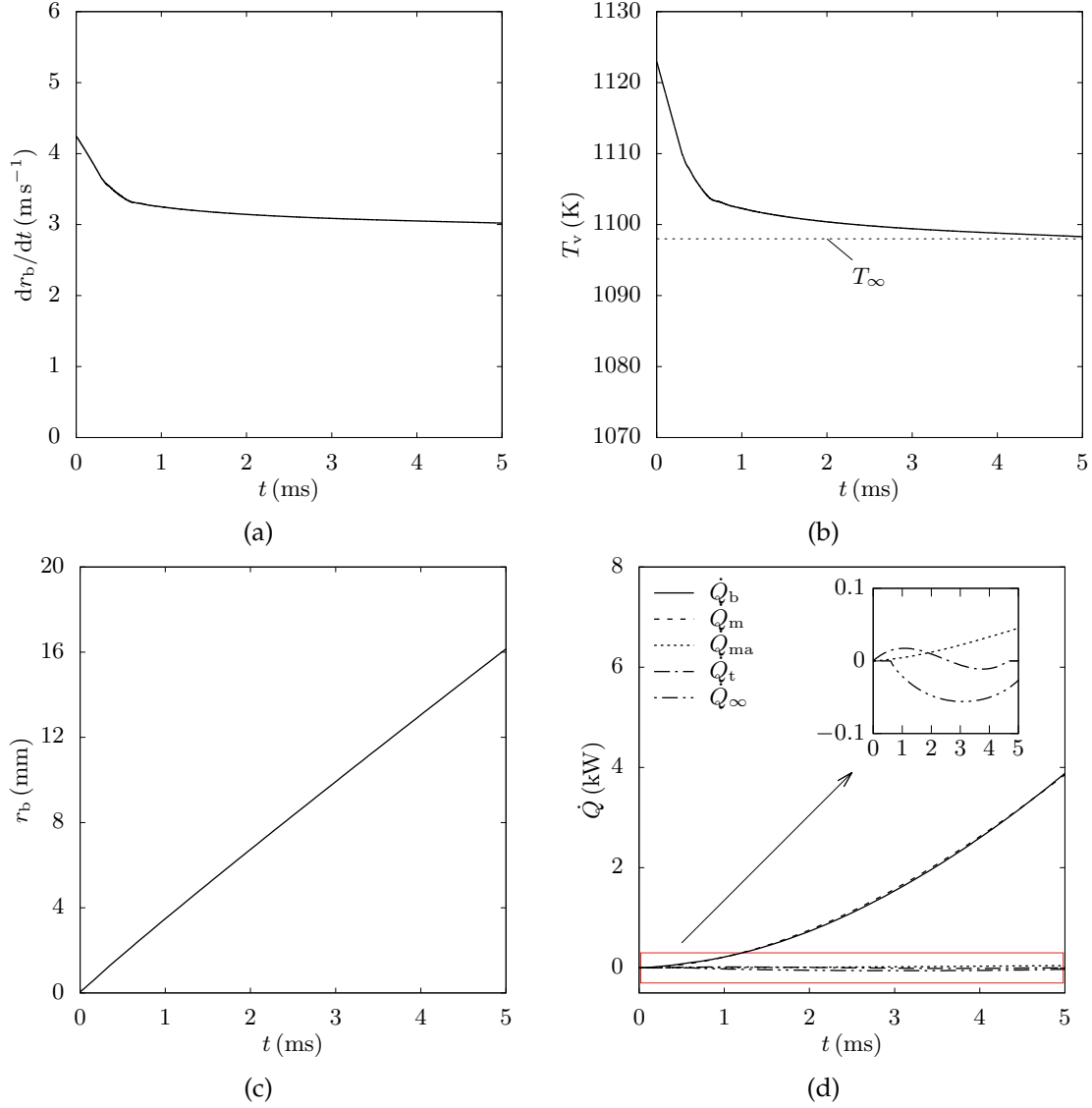


Figure 4.8: Bubble growth and heat transfer characteristics in sodium pool boiling at a superheat of 50 K and bulk liquid temperature of $T_\infty = 1098$ K: (a) bubble growth rate, (b) vapour temperature, (c) bubble radius and (d) rate of heat transferred from the microlayer \dot{Q}_m , the macrolayer \dot{Q}_{ma} , the thermal boundary layer \dot{Q}_t and bulk liquid \dot{Q}_∞ to the bubble.

bubble undergoes condensation as it comes in contact with the cooler liquid towards the top of the thermal boundary layer. At $t = 4.6$ ms, \dot{Q}_t becomes zero as all the liquid in the thermal boundary layer is trapped in the macrolayer.

The bulk liquid heat transfer rate \dot{Q}_∞ is zero until $t = 0.6$ ms as seen in Fig. 4.8d because immediately after nucleation the bubble is submerged in the thermal boundary layer. Thereafter, \dot{Q}_∞ is negative throughout the growth period since the bulk liquid is cooler than the vapour in the bubble. Thus, the bubble undergoes condensation in the portion in contact with the bulk liquid. The magnitude of \dot{Q}_∞ depends on the

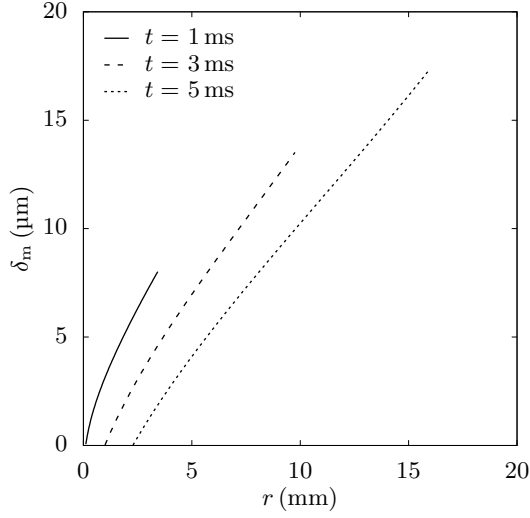


Figure 4.9: Sodium microlayer thickness for a wall superheat of 50 K and bulk liquid temperature of $T_\infty = 1098$ K.

area of the bubble in contact with the bulk liquid A_∞ and the temperature difference $T_\infty - T_v$. Initially, the magnitude of \dot{Q}_∞ increases with time primarily due to an increase in A_∞ with time. After $t = 3$ ms, the effect of temperature difference becomes more pronounced. As the bubble grows, the vapour temperature approaches the bulk liquid temperature as seen in Fig. 4.8b, i.e. the temperature difference $T_\infty - T_v$ decreases. Hence the magnitude of \dot{Q}_∞ decreases during the latter stages of bubble growth.

Figure 4.9 shows the variation of microlayer thickness δ_m with radial distance at different times during the growth of a sodium bubble. As the bubble grows and the contact radius r_c increases, the amount of liquid in the microlayer increases. Thus, the radial extent and thickness of the microlayer increases with time. The maximum thickness of the microlayer is $17.3 \mu\text{m}$ at time $t = 5$ ms. The microlayer profiles at different times are almost parallel, which is consistent with observations made in boiling of high Prandtl number fluids [131].

Figure 4.10 shows the transient variation in the non-dimensional parameter E defined in Eq. (4.32) during the growth of a sodium bubble at a wall superheat of 50 K and a bulk liquid temperature of $T_\infty = 1098$ K. The contribution of microlayer heat transfer to bubble growth E_m increases with time due to an increase in the bubble contact area $A = \pi (r_c^2 - r_d^2)$. As seen from Fig. 4.10, the microlayer accounts for 50% of the total heat transferred to the bubble immediately after nucleation and almost all of the heat transferred for $t > 1.5$ ms. The contribution of the macrolayer is found to be small throughout the bubble growth process as $r_c \approx r_t$ due to the high contact angle of the bubble. At $t = 0$, the bubble is surrounded by the liquid in the thermal boundary layer, and thus its contribution is high. Subsequently, E_t decreases with an increase in the contribution of the microlayer heat transfer. During the initial bubble growth period $t < 0.6$ ms, the bubble is immersed in the thermal boundary layer. In this period, bubble growth is driven by heat transfer from the microlayer, the macrolayer and the thermal

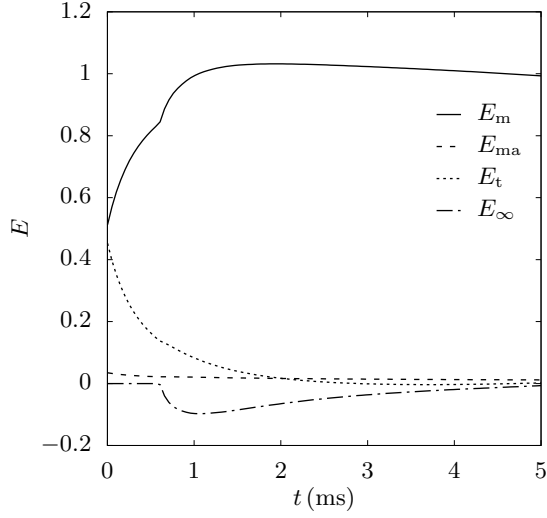


Figure 4.10: Variation in the parameter E with time in sodium pool boiling at a wall superheat of 50 K and a bulk liquid temperature of $T_\infty = 1098$ K.

boundary layer, while the bulk liquid does not contribute to bubble growth. Once the bubble comes in contact with the cooler bulk liquid, it undergoes condensation. The magnitude of the E_∞ initially increases and then decreases due to the decrease in the temperature difference $T_\infty - T_v$ with time.

The results discussed in this section are obtained assuming the value of the empirical constant $C = 0.6$ in the initial microlayer profile δ_0 relation given by Eq. (4.7). Since this value of C has not been validated for sodium boiling, a sensitivity study is performed to assess its effect on microlayer heat transfer rate and bubble radius. Cooper and Lloyd [83] performed experiments on bubble growth at low pressures and suggested values of C in the range of 0.5–1. Hence, to assess the influence of C on sodium bubble growth, simulations were performed assuming the value of the coefficient $C = 0.5, 0.6, 0.8, 1$ in Eq. (4.7). A marginal decrease in the microlayer heat transfer rate was observed on increasing the value of C due to the formation of a thicker microlayer. A thicker microlayer leads to less heat transferred to the bubble due to an increase in the conduction resistance δ_m/k_l . On increasing the value of C from 0.5 to 1, the microlayer heat transfer rate and bubble radius decreased by 2.5% and 0.2%, respectively at $t = 5$ ms. Thus, the results from the model were found to be insensitive to the value of C .

4.8.2 Effect of wall superheat

Sodium boiling systems typically require a large superheat to initiate the bubble growth process compared to high Prandtl number fluids like water. The effect of the wall superheat on the bubble growth and heat transfer characteristics are investigated in this section. Here, the bulk liquid is assumed to be at a temperature of $T_\infty = (T_{w,0} + T_{\text{sat}})/2$. Thus, as the superheat increases, the wall temperature and the bulk liquid temperature increase.

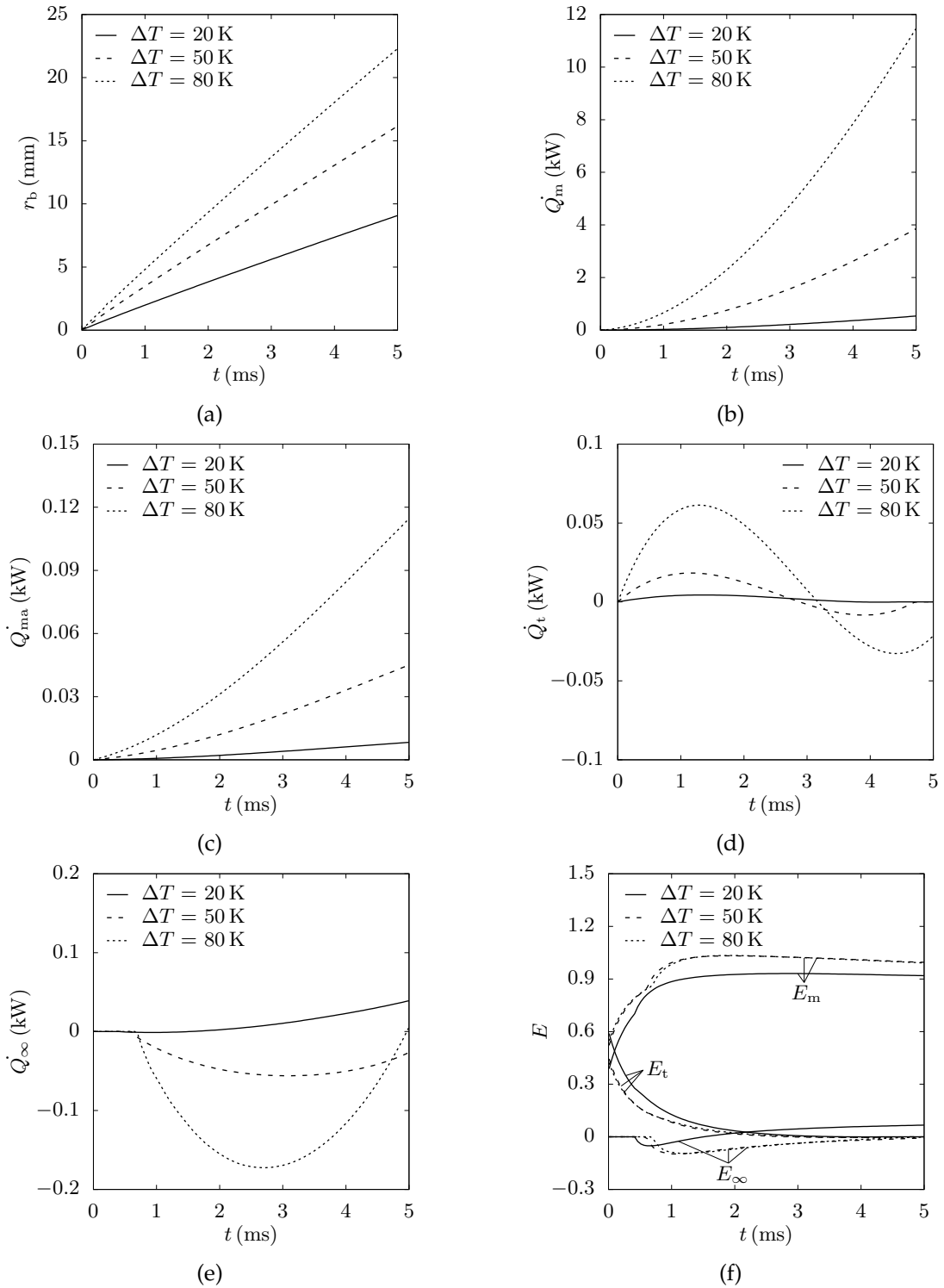


Figure 4.11: Effect of wall superheat on the (a) bubble radius, (b) microlayer heat transfer rate \dot{Q}_m , (c) macrolayer heat transfer rate \dot{Q}_{ma} , (d) thermal boundary layer heat transfer rate \dot{Q}_t , (e) bulk liquid heat transfer rate \dot{Q}_∞ and (f) transient variation of parameter E in sodium pool boiling.

Figure 4.11 shows the effect of increasing the wall superheat on the bubble radius, the rate of heat transferred from the microlayer, the macrolayer, the thermal boundary layer and the bulk liquid, and the variation in the parameter E in a sodium pool at $p_\infty = 0.5$ atm. The bubble radius increases with an increase in superheat as seen in Fig. 4.11a. At bubble nucleation, i.e. $t = 0$, the vapour temperature is equal to the wall temperature ($T_{w,0} = T_{\text{sat}} + \Delta T$) and the vapour pressure in the bubble is equal to the saturation pressure corresponding to the vapour temperature. Thus, as the superheat increases, the vapour temperature and the pressure inside the bubble increases. On the other hand, the bulk liquid is maintained at a pressure of $p_\infty = 0.5$ atm. Thus, larger the superheat, larger is the pressure difference $p_v - p_\infty$, which drives the growth of the bubble and leads to larger growth rate and bubble sizes. The increase in bubble growth rate and radius with superheat results in a larger bubble contact area, $A = \pi(r_c^2 - r_d^2)$ which leads to a larger heat transfer rate from the microlayer as seen in Fig. 4.11b. As the bulk liquid temperature increases with an increase in the superheat, the thermal boundary layer thickness also increases. This leads to more liquid being trapped in the macrolayer and a larger portion of the bubble to be exposed to the thermal boundary layer. Thus, the rate of heat transferred from the macrolayer and the thermal boundary layer increases with an increase in superheat as observed in Fig. 4.11d. For all superheats, the transient variation in \dot{Q}_t is found to be similar. It increases initially when the bubble is small and is in contact with the higher temperature liquid close to the wall in the boundary layer. Subsequently, it decreases and becomes negative as the bubble interface comes in contact with the cooler liquid towards the top of the thermal boundary layer.

The transient variation in the bulk liquid heat transfer rate \dot{Q}_∞ is shown in Fig. 4.11e. The bulk liquid heat transfer rate is negative throughout the bubble growth period for the $\Delta T = 50$ K and $\Delta T = 80$ K cases as the temperature difference $T_\infty - T_v$ is found to be negative. As explained previously, the magnitude of \dot{Q}_∞ initially increases due to an increase in the area A_∞ and thereafter decreases due to a decrease in the temperature difference $T_\infty - T_v$. For a bubble growing at a low superheat of 20 K, the mechanism of the bulk liquid heat transfer rate changes at $t = 1.5$ ms from condensation to evaporation as the vapour temperature decreases below the bulk liquid temperature. This leads to a positive $T_\infty - T_v$ value and evaporation in the portion of the bubble in contact with the bulk liquid.

The effect of wall superheat on the parameter E , representing the contribution of the different heat transfer mechanisms, is shown in Fig. 4.11f. On increasing the superheat from 20 K to 80 K, a proportional increase in the microlayer, macrolayer, thermal boundary layer and bulk liquid heat transfer is observed. Therefore, the magnitude and trend in their contribution to the overall heat transferred to the bubble are approximately the same for all superheats. Thus, irrespective of the superheat, as a sodium bubble grows in a liquid pool of temperature $(T_{w,0} + T_{\text{sat}})/2$, the contribution of the microlayer heat transfer to bubble growth increases. At the same time, the influence of the thermal

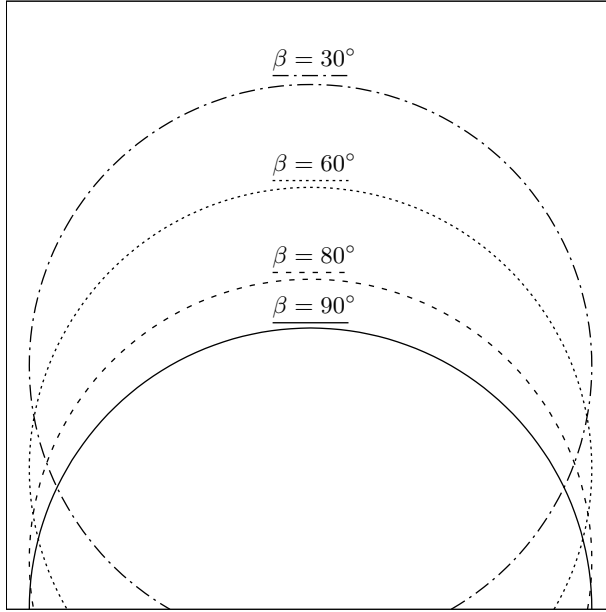


Figure 4.12: Schematic of bubble profile for different contact angles.

boundary layer heat transfer decreases. The bulk liquid heat transfer has a smaller impact on bubble growth compared to the other mechanisms. Initially, its contribution is zero when the bubble is in the thermal boundary layer and decreases with time as the temperature difference between the bulk liquid and the vapour decreases. The value of the parameter E_{ma} , representing the contribution of the macrolayer heat transfer for all three superheats, is found to be very less and hence not shown in the figure. The highest value of E_{ma} is found to be 0.035 at $t = 0$ for the $\Delta T = 80$ K case.

4.8.3 Effect of contact angle

In the preceding sections, the simulation results presented were limited to a bubble with a contact angle of $\beta = 80^\circ$. During the bubble growth process, the contact angle will change as the bubble transitions from the inertial controlled to heat transferred controlled growth stage. Since the actual contact angle is not known, a parametric study is conducted to study its effect on the heat transfer and growth characteristics of a sodium bubble growing in a liquid pool maintained at a temperature of 1098 K and at a wall superheat of 50 K. Four contact angles are chosen for the study ranging from 30° – 90° . A schematic of the bubble shapes for the assumed contact angles is shown in Fig. 4.12.

Figure 4.13 shows the effect of contact angle on the bubble radius, vapour temperature and the microlayer, macrolayer, thermal boundary layer and bulk liquid heat transfer rate. A bubble growing with a higher contact angle is larger compared to a bubble growing with a lower contact angle, as shown in Fig. 4.13a. With an increase in the contact angle, the bubble contact area $A = \pi(r_c^2 - r_d^2)$ increases as seen from the

schematic in Fig. 4.12. This leads to larger heat transferred from the microlayer as the contact angle increases as observed in Fig. 4.13b. The shape of the bubble tends to be more spherical with a decrease in the contact angle, and hence a larger amount of liquid is trapped below the bubble in the macrolayer. This results in an increase in the macrolayer heat transfer rate with a decrease in the contact angle as shown in Fig. 4.13c. In hemispherical bubbles ($\beta = 90^\circ$), a macrolayer is not formed. Hence the macrolayer heat transfer rate is zero. The magnitude of the thermal boundary layer heat transfer rate for bubbles growing with a contact angle of 30° – 80° is small as shown in Fig. 4.13d as most of the liquid in the thermal boundary layer is confined to the macrolayer. In 30° and 60° contact angle bubbles, after 1 ms and 1.5 ms, respectively, all of the liquid in the thermal boundary layer is trapped in the macrolayer and hence $\dot{Q}_t = 0$. In hemispherical bubbles, since a macrolayer is not formed, a larger surface area of the bubble is in contact with the liquid in the thermal boundary layer. Thus, the magnitude of \dot{Q}_t is large for a $\beta = 90^\circ$ bubble compared to the bubbles growing with a lower contact angle.

The transient variation in bulk liquid heat transfer rate for different contact angles is shown in Fig. 4.13e. For a bubble growing with a contact angle of 30° and 60° , throughout the growth period, the bubble undergoes evaporation in the portion in contact with the bulk liquid. This is a result of the direct proportional relationship of bulk liquid heat transfer and the temperature difference $T_\infty - T_v$. During the initial growth period, the bubble is completely inside the thermal boundary layer, hence \dot{Q}_∞ is zero. Thereafter, the temperature of the bulk liquid is higher than the vapour as seen in Fig. 4.13f and $T_\infty - T_v$ is positive. The magnitude of \dot{Q}_∞ for a 30° contact angle bubble is higher compared to a 60° contact angle bubble as the area of the bubble in contact with the bulk liquid A_∞ and the temperature difference $T_\infty - T_v$ increases with a decrease in the contact angle. For bubbles growing with a higher contact angles, i.e. 80° and 90° , the bulk liquid is cooler than the vapour throughout the growth period. Hence the bubble undergoes condensation in the bulk liquid and \dot{Q}_∞ is negative.

Figure 4.14 shows the effect of the contact angle on the parameter E in sodium pool boiling at a wall superheat of 50 K. For bubbles growing with contact angles $\beta \geq 60^\circ$, the microlayer is the dominant mechanism of heat transfer as seen in Fig. 4.14a. As the contact angles decreases, the amount of liquid in the macrolayer increases. Thus, the contribution of macrolayer to bubble growth increases with a decrease in the contact angle as shown in Fig. 4.14b. The value of $E_t \approx 0.2$ for a hemispherical bubble growing in a sodium pool as shown in Fig. 4.14c. This implies that the thermal boundary layer contributes to nearly 20% of the total heat transferred to the bubble throughout the growth period. For all other contact angles, the heat transferred from the thermal boundary layer affects the growth of a bubble during its initial stages, just after nucleation and decreases with time. The influence of bulk liquid condensation for a bubble growing with a contact angle of $\beta \geq 80^\circ$ decreases with contact angle as shown in Fig. 4.14d.

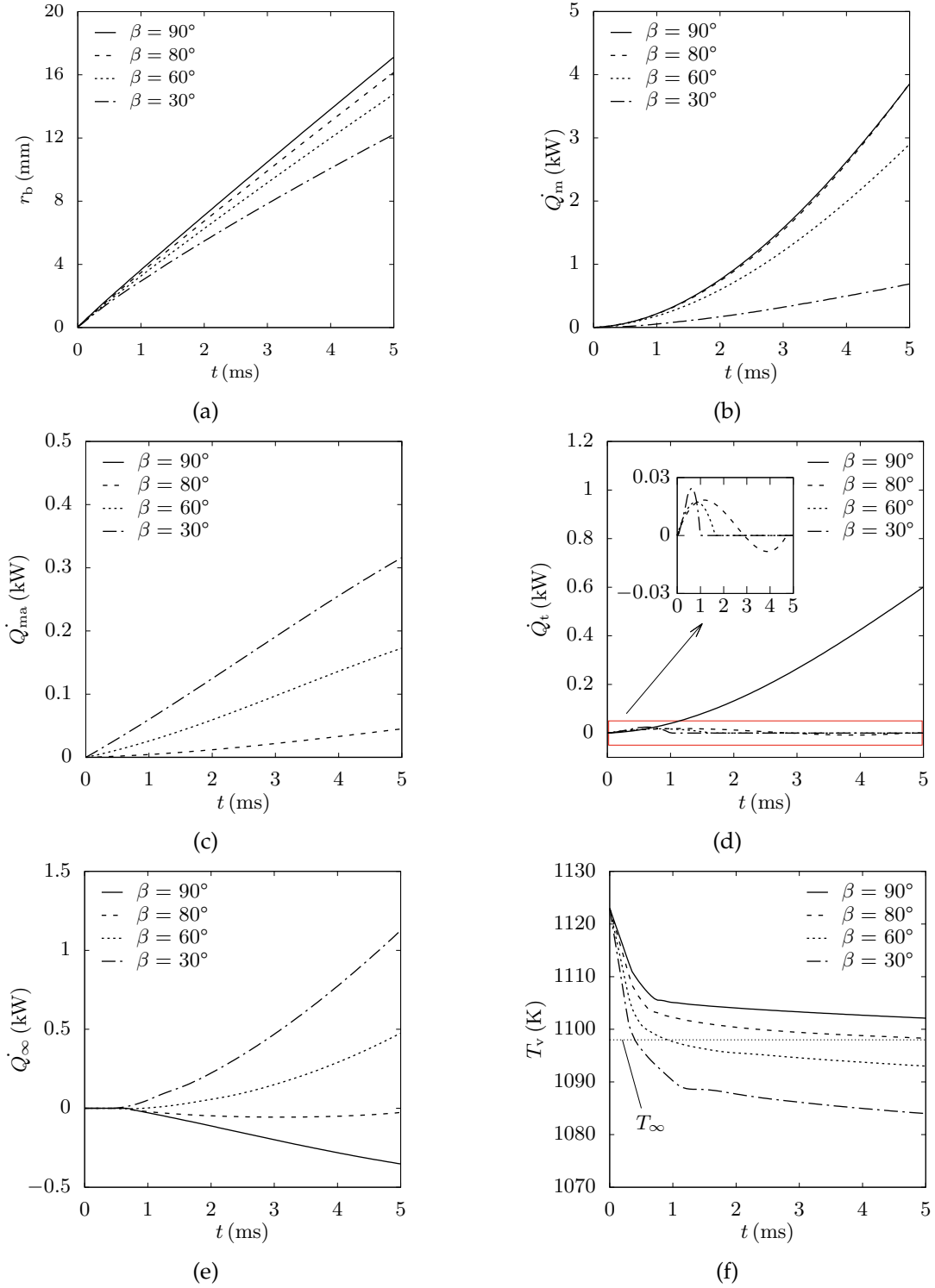


Figure 4.13: Effect of contact angle on (a) bubble radius, (b) microlayer heat transfer rate \dot{Q}_m (c) macrolayer heat transfer rate \dot{Q}_{ma} , (d) thermal boundary layer heat transfer rate \dot{Q}_t , (e) bulk liquid heat transfer rate \dot{Q}_∞ and (f) vapour temperature in sodium pool boiling at a wall superheat of 50 K and a bulk liquid temperature of $T_\infty = 1098$ K.

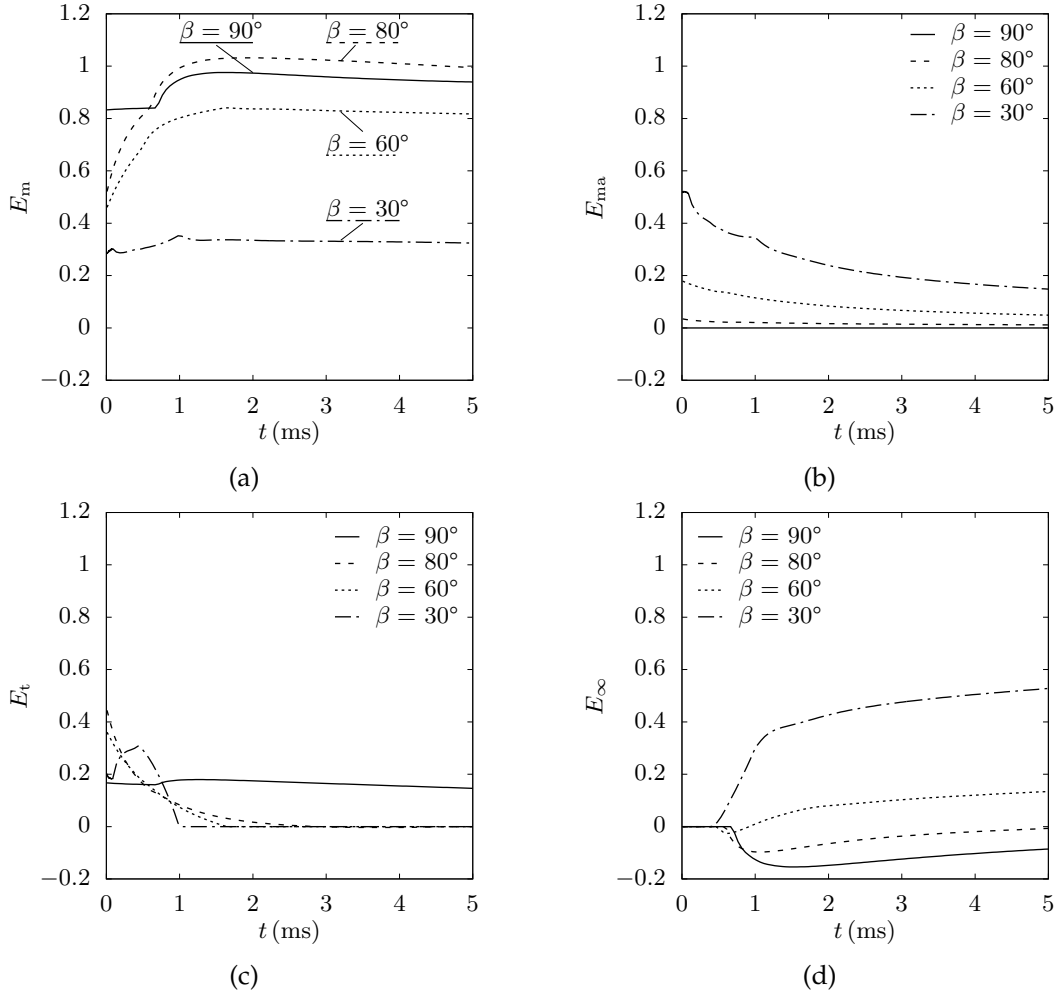


Figure 4.14: Effect of contact angle on the parameter (a) E_m , (b) E_{ma} , (c) E_t and (d) E_∞ in sodium pool boiling at a wall superheat of 50 K and a bulk liquid temperature of $T_\infty = 1098$ K.

On the contrary, for $\beta \leq 60^\circ$, the influence of bulk liquid evaporation increases with a decrease in the contact angle as the area of the bubble in contact with the bulk liquid increases.

4.8.4 Effect of bulk liquid temperature

The thickness of the thermal boundary layer depends on the difference in temperature between the wall and the bulk liquid. Thus, the knowledge of the bulk liquid temperature is important to predict the growth characteristics of a bubble in a liquid pool. The effect of varying the bulk liquid temperature on the growth of a $\beta = 80^\circ$ sodium bubble at a superheat of 50 K is presented in this section. Three values of bulk liquid temperature $T_\infty = 1098$ K, 1110.5 K, 1123 K are chosen which result in thermal boundary layer thickness of $\delta_t = 2.5$ mm, 1.25 mm, 0 mm, respectively. A thermal boundary layer is not formed when the bulk liquid temperature is equal to the wall temperature.

Figure 4.15 shows the effect of bulk liquid temperature on the bubble radius, vapour temperature, and the rate of heat transferred from the microlayer and the bulk liquid to a sodium bubble. The bubble radius increases as T_∞ increases as seen in Fig. 4.15a due to an increase in the total heat transferred to the bubble. For a bubble growing in a lower temperature liquid pool, the vapour temperature in the bubble is lower owing to smaller growth rate compared to a bubble growing in a higher temperature liquid pool, as shown in Fig. 4.15b.

The microlayer heat transfer rate increases with an increase in the temperature of the liquid pool as shown in Fig. 4.15c. For the same contact angle, with an increase in the bubble radius with T_∞ , the bubble contact area increases. This leads to an increase in

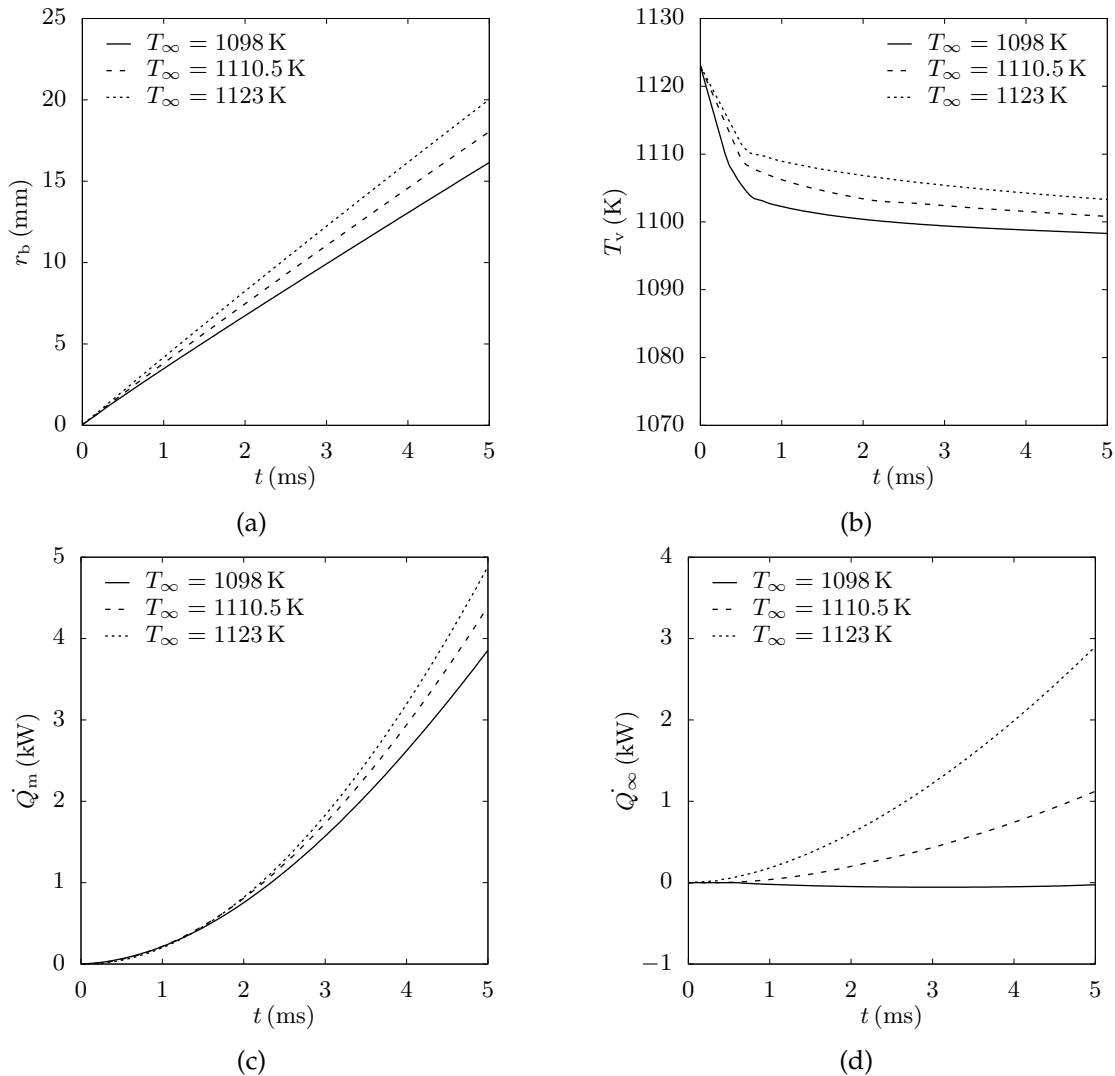


Figure 4.15: Effect of bulk liquid temperature on the (a) bubble radius, (b) vapour temperature, (c) microlayer heat transfer rate \dot{Q}_m and (d) bulk liquid heat transfer rate \dot{Q}_∞ in sodium pool boiling at a wall superheat of 50 K.

the rate of heat transferred from the microlayer to the bubble as the temperature of the liquid pool increases.

Figure 4.15d shows the effect of bulk liquid temperature on the rate of heat transferred from the bulk liquid to a bubble in sodium pool boiling. For a bubble growing in a sodium pool of temperature $T_\infty = 1098\text{ K}$, the bulk liquid is found to be cooler than the vapour in the bubble throughout the growth period. Hence the bubble undergoes condensation in the portion in contact with the bulk liquid and \dot{Q}_∞ is negative. When the bulk liquid is maintained at $T_\infty = 1110.5\text{ K}$ and $T_\infty = 1123\text{ K}$, $T_\infty > T_v$ throughout the growth period. Thus, \dot{Q}_∞ is positive and the bubble grows due to evaporation of the bulk liquid. The macrolayer heat transfer rate is found to be significantly less than the microlayer heat transfer rate since the contact angle of the bubble is high for all cases. Similarly, the thermal boundary layer heat transfer rate is also insignificant except for the initial period of bubble growth immediately after nucleation when the bubble is submerged in the thermal boundary layer. The maximum value of \dot{Q}_t is found to be 0.035 kW for a bubble growing in a sodium pool of temperature $T_\infty = 1098\text{ K}$.

Figure 4.16 shows the effect of bulk liquid temperature on the parameter E . Throughout the growth period, the contribution of the macrolayer is found to be negligible and hence not plotted. The contribution of the microlayer heat transfer rate on bubble growth decreases as the bulk liquid temperature increases as seen in Fig. 4.16a. This is primarily due to an increase in the contribution of the bulk liquid heat transfer rate with T_∞ as shown in Fig. 4.16b. For the $T_\infty = 1098\text{ K}$ case, the bubble grows mainly because of heat transferred from the microlayer while the growth rate reduces because of condensation in the bulk liquid. For the other two cases, as the temperature of the bulk liquid increases, the contribution of evaporation from the bulk liquid on bubble growth also increases. This is due to an increase in the temperature difference $T_\infty - T_v$ and the area of the bubble exposed to the bulk liquid. For a bubble growing in a liquid pool of $T_\infty = 1123\text{ K}$, since a thermal boundary layer is not formed, all of its curved surface area is exposed to the bulk liquid. Thus, the bulk liquid has a significant influence on bubble growth. It contributes to almost 60% of the total heat transferred to the bubble at the instant of nucleation and 40% at $t = 5\text{ ms}$. The thermal boundary layer heat transfer is significant only during the early stages of bubble growth and its contribution rapidly reduces as the bubble grows as seen in Fig. 4.16c.

4.8.5 Effect of accommodation coefficient

The results discussed in the preceding sections were obtained assuming the accommodation coefficient to be one. A value of one indicates that all the sodium molecules hitting the liquid-vapour interface of the bubble undergo a phase change. However, factors such as the presence of impurities, system pressure and the interface shape may

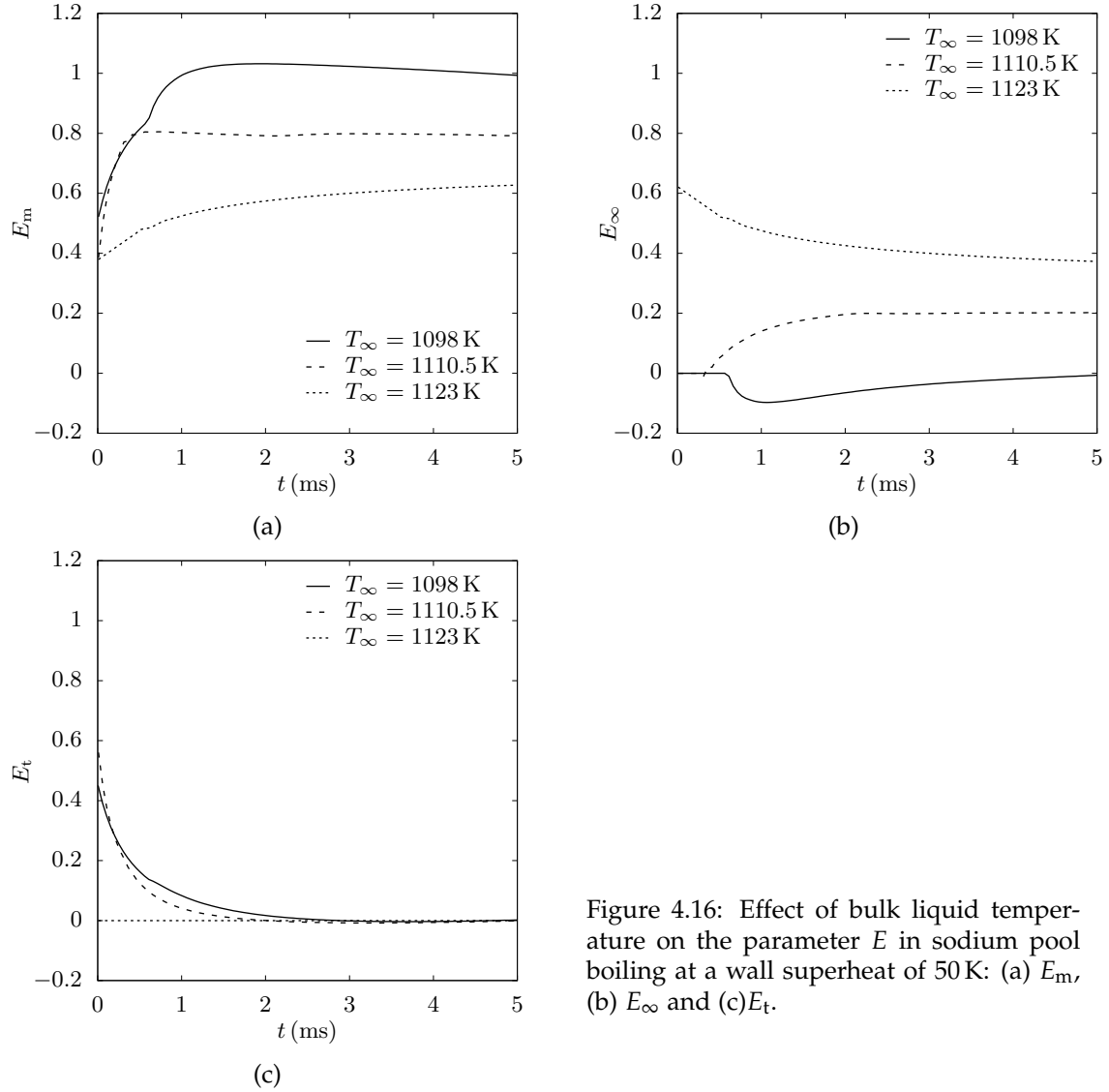


Figure 4.16: Effect of bulk liquid temperature on the parameter E in sodium pool boiling at a wall superheat of 50 K: (a) E_m , (b) E_∞ and (c) E_t .

affect the accommodation coefficient and lower its value [153]. An accurate estimation of the accommodation coefficient will require detailed experiments and molecular dynamic simulations which haven't been performed for sodium as also highlighted in Section 3.5.5. Hence a sensitivity study is conducted to assess its influence on bubble growth in sodium. Four values of f ranging from 0.25–1 are considered for the study.

Figure 4.17 shows the effect of accommodation coefficient on the bubble radius, total heat transfer rate \dot{Q}_b , vapour temperature and rate of heat transferred from the bulk liquid to a bubble in sodium pool boiling at a wall superheat of 50 K. On decreasing the value of the accommodation coefficient from 1 to 0.25, the interface thermal resistance increases according to Eq. (2.17). This results in a lower rate of heat transferred to the bubble and consequently smaller bubble sizes as depicted in Figs. 4.17a and 4.17b. With a decrease in the value of f , the vapour temperature decreases due to a decrease

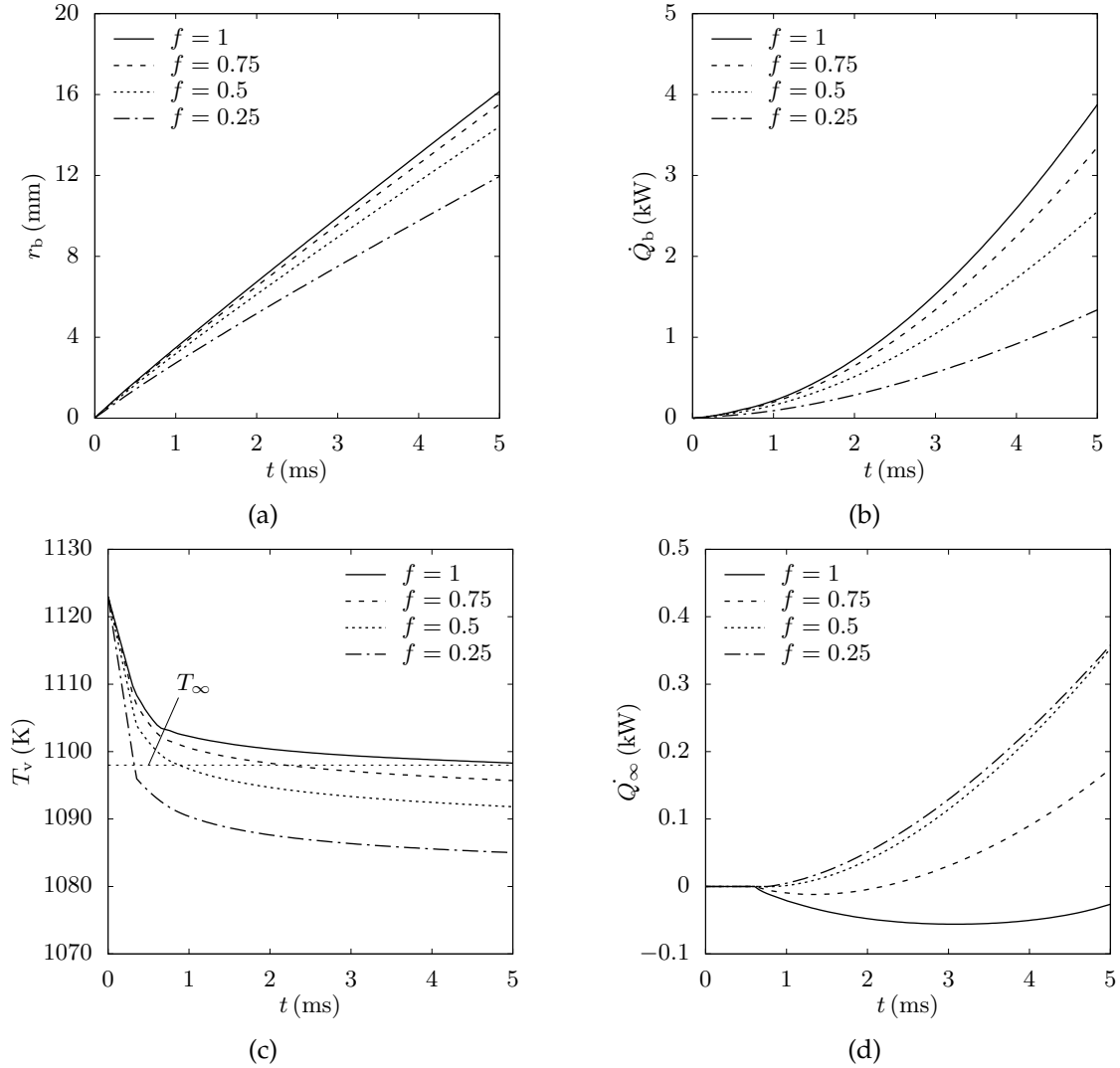


Figure 4.17: Effect of accommodation coefficient on (a) bubble radius, (b) total bubble heat transfer rate, (c) vapour temperature, (d) and bulk liquid heat transfer rate in sodium pool boiling at a wall superheat of 50 K and a bulk liquid temperature of $T_\infty = 1098$ K.

in the bubble growth rate as seen in Fig. 4.17c. The vapour temperature throughout the growth period is higher than the bulk liquid temperature for $f = 1$. Thus, for this case, the bulk liquid heat transfer rate \dot{Q}_∞ is negative as shown in Fig. 4.17d, leading to condensation in the portion of the bubble in contact with the bulk liquid. For $f = 0.75$ and $f = 0.5$, the mechanism of bulk liquid heat transfer changes from condensation to evaporation as the vapour temperature decreases during the bubble growth process. For $f = 0.25$, the bulk liquid heat transfer rate throughout the growth period is found to be positive as the temperature difference $T_\infty - T_v$ is positive. For all cases, \dot{Q}_∞ is initially zero as the bubble is submerged in the thermal boundary layer.

Figure 4.18 shows the effect of accommodation coefficient on the parameter E . The

influence of the macrolayer is found to be significantly lower with values of $E_{ma} < 0.035$ and hence is not shown in the figure. The effect of increasing the accommodation coefficient or decreasing the interface thermal resistance is similar to increasing the wall superheat. Irrespective of the accommodation coefficient, the microlayer contribution E_m increases with time while the contribution of heat transfer from the thermal boundary layer decreases with time as shown in Figs. 4.18a and 4.18b, respectively. On decreasing the accommodation coefficient from 1 to 0.25, the contribution of the microlayer on bubble growth decreases. Consequently, the contribution of the thermal boundary layer heat transfer rate increases with a decrease in f as observed in Fig. 4.18b. The influence of bubble condensation in the bulk liquid decreases with a decrease in f as seen in Fig. 4.18c due to a decrease in the temperature difference $T_v - T_\infty$. For $f \leq 0.5$, the temperature of vapour in the bubble drops below the bulk liquid temperature and the bulk liquid heat transfer mechanism switches from condensation to evaporation as explained above. With a decrease in the value of f beyond 0.5, the value of $T_\infty - T_v$ increases and thus the influence of bulk liquid evaporation on bubble growth increases.

4.8.6 Comparison with the theoretical relationship of Dwyer

In this section, the heat transfer and the bubble growth rate predicted by the model proposed in this chapter is compared to the Dwyer relationships represented by Eqs. (2.52)–(2.54) and reproduced here to highlight the effect of the assumptions made in deriving the theoretical equations.

$$\dot{Q}_m = 2\pi \int_0^{r_b} q_m'' r dr = \frac{2r_b^2}{\sqrt{t}} (\pi k_w c_{p,w} \rho_w)^{1/2} (T_{w,0} - T_v), \quad (4.33)$$

$$\dot{Q}_\infty = q_\infty'' A_\infty = \frac{\sqrt{3}k_1 (T_{w,0} - T_v)}{\sqrt{\pi\alpha_1 t}} (2\pi r_b^2) = \frac{2\sqrt{3}r_b^2}{\sqrt{t}} (\pi k_1 c_{p,l} \rho_l)^{1/2} (T_{w,0} - T_v), \quad (4.34)$$

$$r_b = \frac{8(\Delta T)C^2}{3C_1^4} \left[\left(C_1^2 + \frac{C_1^4 t}{4(\Delta T)^2 C^2} \right)^{3/2} - C_1^3 \right] - \frac{C_1^2 t^{3/2}}{3\Delta T C}. \quad (4.35)$$

A detailed description of the above equations and the assumptions made in deriving them is provided in Section 2.6.2. Since the Dwyer relations were developed for a hemispherical bubble in a superheated liquid pool considering only the heat transfer from the microlayer and the bulk liquid, a contact angle of $\beta = 90^\circ$ and a bulk liquid temperature equal to the wall temperature, i.e. $T_\infty = T_w = 1123 \text{ K}$ are used for the simulation. This bulk liquid temperature implies that a thermal boundary layer is not formed and the bubble grows only due to evaporation of the microlayer and the bulk liquid.

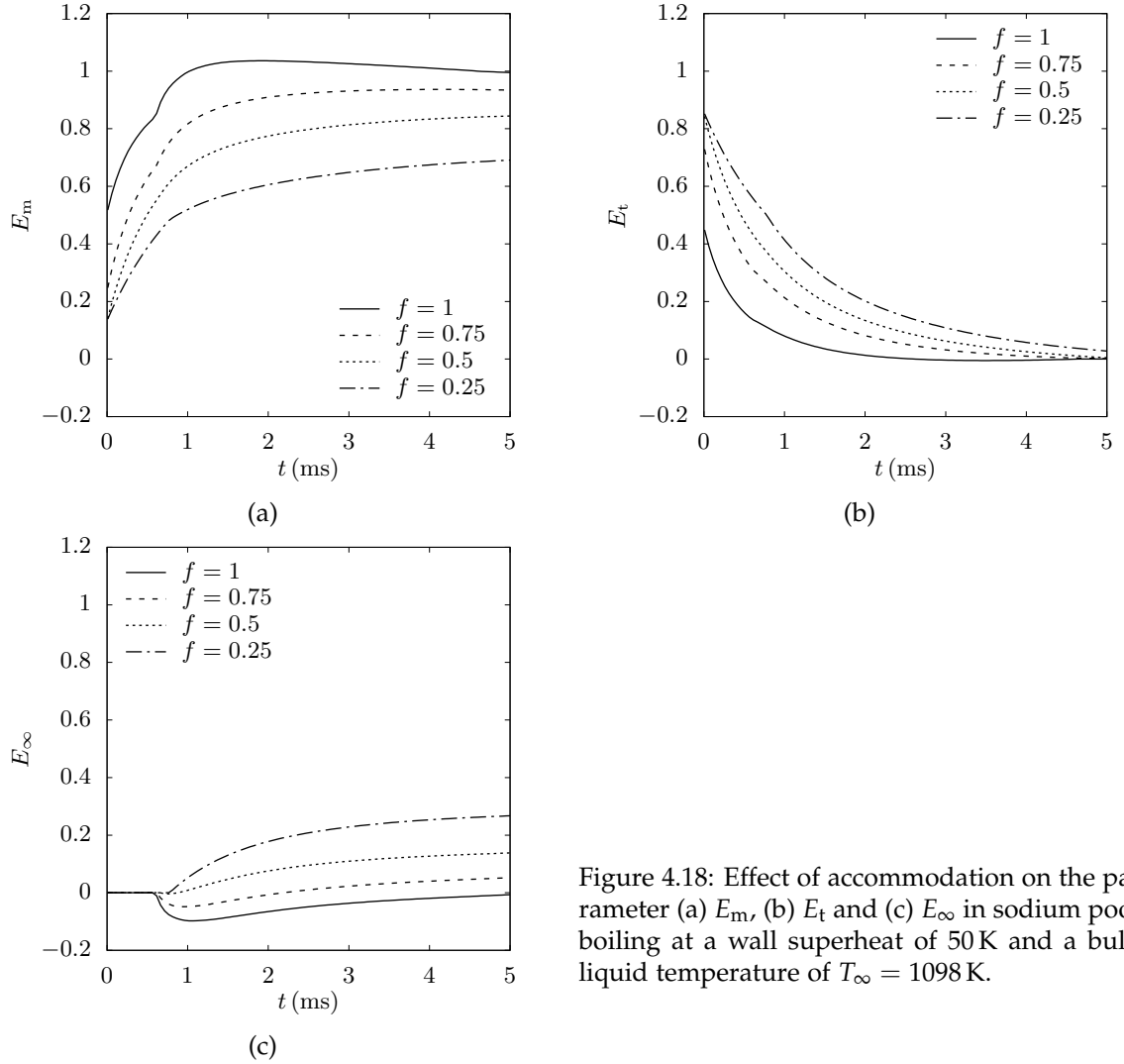


Figure 4.18: Effect of accommodation on the parameter (a) E_m , (b) E_t and (c) E_∞ in sodium pool boiling at a wall superheat of 50 K and a bulk liquid temperature of $T_\infty = 1098$ K.

Figure 4.19 shows the comparison of the bubble radius, heat transfer and contribution of microlayer and bulk liquid heat transfer obtained from the present model with the theoretical relation of Dwyer for a hemispherical sodium bubble growing on a nickel heater at a wall superheat of 50 K and bulk liquid temperature of $T_\infty = 1123$ K. Compared to the radius obtained from the Dwyer model, the predicted bubble radius from the model developed in this work is lower, as shown in Fig. 4.19a. This is due to the lower microlayer and bulk liquid heat transfer obtained from the developed model, as shown in Fig. 4.19b. In the Dwyer model, the resistance to the heat transfer in the microlayer is calculated based on the thermal penetration depth in the solid ($\sqrt{\pi\alpha_w t}$). This resistance was found to be smaller than the total thermal resistance in the microlayer considered in the developed model leading to a prediction of higher microlayer heat transfer. The resistance to heat transfer from the bulk liquid to the bubble in the theoretical relation was computed based on the growth of a thermal boundary layer adjacent

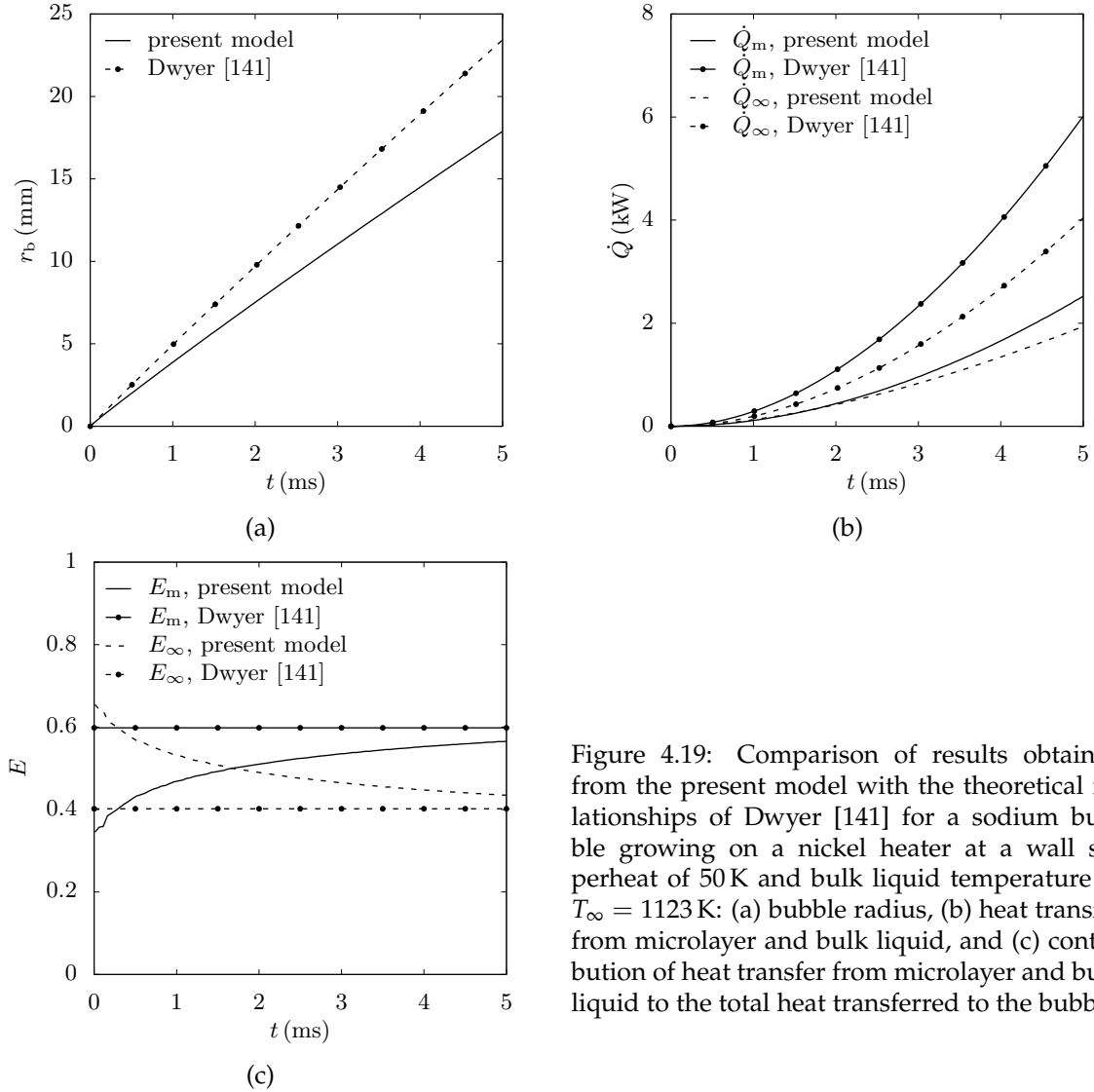


Figure 4.19: Comparison of results obtained from the present model with the theoretical relationships of Dwyer [141] for a sodium bubble growing on a nickel heater at a wall superheat of 50 K and bulk liquid temperature of $T_\infty = 1123$ K: (a) bubble radius, (b) heat transfer from microlayer and bulk liquid, and (c) contribution of heat transfer from microlayer and bulk liquid to the total heat transferred to the bubble.

to a sphere in a uniformly heated liquid and did not account for the interface resistance. This is lower than the resistance considered in the present study. Thus, the bulk liquid heat transfer rate obtained from the theoretical model is larger than that obtained from the model developed in this work.

The contribution of heat transferred from the microlayer and bulk liquid to the bubble as predicted from the present model and the theoretical relation of Dwyer is shown in Fig. 4.19c. The contribution of the microlayer and the bulk liquid heat transfer obtained from the present model varies with time, as explained in Section 4.8.1. In contrast, Dwyer theoretical relationships predict a constant contribution of the heat transfer mechanisms to the total heat transferred to the bubble. The theoretical relationships depend on the initial wall superheat and the thermophysical properties which are constant. The theoretical relationship for the microlayer heat transfer did not account for

the variation in wall temperature with time as the liquid in the microlayer evaporates. Thus, the difference in the magnitudes of the contribution of the heat transfer mechanisms in the theoretical relationships is only due to the thermophysical properties of the wall and the liquid. This is fundamentally different from the model developed in this work where variation in the wall temperature with radial distance below the bubble is considered.

4.9 Accuracy consideration

The assumed temperature distribution in the thermal boundary layer introduces an error in the computed thermal boundary layer heat transfer as presented in Section 4.6. However, for all cases studied in this work, the magnitude of the thermal boundary layer heat transfer is found to be significantly less than the microlayer heat transfer. In addition, in an actual boiling system, as the bubble grows, the contact angle of the bubble will reduce. Thus, the amount of liquid in the macrolayer will increase resulting in a smaller area of the bubble in contact with the liquid in the thermal boundary layer. Hence the error in the thermal boundary layer heat transfer calculation does not have a significant influence on the bubble growth characteristics. Nevertheless, the development of a more accurate thermal boundary layer heat transfer model accounting for the influence of forced convection in the liquid is necessary. This will be pursued as part of future work.

4.10 Summary

A reduced-order heat transfer model to study the growth of a bubble in a sodium pool has been proposed in this chapter. Bubble growth was modelled based on the heat transferred from the microlayer, the macrolayer, the thermal boundary layer and the bulk liquid surrounding the bubble. The model accounted for the variation in vapour temperature as the bubble grows. The cooling of the wall below the bubble due to microlayer and macrolayer evaporation was modelled by solving a transient 2D conduction equation. The developed model was used to study the growth of a sodium bubble in a liquid pool to gain a fundamental understanding of the boiling process. The input parameters to the model included the wall superheat, contact angle, bulk liquid temperature and the accommodation coefficient. These parameters were found to have a significant influence on the growth of a sodium bubble and were studied extensively.

The heat transferred through the microlayer was found to be the dominant mechanism controlling the growth of a 80° contact angle sodium bubble in a liquid pool of temperature 1098 K at a wall superheat of 50 K. As the bubble grows, the amount of

liquid trapped in the microlayer region increases. This leads to a larger contact area, and thus more heat transferred through the microlayer.

A parametric analysis was performed to understand the influence of the wall superheat, contact angle, bulk liquid temperature and the accommodation coefficient on bubble growth in sodium. The influence of the wall superheat was found to be consistent with observed bubble growth characteristics in high Prandtl number fluids. On increasing the wall superheat, the bubbles tended to be larger due to an increase in the overall heat transferred to the bubble. With an increase in wall superheat from 20 K to 80 K, the bubble radius increased by 2.5 times. The bubble growth rate and radius decreased with a decrease in the contact angle. The influence of microlayer heat transfer on bubble growth decreased while the influence of the macrolayer heat transfer increased, with a decrease in the contact angle. Increasing the bulk liquid temperature was found to increase the bubble size due to an increase in the rate of heat transferred from the microlayer and the bulk liquid. The influence of reducing the accommodation coefficient was found to be similar to decreasing the wall superheat. On decreasing the accommodation coefficient, the total rate of heat transferred to the bubble and the bubble radius decreased due to an increase in the interface thermal resistance.

Lastly, the results from the model were compared to the theoretical bubble growth relationships of Dwyer [141]. For the same heater wall material and conditions of the liquid pool, the bubble radius predicted using the developed model was 22% less compared to the theoretical relation. The model developed in this study accounted for the variation in the heater wall temperature and the interface resistance, both of which were neglected in derivation of the theoretical relation by Dwyer, which led to a lower heat transfer prediction and hence smaller bubble sizes.

Development and validation of a mechanistic bubble growth model³

In the previous chapter, a heat transfer model was proposed assuming a bubble to grow with a constant contact angle. However, experimental results on pool boiling reported in literature show that the bubble contact angle and shape changes with time as the bubble grows in a liquid pool. Thus, building upon the heat transfer model developed in the last chapter, a mechanistic model to study the growth of a bubble from nucleation to departure in pool boiling valid for all fluids is proposed in this chapter. The model accounts for the change in shape of a bubble as it grows. The model comprises three sub-models: (a) a heat transfer sub-model proposed in Chapter 4 to compute the bubble growth rate based on the evaporation of the microlayer, the macrolayer, the thermal boundary layer and the bulk liquid surrounding the bubble; (b) a force sub-model to calculate the forces acting on a bubble; and (c) a contact angle and bottleneck sub-model to account for the change in shape of the bubble. Analysis of past experimental data on bubble growth in nucleate pool boiling indicate that the shape of a bubble transitions from a truncated sphere to a balloon-like shape before departure. In the model proposed in this chapter, this balloon-like shape is modelled as a truncated sphere atop a conical bottleneck. The model is verified and validated against high-fidelity CFD simulations and pool boiling experiments of water and methanol reported in literature.

5.1 Introduction

The development of a mechanistic bubble growth model coupling the heat transfer to a bubble with the forces acting on it, is of great interest. The development of such a model was initiated by the pioneering work of Klausner et al. [108]. The authors proposed a model to compute the forces acting on a bubble to determine its departure diameter in

³Material in this chapter has been published as: S. Iyer, A. Kumar, J. Coventry and W. Lipiński, Modelling of bubble growth and detachment in nucleate pool boiling, *International Journal of Thermal Sciences*, vol. 185, p. 108041, 2023.

pool boiling. Subsequently, other authors improved upon this work and proposed more advanced models. Zhao et al. [85] developed a bubble growth model incorporating the effect of evaporation of the microlayer and used an analytical expression to determine the bubble departure diameter. The model was validated against in-house pool boiling experiments and showed good agreement. Das et al. [66] modelled the growth of a bubble based on the evaporation of the microlayer and the macrolayer. Their model incorporated the effect of the variation in wall temperature below the bubble and was validated against the experiments of Zhao et al. [85]. Later, Jiang et al. [60] proposed a dynamic boiling model considering the effect of contact-line evaporation and influence of heat transfer from the thermal boundary layer. In addition, the model accounted for the change in contact angle of a bubble as it grows. The authors showed that the contact angle reduces asymptotically with time and a bubble departs when the radius of the base of the bubble reduces to zero. More recently, Ding et al. [18] proposed a comprehensive mechanistic model coupling the evaporation from the microlayer, the macrolayer and the condensation from the bulk liquid to a model computing the forces acting on a bubble. A dynamic microlayer sub-model was incorporated in the mechanistic model to track the expansion and the depletion of the bubble base as the liquid in the microlayer evaporates. The model was validated against direct numerical simulation and experiments on pool boiling of water.

Though significant effort has been dedicated to developing physics-based mechanistic models, the transition in shape of a bubble has not been accurately modelled. As a bubble grows, the shape of the bubble transitions from a hemisphere to a balloon-like shape before departure [13, 79, 121] as previously reviewed in Section 2.5. Capturing this change in shape of the bubble is critical to understand the dynamics of the bubble growth process. Most of earlier numerical works either assumed the bubble to grow with a constant shape [74, 78, 108, 122] or approximated the balloon-like shape to be a sphere atop a cylindrical bottleneck [18, 124]. Though the formation of a neck has been included in mechanistic models, the balloon-like shape has not been modelled accurately before which is the focus of the present work.

The aim of the present work is to develop a mechanistic model to accurately predict the shape of a bubble and understand the bubble growth dynamics in nucleate pool boiling. A dynamic contact angle and shape sub-model is implemented to account for the change in the contact angle of a bubble as it grows and to track the shape of the bubble in pool boiling. During the departure phase, the shape of the bubble is modelled as a sphere atop a conical neck based on an analysis of experimental data on bubble growth in pool boiling [13, 121]. An energy balance model accounting for the heat transferred to the bubble from different paths is coupled to a force balance model to predict the bubble growth rate and departure radius. Results from the model are compared against pool boiling experimental data and high fidelity CFD simulations to validate and verify the model.

5.2 Bubble shape transition in pool boiling

Experiments on bubble growth in pool boiling have shown that the shape of a bubble changes from a hemisphere to a balloon-like shape prior to departure, as shown in Figs. 2.6 and 2.7 [13, 121]. A schematic of the bubble profile at different stages during the growth of a bubble is shown in Fig. 5.1. The growth process starts with the nucleation of a bubble from a cavity at time $t = t_1$. During this initial stage, the bubble expands rapidly as the pressure inside the bubble p_v is substantially greater than that of the surrounding liquid p_∞ . This expansion of the bubble is countered by the inertia of the surrounding liquid which causes the bubble to spread on the heater surface and assume a hemispherical shape. At the same time, a microlayer is formed below the bubble. The evaporation of this layer, along with the liquid in the thermal boundary layer and surrounding bulk liquid, supply the vapour required for bubble growth. As the bubble continues to grow, at $t = t_2$ the shape of the bubble transitions from a hemisphere to a truncated sphere due to the surface tension force acting on it. During this stage, the bubble radius and the contact radius increases, and the evaporation of the microlayer creates a dry patch below the bubble. At $t = t_3$ the forces acting downward that keep the bubble attached to the wall are balanced by the forces acting upward. Owing to this force balance, the main body of the bubble starts to lift-off from the wall but the evaporation of the microlayer still produces enough vapour to keep the bubble attached to the wall [18]. This leads to the formation of a bottleneck through which the bubble remains attached to the wall, as shown by the red interface in Fig. 5.1. In this work, the bottleneck is assumed to be conical based on experimental observations of the shape of a bubble undergoing departure [13]. Beyond time t_3 the contact radius of the bubble decreases while the dryout radius and the height of the bottleneck increases as the microlayer evaporates. At time $t = t_5$ the microlayer evaporates completely. At this

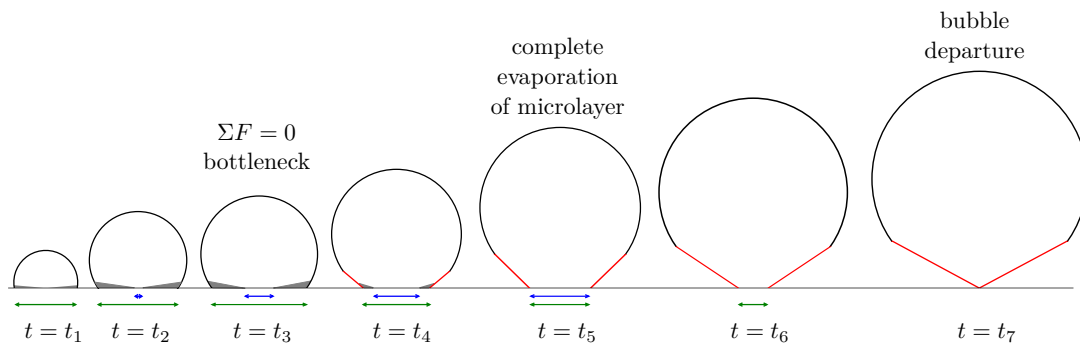


Figure 5.1: Schematic of transition in bubble shape from nucleation to departure. The shaded grey region at the bottom of the bubble represents the microlayer. The red interface represents the bottleneck formed after the forces are balanced. The green and the blue arrows represent the diameter of the contact and dryout region, respectively.

stage, the dryout radius of the bubble becomes equal to the contact radius. Following this, the base diameter of the bubble decreases rapidly as shown by the bubble profile at $t = t_6$, since the microlayer no longer supplies vapour to keep the bubble attached to the wall. Once the contact diameter of the bubble reduces to zero at $t = t_7$, the bubble departs from the wall. Thus, the shape of a bubble undergoes a transition from a hemisphere at nucleation to a balloon-like shape at departure.

5.3 Mechanistic model

A mechanistic model coupling the heat transferred to the bubble with the forces acting on it is developed in this work to study the growth and departure of a bubble in a liquid pool. The following assumptions are made in developing the model:

1. The bubble is axisymmetric.
2. Heat transfer in the microlayer and macrolayer is governed by 1D conduction perpendicular to the wall owing to the small thickness of the fluid layer.
3. Thickness of the thermal boundary layer is constant throughout the growth period.
4. The vapour inside the bubble is saturated.

The mechanistic model comprises of three sub-models: (i) a heat transfer sub-model proposed in Chapter 4 to compute the rate of heat transferred from the microlayer, the macrolayer, the thermal boundary layer and the bulk liquid to the bubble; (ii) a force sub-model to calculate the growth, drag, contact pressure, buoyancy and surface tension forces acting on a bubble as detailed in Section 2.4; and (iii) a contact angle and bottleneck sub-model accounting for the change in shape of the bubble as it grows. In the following subsection, the contact angle and bottleneck sub-model is explained and the associated governing equations are formulated. The heat transfer and force sub-models are not repeated here for brevity.

5.3.1 Contact angle and bottleneck sub-model

Modelling the change in contact angle of a bubble is difficult as it depends on accurately predicting the forces acting on a bubble. Previous experiments have shown that the contact angle of a bubble reduces with time as the bubble grows [101]. A bubble is hemispherical at nucleation with a contact angle of 90° . As it grows, the shape of the bubble changes to a truncated sphere with a lower contact angle. In this work, the instantaneous contact angle of the bubble is derived by integrating the rate of change of the contact angle $d\beta/dt$ using an explicit Euler time integration scheme. Since a universal contact angle relation valid under all conditions is not available, in the present

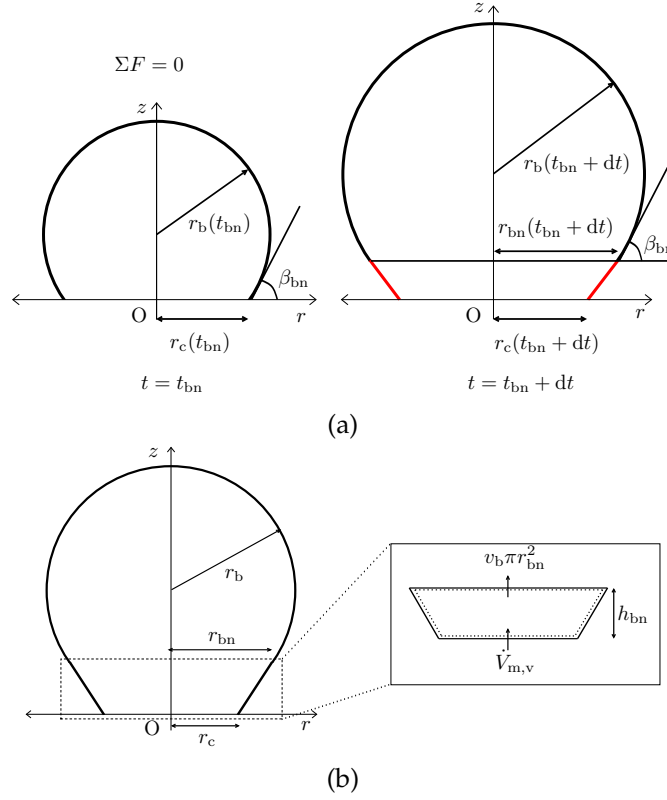


Figure 5.2: Bottleneck in a bubble: (a) schematic of the bubble shape during the bottleneck phase showing the major dimensions used to model the growth of the bottleneck and (b) control volume used to model the growth of the bottleneck.

study the rate at which the contact angle of a bubble varies $d\beta/dt$, is obtained from past studies reported in literature [60].

As the bubble grows, at a certain instant of time, the forces acting upward will be equal to the forces acting downward. This signals the beginning of the bottleneck phase [18]. Figure 5.2 highlights the dimensions used to describe the bottleneck and control volume used to model the growth of the bottleneck. In the developed model, it is assumed that once the bottleneck starts to form, the spherical portion of the bubble continues to grow with a constant contact angle β_{bn} , as shown in Fig. 5.2a, i.e.

$$\beta_{bn} = \beta(t = t_{bn}). \quad (5.1)$$

In the above equation, t_{bn} is the time at which the forces are balanced and the bottleneck starts to form. The radius of the top of the bottleneck referred to as r_{bn} is given by

$$r_{bn} = r_b \sin \beta_{bn}. \quad (5.2)$$

The contact radius of the bubble in the bottleneck phase is obtained by solving a volume

conservation equation based on the method proposed by Ding et al. [18]. For the control volume shown in Fig. 5.2b, the equation for conservation of vapour volume in the bottleneck can be formulated as

$$\frac{dV_{bn}}{dt} = \dot{V}_{m,v} - v_b \pi r_{bn}^2, \quad (5.3)$$

where V_{bn} , $\dot{V}_{m,v}$ and h_{bn} are the volume of the conical bottleneck, volume of liquid evaporated from the microlayer and the bottleneck height, respectively, defined as

$$V_{bn} = \frac{\pi}{3} h_{bn} (r_c^2 + r_c r_{bn} + r_{bn}^2), \quad (5.4)$$

$$\dot{V}_{m,v} = 2\pi \frac{\rho_l}{\rho_v} \int_{r_d}^{r_c} \frac{d\delta_m}{dt} r dr, \quad (5.5)$$

$$h_{bn} = h_{bn}(t - \Delta t) + v_b \Delta t, \quad (5.6)$$

where Δt is the time step size used in the numerical simulation. The height of the bottleneck at the start of the bottleneck phase is zero, i.e. $h_{bn}(t = t_{bn}) = 0$. The total surface area of the bubble used to compute the bubble growth rate using Eq. (4.20) and the volume of the bubble in the bottleneck phase are calculated as follows:

$$A_b = 2\pi r_b^2 (1 + \cos \beta_{bn}) + \pi (r_{bn} + r_c) \sqrt{(r_{bn} - r_c)^2 + h_{bn}^2}, \quad (5.7)$$

$$V_b = \frac{\pi}{3} r_b^3 (2 + 3 \cos \beta_{bn} - \cos^3 \beta_{bn}) + V_{bn}. \quad (5.8)$$

The complete computational procedure is shown in Fig. 5.3. Based on the input conditions and data, the model calculates the heat transferred to the bubble from different mechanisms, bubble radius, dryout radius, contact radius and the forces acting on the bubble. The computation of the bottleneck parameters such as the volume of the bottleneck V_{bn} , volume of vapour evaporated from the microlayer $\dot{V}_{m,v}$, bottleneck height h_{bn} , radius of the top of the bottleneck r_{bn} and the contact radius in the bottleneck phase r_c , starts once the forces are balanced. The model checks for bubble departure in the bottleneck phase. The bubble departs when the contact radius reduces to zero as detailed in Section 5.2.

5.3.2 Boundary and initial conditions

As the microlayer and the macrolayer evaporates, the wall below the bubble gets cooled. This transient variation in the wall temperature is computed by solving the transient heat conduction equation in the wall represented by Eq. (4.22) subject to the boundary conditions reported in Section 4.4 in Chapter 4.

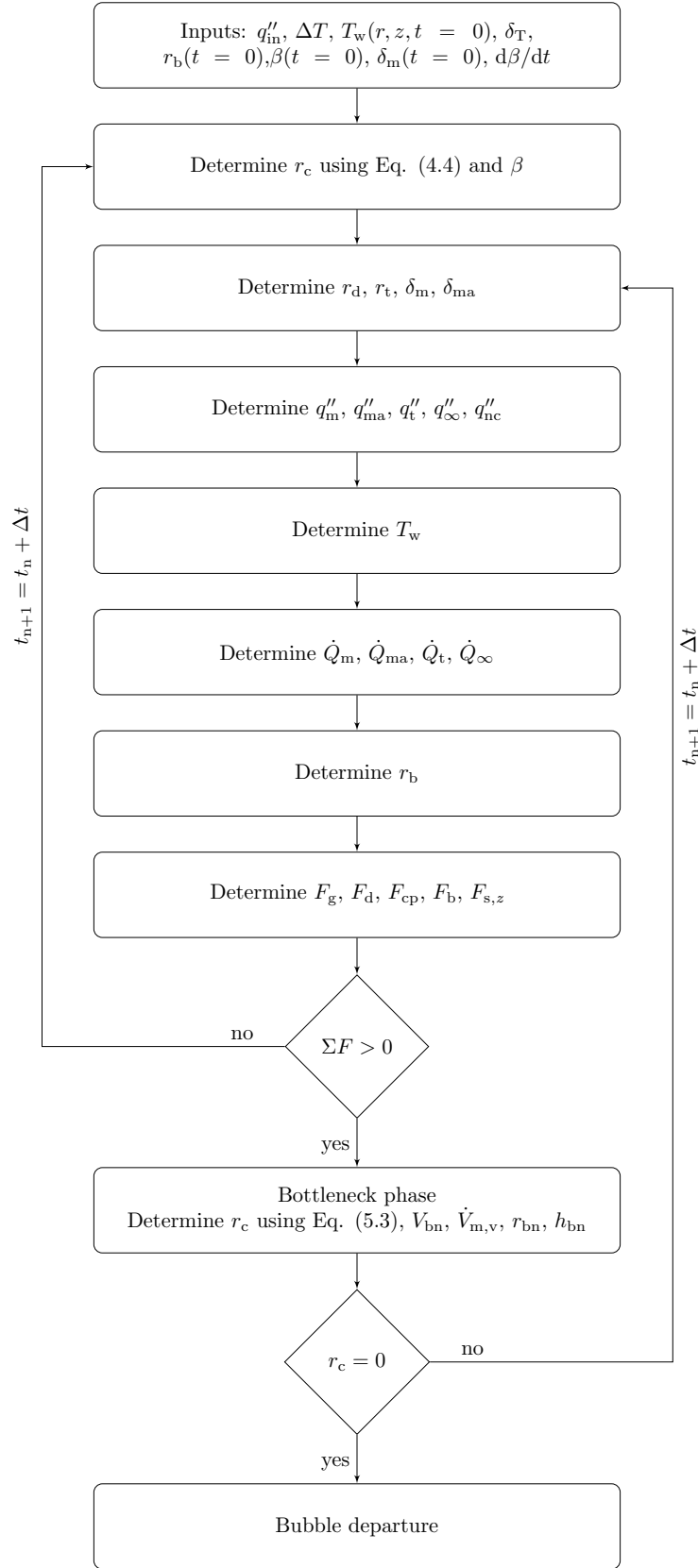


Figure 5.3: Flow chart of the model.

The numerical simulations are initialised from a hemispherical bubble of radius $50\text{ }\mu\text{m}$ and by assuming the wall to be at a uniform temperature equal to the temperature required to initiate the growth of a bubble given by

$$T_w = T_{\text{sat}} + \Delta T, \quad (5.9)$$

where ΔT is the wall superheat. The value of the wall superheat will depend on the structure and the size of the cavities on the heater wall [39, 60, 160, 161]. Modelling the thermo-fluid dynamic phenomena in the cavities on a rough wall will require detailed CFD simulations which are beyond the scope of the present work. Hence, the value of the wall superheat obtained from pool boiling experiments detailed in Section 5.4 is used as an input to the developed model. In addition to the wall superheat, a relation for the initial microlayer profile, i.e. the variation in the thickness of the microlayer immediately after bubble nucleation is needed to initiate the numerical simulation. In this work, the equations describing the initial microlayer profile are adopted from the experimental studies by Utaka et al. [94] and Cooper et al. [83, 85] for water and other organic liquids, respectively.

$$\delta_0 = \begin{cases} 4.46 \times 10^{-3} r & \text{water} \\ \frac{0.64 \nu_l \rho_v h_{lv}}{2k_l \Delta T} r & \text{organic liquids} \end{cases} \quad (5.10)$$

5.4 Experimental and computational data sets for validation and verification

The results from the model are quantitatively and qualitatively validated and verified with the pool boiling experiments of Duan et al. [13], Cole et al. [79] and the CFD simulation results of Sato et al. [15]. Duan et al. [13] performed experiments to study bubble growth in pool boiling of water on a transparent indium-tin-oxide (ITO) heater mounted on a sapphire plate of 50 mm diameter and 0.25 mm thickness. The liquid pool was maintained at a temperature of 372.5 K and a pressure of 1 atm. An input heat flux of $q''_{\text{in}} = 28.7\text{ kW m}^{-2}$ was supplied to the heater and a bubble was found to nucleate at a wall superheat of $\Delta T = 9\text{ K}$. This wall superheat corresponds to a nucleation site of radius $3\text{ }\mu\text{m}$ [13]. The growth of the bubble was observed using a high speed video (HSV) camera and the temperature distribution on the heater surface was measured using an infrared camera positioned below the heater. Images captured using the HSV camera showed that the bubble shape was a truncated sphere till $t = 6.9\text{ ms}$ and then transitioned to a balloon-like shape before departing from the wall. The departure diameter and departure time of the bubble was found to be approximately 4 mm and 15 ms, respectively.

Sato et al. [15] proposed a depletable microlayer model and coupled it to their in-

house CFD solver to simulate bubble growth in pool boiling. The microlayer model was used to compute the thickness of the fluid film underneath the bubble and account for the effect of microlayer evaporation on the growth of a bubble. The liquid–vapour interface of the bubble was explicitly delineated using a colour function approach to observe the bubble shape in the liquid pool. The results from the simulation were compared against several experimental datasets including the experiment of Duan et al. [13] and showed good agreement.

The predictions from the model are also compared against data obtained from a methanol pool boiling experiment by Cole et al. [79]. The authors performed experiments to study bubble growth in methanol on a zirconium test section of diameter 25.4 mm and thickness 0.25 mm. The test section was electrically heated to provide an input heat flux of 29.12 kW m^{-2} . The methanol liquid pool was maintained at a sub-atmospheric pressure of 0.71 atm using a vacuum pump. The growth of a bubble on the test section was observed using a camera capable of operating at speeds of 16000 frames per second. Based on the data recorded from the camera, the authors reported the variation in the equivalent radius of the bubble with time. The departure radius and departure time were found to be 1.9 mm and 14.5 ms, respectively.

5.5 Results and discussion

The two dimensional transient conduction equation in the wall is numerically solved in time and space by discretising it using a finite volume method and employing a first order implicit time integration scheme in the commercial CFD code ANSYS Fluent 17.1 [156]. Past experiments and numerical computations have shown that the contact angle of a bubble decreases asymptotically with time [60, 101]. Accurately modelling this decrease in contact angle as the bubble grows is difficult. Hence, in the absence of a universal contact angle model, the contact angle of the bubble in this work for water and methanol is assumed to decrease according to the relation $d\beta/dt = -6^\circ/t$ where t is time in ms based on computational results of Jiang et al. [60]. A parametric analysis is also performed to study the effect of different rate of change of contact angle relations on bubble growth and departure in methanol. The thermophysical properties of the wall and the fluid used in this study are provided in Tables 5.1 and 5.2. To ensure that the numerical simulation results are independent of the mesh resolution, the experiment of Duan et al. [13] is simulated for different cell and time step sizes. The cell size in the axial direction is $\Delta z = 50 \mu\text{m}$ for all simulations. Figure 5.4 shows the wall temperatures at $t = 2.5 \text{ ms}$ obtained from the simulations. As seen from the figure, the results from the simulation are insensitive for time step size less than $\Delta t = 1 \mu\text{s}$, and cell size less than $\Delta r = 50 \mu\text{m}$ in the radial direction. Thus, a time step of $\Delta t = 1 \mu\text{s}$, and a cell size of $\Delta r = 50 \mu\text{m}$ and $\Delta z = 50 \mu\text{m}$ is selected for this study.

Table 5.1: Thermophysical properties of water and sapphire used to simulate the water pool boiling experiment of Duan et al. [13].

Material	Parameter	Symbol	Value	Unit	Ref.
Water	Saturation temperature	T_{sat}	373	K	[162]
	Thermal conductivity	k_l	0.6791	$\text{W m}^{-1} \text{K}^{-1}$	[162]
	Liquid density	ρ_l	958.35	kg m^{-3}	[162]
	Vapour density	ρ_v	0.597	kg m^{-3}	[162]
	Dynamic viscosity	μ_l	2.79×10^{-4}	Pa s	[162]
	Latent heat	h_{lv}	2256.5×10^3	J kg^{-1}	[162]
	Surface tension	σ	0.059	N m^{-1}	[162]
	Accommodation coefficient	f	0.03	–	[158]
Sapphire	Density	ρ_w	3980	kg m^{-3}	[15]
	Specific heat	$c_{p,w}$	750	$\text{J kg}^{-1} \text{K}^{-1}$	[15]
	Thermal conductivity	k_w	35	$\text{W m}^{-1} \text{K}^{-1}$	[15]

Table 5.2: Thermophysical properties of methanol and zirconium used to simulate the pool boiling experiment of Cole et al. [79].

Material	Parameter	Symbol	Value	Unit	Ref.
Methanol	Saturation temperature	T_{sat}	328.97	K	[163]
	Thermal conductivity	k_l	0.1943	$\text{W m}^{-1} \text{K}^{-1}$	[163]
	Liquid density	ρ_l	756.98	kg m^{-3}	[163]
	Vapour density	ρ_v	0.875	kg m^{-3}	[163]
	Dynamic viscosity	μ_l	3.62×10^{-4}	Pa s	[163]
	Latent heat	h_{lv}	1115.5×10^3	J kg^{-1}	[163]
	Surface tension	σ	0.0196	N m^{-1}	[163]
	Accommodation coefficient	f	0.06	–	[164]
Zirconium	Density	ρ_w	6490	kg m^{-3}	[159]
	Specific heat	$c_{p,w}$	270	$\text{J kg}^{-1} \text{K}^{-1}$	[159]
	Thermal conductivity	k_w	22	$\text{W m}^{-1} \text{K}^{-1}$	[159]

5.5.1 Model verification and validation

The bubble radius, wall temperature, bubble shape and microlayer profile obtained from the present model are compared with data recorded from experiments and CFD simulations to validate and verify the model. The results from this verification and validation study are presented in this section.

Bubble radius. Figure 5.5 shows the comparison of the bubble and contact radius obtained from the present model with the data recorded from the water boiling experiment of Duan et al. [13] and the CFD simulation of Sato et al. [15]. Since the shape of the bubble changes during its growth, the radius of the bubble is represented by an equivalent radius which is calculated assuming the bubble to be spherical as follows:

$$r_{b,\text{eq}} = \left(\frac{3}{4\pi} V_b \right)^{1/3}, \quad (5.11)$$

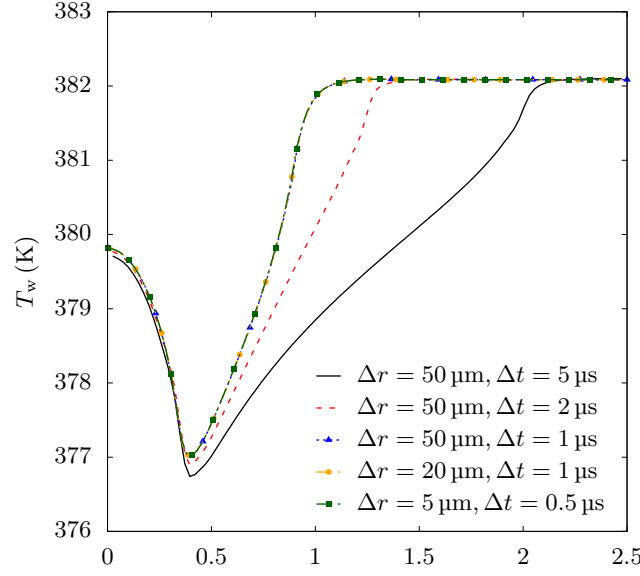


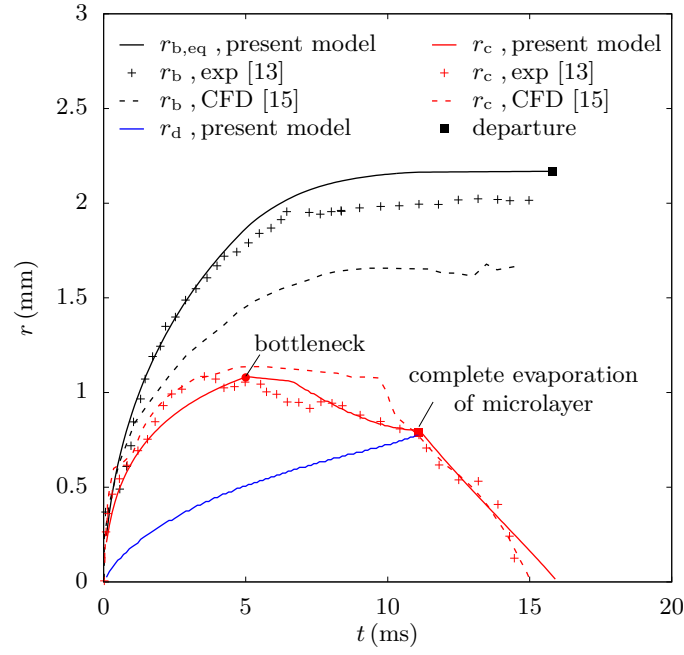
Figure 5.4: Wall temperatures obtained for different cell sizes and time step sizes at time $t = 2.5$ ms.

where V_b is the volume of the bubble.

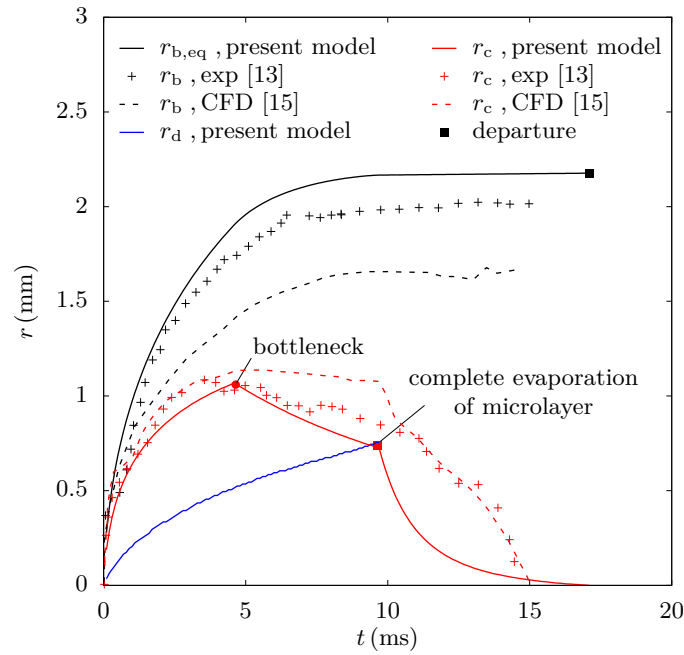
As mentioned previously, prior efforts to model the shape of the bubble before departure, assumed, for simplicity, that a bubble grows as a truncated sphere with an elongating cylindrical bottleneck [18, 124]. However, in the model developed in this work, the bottleneck is assumed to be conical. Thus, to highlight the importance of accurately modelling the shape of the bottleneck, the bubble and contact radius obtained assuming the formation of a cylindrical bottleneck is also studied. For a bubble growing with a cylindrical bottleneck, the radius of the top of the bottleneck will be equal to the contact radius, i.e. $r_{bn} = r_c$ and the rate at which the contact radius varies during the bottleneck phase is calculated using Eq. (5.3) where the volume of the bottleneck is

$$V_{bn} = \pi r_c^2 h_{bn}. \quad (5.12)$$

Figure 5.5a shows the temporal variation in the equivalent bubble radius, contact radius and the dryout radius assuming the formation of a conical bottleneck. A comparison of the bubble and contact radius with the experimental and CFD data is also presented. The bubble growth rate is initially high and reduces as the bubble grows as seen from the trend of the equivalent radius. A similar trend is observed in the experimental data and the CFD simulation results. The contact radius r_c of the bubble increases monotonically with time till $t = 5$ ms. At 5 ms, the forces acting on the bubble are balanced and a bottleneck starts to grow. In the bottleneck phase, the contact radius of the bubble reduces as the amount of liquid in the microlayer decreases. At 11.1 ms, the dryout radius of the bubble, which increases monotonically with time, becomes equal



(a)



(b)

Figure 5.5: Comparison of equivalent bubble radius $r_{b,eq}$ and contact radius r_c obtained from the present model with data recorded from the experiments of Duan et al. [13] and CFD simulation of Sato et al. [15] assuming the formation of a (a) conical bottleneck and (b) cylindrical bottleneck. The variation in the dryout radius r_d with time is also shown.

to the contact radius. This indicates that the microlayer has completely evaporated. Immediately after this, the contact radius decreases rapidly, as the microlayer no longer provides vapour to keep the bubble attached to the wall.

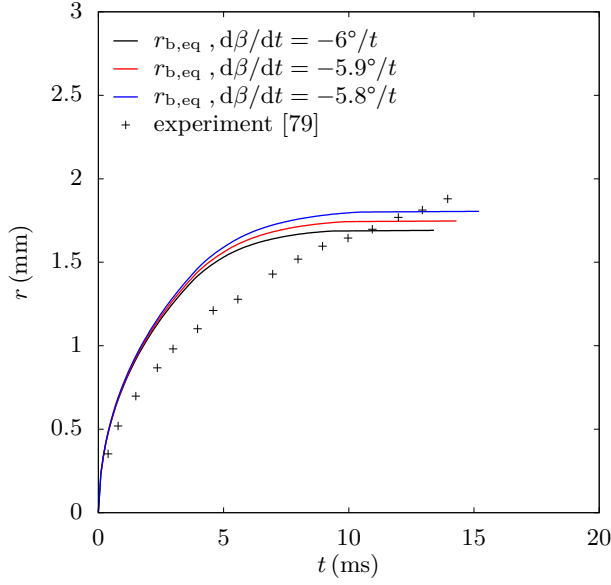


Figure 5.6: Comparison of bubble radius obtained from the present model with the radius recorded from the methanol pool boiling experiment of Cole et al. [79].

The present model, assuming the formation of a conical bottleneck accurately predicts the contact radius r_c and slightly over-predicts the departure time as shown in Fig. 5.5a. The departure radius is found to be 7.6% larger compared to the data obtained from the experiment. This discrepancy can be attributed to the assumptions made in the model as discussed below. In the simulation performed in this work, a bubble is assumed to be spherical with an asymptotic decrease in the contact angle. In addition, the heat transfer from the wall to the bubble is simplified using 1D conduction equations and the effect of fluid motion around the bubble is ignored. In reality, local motion of the fluid as the bubble grows will affect the shape of the bubble and the amount of heat transferred to it. Such effects are difficult to accurately capture using a reduced-order model. Given the assumptions made in this work, the bubble growth characteristics predicted by the model are found to be reasonable.

A comparison of the bubble and contact radius with experimental and CFD data assuming the formation of a cylindrical bottleneck is shown in Fig. 5.5b. The bubble radius is over-predicted for the case of a cylindrical bottleneck as well due to the reasons outlined above. A clear difference is observed between the two models with regards to the change in the contact radius with time. Whereas a good match with experimental and CFD data is observed for the conical bottleneck model after the point of complete evaporation of the microlayer, the same is not true for the cylindrical bottleneck model. Instead, the contact radius initially reduces rapidly for this model, and then begins to asymptote to zero when the bubble departs due to the different geometry of the bottleneck. This has the additional result that the time to bubble departure is over-predicted, at 17.2 ms which is significantly later than is the case in the experiment and compared to the case with a conical bottleneck.

Figure 5.6 shows the comparison of the equivalent bubble radius obtained from the present model with the experimental result of Cole et al. [79]. for three different rate of change of contact angle relations. As the magnitude of the $d\beta/dt$ decreases, the contact angle of the bubble increases. This leads to a larger bubble contact radius according to Eq. (4.4) and more heat transferred to the bubble from the microlayer. Consequently, the bubble size and the bubble departure radius increases. A larger bubble contact radius also implies that more liquid is trapped in the microlayer. Thus, the amount of time needed for the microlayer to completely evaporate and the contact radius to decrease to zero increases with a decrease in the magnitude of the $d\beta/dt$. The prediction of the departure time for $d\beta/dt = -5.9/t^\circ \text{ms}^{-1}$ is found to be reasonable while the departure radius is under-predicted by 8.4%. The bubble growth rate predicted from the model also differs compared to the growth rate observed in the experiment. In the analysis of the experimental data, Cole et al. [79] assumed the bubble to be ellipsoidal and the equivalent radius of the bubble was calculated from the area of the base and the height of the ellipsoid. This is different from the current model where the bubble is assumed to be spherical. In addition, the bubble growth rate depends on accurately modelling the contact angle of the bubble. The rate at which the contact angle varies is assumed in this work. However, in reality, the local pressure distribution on the liquid–vapour interface as the bubble grows will affect the forces acting on the bubble and the contact angle. Such affects are difficult to model and neglected in this work.

Wall temperature. The growth of a bubble in a liquid pool is partly fuelled by the evaporation of the microlayer and the macrolayer. As the liquid in the microlayer and the macrolayer evaporates, the wall below the bubble is cooled. This leads to a temporal and spatial variation in the wall temperature. A comparison of the wall temperature predicted by the present model with the temperature recorded from the experiment of Duan et al. [13] and the CFD simulation of Sato et al. [15] is presented in this section.

Figure 5.7 shows the comparison of the wall temperature obtained from the model with the experimental and CFD data at four different times during the growth of a bubble in pool boiling of water. The results from the model show that at all times, the temperature drops from the nucleation site ($r = 0$) to a minimum value due to evaporation of the microlayer and then increases to the initial wall temperature. This qualitative behaviour in the variation of the wall temperature is also seen in the experiment and CFD simulations results. The discrepancy in the values of the wall temperatures obtained from the present model compared to the experiment data is due to simplifications made in the model. As the microlayer and the macrolayer evaporate, fresh liquid from the pool will be pulled in towards the nucleation site. This liquid motion will induce forced convection heat transfer which will affect the temperature of the wall underneath the bubble [15]. This affect is neglected in the current model and in the CFD simulations due to difficulty in accurately modelling the flow in the microlayer and macrolayer regions.

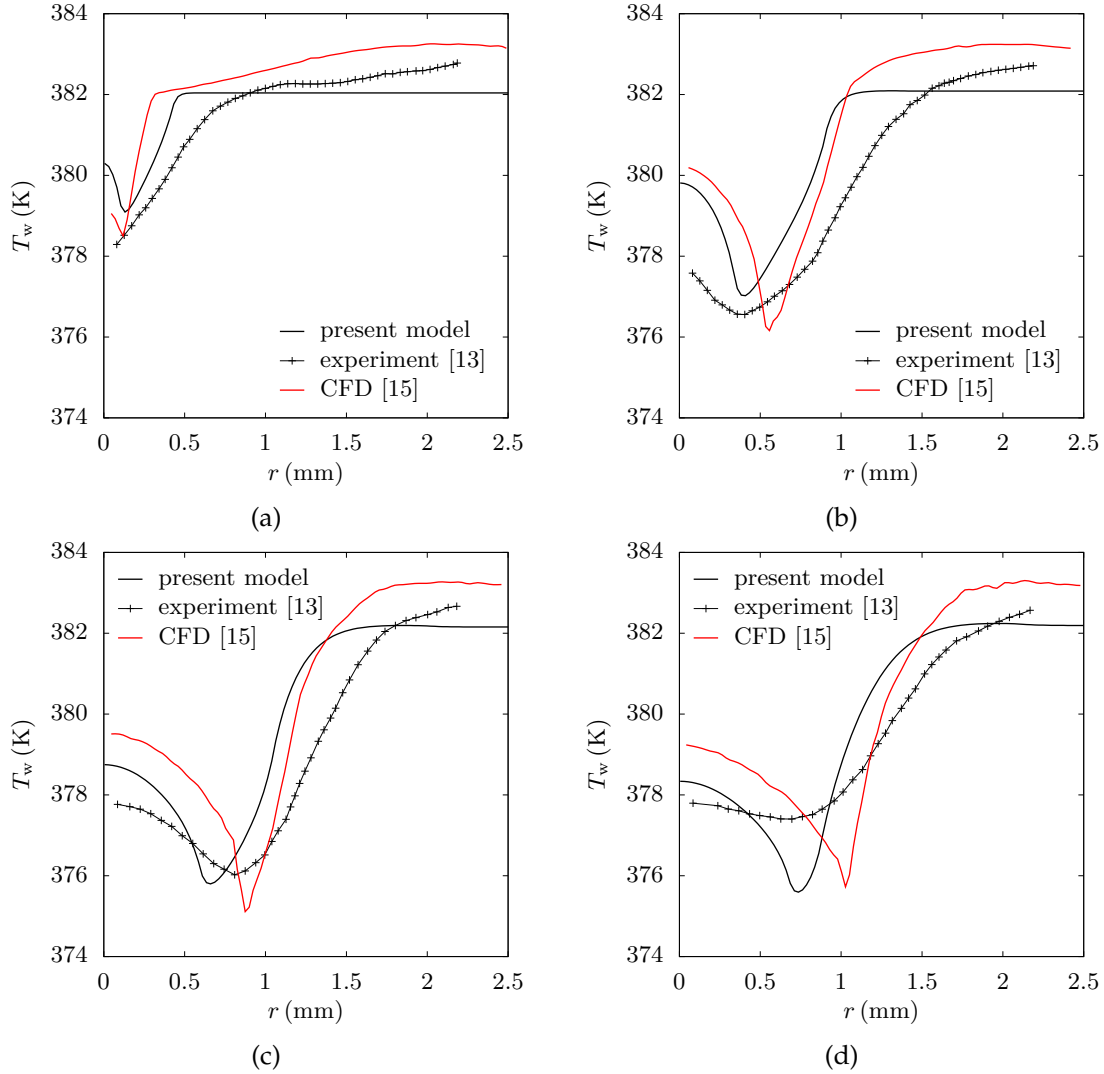


Figure 5.7: Comparison of wall temperatures obtained from the present model with experiments of Duan et al. [13] and CFD simulation of Sato et al. [15] at time (a) $t = 0.4$ ms, (b) $t = 2.5$ ms, (c) $t = 6.7$ ms and (d) $t = 8.8$ ms.

Bubble shape. Images of a bubble growing in a liquid pool have shown that the shape of the bubble changes from a truncated sphere to a balloon-like shape prior to departure [13]. However, due to the difficulty in accurately modelling this transition in shape, as mentioned previously, the bubble profile has been idealised as a sphere atop a cylindrical neck in previous works [18, 124]. In the present work, the assumptions around the geometric description of this balloon-like shape have been improved by incorporating the formation of a conical bottleneck, and the benefit of this improvement is further highlighted by qualitative results in this section.

Figure 5.8 presents a comparison of the bubble shape predicted by the developed model with experimental results of Duan et al. [13] and CFD simulation results of Sato

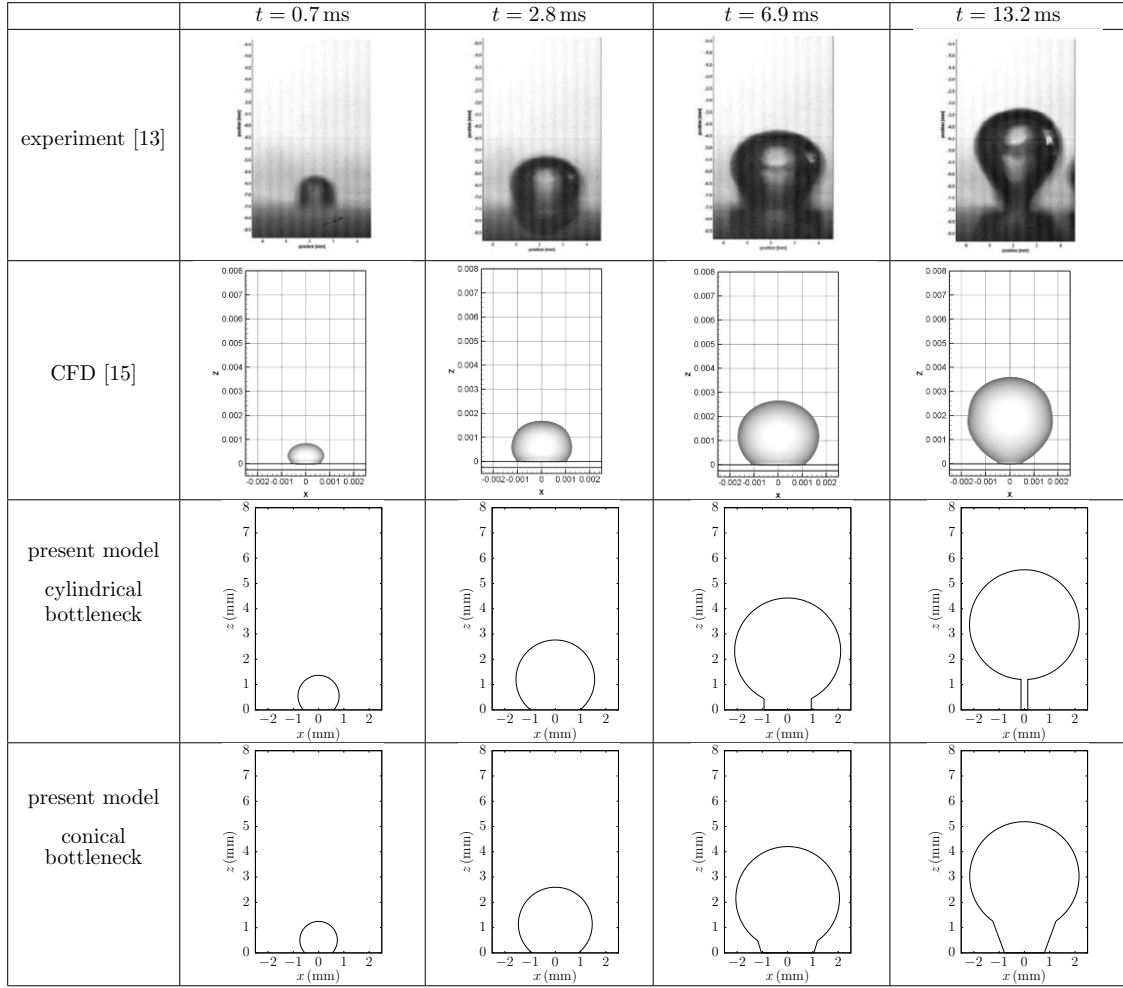


Figure 5.8: Comparison of bubble shape obtained from the present model assuming the formation of a conical and cylindrical bottleneck with experimental observations of Duan et al. [13] and CFD simulation results of Sato et al. [15].

et al. [15]. In the experiment, the bubble shape was recorded using a HSV camera at four points in time. During the initial growth period, i.e. at $t = 0.7$ ms and $t = 2.8$ ms, the bubble shape is a truncated sphere, as seen from the experiment and CFD simulation results. In the later stages of bubble growth, at $t = 6.9$ ms and just prior to departure at $t = 13.2$ ms, the bubble has a balloon-like shape as shown in the first two rows of the figure. The third and the fourth row show the bubble shape predicted by the model developed in this work assuming the formation of a cylindrical and conical bottleneck, respectively. From the figure, it is clearly seen that the bubble profile in the last column more closely resembles those obtained from the experimental results and CFD simulation studies. Though the present model over-predicts the bubble radius a little as explained before, the transition in bubble shape is qualitatively well predicted by the model. The figure also highlights the improvement of the present model over previously

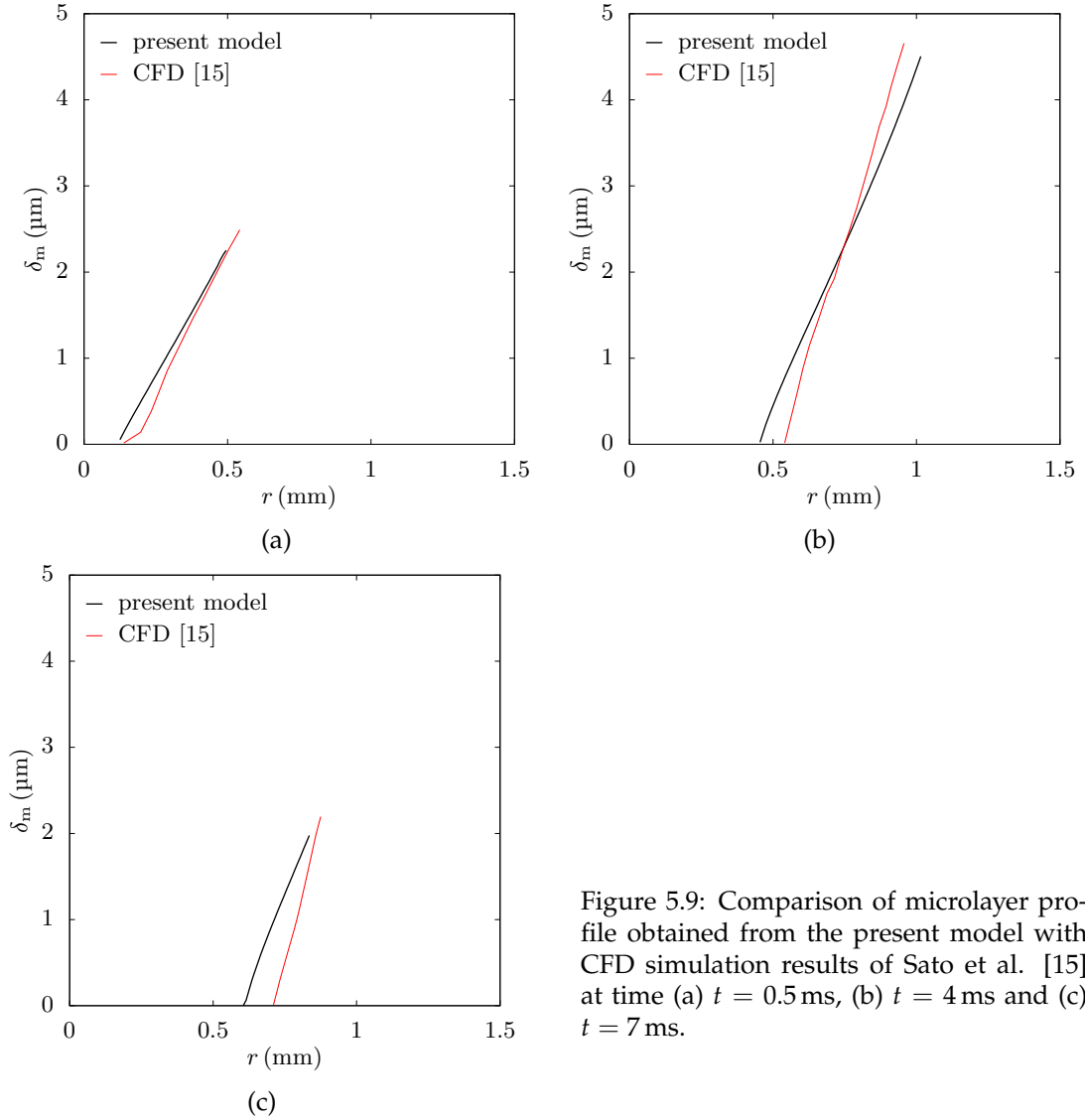


Figure 5.9: Comparison of microlayer profile obtained from the present model with CFD simulation results of Sato et al. [15] at time (a) $t = 0.5$ ms, (b) $t = 4$ ms and (c) $t = 7$ ms.

proposed models where the bubble shape was simplified as a spherical bubble growing on top of a cylindrical bottleneck.

Microlayer profile. The microlayer profile of the bubble changes with time and radial distance as the liquid below the bubble evaporates. Figure 5.9 shows a comparison of the microlayer profile obtained from the present model at three points in time during the growth of a bubble in water with the results of Sato et al. [15]. The microlayer profiles predicted by the model are in good agreement with the CFD simulation results. During the initial period of bubble growth prior to the formation of the bottleneck, the amount of liquid trapped in the microlayer increases as the bubble grows. Thus, the radial extent and the thickness of the microlayer increases with time as seen in Figs. 5.9a and 5.9b. A bottleneck starts to form at 5 ms as reported above. In the bottleneck phase, the contact radius of the bubble reduces as the amount of liquid in the microlayer

reduces. This leads to a decrease in the microlayer thickness as shown in Fig. 5.9c. The microlayer profile at different times obtained from the model are almost parallel which is consistent with the observations made from the CFD simulation results.

5.5.2 Heat transfer and forces acting on a bubble

A bubble grows because of heat transferred from the microlayer, the macrolayer, the thermal boundary layer and the bulk liquid surrounding the bubble. The contribution of each of these heat transfer mechanisms on the growth of a bubble in pool boiling of water for the experimental conditions of Duan et al. [13], along with a discussion on the forces acting on a bubble, is provided in this section.

Figure 5.10 shows the temporal variation in the rate of heat transferred from different mechanisms in pool boiling of water. During the initial growth phase up to 5 ms, the contact radius of the bubble increases with time as seen in Fig. 5.5a. Thus, the area occupied by the microlayer $A = \pi (r_c^2 - r_d^2)$ increases, which leads to an increase in the heat transferred from the microlayer. The bottleneck starts to form at 5 ms. In the bottleneck phase, the microlayer depletes and hence the contribution of the microlayer decreases till 11.1 ms when the microlayer has completely evaporated. The rate of heat transferred from the macrolayer is significantly less compared to the microlayer for a majority of the bubble growth period. The heat transferred from the macrolayer increases with time for the initial period of 5 ms. In the bottleneck phase, as the shape of the bubble changes, the area of the macrolayer below the bubble decreases and this leads to a decrease in the macrolayer heat transfer. The macrolayer is the dominant mechanism of heat transfer once the microlayer has fully evaporated. The rate of heat transferred from the thermal boundary layer \dot{Q}_t and the bulk liquid heat transfer \dot{Q}_∞ have a negligible influence on the bubble growth process. The thermal boundary layer heat transfer contributes to bubble growth only during the period immediately after nucleation when the bubble is completely submerged in the superheated thermal boundary layer. Bubble growth in water for a majority of the growth period is heat transfer controlled where the temperature of the vapour in the bubble is equal to the saturation temperature. Since the temperature of the bulk liquid in the experiment of Duan et al. [13] is approximately equal to the saturation temperature and the vapour temperature in the bubble, i.e. $T_\infty \approx T_{\text{sat}} = T_v$, \dot{Q}_∞ is negligible throughout the growth period.

Figure 5.11 shows the magnitude of the forces acting on the bubble in pool boiling of water at the start of the bottleneck phase and at departure. At the instant when the forces are balanced and the bottleneck starts to form, the buoyancy and the surface tension force have the largest magnitude, as seen in Fig. 5.11a. The magnitude of the contact pressure force is found to be small which is consistent with the observations of Thorncroft et al. [74]. The growth and drag force are relatively small as they are

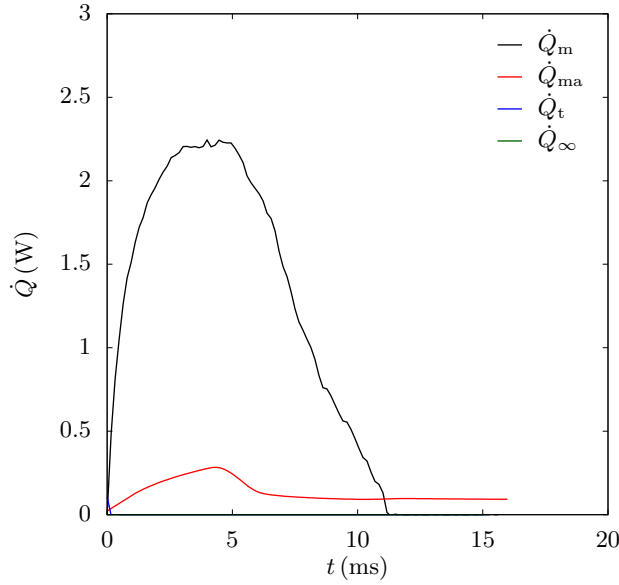


Figure 5.10: Temporal variation in the rate of heat transferred to a bubble from the microlayer \dot{Q}_m , the macrolayer \dot{Q}_{ma} , the thermal boundary layer \dot{Q}_t and the bulk liquid surrounding the bubble \dot{Q}_∞ in pool boiling of water.

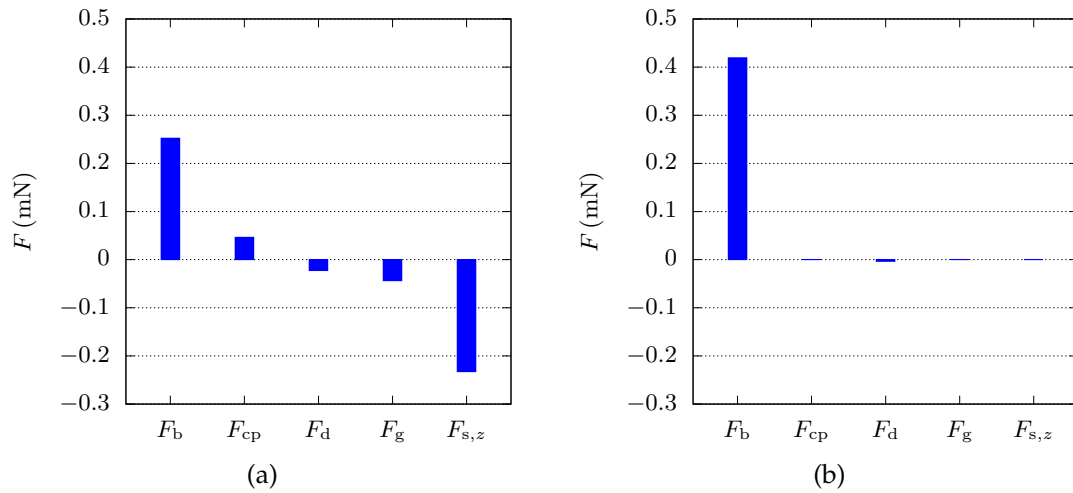


Figure 5.11: Forces acting on a bubble in pool boiling of water (a) at the start of the bottleneck phase and (b) at departure.

proportional to the bubble growth rate, which is typically small in high Prandtl number liquids like water. At departure, the buoyancy force is the dominant force component owing to the large size of the bubble, as shown in Fig. 5.11b. The contact pressure, growth and the surface tension force are zero as they depend on the contact radius, which is zero at departure.

5.6 Summary

A mechanistic model to predict the growth dynamics and the shape of a bubble in nucleate pool boiling has been proposed in this chapter. The model couples a heat transfer,

force and bottleneck sub-model to simulate the entire growth cycle of a bubble from nucleation to departure. The model accounts for the temporal variation in the microlayer thickness as the liquid below the bubble evaporates. A transient 2D conduction equation was solved to compute the variation in wall temperature. The change in contact angle of the bubble as it grows, and the formation of a conical bottleneck prior to bubble departure, are considered to accurately model the transition in shape of the bubble in pool boiling.

The developed model was validated and verified against experimental data and CFD simulation of nucleate pool boiling of water and methanol. Furthermore, the size of the contact radius and time to departure of the bubble was predicted with significantly better accuracy using the proposed conical bottleneck model than with a cylindrical bottleneck model, such as has been used in previous work. The prediction of the bubble departure time was found to be reasonable, while the departure radius was over-predicted by 7.6% in water and under-predicted by 8.4% in methanol. This discrepancy in the predicted bubble radius is due to the assumptions made in the model, namely axisymmetric bubble growth and 1D conduction heat transfer in the microlayer and the macrolayer. It was also found that the the model accurately predicted the temporal variation in the contact radius further confirming the validity of the proposed bottleneck model in this work. In addition, good matches between the wall temperature and bubble shape obtained from the model and experimental data were demonstrated.

The model was also used to investigate the influence of different heat transfer mechanisms and forces on the growth of a bubble in water. Results from the model showed that the evaporation of the microlayer was the dominant heat transfer mechanism during the initial period of bubble growth. After complete evaporation of the microlayer, the heat transferred from the macrolayer had the largest influence on the growth rate. An analysis of the forces acting on the bubble revealed that the buoyancy force balances the surface tension force at the start of the bottleneck phase, while at departure, buoyancy was the dominant force component.

Mechanistic modelling of bubble growth in sodium pool boiling⁴

In the previous chapter, a mechanistic model to simulate the growth of a bubble from nucleation to departure was proposed, validated with experimental data and verified with CFD data from literature. In this chapter, the model is extended to study the heat transfer and growth characteristics of a sodium bubble from nucleation to departure. The heat transfer from different mechanisms to the bubble is analysed and quantified. In addition, the effect of wall superheat, rate of change of contact angle, bulk liquid temperature and accommodation coefficient on the bubble growth rate and departure diameter in sodium pool boiling are investigated.

6.1 Introduction

Mechanistic models like the one proposed in Chapter 5 can provide valuable insights into the bubble growth and departure processes in boiling systems, which can guide the safe and efficient design of sodium boilers. Such systems in CSP plants have the potential to provide near-isothermal heat for thermochemical processes like plastic pyrolysis and gasification of carbonaceous feedstocks [23, 30, 48, 165–168]. Previous attempts to study bubble growth in sodium used several simplifying assumptions to quantify the total heat transferred to a bubble, and used empirical correlations to estimate the departure diameter of a bubble, validated only for water [36, 58]. These studies did not account for the temporal variation in the shape of a bubble. Thus, the aim of the present work is to bridge this gap in knowledge by extending the mechanistic model developed in the previous chapter to understand the bubble growth dynamics in sodium pool boiling. An energy balance model to compute the heat transferred to a bubble from different mechanisms is coupled to a force balance model to predict the growth rate and

⁴Material in this chapter has been published as: S. Iyer, A. Kumar, J. Coventry and W. Lipiński, Mechanistic modelling of bubble growth in sodium pool boiling, *Applied Mathematical Modelling*, vol. 116, pp. 1–24, 2023.

departure radius. The model accounts for the variation in the temperature of the vapour in a sodium bubble as it grows using Eq. (4.21) introduced in Chapter 4. A dynamic contact angle model is implemented to track the shape of the bubble as it grows. The bottleneck model introduced in Section 5.3.1 accounts for the transition in bubble shape and the shrinkage of the bubble base prior to departure. The mechanistic model is used to study the growth and departure dynamics of a bubble in sodium pool boiling. The effects of wall superheat, rate of change of contact angle, bulk liquid temperature and accommodation coefficient on the bubble growth dynamics is presented.

6.2 Problem statement

The validated model developed in Chapter 5 is extended to investigate the heat transfer and growth characteristics of a sodium bubble growing on a nickel plate of thickness 1 mm and radius 12 cm. The results from the numerical simulation are discussed in next section. The thermophysical properties of nickel and sodium used in the simulation are obtained from Refs. [59, 150, 159]. An input heat flux of $q''_{\text{in}} = 500 \text{ kW m}^{-2}$ is prescribed for all the simulations, which is approximately equal to the heat flux to achieve stable boiling [58]. The liquid pool is maintained at a pressure of $p_{\infty} = 0.5 \text{ atm}$ which corresponds to a saturation temperature of $T_{\text{sat}} = 1073 \text{ K}$. These input conditions are similar to those used in Chapter 4. The parametric study presented in Chapter 4 was limited to a minimum bulk liquid temperature of 1098 K, since the contact angle was assumed to be constant. In this work, since the contact angle changes, the study has been extended to model bubble growth in a lower temperature liquid pool of $T_{\infty} = T_{\text{sat}} = 1073 \text{ K}$. Since no experimental data on the rate at which the contact angle reduces in sodium boiling has been reported in literature, a value of $d\beta/dt = -6^{\circ}/t$ is assumed based on past modelling results of pool boiling of water [60]. This value may be different for sodium owing to the vastly different thermophysical properties of the liquid metal compared to water. Hence a parametric study is performed to study its influence on the bubble growth process and reported in Section 6.3.3. In addition, the effect of wall superheat, bulk liquid temperature and accommodation coefficient are also investigated and reported in this section. A summary of all simulation parameters used in the analyses is provided in Table 6.1. The parametric study is conducted by varying one parameter while other parameters are held constant at their baseline value.

The parameter E defined in Section 4.8 is used to quantify the contribution of the microlayer, the macrolayer, the thermal boundary layer and the bulk liquid heat transfer to the total heat transferred to a bubble.

Parameter	Values
q''_{in}	500 kW m⁻²
p_{sat}	0.5 atm
T_{sat}	1073 K
ΔT	[20 K, 50 K , 80 K]
$d\beta/dt$	$[-6^\circ/t, -5^\circ/t, -4^\circ/t, -3^\circ \text{ ms}^{-1}]$
T_∞	[1073 K, $(T_{\text{sat}} + T_{w,0})/2$, 1123 K]
f	[0.25, 0.5, 0.75, 1]

Table 6.1: Simulation parameters. The values in bold are for the baseline simulation case.

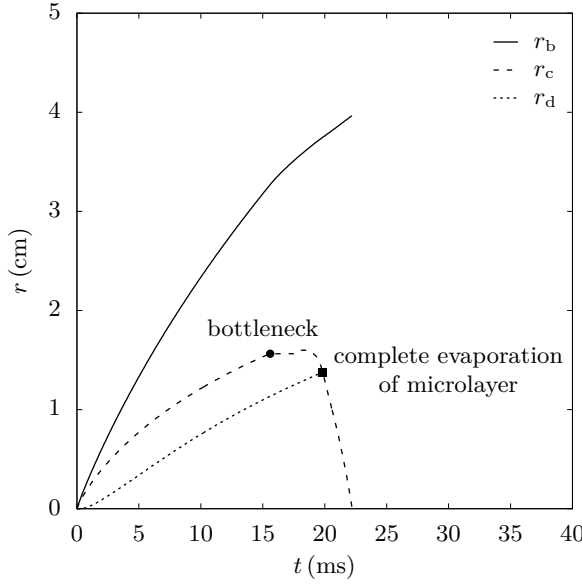


Figure 6.1: Time histories of the bubble radius r_b , contact radius r_c and dryout radius r_d in sodium pool boiling.

6.3 Results and discussion

6.3.1 Sodium bubble growth characteristics

The bubble growth characteristics in sodium pool boiling for a superheat of 50 K, bulk liquid temperature of $(T_{\text{sat}} + T_{w,0})/2 = 1098$ K and $d\beta/dt = -6^\circ/t$ are presented in this section.

Figure 6.1 shows the time histories of the bubble, contact and the dryout radius in sodium pool boiling. The radius of the bubble increase monotonically with time from nucleation to departure. A bubble departs when the contact radius of the bubble reduces to zero. At departure, the bubble radius is 3.97 cm. This is significantly larger than departure sizes typically found in conventional high Prandtl number liquids like water and refrigerants, where departure radius is of the order of a few millimetres [13, 19, 20]. High growth rates and large departure sizes are characteristic of liquid metal boiling which is correctly captured by the model developed in this work. From the numerical simulations, it is observed that a bottleneck starts to form at 15.6 ms when the forces acting on the bubble are balanced. Thereafter, the growth rate of the bubble

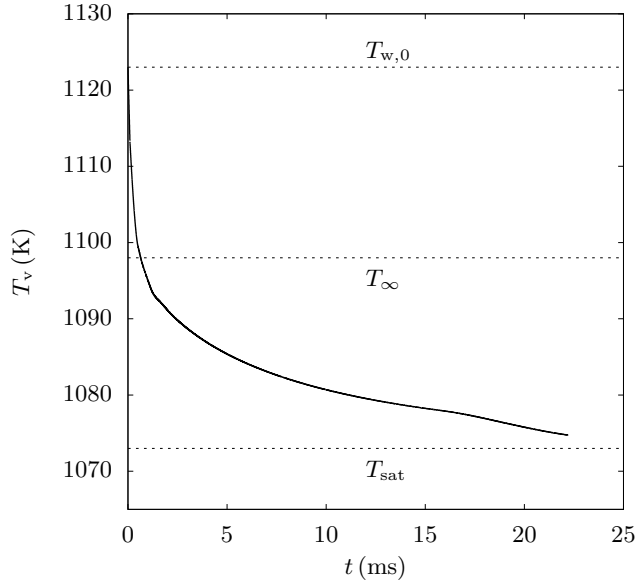


Figure 6.2: Variation of vapour temperature in the bubble in sodium pool boiling.

reduces slightly as the amount of liquid in the microlayer starts depleting. At 20.3 ms, the dryout radius of the bubble which increases monotonically with time becomes equal to the contact radius. This indicates that the microlayer has completely evaporated. Immediately after this, the contact radius decreases rapidly, as the microlayer no longer provides vapour to keep the bubble attached to the wall and the bubble departs at 22.3 ms.

Figure 6.2 shows the transient variation in the temperature of the vapour in the bubble. At $t = 0$, the vapour temperature is approximately equal to the wall temperature required for nucleation, i.e. $T_v \approx T_w = 1123 \text{ K}$ while the vapour pressure is the saturation pressure corresponding to the vapour temperature, i.e. $p_v = p_{\text{sat}}(T_v)$. As the bubble grows, and transitions from the inertia controlled to the heat transfer controlled growth stage, the vapour pressure in the bubble reduces. This leads to a decrease in the vapour temperature. The vapour temperature at departure is approximately equal to the saturation temperature, which indicates that the bubble is approaching the heat transfer controlled growth stage.

Figure 6.3 shows the rate of heat transferred from the microlayer \dot{Q}_m , the macrolayer \dot{Q}_{ma} , the thermal boundary layer \dot{Q}_t and the bulk liquid \dot{Q}_∞ to a sodium bubble. The influence of microlayer heat transfer on bubble growth increases with time until the start of the bottleneck phase at 15.6 ms. During the bottleneck phase, as the dryout radius approaches the contact radius, the amount of liquid in the microlayer reduces. This leads to a drop in the microlayer heat transfer. At 20.3 ms, the microlayer has completely evaporated and $\dot{Q}_m = 0$. A similar trend is observed for the macrolayer heat transfer except for the period just before departure. The trend of the macrolayer heat transfer depends on the area of the wall exposed to the macrolayer $A = \pi (r_t^2 - r_c^2)$. Just

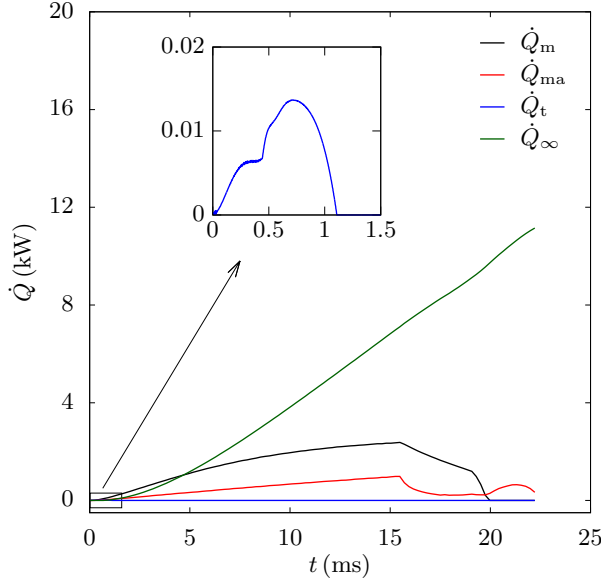


Figure 6.3: Rate of heat transferred from the microlayer \dot{Q}_m , macrolayer \dot{Q}_{ma} , thermal boundary layer \dot{Q}_t and the bulk liquid \dot{Q}_∞ to a bubble in sodium pool boiling.

prior to departure, once the microlayer has completely evaporated, the contact radius r_c drops rapidly. This leads to an increase in the macrolayer area and hence a small increase in the macrolayer heat transfer rate. The thermal boundary layer heat transfer contributes to bubble growth only during the period immediately after nucleation when the bubble is small and exposed to the high temperature liquid in the thermal boundary layer. Beyond 1.1 ms, \dot{Q}_t is zero as all the liquid in the thermal boundary layer is trapped underneath the bubble in the macrolayer. The bulk liquid heat transfer rate increases monotonically as its magnitude depends on the area of the bubble exposed to the bulk liquid, A_∞ and the temperature difference, $T_\infty - T_v$ both of which increases with time.

The temporal variation of the forces acting on a sodium bubble in a liquid pool at a superheat of 50 K is shown in Fig. 6.4. Among the forces acting on a bubble, the buoyancy, growth and drag forces are dominant. The growth force depends on the growth rate and acceleration. It initially keeps the bubble attached to the wall. However, as the bubble grows and the growth rate reduces, at 15.6 ms, the growth force changes direction and aids in bubble departure. The drag force also depends on the growth rate. The magnitude of the drag force increases till the bottleneck starts to form and then decreases as the growth rate decreases. The buoyancy force increases monotonically with time as the bubble volume increases. It is significant as bubbles in sodium tend to be large. The contact pressure and the surface tension force are found to have a negligible influence on bubble departure.

The temporal variation in the shape of a sodium bubble at intervals of $t^* = t/t_{\text{dep}} = 0.1$ is shown in Fig. 6.5. During the initial growth phase from nucleation to the start of bottleneck formation, the bubble grows as a truncated sphere as seen from the bubble profile for times $t^* < 0.8$. At $t^* = 0.8$, a small bottleneck is observed. The height of the

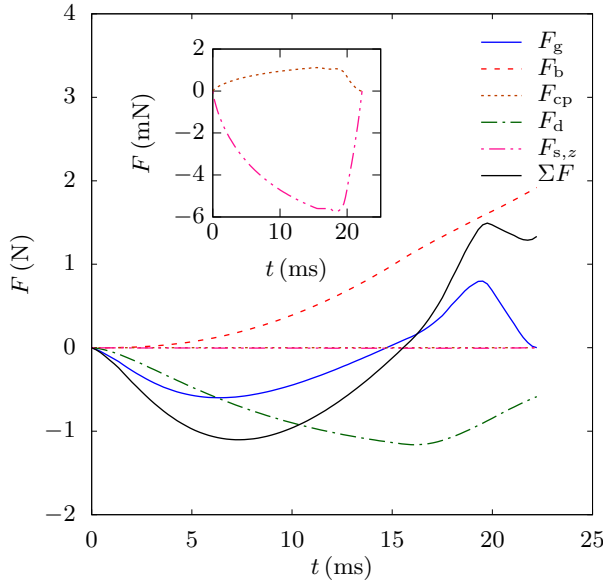


Figure 6.4: Forces acting on a sodium bubble.

bottleneck increases with time till the bubble departs at $t^* = 1$. It is worth noting that in sodium, for a wall superheat of $\Delta T = 50$ K and $d\beta/dt = -6^\circ/t$, once the bottleneck starts to form, the contact radius drops rapidly to zero and the bubble departs. Hence, the bottleneck height computed using Eq. (5.6) compared to the height of the bubble at departure is small, and the bubble appears spherical at departure in sodium. This is contrary to observations made in bubble growth in high Prandtl number liquids like water, where the contact radius drops gradually in the bottleneck phase [15]. Thus, the bottleneck height at departure is large in water and the bubble has a balloon-like shape.

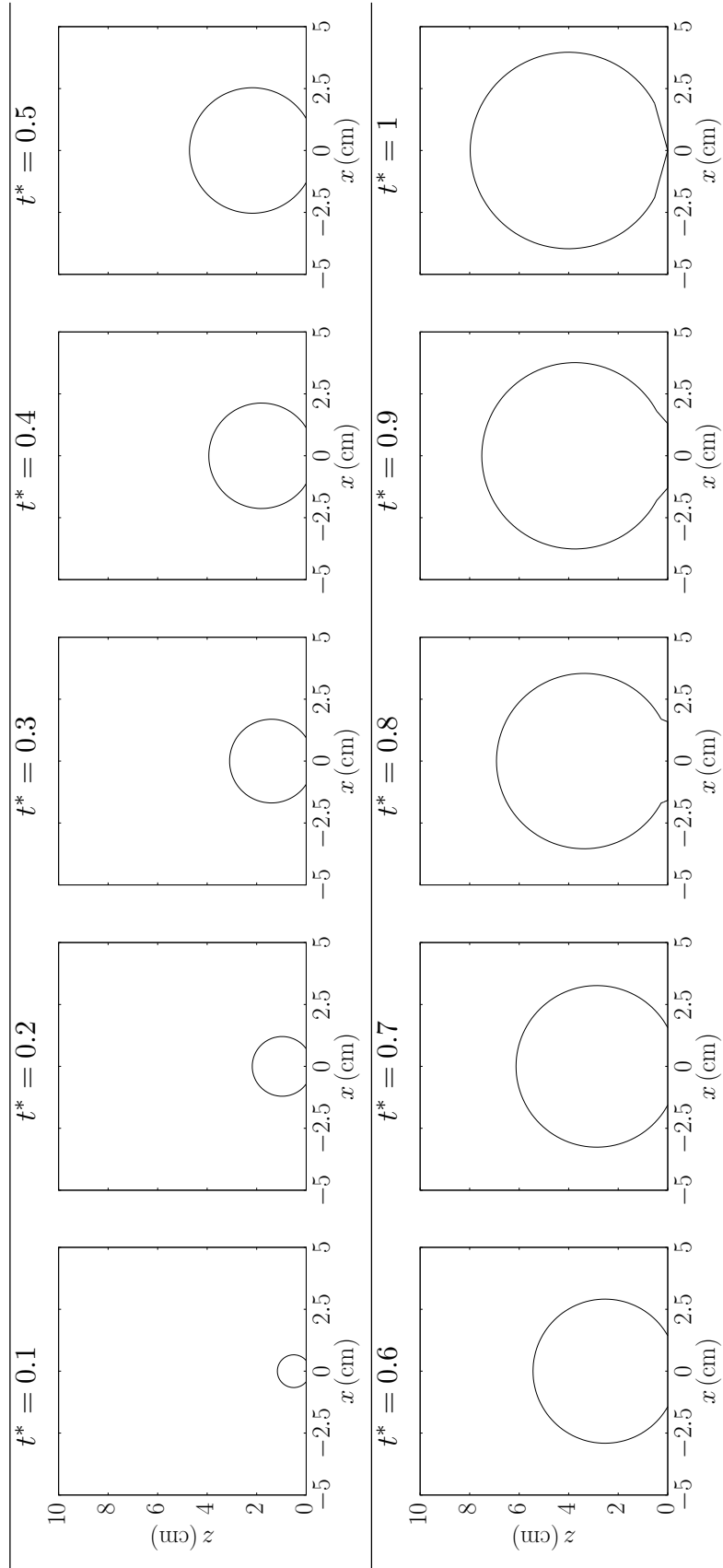
6.3.2 Effect of wall superheat

Sodium boiling systems require a substantial superheat to begin the bubble growth process compared to high Prandtl number fluids such as water [40]. The boiling superheat of sodium is influenced by several factors such as gas entrainment levels, oxide levels, surface conditions, heating surface material, and heat flux [36]. This section discusses the influence of the wall superheat on the bubble dynamics.

Figure 6.6 shows the effect of wall superheat on the bubble radius and the contact radius in sodium pool boiling assuming $d\beta/dt = -6^\circ/t$. With an increase in wall superheat, the bubble growth rate and the departure radius increases while the departure

ΔT (K)	t_{bn} (ms)	t_{dep} (ms)	r_{dep} (cm)
20	11.03	45.16	2.22
50	15.60	22.30	3.97
80	18.13	18.39	5.10

Table 6.2: Bottleneck time, departure time and departure radius in sodium pool boiling at different wall superheats.

Figure 6.5: Temporal variation in the shape of a sodium bubble in pool boiling where $t^* = t/t_{\text{dep}}$.

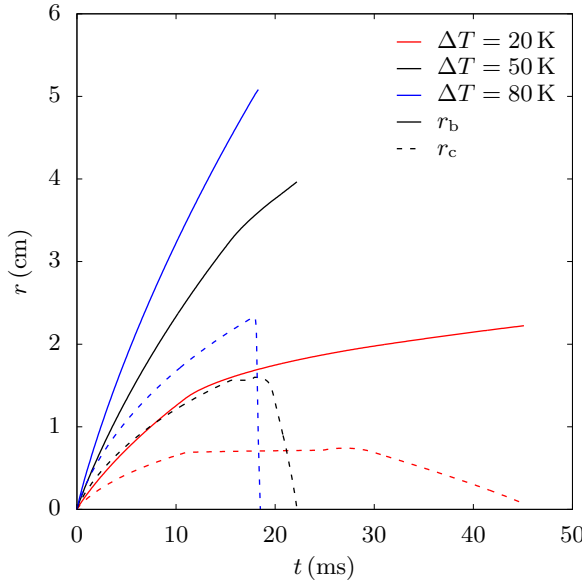


Figure 6.6: Effect of wall superheat on the bubble radius r_b and contact radius r_c .

time decreases. As the wall superheat increases, the wall temperature increases. This leads to more heat transferred from the microlayer and the macrolayer which are in contact with the wall, and consequently higher growth rates. The increase in wall temperature with superheat also results in a decrease in the amount of time required for the microlayer to completely evaporate in the bottleneck phase and the contact radius to drop to zero. This can be seen from the plot of contact radius with time. At a superheat of 80 K, the microlayer evaporates instantaneously after the bottleneck is formed as seen from the near vertical drop in the contact radius. Thus, the departure time is approximately equal to the time at which the bottleneck starts to form, i.e. $t_{bn} \approx t_{dep}$ at very high superheats. In contrast, for a wall superheat of 20 K, a substantial amount of time is required for the contact radius to decrease to zero which leads to a large departure time. Table 6.2 lists the time at which the bottleneck starts to form, the departure time and the departure radius for different wall superheats.

Figure 6.7 shows the effect of the wall superheat on the rate of heat transferred to the bubble from the microlayer, the macrolayer and the bulk liquid, and the contribution of each mechanism to the bubble growth process assuming $d\beta/dt = -6^\circ/t$. The thermal boundary layer heat transfer rate \dot{Q}_t is negligible and has an influence only during the period immediately after nucleation. Thereafter its value is zero and hence not shown. The rate of heat transferred from the microlayer, the macrolayer and the bulk liquid increases with an increase in the wall superheat as seen in Figs. 6.7a–6.7c. Generally, the larger the wall superheat, the larger is the wall temperature and hence more heat is transferred from the microlayer to the bubble as seen in Fig. 6.7a. Similarly, the bulk liquid temperature also increases with wall superheat. This leads to an increase in the rate of heat transferred from the bulk liquid to the bubble with wall superheat

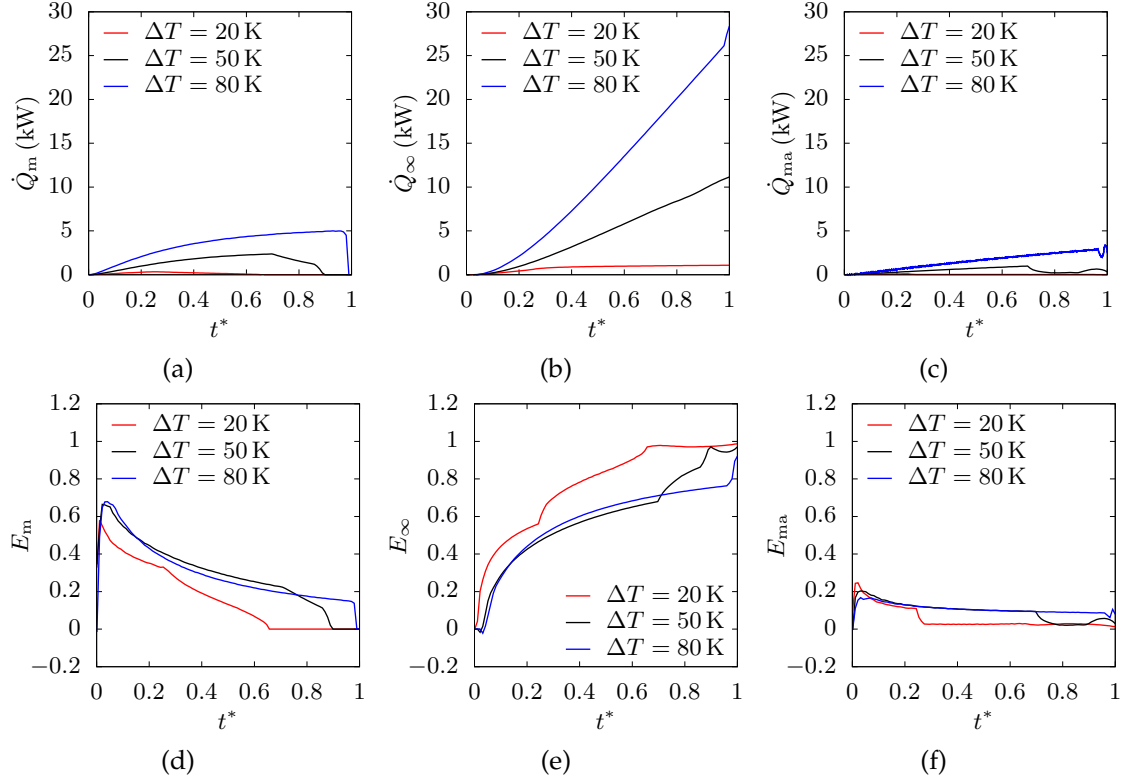


Figure 6.7: Effect of wall superheat on the: (a) microlayer heat transfer rate \dot{Q}_m , (b) bulk liquid heat transfer rate \dot{Q}_∞ , (c) macrolayer heat transfer rate \dot{Q}_{ma} , (d) contribution of microlayer heat transfer E_m (e) contribution of bulk liquid heat transfer E_∞ and (f) contribution of macrolayer heat transfer E_{ma} in sodium pool boiling where $t^* = t/t_{\text{dep}}$.

as shown in Fig. 6.7b. The macrolayer heat transfer rate depends on the thickness of the thermal boundary layer. On increasing the wall superheat from 20 K to 80 K, the thermal boundary layer thickness, defined by Eq. (4.2) increases from 1.02 mm to 4 mm. This increase in thickness leads to more liquid being trapped in the macrolayer and thus more heat transferred from the macrolayer to the bubble as shown in Fig. 6.7c.

Figures 6.7d–6.7f show the contribution of the heat transferred from each mechanism to the total heat transferred to a sodium bubble. The trend in E_m , E_{ma} and E_∞ is found to be similar for all superheats. The microlayer heat transfer rate is dominant during the initial phase of bubble growth while bulk liquid heat transfer has the largest influence during the later stages of bubble growth prior to departure. This is expected as during the later stages of bubble growth after bottleneck formation, the contact radius reduces. This decreases the amount of liquid in the microlayer and hence the microlayer contribution to bubble growth decreases leading to a corresponding increase in the influence of the bulk liquid heat transfer. The contribution of the macrolayer is found to be around 20% prior to bottleneck formation for all superheats and reduces during the bottleneck phase as seen in Fig. 6.7f.

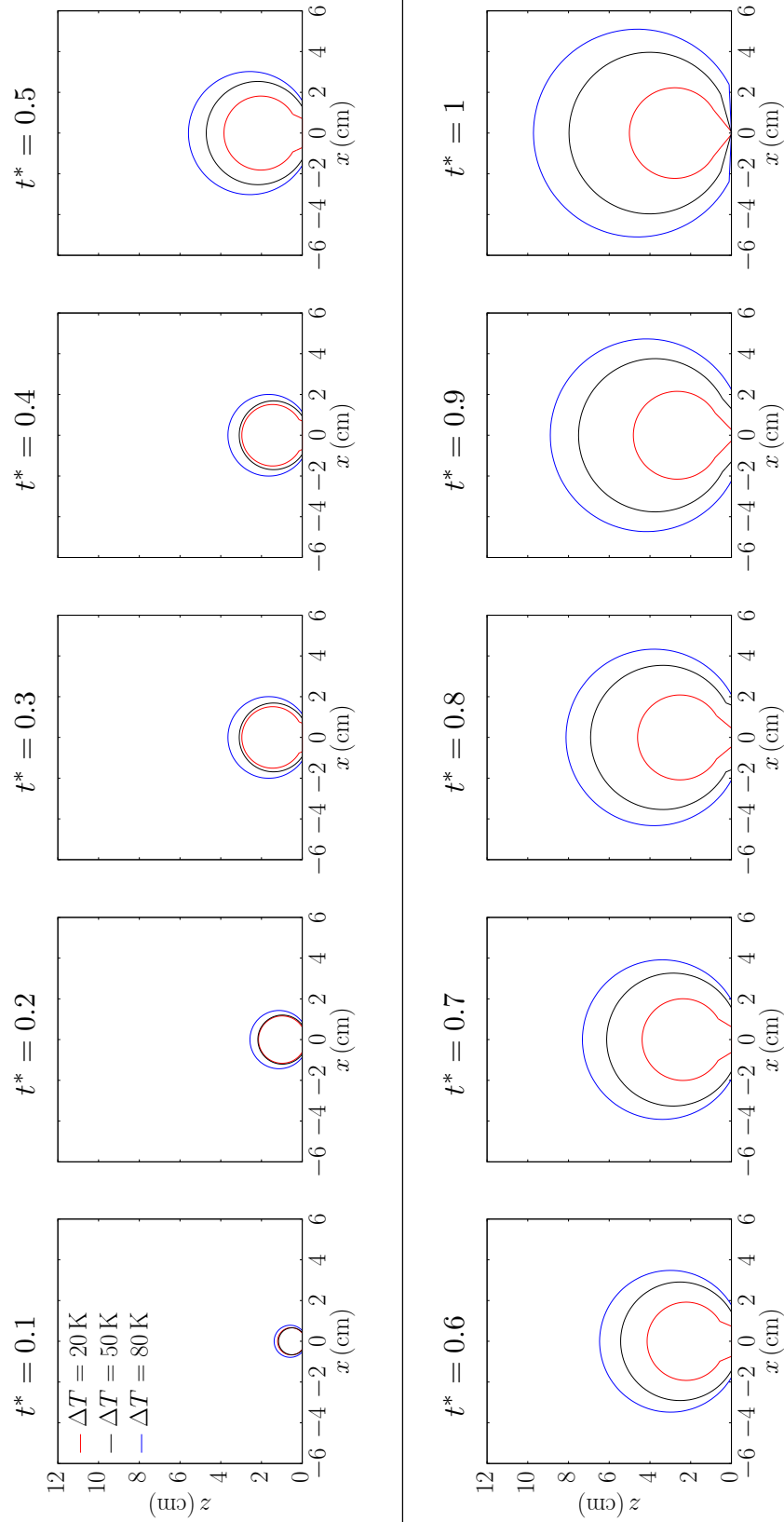


Figure 6.8: Temporal variation in the shape of a bubble in sodium pool boiling at different wall superheats where $t^* = t/t_{\text{dep}}$.

The bubble shape at intervals of $t^* = 0.1$ for different wall superheats is shown in Fig. 6.8. The wall superheat affects the amount of time taken for the microlayer to completely evaporate in the bottleneck phase as mentioned previously. This, in turn, has a significant influence on the shape of a bubble. The larger the time required for the microlayer to evaporate, the larger is the bottleneck height and the greater is the tendency of the bubble to have a balloon-like shape. This can be seen in the shape of the bubble growing on a wall at a superheat of 20 K. On the contrary, at a wall superheat of 80 K, the microlayer evaporates instantaneously after the forces are balanced. Hence the bottleneck height is negligible and the bubble has a truncated spherical shape at departure.

6.3.3 Effect of the rate of change of the contact angle

In the preceding sections, the simulation results presented were limited to a bubble growing with a rate of change of the contact angle of $d\beta/dt = -6^\circ/t$. Experimental data on bubble shape or validated contact angle models for sodium boiling are absent in literature. Hence a parametric study is presented in this section to assess the effect of different contact angle change rates on bubble growth in sodium. Four rates of change of contact angle relationships are chosen for the study: three asymptotically decreasing relations and a constant value as shown in Table 6.1. A constant value is chosen to highlight the generality of the developed model. It is not limited to asymptotically decreasing $d\beta/dt$ relations.

Figure 6.9 shows the effect of $d\beta/dt$ on the bubble radius, contact radius and the contact angle in sodium pool boiling at a wall superheat of 50 K. The slope of the radius versus time curve, i.e. the bubble growth rate, depends on the contact angle of the bubble. Figure 6.9b shows the temporal variation of the contact angle of a bubble for the four $d\beta/dt$ relations. The contact angles are calculated until the start of bottleneck phase as explained in Section 5.3.1. Past experiments on bubble growth in pool boiling of high Prandtl liquids show that the higher the contact angle of a bubble, the greater is the influence of inertia, and the larger is the bubble growth rate [118]. A similar trend is predicted by the developed model for bubble growth in sodium, as seen in Fig. 6.9a.

The rate at which the contact angle varies has a significant influence on the bubble departure radius and departure time. A comparison of the temporal variation of the bubble contact radius for the four contact angle rates is shown in Figure 6.9a, while the time at which the bottleneck phase starts, departure time and departure radius are listed in Table 6.3. For all cases, the contact radius initially increases with time until the start of the bottleneck phase. In the bottleneck phase, the contact radius decreases a little initially and then reduces rapidly once the microlayer has completely evaporated.

The amount of time a bubble stays attached to the wall depends on the forces acting

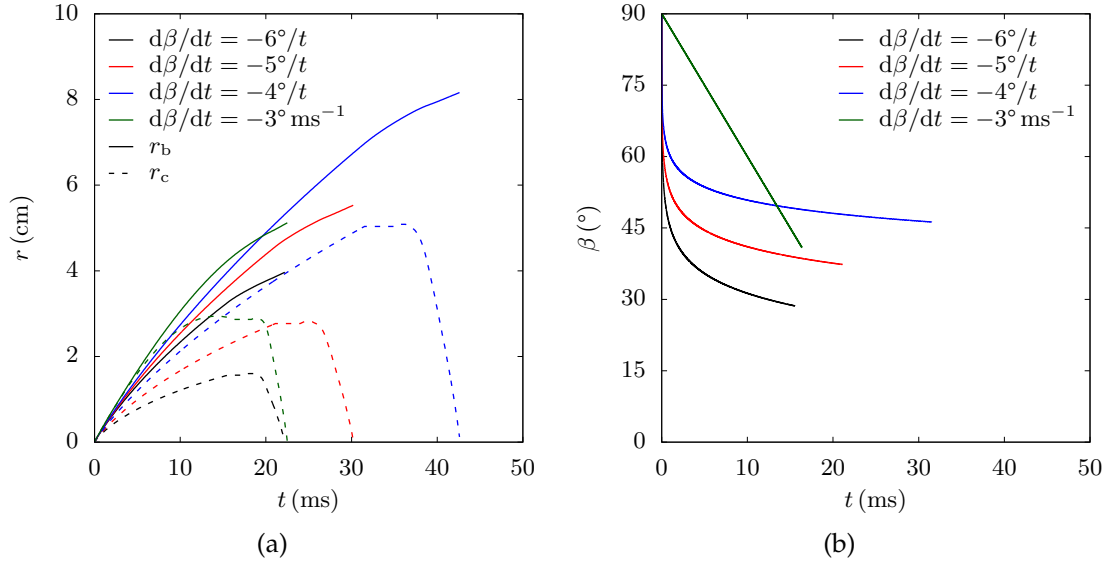


Figure 6.9: Effect of rate of change of contact angle on: (a) bubble and contact radius, and (b) the contact angle in sodium pool boiling at a wall superheat of 50 K.

Table 6.3: Bottleneck time, departure time and departure radius in sodium pool boiling for different rate of change of contact angle relations.

Case	$d\beta/dt$	t_{bn} (ms)	t_{dep} (ms)	r_{dep} (cm)
1	$-6^\circ/t$	15.60	22.30	3.97
2	$-5^\circ/t$	21.11	30.24	5.53
3	$-4^\circ/t$	31.50	42.68	8.17
4	-3° ms^{-1}	16.40	22.51	5.12

on it. Figure 6.10 shows the effect of the rate of change of contact angle on the forces acting on a sodium bubble. The magnitude of the contact pressure and surface tension forces are negligible compared to other forces and hence their temporal variation is not shown. The magnitude of the growth and the drag force is directly proportional to the bubble growth rate according to Eqs. (2.36) and (2.37). The larger the contact angle of a bubble, the larger is the growth rate. For example, a larger drag and growth force acts on a bubble growing with $d\beta/dt = -4^\circ/t$ compared to a bubble growing with $d\beta/dt = -6^\circ/t$, as shown in Figs. 6.10b and 6.10c. This delays the start of the bottleneck phase and the bubble remains attached to the wall for a longer time with an associated increase in the contact angle of the bubble. At the start of bottleneck phase, the buoyancy force is significant and balances the drag and the growth forces, as shown in Figs. 6.10a and 6.10d. In the bottleneck phase, the rate at which the contact radius decreases depends on the rate at which the microlayer evaporates and is found to be approximately equal for cases 1–3.

The departure times for cases 1 and 4 are approximately equal, though their growth rates are vastly different. For case 4, the peak magnitude of growth and drag force is

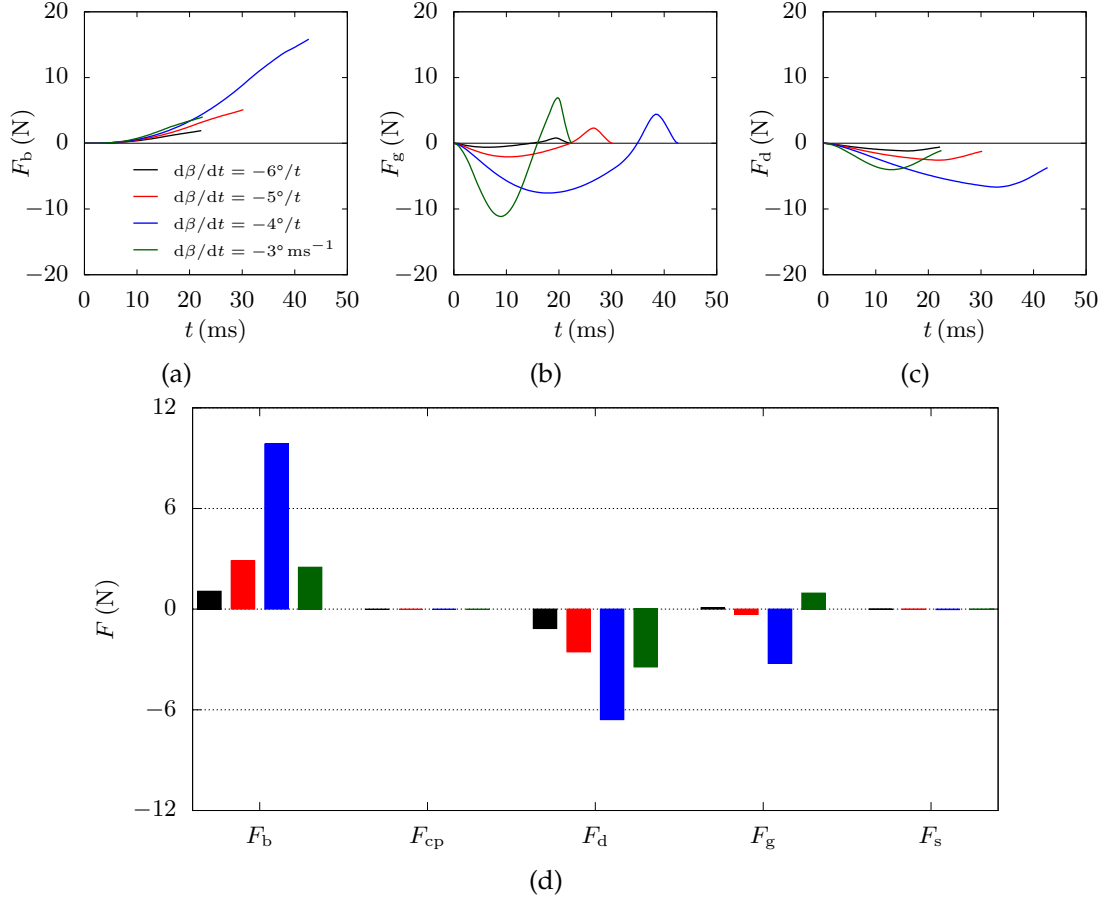


Figure 6.10: Effect of rate of change of contact angle on the forces acting on a sodium bubble in sodium pool boiling at a wall superheat of 50 K: (a) Temporal variation in the buoyancy force, (b) temporal variation in the growth force, (c) temporal variation in the drag force and (d) forces acting on the bubble at the start of bottleneck formation.

substantially higher compared to case 1 owing to the high growth rate. However, as the bubble shape changes, the growth and the drag forces decrease rapidly for case 4 and the forces are balanced at 16.4 ms. The rate at which the contact radius decreases in the bottleneck phase is larger for case 4 compared to case 1. During the bottleneck phase, the rate at which the contact radius varies is given by Eq. (5.3). Once the microlayer completely evaporates, the $\dot{V}_{m,v}$ term is zero and the decrease in the contact radius is proportional to the $v_b \pi r_{bn}^2$ term representing the rate of decrease of volume of vapour in the bottleneck. The radius of the top of the bottleneck r_{bn} depends on the contact angle at which the bottleneck starts to form β_{bn} , which is larger for case 4 compared to case 1. In addition, the bubble growth rate v_b is also larger for case 4. Thus, the term $v_b \pi r_{bn}^2$ and the rate at which the contact radius decreases, after complete microlayer evaporation, is significantly larger for case 4 compared to case 1 and the departure time for the two cases is found to be approximately equal.

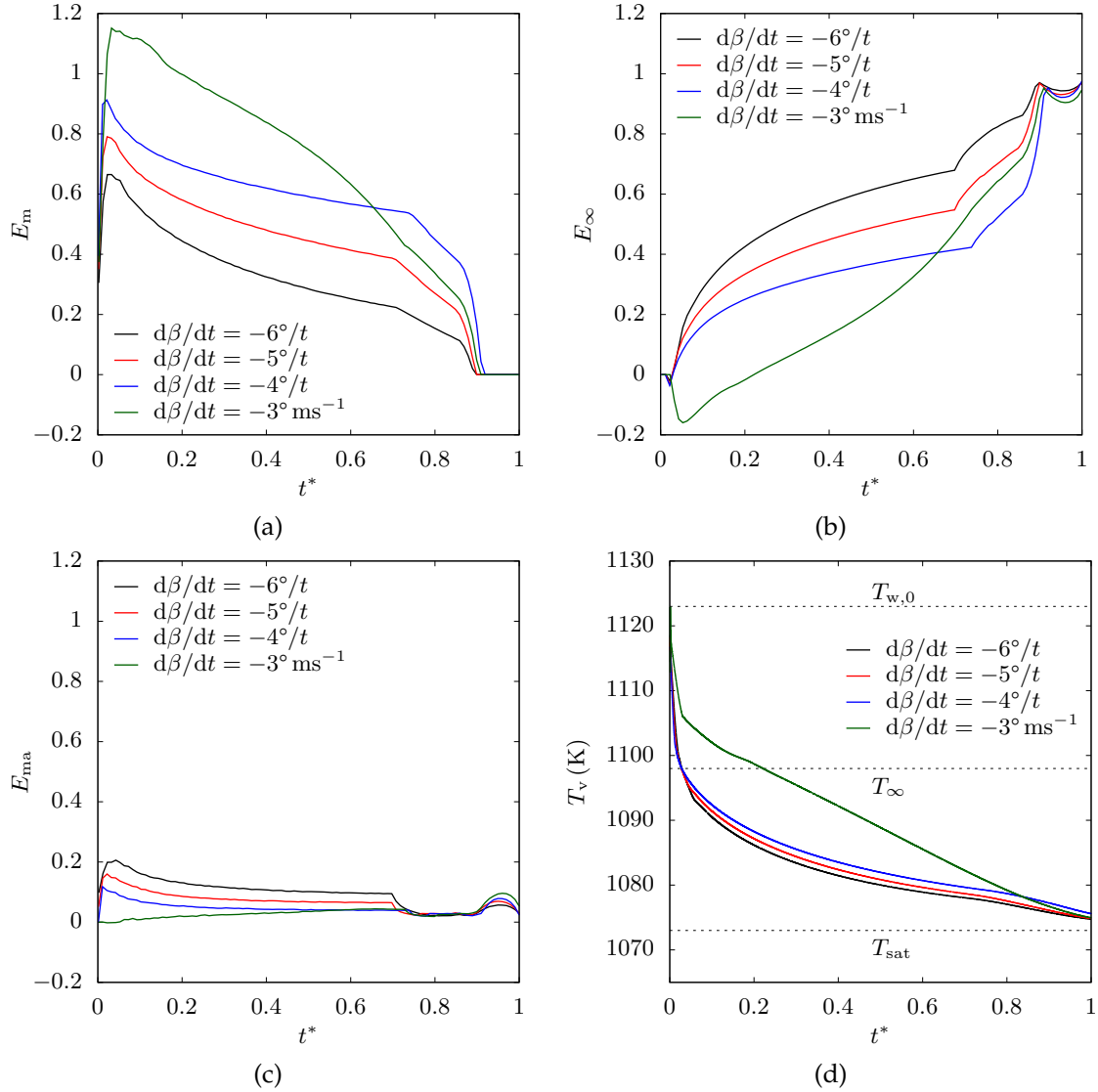


Figure 6.11: Effect of rate of change of contact angle on the parameter (a) E_m , (b) E_∞ (c) E_{ma} and (d) the temperature of vapour in the bubble in sodium pool boiling at a wall superheat of 50 K where $t^* = t/t_{\text{dep}}$.

Figure 6.11 shows the effect of $d\beta/dt$ on the parameter E and temperature of vapour in the bubble where $t^* = t/t_{\text{dep}}$. The contribution of the thermal boundary layer heat transfer E_t is found to be negligible for all cases and hence is not shown. The magnitude of the heat transferred from the microlayer depends on the bubble contact radius and contact area $A = \pi (r_c^2 - r_d^2)$. The contact radius, in turn, depends on the contact angle of a bubble according to Eq. (4.4). Thus, the larger the contact angle of the bubble, the larger is the bubble contact area with respect to the overall surface area of the bubble and hence the larger is the influence of the microlayer heat transfer on the bubble growth rate. This can be seen in Fig. 6.11a.

As the contribution of the microlayer heat transfer decreases with time for all cases, the contribution of the bulk liquid heat transfer to bubble growth increases with time, as shown in Fig. 6.11b. The magnitude of heat transferred from the bulk liquid depends on the area of the bubble exposed to the bulk liquid and the temperature difference $T_\infty - T_v$, which is larger for bubbles growing with a smaller contact angle as shown in Fig. 6.11d. Immediately after nucleation, the temperature of the vapour in the bubble is high and $T_\infty - T_v$ is negative for all cases. Thus, E_∞ is negative for all cases, which indicates that the bubble undergoes condensation in the bulk liquid.

The contribution of the macrolayer heat transfer to bubble growth is found to be smaller compared to the microlayer and the bulk liquid heat transfer for all cases as observed from Fig. 6.11c. In general, it can be observed that lower the contact angle of a bubble, the higher is the contribution of the macrolayer. However, in the bottleneck phase prior to bubble departure, for all cases, the value of E_{ma} is found to be approximately equal. Thus, irrespective of the chosen rate of change of contact angle relation, from Fig. 6.11, it can be concluded that the microlayer heat transfer is dominant during the initial period of bubble growth after nucleation while the bulk liquid heat transfer dominates during the later stages of bubble growth prior to departure.

The temporal variation in the shape of a sodium bubble at intervals of $t^* = 0.1$ for the different rate of change of contact angle relations is shown in Fig. 6.12. The rate of change of contact angle relation has a significant influence on the shape of a bubble. For a bubble growing with a $d\beta/dt = -3^\circ \text{ms}^{-1}$, up to $t^* = 0.3$, the bubble appears to be hemispherical owing to the high contact angle of the bubble. For other cases, the bubble shape resembles a truncated sphere. The presence of a bottleneck can be observed for all cases at $t^* = 0.8$. In the bottleneck phase, once the microlayer has completely evaporated, the contact radius drops rapidly. At departure, i.e. $t^* = 1$, irrespective of the contact angle relation, the shape of a bubble in sodium for a wall superheat of 50 K tends to be a truncated sphere with a small bottleneck.

6.3.4 Effect of the bulk liquid temperature

The temperature of the bulk liquid affects the thickness of the thermal boundary layer and the overall dynamics of the bubble growth process. Thus, a parametric study is conducted to investigate the effect of varying the bulk liquid temperature on the growth of a sodium bubble for a superheat of 50 K and assuming $d\beta/dt = -6^\circ/t$. Three values of bulk liquid temperature are selected for the study: $T_\infty = 1073, 1098, 1123$ K. The thermal boundary layer thickness for the selected T_∞ values are 5 mm, 2.5 mm and 0, respectively. A thermal boundary layer is not formed when the bulk liquid temperature is equal to the wall temperature.

Figure 6.13 shows the effect of the bulk liquid temperature on the bubble radius and

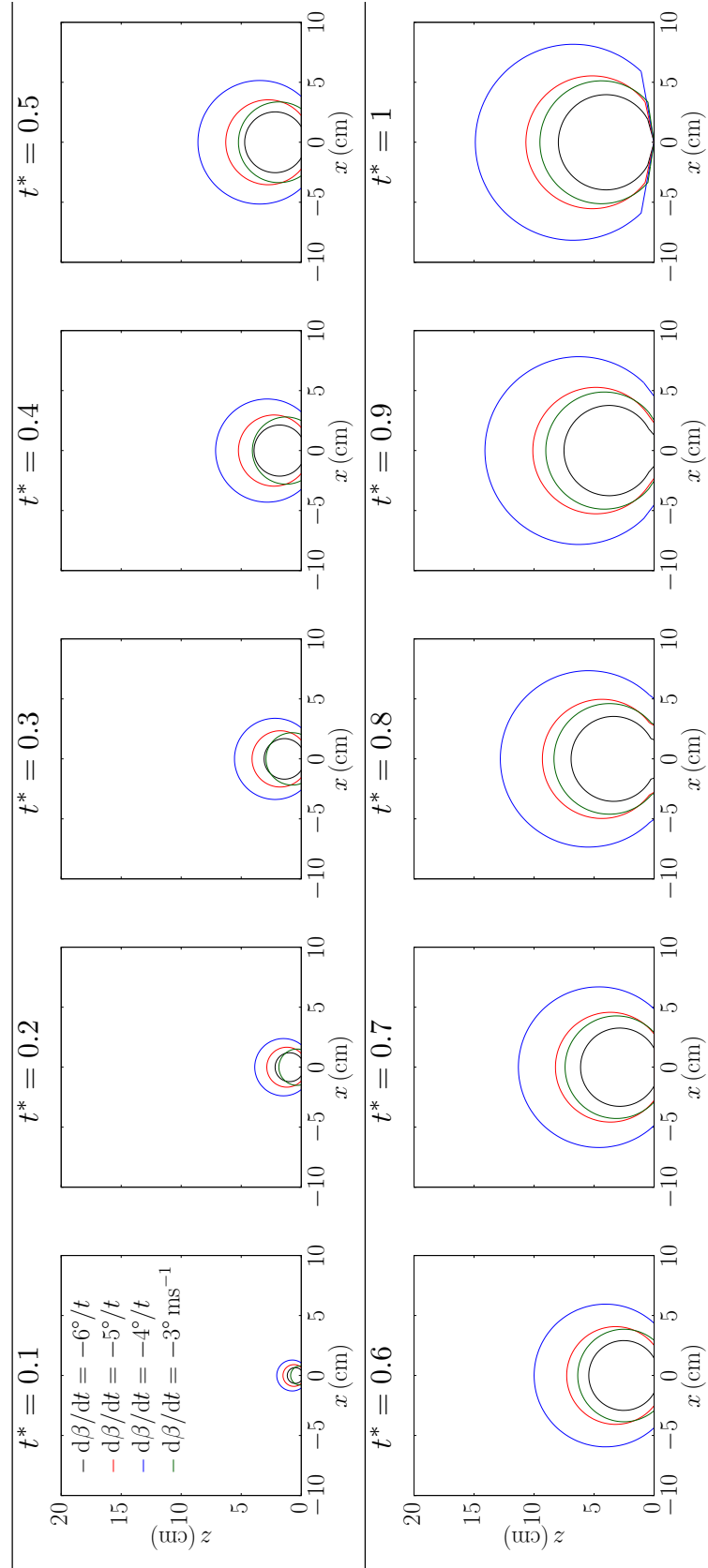


Figure 6.12: Effect of rate of change of contact angle on the temporal variation in the shape of a bubble in sodium pool boiling where $t^* = t/t_{\text{dep}}$.

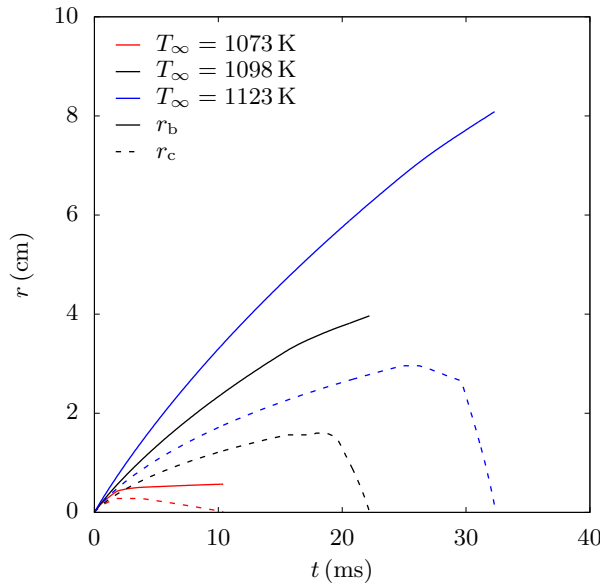


Figure 6.13: Effect of bulk liquid temperature on the bubble and contact radius in sodium pool boiling at a wall superheat of 50 K.

the contact radius. With an increase in the temperature of the liquid pool, the bubble radius and the contact radius increases. This is expected, as the higher the temperature of the liquid pool, the larger will be the amount of heat transferred from the bulk liquid to the bubble, and thus the larger will be the bubble size. In addition, for a bubble growing in a saturated liquid pool, i.e. $T_\infty = T_{\text{sat}} = 1073 \text{ K}$, the bulk liquid is cooler than the vapour in the bubble. Thus, the bubble will undergo condensation which limits its growth rate.

Figure 6.14 shows the effect of the bulk liquid temperature on the contribution of the different heat transfer mechanisms to the bubble growth process. For a bubble growing in a 1073 K liquid pool, the contribution of the microlayer evaporation increases immediately after nucleation which corresponds to an increase in the condensation heat transfer in the thermal boundary layer, as observed in Fig. 6.14a. As the thermal boundary layer is substantially thick, the effect of the thermal boundary layer and macrolayer heat transfer is significant compared to a bubble growing in a higher temperature liquid pool. The bulk liquid heat transfer is found to have the least influence on bubble growth. During the initial phase of bubble growth up to $t^* = 0.15$, $E_\infty = 0$ since the bubble is completely inside the thermal boundary layer. From $t^* = 0.15$ to $t^* = 0.25$, a part of the bubble is exposed to the bulk liquid where it undergoes condensation. Beyond $t^* = 0.25$, the temperature of the vapour in the bubble is found to be equal to the saturation temperature and hence the bulk liquid no longer contributes to the bubble growth process.

Figures 6.14b and 6.14c show the influence of different heat transfer mechanisms on a bubble growing in a liquid pool of temperatures 1098 K and 1123 K, respectively. In a 1098 K liquid pool, the microlayer heat transfer is dominant during the initial phase

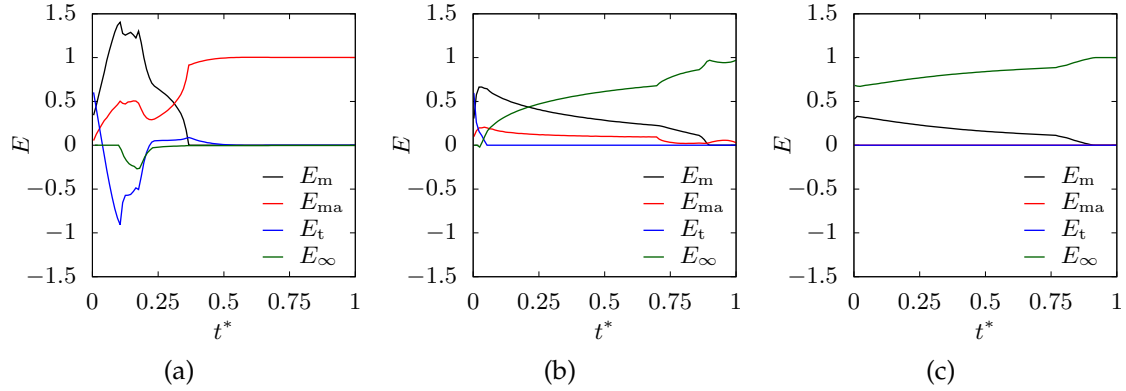


Figure 6.14: Effect of bulk liquid temperature on the parameter E for a bubble growing in a sodium pool of temperature (a) $T_\infty = 1073$ K, (b) $T_\infty = 1098$ K and (c) $T_\infty = 1123$ K where $t^* = t/t_{\text{dep}}$.

of bubble growth up to $t^* = 0.25$ and thereafter the evaporation from the bulk liquid dominates bubble growth, as explained previously in Section 6.3.1. In a 1123 K liquid pool, a thermal boundary layer is not formed as the wall temperature is equal to the bulk liquid temperature. Thus, the heat transfer from the thermal boundary layer and the macrolayer do not have any influence on the bubble growth process. Throughout the growth period, the heat transfer from the bulk liquid increases with time and is found to be greater than the microlayer heat transfer.

6.3.5 Effect of accommodation coefficient

The results discussed in the preceding sections were obtained assuming the accommodation coefficient to be one. However, factors such as the shape of the liquid–vapour interface, system pressure and the presence of impurities may lower its value [153]. Hence a parametric study is performed to investigate the influence of the accommodation coefficient on the growth and departure of a sodium bubble. Four values of f ranging from 0.25–1 are considered for the study.

Figures 6.15 and 6.16 show the effect of the accommodation coefficient on the bubble radius and the contact radius, and the total heat transferred to a bubble, respectively. On decreasing the accommodation coefficient, the bubble growth rate decreases while the bubble departure radius is found to be approximately equal. With a decrease in the accommodation coefficient, the interface thermal resistance given by Eq. (2.17) increases. This results in less overall heat transferred to the bubble from the different heat transfer mechanisms as seen in Fig. 6.16 and consequently lower bubble growth rates. As less heat is transferred to the bubble, the amount of time taken for the microlayer to completely evaporate and the contact radius to reduce to zero also increases. Thus, with a decrease in the accommodation coefficient the bubble departure time increases, as seen from the temporal variation of the contact radius in Fig. 6.15.

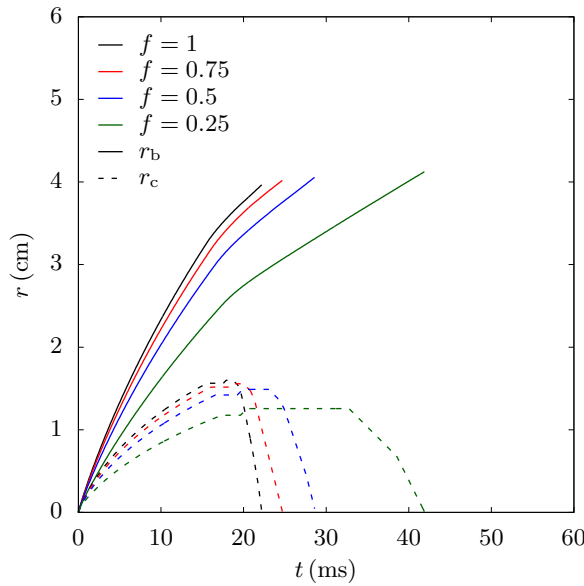


Figure 6.15: Effect of accommodation coefficient on the bubble and contact radius in sodium pool boiling at a wall superheat of 50 K.

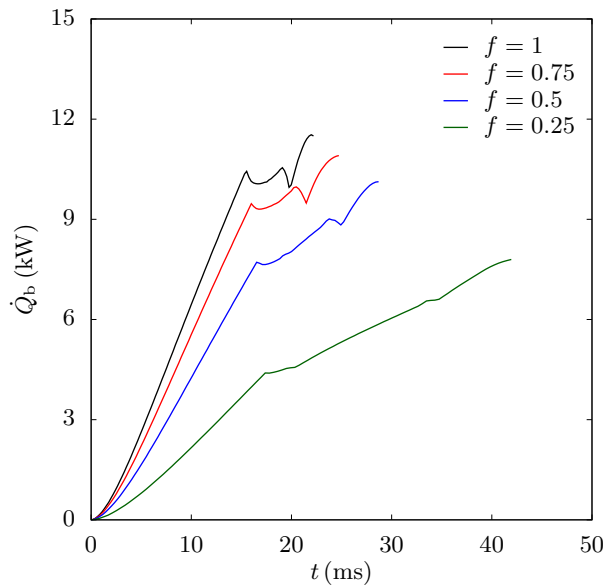


Figure 6.16: Effect of accommodation coefficient on the total heat transferred to a bubble in sodium pool boiling at a wall superheat of 50 K.

6.4 Summary

The mechanistic model developed in the previous chapter has been extended to study the growth of a sodium bubble from nucleation to departure in this chapter. The model couples the heat transferred to a bubble from the microlayer, the macrolayer, the thermal boundary layer and the bulk liquid surrounding the bubble with the forces acting on it. The change in the contact angle of the bubble as it grows was accounted for by using, as an input, the rate of change of the contact angle value. The formation of a conical bottleneck and the shrinkage of the base of the bubble prior to departure were also considered in the model. The developed model was used to investigate the

bubble growth characteristics in sodium pool boiling and study the effect of different parameters like the wall superheat, the rate of change of contact angle, the bulk liquid temperature and the accommodation coefficient on the bubble dynamics.

The numerical simulations performed to study the growth of a sodium bubble at a wall superheat of 50 K, a bulk liquid temperature of 1098 K and a rate of change of contact angle of $-6^\circ/t$ indicated that for a majority of the growth period, the evaporation from the bulk liquid was the dominant mechanism of heat transfer. An analysis of the bubble shape showed that, for the given input conditions, the bubble resembled a sphere with a small bottleneck at departure. The parametric analysis showed that the wall superheat had a significant effect on the bubble shape. With a decrease in the superheat, the amount of time needed for the microlayer to completely evaporate increased. This led to an increase in the bottleneck height and the bubble tended to have a balloon-like shape at departure. An analysis of the effect of the rate of change of contact angle on the bubble dynamics in sodium showed that the larger the contact angle, the greater was the growth and the drag force keeping the bubble attached to the wall and thus the larger was the departure radius and departure time. With an increase in the bulk liquid temperature, the bubble size increased due to there being more heat transferred from the bulk liquid to the bubble. Lastly, with a decrease in the accommodation coefficient, the interface resistance increases. This reduces the heat transferred to a bubble and in turn, decreases the growth rate.

Summary and conclusions

Understanding the heat and mass transfer process in nucleate boiling of liquid metals like sodium is an emerging field of study, in particular for the development of next generation CSP plants with boiling sodium as the heat transfer fluid. The research presented in this doctoral project was focused on advancing the knowledge of sodium boiling by developing comprehensive, physics-based, mechanistic bubble growth models. Such models highlight the governing heat transfer and hydrodynamic phenomena dominating the bubble growth process in sodium, thus aiding the development of efficient sodium boiling systems.

7.1 Summary

The first part of this doctoral study was dedicated to understanding heat transfer by different mechanisms to a bubble in sodium pool boiling and to developing models to describe them. A bubble grows due to microscale heat transfer from the contact line and the microlayer region formed underneath the bubble. In addition to these microscopic heat transfer phenomena, the evaporation of the liquid in the macrolayer, the thermal boundary and the bulk liquid surrounding the bubble contribute to bubble growth. The combined effect of these heat transfer processes cause a bubble to grow from its initial micron size to its departure size, where forces acting on the bubble lead to its detachment from the wall.

The microscale heat transfer in boiling flows have a significant influence on the bubble growth process. In literature, this microscale heat transfer is quantified by analysing the thermo-fluid dynamic phenomena in either the contact line or the microlayer region. Due to the lack of experimental data on sodium boiling, the dominating microscale heat transfer mechanisms for sodium are unknown. Thus, in this work, the contact line region and the microlayer region were modelled to provide an insight into the heat transferred from each region.

First, the heat transfer from the contact line region was studied. A boundary-value problem model was proposed to quantify the heat transfer from the contact line region

to a sodium bubble. The influence of an electron pressure component on the evaporation of the fluid film in the contact line region in sodium was considered, which to the best of the author's knowledge, has not been studied yet. The model highlighted the major differences in the contact line dynamics between sodium and a high Prandtl number fluid, the fluorocarbon FC-72. The electron pressure was identified to have a significant influence on the evaporation of the contact line region. By increasing the electron pressure parameter from 0 to 100 at a constant superheat, the length of the contact line region was found to increase, while the integrated heat flux reduced by 15%. A method to integrate the model into high-fidelity CFD simulations using a look-up table was proposed to guide future studies on simulating bubble growth in sodium pool boiling.

To further understand the heat transfer to a bubble in sodium pool boiling, a reduced-order heat transfer model incorporating the evaporation of the microlayer, the macrolayer, the thermal boundary layer and the bulk liquid was developed. Existing sodium bubble growth heat transfer models proposed in literature are not comprehensive enough in treating the underlying physics, especially the depletion of the microlayer as the bubble grows. This is improved in the present work by accounting for the temporal and spatial variation in the microlayer profile during the bubble growth process. A two-dimensional heat conduction equation was solved to compute the variation in the temperature of the wall underneath the bubble as the microlayer and the macrolayer evaporates. The model was used to investigate the heat transfer and growth characteristics, up to 5 ms, of a bubble in sodium pool boiling with the aim of identifying the most dominant heat transfer mechanism. In addition, insights were provided on the influence of the wall superheat, bulk liquid temperature, accommodation coefficient and the contact angle on the growth of a sodium bubble. An analysis of the results showed that for a bubble growing with a high contact angle of 80° , irrespective of the wall superheat and the bulk liquid temperature, the microlayer was the most dominant heat transfer mechanism during the period after nucleation. However, the influence of microlayer heat transfer on bubble growth decreased with a decrease in the contact angle. This led to a corresponding increase in the influence of the macrolayer heat transfer.

Building upon the conclusions of the heat transfer model, the development of a comprehensive mechanistic model accounting for the variation in the contact angle and the shape of a bubble was pursued in the second part of this work. The previously developed heat transfer model was coupled to a force and a contact angle sub-model to study the complete bubble growth process from nucleation to departure in pool boiling. A novel method to approximate the balloon-like shape of a bubble prior to departure as a truncated sphere atop a conical bottleneck was presented. The developed model was verified and validated against high-fidelity CFD simulations and experimental data on pool boiling of water and methanol. The model accurately predicted the wall tem-

perature, bubble departure time and the variation in the microlayer profile during the bubble growth process. An assessment of the model against previously published bubble growth models, where the shape of the bubble was approximated as a sphere atop a cylindrical bottleneck, demonstrated significant improvement in the prediction of the transition in the shape of the bubble.

Simulation of the sodium bubble growth process using the validated mechanistic model was pursued in the last part of this project. Results from the model showed that a bubble in sodium resembles a truncated sphere at departure with a small bottleneck. The heat transfer from the microlayer was found to be dominant during the initial phase of bubble growth immediately after nucleation, while for a majority of the growth period, the bulk liquid heat transfer had the largest influence. This is contrary to the findings in previous studies, where the microlayer heat transfer in sodium was assumed to be dominant throughout the growth period. The effects of wall superheat, the rate of change of contact angle, bulk liquid temperature and accommodation coefficient on the bubble dynamics were investigated. The wall superheat was found to have a significant influence on the bubble shape. The tendency of the bubble to assume a balloon-like shape increased with a decrease in the superheat owing to an increase in the amount of time needed for the microlayer to completely evaporate. In addition, it was found that the larger the contact angle of a sodium bubble, the larger was the departure radius and departure time. With an increase in the bulk liquid temperature and the accommodation coefficient, the bubble growth rate increased due to having a larger evaporation rate from the bulk liquid and a lower interface thermal resistance, respectively.

7.2 Outlook

In this work, numerical models were developed to fundamentally understand the growth of a bubble in sodium pool boiling. To further enhance understanding of the bubble growth process and overcome some of the limitations of this work, experimental and numerical studies are recommended, and are detailed in this section.

A major limitation of this work is the lack of experimental validation. Performing experiments on sodium boiling and gathering meaningful data on the bubble growth process using traditional measurements techniques like optical cameras is challenging. However, in recent years, advanced measurement techniques like ultrasound transit-time-technique (UTTT) [169] and contactless inductive flow tomography (CIFT) [170] have been developed which can be used to experimentally study the bubble growth process in sodium boiling flows. The application of such techniques to detect bubbles in liquid metals have been demonstrated before [171]. These techniques are promising and should be used in experimental set-ups to obtain data to validate the current models. In addition, the use of thermocouples embedded in a heater wall below a bubble can

provide valuable data on the temperature profile in the wall. An analysis of the variation in the wall temperature can be used to compute the rate of evaporation of the microlayer.

Interface-tracking CFD simulations could be performed to gain a deeper understanding of the bubble growth process in sodium pool boiling. Such simulations can accurately predict the evaporative mass flux at the interface of a bubble based on the local temperature gradient across the liquid–vapour interface of the bubble and do not rely on an input contact angle rate value to track the shape of the bubble. Future work could also be aimed at coupling the contact line model to CFD simulations using the proposed look-up table method, to quantify the influence of the heat transferred from the contact line region to the overall bubble growth processes. Such simulations have been performed for high Prandtl number fluids [62]. Results from the CFD simulations can be used to find the dominating microscale heat transfer phenomena in sodium boiling, which is currently unknown. The contact line model could also be improved by accounting for fluid flow in the contact line region and incorporating a physics-based equation to model the electron pressure. The effect of surface roughness on the heat transfer from the contact line and microlayer region should also be analysed.

The reduced-order model developed in this work could be extended to study the growth of multiple bubbles and investigate the influence of dissolved inert gases on the bubble growth process in sodium. An uncertainty quantification analyses could be performed which would provide further insights on the influence of parameters like the accommodation coefficient on the bubble growth dynamics. In addition, the influence of more realistic conditions expected in commercial scale applications like bulk liquid flow, non-uniform heat fluxes in the wall, and in the case of flow boiling in vertical pipes, the heater wall orientation on the overall sodium boiling process could be studied. Such studies will aid in designing stable sodium boiling systems in CSP plants.

Bibliography

1. Renewables information: Overview, Tech. Rep., International Energy Agency, 2019.
2. K. K. Lovegrove, D. Alexander, R. Bader, S. Edwards, M. Lord, A. Mojiri, J. Rutovitz, H. Saddler, C. Stanley, K. Urkalan, and M. Watt, Renewable energy options for industrial process heat, Tech. Rep., Australian Renewable Energy Agency, 2019.
3. T. Wetzel, J. Pacio, L. Marocco, A. Weisenburger, A. Heinzl, W. Hering, C. Schroer, G. Muller, J. Konys, R. Stieglitz, J. Fuchs, J. Knebel, C. Fazio, M. Daubner, and F. Fellmoser, Liquid metal technology for concentrated solar power systems: Contributions by the German research program, *AIMS Energy*, vol. 2, pp. 89–98, 2014.
4. R. W. Bradshaw and R. W. Carling, A review of the chemical and physical properties of molten alkali nitrate salts and their effect on materials used for solar central receivers, in *Proceedings of The Electrochemical Society*, pp. 959–969, 1987.
5. C. Turchi, S. Gage, J. Martinek, S. Jape, K. Armijo, J. Coventry, J. Pye, C. A. Asselineau, F. Venn, W. Logie, A. Fontalvo, S. Wang, R. McNaughton, D. Potter, T. Steinberg, and G. Will, CSP Gen3: Liquid-Phase Pathway to SunShot, Tech. Rep. NREL/TP-5700-79323, National Renewable Energy Laboratory, 2021.
6. H. M. Kottowski and C. Savatteri, Evaluation of sodium incipient superheat measurements with regard to the importance of various experimental and physical parameters, *International Journal of Heat and Mass Transfer*, vol. 20, no. 12, pp. 1281–1300, 1977.
7. A. Chenu, *Single- and Two-phase Flow Modeling for Coupled Neutronics/Thermal-Hydraulics Transient Analysis of Advanced Sodium-Cooled Fast Reactors*. PhD thesis, École Polytechnique fédérale de Laussane, 2011.
8. I. Michiyoshi, Boling heat transfer in liquid metals, *Applied Mechanics Review*, vol. 41, no. 3, pp. 129–149, 1988.
9. C. E. Andracka, J. B. Moreno, R. B. Diver, W. C. Ginn, V. Dudley, and K. S. Rawlinson, Reflux pool-boiler as a heat-transport device for Stirling engines: On-sun test program results, in *Proceedings of the 25th Intersociety Energy Conversion Engineering Conference*, vol. 5, pp. 274–280, 1990.

10. I. L. Pioro, W. Rohsenow, and S. S. Doerffer, Nucleate pool-boiling heat transfer. I: review of parametric effects of boiling surface, *International Journal of Heat and Mass Transfer*, vol. 47, no. 23, pp. 5033–5044, 2004.
11. J. Kim, Review of nucleate pool boiling bubble heat transfer mechanisms, *International Journal of Multiphase Flow*, vol. 35, no. 12, pp. 1067–1076, 2009.
12. V. K. Dhir, G. R. Warrier, and E. Aktinöl, Numerical simulation of pool boiling: a review, *Journal of Heat Transfer*, vol. 135, no. 6, p. 061502, 2013.
13. X. Duan, B. Phillips, T. McKrell, and J. Buongiorno, Synchronized high-speed video, infrared thermometry, and particle image velocimetry data for validation of interface-tracking simulations of nucleate boiling phenomena, *Experimental Heat Transfer*, vol. 26, no. 2-3, pp. 169–197, 2013.
14. T. Yabuki and O. Nakabeppu, Heat transfer mechanisms in isolated bubble boiling of water observed with MEMS sensor, *International Journal of Heat and Mass Transfer*, vol. 76, pp. 286–297, 2014.
15. Y. Sato and B. Niceno, A depletable micro-layer model for nucleate pool boiling, *Journal of Computational physics*, vol. 300, pp. 20–52, 2015.
16. T. Yabuki and O. Nakabeppu, Microscale wall heat transfer and bubble growth in single bubble subcooled boiling of water, *International Journal of Heat and Mass Transfer*, vol. 100, pp. 851–860, 2016.
17. S. Narayan, A. Srivastava, and S. Singh, Rainbow schlieren-based investigation of heat transfer mechanisms during isolated nucleate pool boiling phenomenon: Effect of superheat levels, *International Journal of Heat and Mass Transfer*, vol. 120, pp. 127–143, 2018.
18. W. Ding, E. Krepper, and U. Hampel, Evaluation of the microlayer contribution to bubble growth in horizontal pool boiling with a mechanistic model that considers dynamic contact angle and base expansion, *International Journal of Heat and Fluid Flow*, vol. 72, pp. 274–287, 2018.
19. S. Narayan, T. Singh, S. Singh, and A. Srivastava, Experiments on the effects of varying subcooled conditions on the dynamics of single vapor bubble and heat transfer rates in nucleate pool boiling regime, *International Journal of Heat and Mass Transfer*, vol. 134, pp. 85–100, 2019.
20. S. Narayan, A. Srivastava, and S. Singh, Rainbow schlieren-based direct visualization of thermal gradients around single vapor bubble during nucleate boiling

- phenomena of water, *International Journal of Multiphase Flow*, vol. 110, pp. 82–95, 2019.
21. S. L. Narayan and A. Srivastava, Non-contact experiments to quantify the micro-layer evaporation heat transfer coefficient during isolated nucleate boiling regime, *International Communications in Heat and Mass Transfer*, vol. 122, p. 105191, 2021.
 22. K. M. Armijo and C. E. Andraka, Phenomenological safety studies on sodium for CSP applications, Tech. Rep. SAND2016-8586, Sandia National Laboratories, 2016.
 23. J. Coventry, C. Andraka, J. Pye, M. Blanco, and J. Fisher, A review of sodium receiver technologies for central receiver solar power plants, *Solar Energy*, vol. 122, pp. 749–762, 2015.
 24. J. Pacio and T. Wetzel, Assessment of liquid metal technology status and research paths for their use as efficient heat transfer fluids in solar central receiver systems, *Solar Energy*, vol. 93, pp. 11–22, 2013.
 25. P. Kesselring and C. Selvage, *The IEA/SSPS Solar Thermal Power Plants*, vol. 1: Central receiver systems. Springer, 1st ed., 1986.
 26. P. Kesselring and C. Selvage, *The IEA/SSPS Solar Thermal Power Plants*, vol. 4: Book of summaries. Springer, 1st ed., 1986.
 27. W. J. C. Schiel and M. A. Geyer, Testing an external sodium receiver up to heat fluxes of 2.5 MW/m^2 : Results and conclusions from the IEA-SSPS high flux experiment conducted at the central receiver system of the Plataforma Solar de Almeria (Spain), *Solar Energy*, vol. 41, pp. 255–265, 1988.
 28. F. G. Casal, *Solar Thermal Power Plants*. Springer, 1st ed., 1987.
 29. Rockwell International, Sodium solar receiver experiment - final report, Tech. Rep. SAND82-8192, Sandia National Laboratories, 1983.
 30. W. Lipiński, E. Abbasi-Shavazi, J. Chen, J. Coventry, M. Hangi, S. Iyer, A. Kumar, L. Li, S. Li, J. Pye, J. F. Torres, B. Wang, Y. Wang, and V. Wheeler, Progress in heat transfer research for high-temperature solar thermal applications, *Applied Thermal Engineering*, vol. 184, p. 116137, 2021.
 31. C. E. Andraka, J. B. Moreno, R. B. Diver, and T. A. Moss, Sodium reflux pool-boiler solar receiver on-sun test results, Tech. Rep. SAND-89-2773, Sandia National Laboratories, 1992.
 32. J. B. Moreno and C. E. Andraka, Test results from bench-scale sodium-pool-boiler solar receiver, Tech. Rep. SAND-89-0899, Sandia National Laboratories, 1989.

33. D. Laing and M. Reusch, Hybrid sodium heat pipe receivers for dish/Stirling systems, in *Proceedings of the 32nd Intersociety Energy Conversion Engineering Conference*, 1997.
34. M. A. White, J. H. Noble, S. G. Emigh, B. A. Ross, G. A. Lehmann, D. L. Nelson, G. L. Hickman, and D. A. Wallace, Preliminary design of an advanced stirling system for terrestrial solar energy conversion, in *Proceedings of the 25th Intersociety Energy Conversion Engineering Conference*, 1990.
35. C. E. Andraka, K. S. Rawlinson, T. A. Moss, D. R. Adkins, J. B. Moreno, D. R. Gallup, P. G. Cordeiro, and S. Johansson, Solar heat pipe testing of the Stirling thermal motors 4-120 Stirling engine, in *Proceedings of the 31st Intersociety Energy Conversion Engineering Conference*, 1996.
36. O. E. Dwyer, *Boiling Liquid-Metal Heat Transfer*. 1st ed., 1976.
37. J. B. Moreno, G. C. Stoker, and K. R. Thompson, X-ray observations of boiling sodium in a reflux-pool-boiler solar receiver, Tech. Rep. SAND91-1538, Sandia National Laboratories, 1992.
38. E. G. Schlechtendahl, Theoretical investigations on sodium boiling in fast reactors, *Nuclear Science and Engineering*, vol. 41, no. 1, pp. 99–114, 1970.
39. Y. Y. Hsu, On the size range of active nucleation cavities on a heating surface, *Journal of Heat Transfer*, vol. 84, no. 3, pp. 207–213, 1962.
40. I. Shai, Mechanism of nucleate pool boiling heat transfer to sodium and the criterion for stable boiling, Tech. Rep., MIT Engineering Projects Laboratory, 1967.
41. R. M. Singer and R. E. Holtz, On the role of inert gas in incipient boiling liquid metal experiments, *International Journal of Heat and Mass Transfer*, vol. 12, no. 9, pp. 1045–1060, 1969.
42. P. J. Marto and W. M. Rohsenow, Effects of surface conditions on nucleate pool boiling of sodium, *Journal of Heat Transfer*, vol. 88, no. 2, pp. 196–203, 1966.
43. S. S. Kutateladze, V. M. Borishanskii, and I. I. Novikov, Heat transfer in liquid metals, *Journal of Nuclear Energy*, vol. 9, no. 1, pp. 214–229, 1959.
44. I. Michiyoshi, N. Takenaka, and O. Takahashi, Dry patch formed boiling and burnout in potassium pool boiling, *International Journal of Heat and Mass Transfer*, vol. 29, no. 5, pp. 689–702, 1986.
45. R. C. Noyes, An experimental study of sodium pool boiling heat transfer, *Journal of Heat Transfer*, 1963.

46. W. Peppler, E. G. Schlechtendahl, and G. F. Schultheiss, Investigation on dynamic boiling in sodium cooled fast reactors, *Nuclear Engineering and Design*, vol. 14, no. 1, pp. 23–42, 1970.
47. W. M. Rohsenow, Film condensation of liquid metals, *Transactions of the Canadian Society for Mechanical Engineering*, vol. 1, no. 1, pp. 5–12, 1972.
48. J. Coventry, J. Pye, A. Kumar, S. Iyer, Z. Kee, and W. Lipiński, A sodium boiler and phase-change energy storage system, in *AIP Conference Proceedings*, vol. 2126, p. 060002, 2019.
49. S. C. P. Cheung, S. Vahaji, G. H. Yeoh, and J. Y. Tu, Modeling subcooled flow boiling in vertical channels at low pressures - Part 1: Assessment of empirical correlations, *International Journal of Heat and Mass Transfer*, vol. 75, pp. 736–753, 2014.
50. C. S. Brooks and T. Hibiki, Wall nucleation modeling in subcooled boiling flow, *International Journal of Heat and Mass Transfer*, vol. 86, pp. 183–196, 2015.
51. B. Končar, E. Krepper, and Y. Egorov, CFD modeling of subcooled flow boiling for nuclear engineering applications, in *Proceedings of the International Conference on Nuclear Energy for New Europe*, 2005.
52. B. Končar, I. Kljenak, and B. Mavko, Modelling of local two-phase flow parameters in upward subcooled flow boiling at low pressure, *International Journal of Heat and Mass Transfer*, vol. 47, no. 6, pp. 1499–1513, 2004.
53. G. H. Yeoh and J. Tu, *Computational Techniques for Multiphase Flows*. 1st ed., 2009.
54. R. Thakrar, J. Murallidharan, and S. P. Walker, An evaluation of the RPI model for the prediction of the wall heat flux partitioning in subcooled boiling flows, in *Proceedings of the 22nd International Conference on Nuclear Engineering*, vol. 5, 2014.
55. E. Krepper, B. Končar, and Y. Egorov, CFD modelling of subcooled boiling—concept, validation and application to fuel assembly design, *Nuclear Engineering and Design*, vol. 237, no. 7, pp. 716–731, 2007.
56. E. Krepper and R. Rzehak, CFD for subcooled flow boiling: Simulation of DEBORA experiments, *Nuclear Engineering and Design*, vol. 241, no. 9, pp. 3851–3866, 2011.
57. M. Colombo and M. Fairweather, Accuracy of Eulerian–Eulerian, two-fluid CFD boiling models of subcooled boiling flows, *International Journal of Heat and Mass Transfer*, vol. 103, pp. 28–44, 2016.

58. C. W. Deane and W. M. Rohsenow, Mechanism and behavior of nucleate boiling heat transfer to the alkali liquid metals, Tech. Rep. TID-25294, MIT Heat Transfer Laboratory, 1969.
59. S. Iyer, A. Kumar, J. Coventry, J. Pye, and W. Lipiński, Micro-scale heat transfer modelling of the contact line region of a boiling-sodium bubble, *International Journal of Heat and Mass Transfer*, vol. 160, p. 120106, 2020.
60. Y. Y. Jiang, H. Osada, M. Inagaki, and N. Horinouchi, Dynamic modeling on bubble growth, detachment and heat transfer for hybrid-scheme computations of nucleate boiling, *International Journal of Heat and Mass Transfer*, vol. 56, no. 1–2, pp. 640–652, 2013.
61. P. Stephan and J. Hammer, A new model for nucleate boiling heat transfer, *Heat Mass Transfer*, vol. 30, no. 2, pp. 119–125, 1994.
62. C. Kunkelmann and P. Stephan, CFD simulation of boiling flows using the Volume-of-Fluid method within OpenFOAM, *Numerical Heat Transfer, Part A: Applications*, vol. 56, no. 8, pp. 631–646, 2009.
63. T. Fuchs, J. Kern, and P. Stephan, A transient nucleate boiling model including microscale effects and wall heat transfer, *Journal of Heat Transfer*, vol. 128, no. 12, pp. 1257–1265, 2006.
64. P. Stephan, T. Fuchs, E. Wagner, and N. Schweizer, Transient local heat fluxes during the entire vapor bubble life time, in *Proceedings of the ECI International Conference on Boiling Heat Transfer*, 2009.
65. S. Fischer, T. Gambaryan-Roisman, and P. Stephan, On the development of a thin evaporating liquid film at a receding liquid/vapour interface, *International Journal of Heat and Mass Transfer*, vol. 88, pp. 346–356, 2015.
66. A. K. Das, P. K. Das, and P. Saha, Heat transfer during pool boiling based on evaporation from micro and macrolayer, *International Journal of Heat and Mass Transfer*, vol. 49, pp. 3487–3499, 2006.
67. V. K. Dhir, Boiling heat transfer, *Annual Review of Fluid Mechanics*, vol. 30, pp. 365–401, 1998.
68. F. D. Moore and R. B. Mesler, The measurement of rapid surface temperature fluctuations during nucleate boiling of water, *AIChE Journal*, vol. 7, no. 4, pp. 620–624, 1961.

69. H. H. Jawurek, Simultaneous determination of microlayer geometry and bubble growth in nucleate boiling, *International Journal of Heat and Mass Transfer*, vol. 12, no. 8, pp. 843–848, 1969.
70. L. D. Koffman and M. S. Plesset, Experimental observations of the microlayer in vapor bubble growth on a heated solid, *Journal of Heat Transfer*, vol. 105, no. 3, pp. 625–632, 1983.
71. S. Jung and H. Kim, An experimental study on heat transfer mechanisms in the microlayer using integrated total reflection, laser interferometry and infrared thermometry technique, *Heat Transfer Engineering*, vol. 36, no. 12, pp. 1002–1012, 2015.
72. S. Hänsch and S. Walker, Microlayer formation and depletion beneath growing steam bubbles, *International Journal of Multiphase Flow*, vol. 111, pp. 241–263, 2019.
73. S. Narayan L and A. Srivastava, On the identification and mapping of three distinct stages of single vapor bubble growth with the corresponding microlayer dynamics, *International Journal of Multiphase Flow*, vol. 142, p. 103722, 2021.
74. G. E. Thorncroft and J. F. Klausner, Bubble forces and detachment models, *Multiphase Science and Technology*, vol. 13, pp. 35–76, 2001.
75. M. S. Plesset and S. A. Zwick, The growth of vapor bubbles in superheated liquids, *Journal of Applied Physics*, vol. 25, no. 4, pp. 493–500, 1954.
76. H. K. Forster and N. Zuber, Growth of a vapor bubble in a superheated liquid, *Journal of Applied Physics*, vol. 25, no. 4, pp. 474–478, 1954.
77. L. Scriven, On the dynamics of phase growth, *Chemical Engineering Science*, vol. 10, no. 1, pp. 1–13, 1959.
78. C. Han and P. Griffith, The mechanism of heat transfer in nucleate pool boiling—Part I: Bubble initiation, growth and departure, *International Journal of Heat and Mass Transfer*, vol. 8, no. 6, pp. 887–904, 1965.
79. R. Cole and H. L. Shulman, Bubble growth rates at high jakob numbers, *International Journal of Heat and Mass Transfer*, vol. 9, no. 12, pp. 1377–1390, 1966.
80. N. Zuber, The dynamics of vapor bubbles in nonuniform temperature fields, *International Journal of Heat and Mass Transfer*, vol. 2, pp. 83–98, 1961.
81. B. B. Mikic, W. M. Rohsenow, and P. Griffith, On bubble growth rates, *International Journal of Heat and Mass Transfer*, vol. 13, no. 4, pp. 657–666, 1970.

82. O. Miyatake, I. Tanaka, and N. Lior, A simple universal equation for bubble growth in pure liquids and binary solutions with a non-volatile solute, *International Journal of Heat and Mass Transfer*, vol. 40, no. 7, pp. 1577–1584, 1997.
83. M. G. Cooper and A. J. P. Lloyd, The microlayer in nucleate pool boiling, *International Journal of Heat and Mass Transfer*, vol. 12, no. 8, pp. 895–913, 1969.
84. G. Son, V. K. Dhir, and N. Ramanujapu, Dynamics and heat transfer associated with a single bubble during nucleate boiling on a horizontal surface, *Journal of Heat Transfer*, vol. 121, pp. 623–631, 1999.
85. Y. Zhao and T. Tsuruta, Prediction of bubble behavior in subcooled pool boiling based on microlayer model, *JSME International Journal Series B*, vol. 45, no. 2, pp. 346–354, 2002.
86. N. R. Snyder and D. K. Edwards, Summary of conference on bubble dynamics and boiling heat transfer, Tech. Rep., Jet Propulsion Laboratory, 1956.
87. M. Potash Jr. and P. C. Wayner Jr., Evaporation from a two-dimensional extended meniscus, *International Journal of Heat and Mass Transfer*, vol. 15, no. 10, pp. 1851–1863, 1972.
88. S. Batzdorf, *Heat transfer and evaporation during single drop impingement onto a superheated wall*. PhD thesis, Technische Universität Darmstadt, 2015.
89. S. Batzdorf, T. Gambaryan-Roisman, and P. Stephan, Direct numerical simulation of the microscale fluid flow and heat transfer in the three-phase contact line region during evaporation, *Journal of Heat Transfer*, vol. 140, no. 3, p. 032401, 2018.
90. H. Wang, S. V. Garimella, and J. Y. Murthy, Characteristics of an evaporating thin film in a microchannel, *International Journal of Heat and Mass Transfer*, vol. 50, no. 19, pp. 3933–3942, 2007.
91. K. Sefiane, D. Benielli, and A. Steinchen, A new mechanism for pool boiling crisis, recoil instability and contact angle influence, *Colloids and Surfaces A: Physicochemical and Engineering Aspects*, vol. 142, no. 2–3, pp. 361–373, 1998.
92. R. W. Schrage, *A theoretical study of interphase mass transfer*. Columbia University Press, 1953.
93. R. Marek and J. Straub, Analysis of the evaporation coefficient and the condensation coefficient of water, *International Journal of Heat and Mass Transfer*, vol. 44, no. 1, pp. 39–53, 2001.

94. Y. Utaka, Y. Kashiwabara, and M. Ozaki, Microlayer structure in nucleate boiling of water and ethanol at atmospheric pressure, *International Journal of Heat and Mass Transfer*, vol. 57, no. 1, pp. 222–230, 2013.
95. A. Guion, D. Langewisch, and J. Buongiorno, Dynamics of the liquid microlayer underneath a vapor bubble growing at a heated wall, in *Proceedings of the ASME Heat Transfer Summer Conference*, 2013.
96. O. E. Dwyer and C. J. Hsu, Liquid microlayer thickness in nucleate boiling on a heated surface, *Letters in Heat and Mass Transfer*, vol. 2, no. 2, pp. 179–187, 1975.
97. A. Guion, S. Afkhami, S. Zaleski, and J. Buongiorno, Simulations of microlayer formation in nucleate boiling, *International Journal of Heat and Mass Transfer*, vol. 127, pp. 1271–1284, 2018.
98. A. Urbano, S. Tanguy, G. Huber, and C. Colin, Direct numerical simulation of nucleate boiling in micro-layer regime, *International Journal of Heat and Mass Transfer*, vol. 123, pp. 1128–1137, 2018.
99. L. Bureš and Y. Sato, On the modelling of the transition between contact-line and microlayer evaporation regimes in nucleate boiling, *Journal of Fluid Mechanics*, vol. 916, 2021.
100. H. Setoodeh, W. Ding, L. Dirk, and U. Hampel, Prediction of bubble departure in forced convection boiling with a mechanistic model that considers dynamic contact angle and base expansion, *Energies*, vol. 12, no. 10, p. 1950, 2019.
101. K. H. Ardron, G. Giustini, and S. P. Walker, Prediction of dynamic contact angles and bubble departure diameters in pool boiling using equilibrium thermodynamics, *International Journal of Heat and Mass Transfer*, vol. 114, pp. 1274–1294, 2017.
102. A. Zou, A. Chanana, A. Agrawal, P. C. Wayner, and S. C. Maroo, Steady state vapor bubble in pool boiling, *Scientific Reports*, vol. 6, no. 20240, pp. 1–8, 2016.
103. D. Sarker, W. Ding, and U. Hampel, Bubble growth during subcooled nucleate boiling on a vertical heater: A mechanistic attempt to evaluate the role of surface characteristics on microlayer evaporation, *Applied Thermal Engineering*, vol. 153, pp. 565–574, 2019.
104. D. Guo, X. Li, H. Zhang, F. Li, W. Su, and H. Zhu, Bubble behaviors during subcooled pool boiling in water and nonionic surfactant aqueous solution, *International Journal of Heat and Mass Transfer*, vol. 159, p. 120087, 2020.

105. S. Raj, M. Pathak, and M. K. Khan, An analytical model for predicting growth rate and departure diameter of a bubble in subcooled flow boiling, *International Journal of Heat and Mass Transfer*, vol. 109, pp. 470–481, 2017.
106. W. E. Ranz and W. R. Marshall, Evaporation from drops, *Chemical Engineering Progress*, vol. 48, no. 3, pp. 141–146, 1952.
107. S. Bankoff and H. K. Choi, Growth of a bubble at a heated surface in a pool of liquid metal, *International Journal of Heat and Mass Transfer*, vol. 19, no. 1, pp. 87–93, 1976.
108. J. F. Klausner, R. Mei, D. M. Bernhard, and L. Z. Zeng, Vapor bubble departure in forced convection boiling, *International Journal of Heat and Mass Transfer*, vol. 36, no. 3, pp. 651–662, 1993.
109. X. Wang, Z. Wu, J. Wei, and B. Sundén, Correlations for prediction of the bubble departure radius on smooth flat surface during nucleate pool boiling, *International Journal of Heat and Mass Transfer*, vol. 132, pp. 699–714, 2019.
110. J. Bhati and S. Paruya, Numerical simulation of bubble dynamics in pool boiling at heated surface, *International Journal of Heat and Mass Transfer*, vol. 152, p. 119465, 2020.
111. S. Paruya, J. Bhati, and F. Akthar, Numerical model of bubble shape and departure in nucleate pool boiling, *International Journal of Heat and Mass Transfer*, vol. 180, p. 121756, 2021.
112. M. Bucci, J. Buongiorno, and M. Bucci, The not-so-subtle flaws of the force balance approach to predict the departure of bubbles in boiling heat transfer, *Physics of Fluids*, vol. 33, no. 1, p. 017110, 2021.
113. Y. Zhang, J. Wei, Y. Xue, X. Kong, and J. Zhao, Bubble dynamics in nucleate pool boiling on micro-pin-finned surfaces in microgravity, *Applied Thermal Engineering*, vol. 70, no. 1, pp. 172–182, 2014.
114. J. Yoo and Y. A. Hassan, Force balance model assessment for mechanistic prediction of sliding bubble velocity in vertical subcooled boiling flow, Tech. Rep. INL/CON-19-53204, Idaho National Laboratory, 2020.
115. D. Chen, L. Pan, and S. Ren, Prediction of bubble detachment diameter in flow boiling based on force analysis, *Nuclear Engineering and Design*, vol. 243, pp. 263–271, 2012.

116. M. Colombo and M. Fairweather, Prediction of bubble departure in forced convection boiling: A mechanistic model, *International Journal of Heat and Mass Transfer*, vol. 85, pp. 135–146, 2015.
117. W. T. Sha and V. L. Shah, Bubble dynamics in a superheated liquid, Tech. Rep. ANL-77-20, Argonne National Laboratory, 1977.
118. M. A. Johnson Jr., J. D. L. Peña, and R. B. Mesler, Bubble shapes in nucleate boiling, *AIChE Journal*, vol. 12, no. 2, pp. 344–348, 1966.
119. N. B. Hospeti and R. B. Mesler, Vaporization at the base of bubbles of different shape during nucleate boiling of water, *AIChE Journal*, vol. 15, no. 2, pp. 214–219, 1969.
120. A. Mukherjee and S. G. Kandlikar, Effect of dynamic contact angle on single bubbles during nucleate pool boiling, in *Proceedings of the ASME International Mechanical Engineering Congress and Exposition*, pp. 555–562, 2004.
121. S. Siedel, S. Cioulachtjian, and J. Bonjour, Experimental analysis of bubble growth, departure and interactions during pool boiling on artificial nucleation sites, *Experimental Thermal and Fluid Science*, vol. 32, no. 8, pp. 1504–1511, 2008.
122. H. K. Forster and N. Zuber, Dynamics of vapor bubbles and boiling heat transfer, *AIChE Journal*, vol. 1, no. 4, pp. 531–535, 1955.
123. A. M. Kiper, Minimum bubble departure diameter in nucleate pool boiling, *International Journal of Heat and Mass Transfer*, vol. 14, no. 7, pp. 931–937, 1971.
124. F. Lesage, S. Siedel, J. S. Cotton, and A. J. Robinson, A mathematical model for predicting bubble growth for low Bond and Jakob number nucleate boiling, *Chemical Engineering Science*, vol. 112, pp. 35–46, 2014.
125. H. T. Phan, N. Caney, P. Marty, S. Colasson, and J. Gavillet, Surface wettability control by nanocoating: The effects on pool boiling heat transfer and nucleation mechanism, *International Journal of Heat and Mass Transfer*, vol. 52, no. 23–24, pp. 5459–5471, 2009.
126. J. Cai, Z. Gong, and B. Tan, Experimental and theoretical investigation of bubble dynamics on vertical surfaces with different wettability for pool boiling, *International Journal of Thermal Sciences*, vol. 184, p. 107966, 2023.
127. Y. Nam, E. Aktinol, V. K. Dhir, and Y. S. Ju, Single bubble dynamics on a superhydrophilic surface with artificial nucleation sites, *International Journal of Heat and Mass Transfer*, vol. 54, no. 7-8, pp. 1572–1577, 2011.

128. J. Cai, Z. Gong, Z. Tang, X. Li, Y. Wang, H. Yin, and X. Yang, Experimental characterization of the bubble neck formation during its growth process on a superhydrophobic surface, *Nuclear Engineering and Design*, vol. 367, p. 110762, 2020.
129. Y. Li, K. Zhang, M. Lu, and C. Duan, Single bubble dynamics on superheated superhydrophobic surfaces, *International Journal of Heat and Mass Transfer*, vol. 99, pp. 521–531, 2016.
130. P. Kangude and A. Srivastava, Understanding the growth mechanism of single vapor bubble on a hydrophobic surface: Experiments under nucleate pool boiling regime, *International Journal of Heat and Mass Transfer*, vol. 154, p. 119775, 2020.
131. H. Kim and J. Buongiorno, Detection of liquid–vapor–solid triple contact line in two-phase heat transfer phenomena using high-speed infrared thermometry, *International Journal of Multiphase Flow*, vol. 37, no. 2, pp. 166–172, 2011.
132. M. Akiyama, F. Tachibana, and N. Ogawa, Effect of pressure on bubble growth in pool boiling, *Bulletin of JSME*, vol. 12, no. 53, pp. 1121–1128, 1969.
133. J. C. Chen, Effect of turbulent flow on incipient boiling superheat, in *Summaries of Presentations from First Meeting, Technical Working Group on Liquid-Metal Thermal Science*, 1969.
134. O. E. Dwyer, G. Strickland, S. Kalish, P. Hlavac, and G. A. Schoener, Incipient-boiling superheat for sodium in turbulent, channel flow: Effects of heat flux and flow rate, *International Journal of Heat and Mass Transfer*, vol. 16, no. 5, pp. 971–984, 1973.
135. G. Giustini, H. Kim, R. I Issa, and M. J Bluck, Modelling microlayer formation in boiling sodium, *Fluids*, vol. 5, no. 4, p. 213, 2020.
136. J. B. Tipton, K. Kihm, and D. M. Pratt, Modeling alkaline liquid metal (Na) evaporating thin films using both retarded dispersion and electronic force components, *Journal of Heat Transfer*, vol. 131, no. 12, p. 121015, 2009.
137. B. V. Derjaguin, L. F. Leonov, and V. I. Roldughin, Disjoining pressure in liquid metallic films, *Journal of Colloid and Interface Science*, vol. 108, no. 1, pp. 207–214, 1985.
138. V. S. Ajaev and D. A. Willis, Thermocapillary flow and rupture in films of molten metal on a substrate, *Physics of Fluids*, vol. 15, no. 10, pp. 3144–3150, 2003.
139. V. S. Ajaev and D. A. Willis, Heat transfer, phase change, and thermocapillary flow in films of molten metal on a substrate, *Numerical Heat Transfer*, vol. 50, no. 4, pp. 301–313, 2006.

140. H. Yi, J. Tipton, K. D. Kihm, D. M. Pratt, A. D. Swanson, and S. Rawal, Effect of disjoining pressure (II) on multi-scale modeling for evaporative liquid metal (Na) capillary, *International Journal of Heat and Mass Transfer*, vol. 78, pp. 137–149, 2014.
141. O. E. Dwyer, Growth rates of hemispherical bubbles in nucleate boiling of liquid metals, *Chemical Engineering Science*, vol. 31, no. 3, pp. 187–193, 1976.
142. R. Cole and W. M. Rohsenow, Correlation of bubble departure diameters for boiling of saturated liquids, in *Proceedings of the Chemical Engineering Progress Symposium Series*, vol. 65, pp. 211–213, 1969.
143. I. E. Dzyaloshinskii, E. M. Lifshitz, and L. P. Pitaevskii, The general theory of van der waals forces, in *Perspectives in Theoretical Physics*, pp. 443–492, 1992.
144. P. Stephan, *Wärmedurchgang bei Verdampfung aus Kapillarrillen in Wärmerohren*. VDI-Verlag, 1992.
145. L. F. Shampine and M. W. Reichelt, The MATLAB ODE suite, *SIAM Journal on Scientific Computing*, vol. 18, no. 1, pp. 1–22, 1997.
146. J. R. Dormand and P. J. Prince, A family of embedded Runge–Kutta formulae, *Journal of Computational and Applied Mathematics*, vol. 6, no. 1, pp. 19–26, 1980.
147. M. Schäfer, Bestimmung der Blasenfrequenz an einer einzelnen Keimstelle mittels numerischer Simulation, Master’s thesis, Technische Universität Darmstadt, 2013.
148. C. Sodtke, J. Kern, N. Schweizer, and P. Stephan, High resolution measurements of wall temperature distribution underneath a single vapour bubble under low gravity conditions, *International Journal of Heat and Mass Transfer*, vol. 49, no. 5–6, pp. 1100–1106, 2006.
149. P. C. Wayner Jr, Y. K. Kao, and L. V. LaCroix, The interline heat-transfer coefficient of an evaporating wetting film, *International Journal of Heat and Mass Transfer*, vol. 19, no. 5, pp. 487–492, 1976.
150. J. K. Fink and L. Leibowitz, Thermodynamic and transport properties of sodium liquid and vapor, Tech. Rep. ANL/RE-95/2, Argonne National Laboratory, 1995.
151. J. N. Israelachvili, *Intermolecular and surface forces*. 3rd ed., 2015.
152. E. A. T. Van Den Akker, A. J. H. Frijns, C. Kunkelmann, P. A. J. Hilbers, P. Stephan, and A. Van Steenhoven, Molecular dynamics simulation of the microregion, *International Journal of Thermal Sciences*, vol. 59, pp. 21–28, 2012.

153. A. H. Persad and C. A. Ward, Expressions for the evaporation and condensation coefficients in the Hertz–Knudsen relation, *Chemical Reviews*, vol. 116, no. 14, pp. 7727–7767, 2016.
154. J. P. Holman, *Heat transfer*. McGraw-Hill, 10th ed., 2010.
155. N. Sheriff and N. W. Davies, Liquid metal natural convection from plane surfaces: A review including recent sodium measurements, *International Journal of Heat and Fluid Flow*, vol. 1, no. 4, pp. 149–154, 1979.
156. ANSYS Inc., ANSYS Fluent Theory Guide 17.1, 2017.
157. R. Siegel and E. G. Keshock, Effects of reduced gravity on nucleate boiling bubble dynamics in saturated water, *AIChE Journal*, vol. 10, no. 4, pp. 509–517, 1964.
158. G. Giustini, S. Jung, H. Kim, K. H. Ardron, and S. P. Walker, Microlayer evaporation during steam bubble growth, *International Journal of Thermal Sciences*, vol. 137, pp. 45–54, 2019.
159. Y. S. Touloukian, *Thermophysical Properties of High Temperature Solid Materials. Volume 1. Elements*. 1966.
160. S. G. Bankoff, Entrapment of gas in the spreading of a liquid over a rough surface, *AIChE journal*, vol. 4, no. 1, pp. 24–26, 1958.
161. P. Griffith and J. D. Wallis, The role of surface conditions in nucleate boiling, Tech. Rep. 14, Massachusetts Institute of Technology, 1958.
162. E. W. Lemmon, M. O. McLinden, and D. G. Friend, *NIST Chemistry WebBook, NIST Standard Reference Database Number 69*, ch. Thermophysical Properties of Fluid Systems. National Institute of Standards and Technology, 1998.
163. I. H. Bell, J. Wronski, S. Quoilin, and V. Lemort, Pure and pseudo-pure fluid thermophysical property evaluation and the open-source thermophysical property library CoolProp, *Industrial & Engineering Chemistry Research*, vol. 53, no. 6, pp. 2498–2508, 2014.
164. C. E. Kolb, P. Davidovits, J. T. Jayne, Q. Shi, and D. R. Worsnop, Kinetics of trace gas uptake by liquid surfaces, *Progress in Reaction Kinetics and Mechanism*, vol. 27, no. 1, pp. 1–46, 2002.
165. R. Bader and W. Lipiński, Solar thermochemical processes, in *Solar Energy*, vol. 2, pp. 345–394, World Scientific, 2016.

166. R. Bader and W. Lipiński, Solar thermal processing, in *Advances in Concentrating Solar Thermal Research and Technology*, pp. 403–459, Woodhead Publishing, 2017.
167. W. Lipiński, ed., *Solar Thermochemistry*, vol. 58 of *Advances in Chemical Engineering*. Academic Press, 2021.
168. J. Chen, A. Kumar, J. Coventry, and W. Lipiński, Heat transfer in directly-irradiated high-temperature solid–gas flows laden with polydisperse particles, *Applied Mathematical Modelling*, vol. 110, pp. 698–722, 2022.
169. A. Andruszkiewicz, K. Eckert, S. Eckert, and S. Odenbach, Gas bubble detection in liquid metals by means of the ultrasound transit-time-technique, *The European Physical Journal Special Topics*, vol. 220, pp. 53–62, 2013.
170. M. Ratajczak, T. Gundrum, F. Stefani, and T. Wondrak, Contactless inductive flow tomography: Brief history and recent developments in its application to continuous casting, *Journal of Sensors*, 2014.
171. T. Gundrum, P. Büttner, B. Dekdouk, A. Peyton, T. Wondrak, V. Galindo, and S. Eckert, Contactless inductive bubble detection in a liquid metal flow, *Sensors*, vol. 16, p. 63, 2016.